THE UNIVERSITY *of* EDINBURGH

Genesis of fault hosted carbonate fracture cements in a naturally high CO_2 province, South Viking Graben, UK North Sea

David Robert Lee

Doctor of Philosophy

The University of Edinburgh

2013

Declaration

I declare that this thesis is entirely my own work except where indicated otherwise and that it has not been submitted, either whole or in part, for any other degree or professional qualification.

David Robert Lee
May 2013

Abstract

Genesis of fault hosted carbonate fracture cements in a naturally high CO_2 province, South Viking Graben, UK North Sea

David Lee

The Late Jurassic Brae oilfields in the South Viking Graben of the northern North Sea contain naturally high concentrations of carbon dioxide (up to 35 mol %). Fields immediately adjacent to the graben bounding fault display the highest concentrations, with CO_2 content decreasing eastward into the basin. It is thought the CO_2 was introduced into the region via this fault. This thesis examines the possible source of the high CO_2 present in the region, focusing on the graben margin fault as a potential conduit for CO_2 flux from depth

Investigation of cored sections penetrating the graben bounding fault revealed numerous carbonate cemented fracture arrays. The morphology of the fractures and cements is attributed to hydraulic fracturing induced by episodic release of overpressured fluids up the margin fault from depth. Periods of rapid subsidence omnipresent throughout the tectonic history of the graben are conducive to the generation of overpressure; a feature commonly reported in the region. Samples from the carbonate fracture cements were analysed using a host of techniques, including SEM, EMPA, fluid inclusion, and stable $\delta^{13}C$ - $\delta^{18}O$ analyses. Using SEM analysis, at least five generations of dolomite cement with concomitant iron sulphide were observed. Cement chemistry and textures indicate precipitation from concentrated CO_2–rich fluids. A reported high salinity basinal influx from depth concomitant with proposed CO_2 charge into the region ~70 Ma is a probable source for the dissolved solids subsequently precipitated as carbonate in the fracture networks. Fluid inclusion analysis provided sufficient evidence to suggest the influx of hot fluids into the region, presumably sourced from deep in the margin fill.

Two distinct $\delta^{13}C$ vs. $\delta^{18}O$ trends are observed in the isotope data from four wells studied. The trends are interpreted as differential mixing between ascending basinal fluids rich in dissolved inorganic carbon and *in situ* formation waters dominated by organically derived carbon following the onset of thermal decarboxylation in the Kimmeridge Clay Formation. Dissolution of Zechstein carbonates underlying the region is a credible source for the isotopically heavy CO_2 found adjacent to the graben margin ($\delta^{13}C_{CO2}$ = -2 to -5 ‰) and incorporated into the carbonate cements. Inferred variations in fluid mixing from well to well have implications on the variability of fluid flow along the graben margin with respect to contrasting fault morphologies. A Rayleigh fractionation model accommodating CO_2 degassing from a hot ascending isotopically heavy fluid can be invoked to explain the observed carbon-oxygen isotopic covariations in the fracture cements. Geochemical modelling simulating the ascent of CO_2-rich waters suggests degassing has limited impact on precipitation volumes, with fluid-rock reactions the most likely driver for extensive carbonate mineralisation observed.

Acknowledgements

I would like to thank EPSRC and members of the SCCS consortium for the funding provided for this project. Many thanks to my supervisors Stuart Haszeldine and Mark Wilkinson for their guidance and for giving me the opportunity to work on this project. I wish to thank Marathon Oil (U.K.) and Colin Turner for access to sample core material essential for the investigation. I also wish to thank the British Geological Survey and the staff at the Gilmerton Corestore, Edinburgh, for access to core material and assistance in sampling. Special thanks to the academic and technical staff in the Grant Institute whose guidance and assistance was invaluable; Nicola Cayzer, Colin Chilcott, John Craven, Mike Hall, and Nic Odling, Many thanks to Adrian Boyce, Tony Fallick, Vincent Gallagher, and Anne Kelly at SUERC for advice and analysis concerning stable and strontium isotope aspects of the study. And finally, extra special thanks to Amy Wynne-Jones. Without her unwavering support and encouragement this thesis would certainly not be here today.

Contents

Chapter 1

Introduction

1.1. Introduction

Increasing global industrialisation since the industrial revolution has led to rising concentrations of carbon dioxide in the atmosphere. The presence of CO_2, the most abundant greenhouse gas, accounts for approximately 64 % of the anthropogenic emissions contributing to global warming (Gale, 2004). Atmospheric concentrations of CO_2 have risen from pre-industrial levels of 280 to 390 parts per million (ppm) in the present day (Tans, 2011), primarily as a result of fossil fuel combustion (Bryant, 1997). Increasing concentration of atmospheric CO_2 has the potential to enhance the Earth's natural greenhouse effect and thus exert a greater warming influence upon the planet's surface. Because of complexities and uncertainties regarding the Earth's climate, the extent of the potential impacts is inconclusive (Bachu, 2003). However, climate scientists argue that atmospheric carbon dioxide levels should not be allowed to exceed 550 ppm

or the effects of global warming could be catastrophic for the Earth in its inhabitants (Schiermeier, 2006).

In the long-term, switching to lower or non-carbon fuels and renewable sources of energy, coupled with efficiency improvements and energy conservation are promising alternatives to fossil fuel use. However, even with favourable projections of technology development and policy regimes, the transition from the current dependence on fossil fuels would take many decades or longer (Anderson & Newell, 2004; Hepple & Benson, 2005).

1.2. Carbon Capture and Storage

As a consequence, the potential application of Carbon Capture and Storage (CCS) is considered a key mechanism for reducing anthropogenic CO_2 emissions into the atmosphere, potentially mitigating the current changing climatic trend if the use of fossil fuels is to be continued (Metz *et al*., 2005; Haszeldine, 2009). The basic concept of CCS is to capture anthropogenic CO_2 at source (e.g. via separation from power station flue gases) prior to transporting and injecting into suitable subsurface geological formations. Following injection, CO_2 can be potentially stored through a series of methods:

- *Stratigraphic and structural trapping* occurs initially when CO_2 is physically stored in gaseous or supercritical phase within the host media. Such a storage mechanism is analogous to hydrocarbon retention in petroleum reservoirs, with the CO_2 storage in porous lithologies sealed by low permeability caprocks or structurally isolated.

- *Residual saturation trapping* whereby injected non-aqueous CO_2 becomes trapped and subsequently stored within the intragranular porespace present in the injected lithology.

- *Solution trapping* relates to the dissolution of injected CO_2 into aqueous phases already present in the selected storage formation (e.g. formation water).

- *Mineral trapping* occurs when CO_2 dissolved in formation waters reacts with the host lithology, precipitating minerals (e.g. carbonates) which trap the CO_2 indefinitely within the crystal lattice (e.g. Caldeira & Rau, 2000).

Each of the above storage mechanisms are achieved over progressively larger timescales with each providing increasing storage safety. For example, through mineral trapping, the injected CO_2 becomes safely stored, with no leakage, whereas the potentially catastrophic effects on human populations resulting from leakage of gaseous phase CO_2 are widely documented (e.g. Lake Nyos; Le Guern *et al.*, 1992). To achieve optimum storage capacity, CO_2 should ideally be injected and stored below approximately 800m depth, where it will be in supercritical phase (Oldenburg & Unger, 2003). Several geological formation types have been proposed for the injection and storage of CO_2 (Figure 1.1);

- *Deep saline aquifers* have the greatest CO_2 storage potential in terms of volume (up to 10,000 Gt CO_2; Gale, 2004). At the current Sleipner CO_2 injection project (offshore Norway) storage is achieved mostly through residual and structural trapping.

- *Coal beds* allow injected CO_2 to be absorbed and stored permanently in the coal matrix at the expense of methane (in a molar ratio 2:1). The displaced methane can be captured; a potentially attractive economic benefit (e.g. Enhanced Coal Bed Methane projects, Alberta, Canada)

- *Existing oil and gas reservoirs* exhibit proven storage potential over geological periods of time and due to existing knowledge and infrastructure represent the most viable near-term CO_2 storage solution.

Numerous authors (e.g. Bachu, 2000; Baines and Worden, 2004) have affirmed the case that since non-aqueous fluids and gases (e.g. petroleum accumulations) are naturally trapped in the subsurface for geological periods of time, then it is plausible that CO_2 can be injected and stored for a period of 10^4 – 10^5 years suggested for stabilisation and

remediation of the atmosphere (Baines & Worden, 2004). The injection of carbon dioxide into hydrocarbon bearing rocks is already employed worldwide in enhanced oil recovery (EOR) programmes due to its properties as a good solvent for organic compounds (Blunt *et al*., 1993). However, the long-term effects of CO_2 containment within such geological media are largely unknown. Coupled to this is the potential risk of leakage. Faults and fracture networks within the vicinity of possible storage sites pose a risk of large-scale leakage and migration of injected CO_2 (Holloway, 1997). This risk is exacerbated by increasing formation pressures through injection, a process which could facilitate the opening of existing fractures (Klusman, 2003).

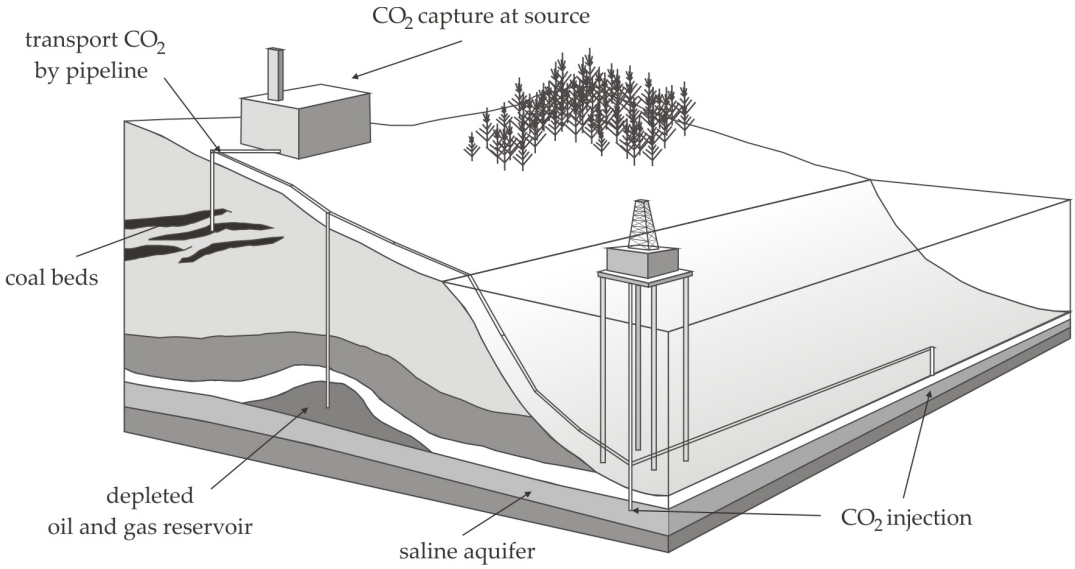

Figure 1.1. Schematic diagram illustrating the process and various storage options for geological storage of CO_2. Modified from Bachu (2003). Illustration not to scale.

Although the effects of weak acids have been investigated since the advent of diagenetic studies there is a relatively new focus on CO_2 in the subsurface and its effects on the geochemical and petrophysical properties of sandstones and mudrocks; the principle lithologies in both oilfields and aquifer systems into which CO_2 injection is proposed. Numerous researchers have attempted to model the long-term effect of dissolved CO_2 upon minerals in the surrounding strata. There are numerous uncertainties associated

with the effect of carbonic acid (H_2CO_3), formed through the dissolution reaction, on both the storage potential and sealing integrity of possible injection formations. Geochemical simulations suggest that a host of dissolution and precipitation reactions over a range of timescales involving both carbonate and silicate minerals occur through the addition of CO_2 (e.g. Caldeira & Rau, 2000; Knauss *et al*., 2005; Xu *et al*., 2005; Zerai *et al*., 2006). As a result, contrasting conclusions regarding the safety and viability of CO_2 storage in the subsurface are often reached.

However, these modelling approaches typically utilise kinetic and thermodynamic data derived from short timescale experiments where reaction rates are significantly increased and thus do not accurately reflect CO_2 reactions in the subsurface at the long timescales (10^4 – 10^5 years) anticipated for effective storage (Gaus *et al*., 2005).

1.3. Natural analogues

One method to evaluate the effect of elevated CO_2 concentrations in the subsurface over timescales recommended for CO_2 storage is to study existing analogous naturally high-CO_2 geological systems. Though relatively rare, significant CO_2 accumulations within geological settings do occur worldwide (Thrasher & Fleet, 1995; Pearce *et al*., 2004). Examination of such natural analogues is vital in understanding the behaviour of CO_2 in the subsurface, with particular emphasis on the effect of CO_2 *in situ* (i.e. storage potential, caprock integrity), and in movement (e.g. fault leakage, buoyant flow). A number of previous studies on natural analogues have been conducted to investigate possible mineralogical reactions in high CO_2 formations regarding mineral trapping (e.g. Moore *et al*., 2005; Worden, 2006; Wilkinson *et al*., 2009) and storage integrity.

For example, in the high CO_2 Miller Field (North Sea), Lu *et al*. (2009) argued that a distinct linear trend of decreasing $\delta^{13}C$ in the overlying caprock represented the dissolution and re-precipitation of carbonate cements in the mudrock due to long-term interaction with CO_2 present in the reservoir. Significantly, the linear trend only extended 12m vertically into the caprock. Given that the CO_2 was estimated to be emplaced ~70 – 80 Ma , this suggests that infiltration and reaction rates between CO_2

and host lithologies is relatively slow, suggesting that subsurface storage of CO_2 has no long term detrimental effect upon sealing caprocks.

Such observations differ markedly to those of Houston *et al.* (2007) who argued that changes in water chemistry from production data in the same field suggested that reactions between injected fluids and the silicate host rock minerals took place within a matter of months. The authors proposed that changes in water chemistry occurred as a result of mineral dissolution or precipitation caused by the change in the mineral saturation state of water. However, irrespective of the differing conclusions, such investigations irrefutably add to the ever increasing research literature concerning the potential for geological carbon storage and aid the calibration and validation of geochemical models for long-term CO_2 reactions in the subsurface.

It has been well documented that natural CO_2 accumulations are predominantly associated with regions heavily influenced by tectonism and/or volcanism (Pearce *et al*., 2004). Where CO_2 is actively leaking at the surface, opportunities arise to study migration pathways and possible leakage mechanisms. For example, Shipton *et al*. (2004) observed active and ancient fault controlled CO_2 leakage conduits in the Paradox Basin, Utah, which have evolved in location over time. Understanding the origin and evolution of CO_2-rich fluids in natural systems is a key aspect in understanding the migration, emplacement, and possible subsequent leakage of CO_2. Though it is often difficult to identify a specific source of CO_2 in geological systems, a number of possible sources exist (Figure 1.2).

A number of studies of active terrestrial CO_2 leaking systems have attempted to determine the source of CO_2 discharges. Bergfeld *et al*. (2001) and Siegel *et al*. (2004) used stable isotope analysis ($\delta^{13}C$ and $\delta^{18}O$) to constrain the source of gaseous CO_2 in The Geysers – Clear Lake region (northern California, USA), and the Saratoga Springs (New York, USA), respectively. Stable isotopes, used in conjunction with other analytical methods (e.g. petrography, geochemistry, fluid inclusion microthermometry), are valuable tools in understanding ancient fluid flow systems and frequently employed in

the investigation of hydrothermal ore deposits (e.g. Winter *et al*., 1995; Malone *et al*., 1996).

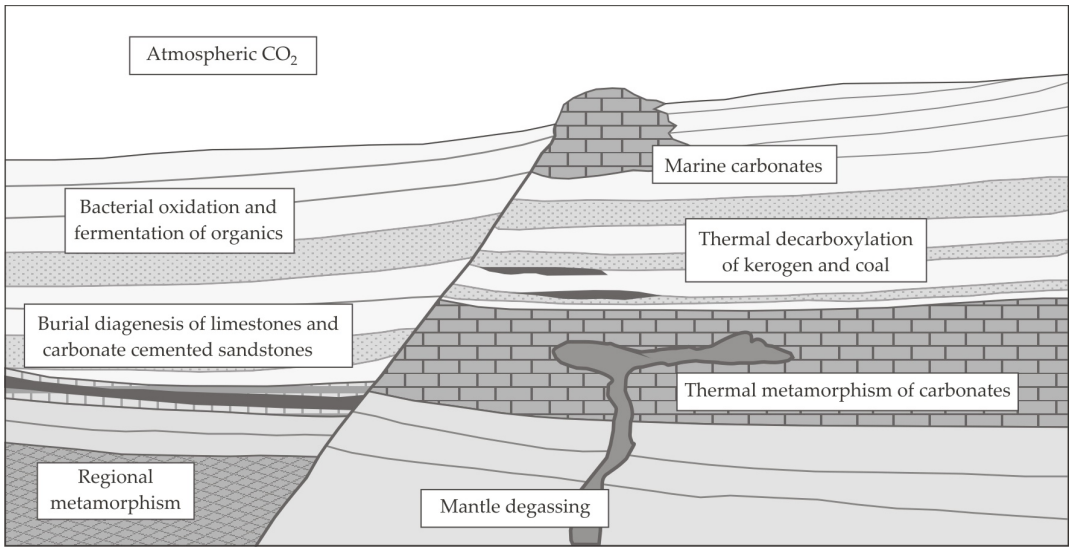

Figure 1.2. Schematic illustration highlighting the range of possible natural CO_2 sources in geological systems. Modified from Baines & Worden (2004).

Previous studies have used such techniques to help delineate the source of CO_2 in ancient fluid flow systems. Isotopic analysis of fracture cements recording the movement of CO_2-rich fluids has been conducted in a range of localities; the Santa Barbara basin (Boles & Grivetti, 2000), the Woodlark Basin, SE Asia (Kopf *et al*., 2003), and the Italian Alps (Sacchi *et al*., 2004). This study adopts a similar approach to demonstrate the fluid flow history of CO_2-rich fluxes responsible for a significant natural CO_2 accumulation in the North Sea, UK.

1.4. Thesis aims and objectives

For this project, the western margin of the South Viking Graben in the North Sea was selected. The Late Jurassic Brae Formation siliciclastic reservoir adjacent to the faulted graben boundary contain up to 35 %mol CO_2 in the hydrocarbons present. The effects of the naturally high CO_2 accumulation has been studied previously, demonstrating the long-term safe storage of CO_2 in the Miller Field (Lu *et al*., 2009) (*see section 1.3*).

However, the source of the localised large volume of CO_2 in the area is enigmatic. Carbon dioxide distribution maps of the region suggest a spatial link between high CO_2 levels and the graben margin. As a result numerous researchers have postulated that the graben bounding fault acted as a conduit, transporting CO_2 into the reservoirs from an undetermined source (e.g. James, 1990; Wycherley *et al*., 1999; Baines & Worden, 2004). A number of possible CO_2 sources deep within the graben fill exist, including; mantle degassing, degradation of Zechstein carbonates, and thermal decarboxylation of organic matter. Given the extensive exploration history of the Brae region, a plethora of existing research regarding most aspects of sedimentary and structural geology is available both commercially and publicly (e.g. Stow & Atkin, 1987; Cherry, 1993; Marchand *et al*., 2001). In view of potential carbon storage options in the North Sea, a number of recent publications specifically focused on the elevated CO_2 levels in the reservoirs of the area are also available (Baines & Worden, 2004; Lu *et al*., 2009).

This thesis aims to provide a greater understanding into the origin of the high-CO_2 concentrations present in the Jurassic hydrocarbon accumulations adjacent to the western graben bounding fault in the South Viking Graben region. Evidence of CO_2 flux up the fault zone will help verify previous assumptions that the graben margin has acted as a conduit for CO_2 transport and subsequent emplacement into the reservoirs (e.g. Baines & Worden, 2004). Through investigation of the fault zone mineralogy, the project aims to constrain a source for the CO_2 in the context of the regional geology whilst providing mechanisms and models for its transport and emplacement based on data acquired in this study in conjunction with previous studies. In addition, the investigation of ancient CO_2 flow in the subsurface can provide a greater understanding of subsurface processes in equivalent present-day terrestrial CO_2 leakages (e.g. Utah, Italy).

The objectives of this study are to:

- Evaluate the fault damage zone on the graben margin and the potential implications this has on the nature and timing of fluid flow in the fault zone, specifically with respect to a hypothesised CO_2 flux.

- Assess the composition and conditions of fluids preserved in the fault zone mineralogy to determine a fluid source and flow history.

- Utilise a range of techniques (including stable isotope analysis and fluid inclusion microthermometry) to establish a source for the CO_2 present in the oilfields.

- Construct geochemical models simulating the movement of CO_2-rich fluids up the fault, assessing the effect of various physical and chemical parameters on the nature and volumes of mineral precipitation and CO_2 exsolution from the ascending host fluid.

From the objectives above, an integrated model of a possible source and emplacement mechanism for the high CO_2 concentrations observed in the Brae region can be determined. Beyond this chapter, the thesis contains a further seven chapters which investigate the application of various approaches and techniques applied in the study. Each chapter contains a discussion and conclusion on the results acquired in the chapter whilst incorporating and adding to the results and conclusions determined in the previous chapters. The results of the chapters are then summarised and synthesised (chapter 8).

Chapter 2: This chapter introduces the geological setting and background of the South Viking Graben and the Brae trend oilfields. The spatial relationship between the graben margin fault, adjacent hydrocarbon fields (e.g. South Brae), and anomalously high CO_2 levels observed in the area is discussed. Consequently, the tectonic history and morphology of the basin bounding fault is described, including extent and timing of fault activity.

Chapter 3: This chapter describes and discusses the origin of several generations of carbonate fracture cement observed in the basin margin fault zone. The chemistry and morphology of the cements is discussed with regard to possible fluid sources and

faulting mechanisms, with their applicability and implications for CO_2-rich fluid flow and precipitation rates in the fault zone considered.

Chapter 4: The chapter details the application of microthermometric analysis to fluid inclusions in carbonate fracture cements present in the fault zone. The aim of the study is to assess whether the fluid inclusions record evidence of CO_2-rich fluid flux up the fault zone in addition to the flow conditions (e.g. temperature). The applicability of microthermometric analysis to the fracture cements is evaluated in context with present-day published reservoir studies for the Brae area.

Chapter 5: This chapter concerns the isotopic analysis of the carbonate fracture cements. Stable ($\delta^{13}C$ and $\delta^{18}O$) isotope measurements suggest a discrete inorganic source for the CO_2. An observed trend present in the dataset is discussed and explained using a Rayleigh degassing-precipitation model based on a flux of basinal CO_2-rich fluid up the fault zone. The distribution of CO_2 sources responsible for the elevated concentrations along the graben margin is also considered.

Chapter 6: In this chapter $^{87}Sr/^{86}Sr$ data from the fracture cements of the fault zone are discussed. The results are discussed with respect to diagenetic trends in the Brae region and resultant formation water compositions. The conclusions are evaluated in relation to a possible fluid source and its evolution both within the fault zone and the Jurassic reservoirs.

Chapter 7: Models simulating the ascent of CO_2-rich fluids up the fault zone are constructed using geochemical modelling software (PHREEQC). The models account for the evolution of the ascending fluid as it undergoes progressive pressure and temperature decreases, resulting in CO_2 degassing and carbonate precipitation. The models are calibrated based on existing and previously discussed data. Model output variations, resulting from differing fluid and fault properties, are evaluated.

Chapter 8: This chapter provides a summary and synthesis of the results and conclusions presented in the previous chapters. An integrated summary is proposed

accounting for the source, timing, and transport of CO_2 into the Brae region, resulting in the elevated CO_2 concentrations observed in the area today. Potential future work is also discussed.

Chapter 2

Geological history of the South Viking Graben and Brae oilfields

2.1. Introduction

The South Viking Graben forms one of a number of key offshore hydrocarbon provinces situated in the northern North Sea. The southernmost region of the extensive North - South trending Viking Graben, it straddles the border between the United Kingdom continental shelf (UKCS) and the equivalent Norwegian sector approximately 220 km ENE of Aberdeen. The asymmetric half-graben is fault-bounded to the west, where it is flanked by the southern tip of the Shetland Platform before gradually shallowing eastward to a less pronounced margin on the Vestland Arch. (Figure 2.1). The South Viking Graben has a long and complex tectonic history, undergoing active deformation from its genesis in the Permian through to the Cenozoic. The region adjacent to the

western margin of the graben is notable for the abnormally high concentrations of CO_2 present within the Jurassic hydrocarbon reservoirs which comprise the Brae Formation (up to 35 % mol) (James, 1990).

This chapter gives a summary of the geological history of the South Viking Graben, with explicit focus on the western graben bounding fault, the apparent control on CO_2 distribution in the region. This is followed by a brief overview of the sedimentology and structure of the Brae oilfields. The concentration and distribution of CO_2 in the fields is also discussed with reference to a possible source and the relationship with the graben bounding fault.

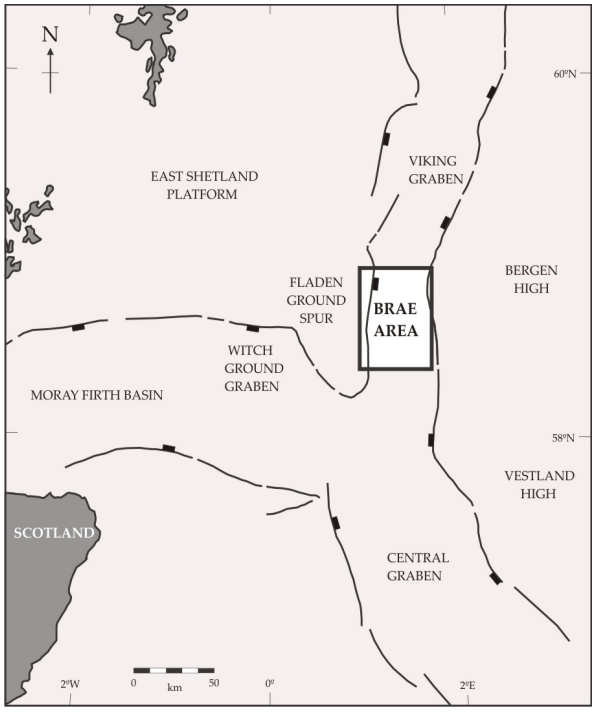

Figure 2.1. Map of the North Sea, illustrating the general location of Brae area adjacent to the Fladen Ground Spur in the South Viking Graben.

2.2. Tectonic History

Similar to the rest of the North Sea basin, the South Viking Graben has experienced a long and complex structural development history, principally related to two major extensional phases in the Permo-Triassic and Mid-Late Jurassic. However, tectonic activity on the graben margin is more prolonged having initiated in the early Permian,

with periodic activity (both extensional and compression), until at least the Palaeocene (Glennie, 1990).

2.2.1. Permian

Following temporary consolidation of Pangaea in the Early Permian, intraplate deformation resulting from thermal subsidence following gravitational collapse of the Variscan fold belt saw the initiation of the breakup of Pangaea and the development of a series of interior rift systems with localised volcanicity (Ziegler, 1982; Ziegler, 1990; Underhill, 2003). The subsidence resulted in the development of two E – W trending depocentres, the Southern and Northern Permian Basins, separated by the Mid-North Sea High. Within the basins a sequence of continental red beds (Rotliegend) overlain by an extensive evaporitic succession (Zechstein) accumulated (Glennie, 1990). It is believed the Northern Permian Basin was formed predominantly by crustal flexure due to thermal re-equilibration following the rifting phase, accommodating up to 1000 m of Zechstein salt in the basin axis by the Late Permian (Smith *et al*., 1993; Thomas & Coward, 1996). The extent and nature of the deposits and their host North Permian Basin are less well understood compared to their Southern Permian Basin equivalents due to strong overprinting by Jurassic rift tectonics (Færseth, 1996; Clark *et al*., 1998), poor seismic resolution at pre-Jurassic depths, and research bias due to exploration targets at shallower depths (Thomas & Coward, 1996).

During this time period, the South Viking Graben was located on the northern margin of the Northern Basin (Hodgson, *et al*., 1992; Jackson & Larsen, 2009). Although the depth and thickness of Zechstein deposits within the graben proper is unknown, a series of 'marginal' carbonate-rich Zechstein evaporite sequences have been encountered in wells of the T-Block Fields, Beryl Embayment, and Crawford Ridge on the Fladen Ground Spur (Figure. 2.2) (Taylor, 1981; Cherry, 1993; Morgan & Cutts, 1993; Gambaro & Donagemma, 2003). Localised fault related subsidence throughout the Permian has been proposed in the South Viking Graben and other marginal areas of the Northern Basin (Badley *et al*., 1988). However, it is unclear whether the faulting patterns evolved

during the Permian or were inherited from the Caledonian basement (Glennie, 1990; Smith *et al*., 1993).

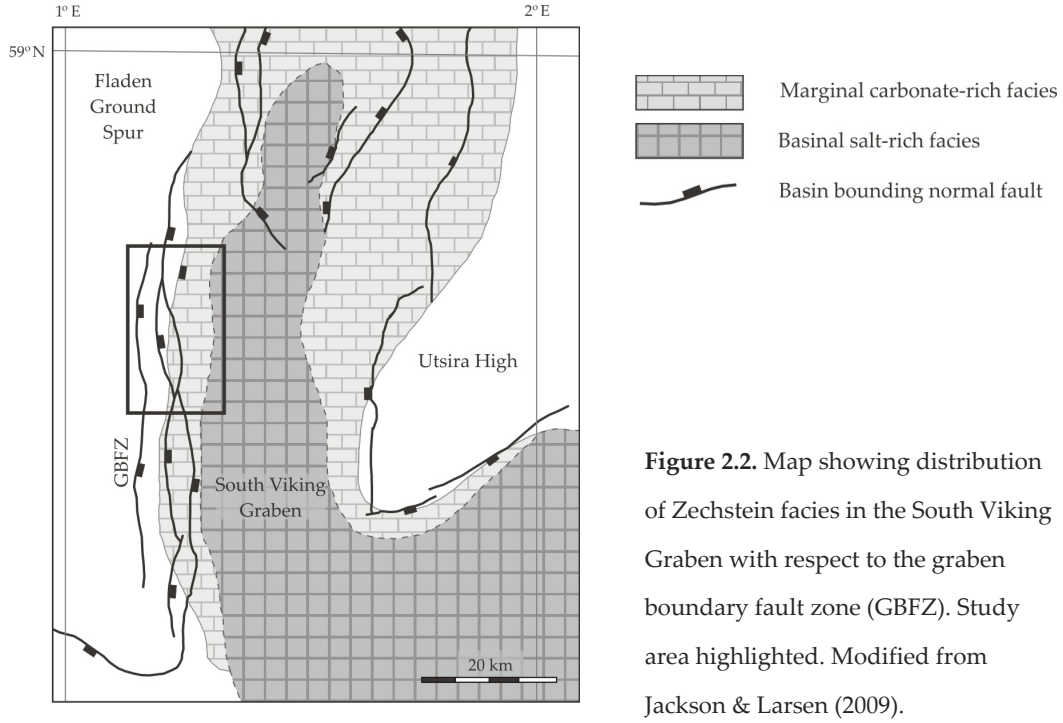

Figure 2.2. Map showing distribution of Zechstein facies in the South Viking Graben with respect to the graben boundary fault zone (GBFZ). Study area highlighted. Modified from Jackson & Larsen (2009).

2.2.2. Triassic

The sedimentary basins established during the Permian continued to subside along the lines established during the initial extensional phase throughout the Triassic. The development of the N – S orientated North Sea rift system in the early Scythian (~245 Ma) saw the Viking and Central Grabens subside, modifying the existing structural framework of the North Sea (Ziegler, 1982; Glennie, 1990). The development of the rifts has been attributed to fracture propagation from the East Greenland – Western Norway rift in response to crustal extension in the Arctic (Ziegler, 1982). Evidence of Early Triassic extension in the North Sea basin is observed in marginal areas where angular discordant faulted blocks of Permian Rotliegend and Zechstein successions are overlain by syn-tectonic sedimentation (Fisher & Mudge, 1998). Extensive Middle Triassic to Lower Triassic overall fining upward sequences observed in the North Sea Basin have generally been assigned as post-rift sequences in response to thermal subsidence following the Permo-Triassic extension (Thomas & Coward, 1996; Underhill, 2003).

Differential extension is observed across a number of faults on the retreating basin margin however, with the temporal variation in subsidence rate controlling the distribution and extent of syn-tectonic wedges (Færseth, 1996). In the South Viking Graben the minor westward thickening of Late Triassic units towards the western basin bounding fault suggests active extension in the graben during this period (Badley *et al*., 1988; Thomas & Coward, 1996; Jackson & Larsen, 2008). Numerous authors advocate that fault block rotation and resultant thickness variation of Triassic sequences in the South Viking Graben was facilitated by thin-skinned gravity slip along low-angle detachment faults along the underlying Zechstein evaporites (Morgon & Cutts, 1993; Thomas & Coward, 1996; Jackson & Larsen, 2009). Although the tectonic history of the Triassic is poorly understood due to later overprinting, most workers agree that if extension did occur in the South Viking Graben during the Triassic, the rifting episode is only of minor importance in the Mesozoic evolution of the graben (Fisher & Mudge, 1998).

2.2.3. Jurassic

Extensive hydrocarbon exploration of the South Viking Graben has provided a detailed understanding of the structural and stratigraphic relationships within the Late Jurassic sequences host to numerous hydrocarbon accumulations. However, Lower and Middle Jurassic sequences are only patchily understood in the area.

Throughout the Early Jurassic grabens within the the North Sea continued to subside. The passage from the Early to Mid Jurassic saw increased tectonic activity in the North Atlantic and Tethyian rift systems, culminating in a major rifting phase and uplift of a large rift dome, terminating the post-rift subsidence phase (Ziegler, 1982; Glennie, 1990). The thermal doming initiated in the Toarcian (~190 Ma) and continued to a maximum in the Aalenian, creating the regional 'Mid-Cimmerian Unconformity' (Underhill & Partington, 1993). The absence of Late Triassic to Mid Jurassic sequences in the South Viking Graben, Central Graben, and Outer Moray Forth is attributed to the doming at what became the Jurassic triple rift junction (Ziegler, 1982; Ziegler, 1990; Underhill & Partington, 1993; Davies *et al*., 1999). As a consequence the stratigraphy of the axial

regions of the graben remains speculative. However, sand-dominated deltaic successions are noted on bounding highs, although their extent is unclear at depth (Thomas & Coward, 1996). The development of a volcanic centre in the triple junction (with subsidiary volcanism in the Viking Graben) coincident with differential deflation of the dome in the Bathonian preceded the initiation of extensive active rifting of the South Viking Graben in the Callovian (Ziegler, 1982; Cockings *et al*., 1992; Underhill & Partington, 1993). The subsequent rise in relative sea level resulted in the deposition of the thick-shallow marine sands of the Hugin Formation (Harris & Fowler, 1987).

Increased activity in the North Atlantic – Arctic rift system in the Late Jurassic marked the main phase of extension in the northern North Sea basin (Ziegler, 1990). Increased subsidence led to deepening in all three rift arms and the development of extensive rotated fault block geometries hosting prolific hydrocarbon reservoirs (Underhill, 1998). The Upper Jurassic rifting of the South Viking Graben saw pronounced movement on the western basin bounding fault; in excess of 4km (Harris & Fowler, 1987). The structural framework of the faulting is widely regarded as being inherited from the earlier Permo-Triassic fault configurations, with relatively few large Jurassic faults interpreted as resulting from nucleation and growth (Færseth, 1996) (Figure 2.3). This is evident on the bounding fault adjacent to Brae fields with high CO_2 concentrations where the reactivated Permo-Triassic faults exhibit planar surfaces with dips of ~60° (Thomas & Coward, 1996). This contrasts with the marginal fault framework further north on the Beryl Embayment which is characterised by shallower gently dipping fault profiles which subsequently connect with planar faults at depth (Færseth, 1996). Such variations in fault geometry have potentially significant implications on the nature and distribution of fluid flow on the graben margin (Andrews-Speed *et al*., 1984).

Extension is believed to have initiated in the Late Callovian-Early Oxfordian with intermittent rifting until the Late Volgian (Tithonian) (Cockings *et al*., 1992; Thomas & Coward, 1996), resulting in the development of the deep asymmetrical graben profile witnessed today (Figure 2.4). As mentioned previously, the period of extension with resultant uplift and erosion of the basin margin footwall culminated in the deposition of

the coarse clastic submarine fans into the graben basin (the Brae Formation). The series of overlapping syn-tectonic wedges defining the 'Brae Trend' fields are indicative of active margin deposition within a subsiding half-graben (e.g. Stow *et al*., 1982; Turner *et al*., 1987). Cessation of the rifting episode in the latest Jurassic (Ryazanian) saw the end of significant block rotation in the graben, with the majority of rift related faults becoming inactive (Badley *et al*., 1988). However, continued activity on the graben bounding fault in the South Viking Graben and adjacent areas (e.g. Witch Ground) during the thermal subsidence phase is well documented (e.g. Cherry, 1993).

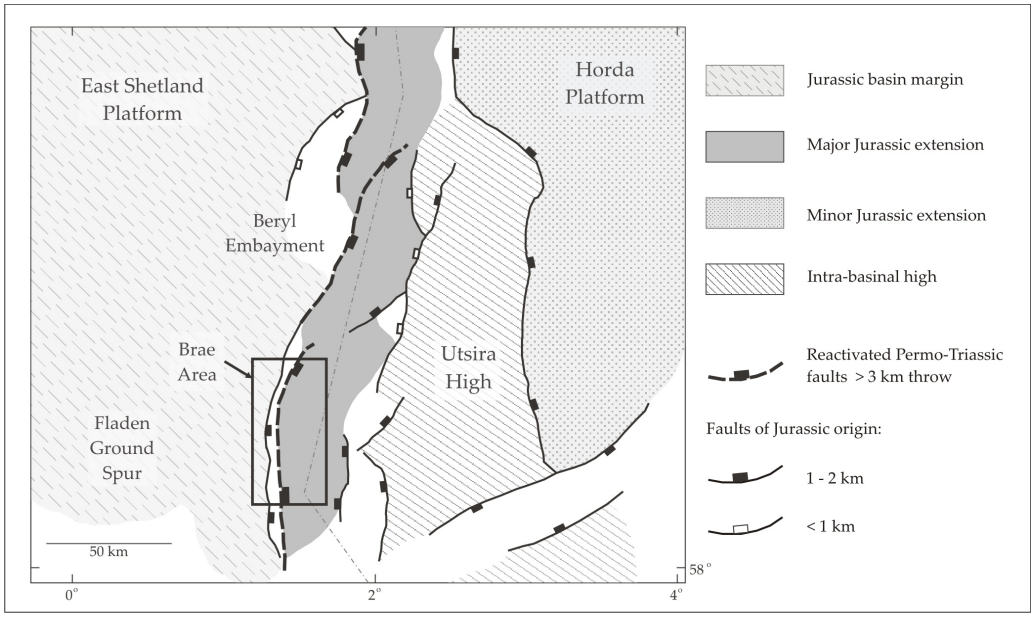

Figure 2.3. Map illustrating the main structural elements of the South Viking Graben resulting from Jurassic extension. The location and magnitude of major fault displacements resulting from reactivation of Permo-Triassic faults and those initiated during the Jurassic are shown, with the western margin of the graben in the 'Brae Trend' area (highlighted) experiencing both faulting types. Modified from Færseth, (1996).

2.2.4. Cretaceous

Given the apparent relationship between the graben bounding fault and high CO_2 concentrations in the adjacent Jurassic reservoirs, appreciation of the post-Jurassic

tectonic activity on the graben margin is pivotal in understanding the possible role of the fault in the origin and transport of CO_2 into the Brae trend oilfields.

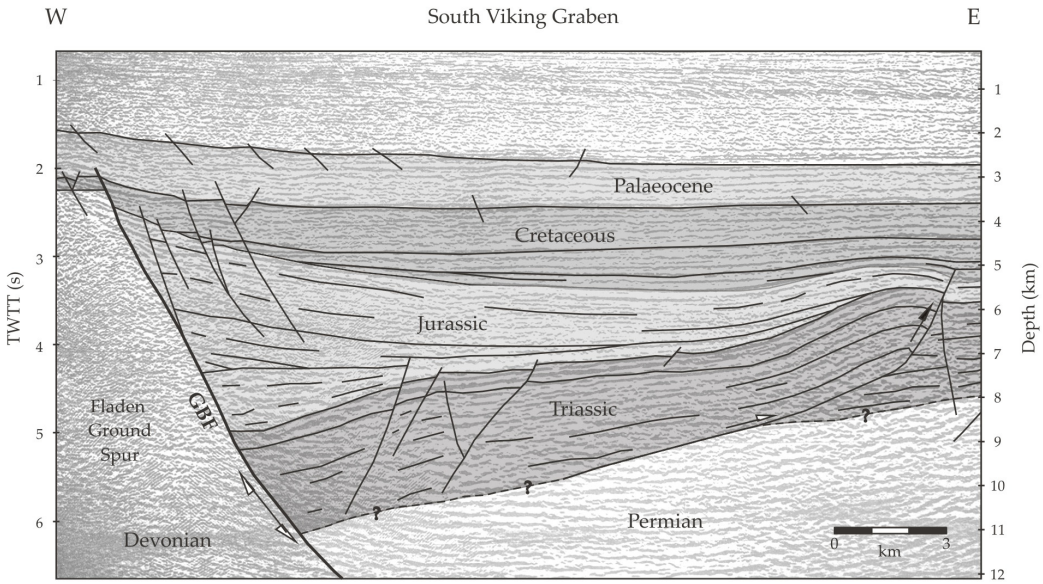

Figure 2.4. Interpreted seismic cross section across western margin of the South Viking Graben showing pronounced asymmetric graben fill during the Jurassic. The steep graben bounding fault (GBF) has undergone periodic reactivation and inversion throughout the history of the graben. The numerous faults and resultant folds present in Triassic sequences are attributed to detachments along Zechstein evaporitic sequences due to movement on the GBF (Jackson & Larsen, 2009). Due to poor resolution of seismic data, the Permian sequences are poorly constrained. Modified from Thomas & Coward (1996).

Synchronous with the cessation of basin extension in the Ryazanian, the North Sea basin experienced a short-lived period of inversion, commonly referred to as the 'Late Cimmerian unconformity', modifying the Jurassic sequences in the graben fills (Cherry, 1993; Oakman & Partington, 1998). On the margin of the South Viking Graben the event is expressed as a series of anticlines and reverse faults forming the crest of the Brae Formation reservoirs (Fletcher, 2003; Hook *et al*., 2003) (e.g. see Figure 2.3). The true extent of the Late Cimmerian event in the South Viking Graben remains uncertain, with numerous authors attributing the observed structures to thin-skinned detachments at depth (*see 2.2.2.*) (e.g. Thomas & Coward, 1996). The Mid-Cretaceous (Mid-Albian to Turonian) saw regional subsidence becoming more widespread in the South Viking

Graben, accommodated by planar extensive normal faulting at the basin margin (Badley *et al*., 1988). Jackson and Larsen (2008) noted an overall westward thickening of Cretaceous units in the graben which they attributed to continual activity on the graben bounding fault during this time.

During the Late Cretaceous, the North Sea basin remained tectonically quiescent, continuing to thermally subside following early extensive rifting events. However, the basin bounding faults experienced intermittent movement as they accommodated the subsidence (Badley *et al*., 1988), and the Laramide rifting pulse (Ziegler, 1982; Fagerland, 1983). Cretaceous movements along transfer faults oblique to the prominent NNE – SSW trend of the basin margin present in the Brae Trend area resulted in differential faulting (Fagerland, 1983). Numerous minor inversion events have been identified throughout the Cretaceous in the T-Block region (Gambaro & Donagemma, 2003), with Cherry (1993) observing localised compression of the graben bounding fault, resulting in disparities within the structural architecture in the area.

However, overall decreased rates of extension in the Cretaceous coupled with high eustatic sea levels terminated major coarse clastic deposition in the South Viking Graben, allowing thick sequences of post-rift mud to onlap across the graben margin fault onto the Devonian footwall completing the asymmetric fill of the graben (Harris & Fowler, 1987; Badley *et al*., 1988).

2.2.5. Cenozoic

Fault activity on the graben margin in the northern North Sea continued into the Tertiary, with further episodes of faulting during the Late Palaeocene and Early Eocene attributed to Alpine tectonism (Ziegler, 1981; 1982) and North Atlantic seafloor spreading (Fagerland, 1983). It has been proposed that these events saw the rejuvenation of the basin bounding fault (Fletcher, 2003), creating the flower structures witnessed along the existing Mesozoic margin fault (Fagerland, 1983). The prolonged and complex tectonic history of the South Viking Graben and specifically the western margin bounding fault has given rise to a host of potential migration pathways for CO_2

(Figure 2.5). The extensive basin fill sequence, in excess of 7 km thickness (Hospers & Ediriweera, 1991), contains a number of horizons capable of generating CO_2, both organic and inorganic. Appreciation of the nature and extent of the fault arrays on the graben margin is thus important in understanding possible controls on the source and distribution of CO_2 in the Brae region.

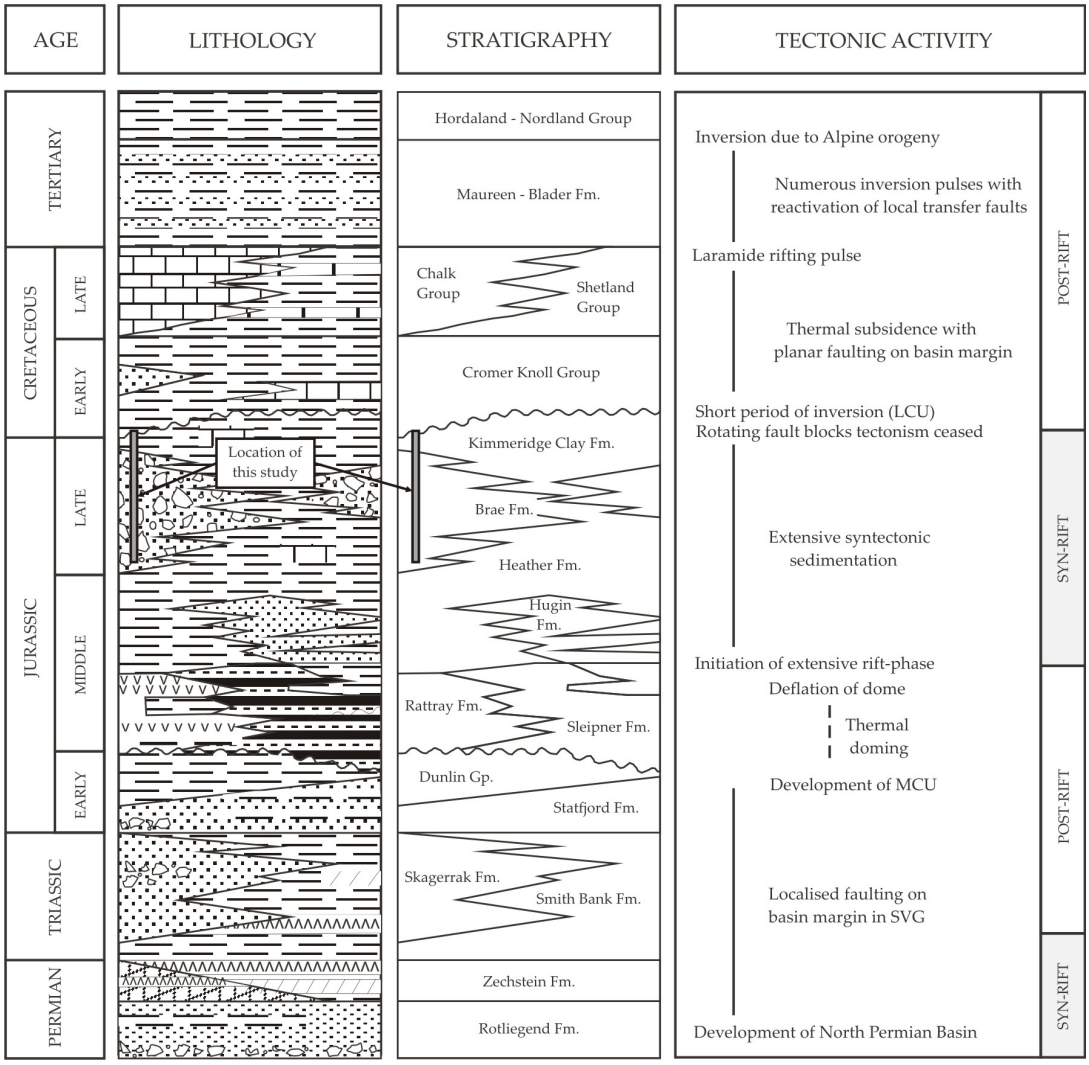

Figure 2.5. Schematic stratigraphic section of the Palaezoic to Cenozoic units in the South Viking Graben (adapted from Harris & Fowler, 1987), with accompanying tectonic summary illustrating the timing and duration of tectonic events affecting the western graben margin. The area concerning this study, the Brae Formation, is highlighted to illustrate its relative position in the graben fill sequence.

2.3. The Brae oilfields

The western margin of the South Viking Graben is host to a conspicuous linear trend of Late Jurassic hydrocarbon accumulations. Adjacent to the graben boundary fault, the fields extend from the Brae-Miller complex (South-, Central-, North-Brae, and Miller Fields) in UKCS license blocks 16/7 and 16/8 southward through the Larch, Birch, Pine, and Elm Fields (informally termed the 'Trees Block') in block 16/12 to the T-Block Fields (Tiffany, Toni, and Thelma) in the south (Block 16/17) (Figure 2.6). From herein, these fields will be collectively referred to as the 'Brae Trend'.

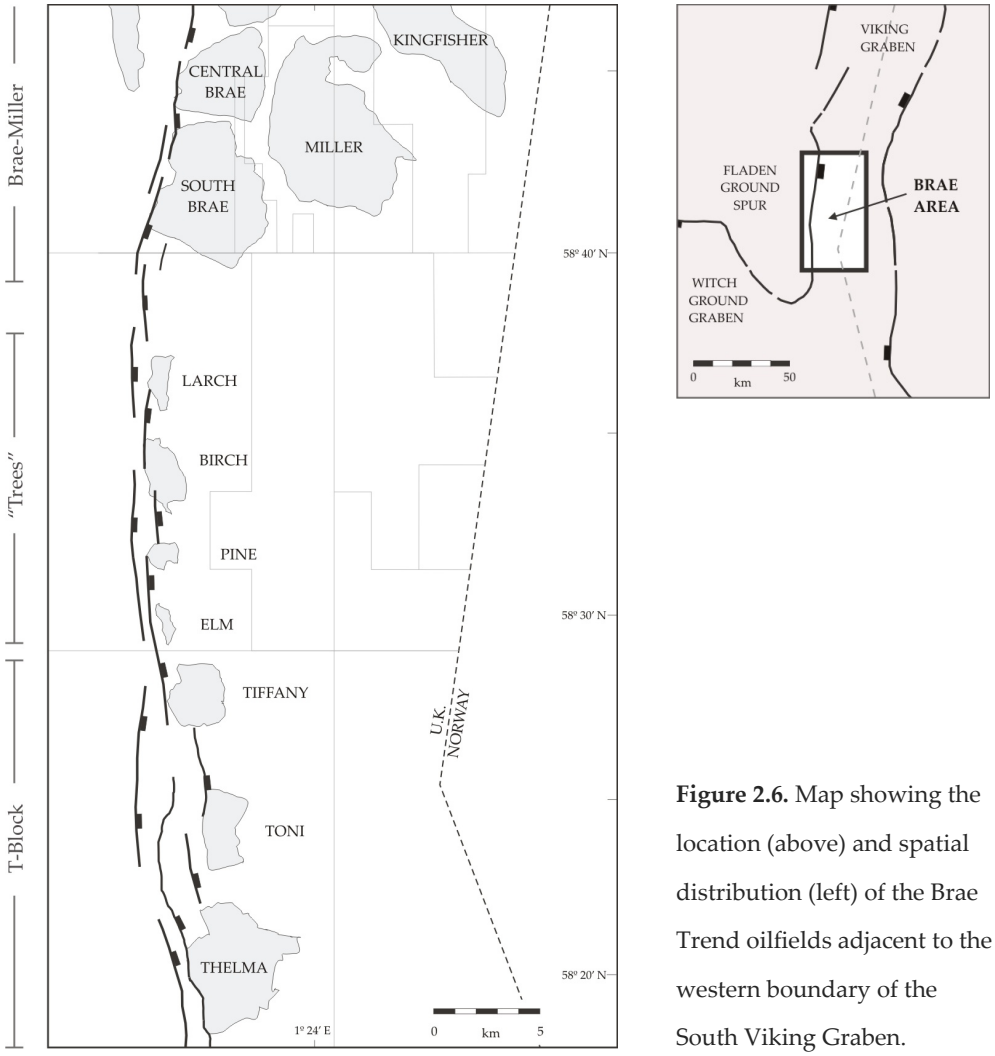

Figure 2.6. Map showing the location (above) and spatial distribution (left) of the Brae Trend oilfields adjacent to the western boundary of the South Viking Graben.

2.3.1. Depositional model

The fields are interpreted as a series of tectonically influenced partly channelised submarine fan systems deposited during the Oxfordian and Volgian (Turner *et al*., 1987; Fletcher, 2003a). Numerous depositional models have been proposed and discussed in several studies regarding the formation of the fans, ranging from sub-aerial and marginal marine deltas (e.g. Harms *et al*., 1981) to a fully marine setting with sediment derived from erosion of the graben margin (e.g. Stow *et al*., 1982; Turner *et al*., 1987). Supported by palaeontological data, the latter proposal (shown in Figure 2.7) is the generally accepted model.

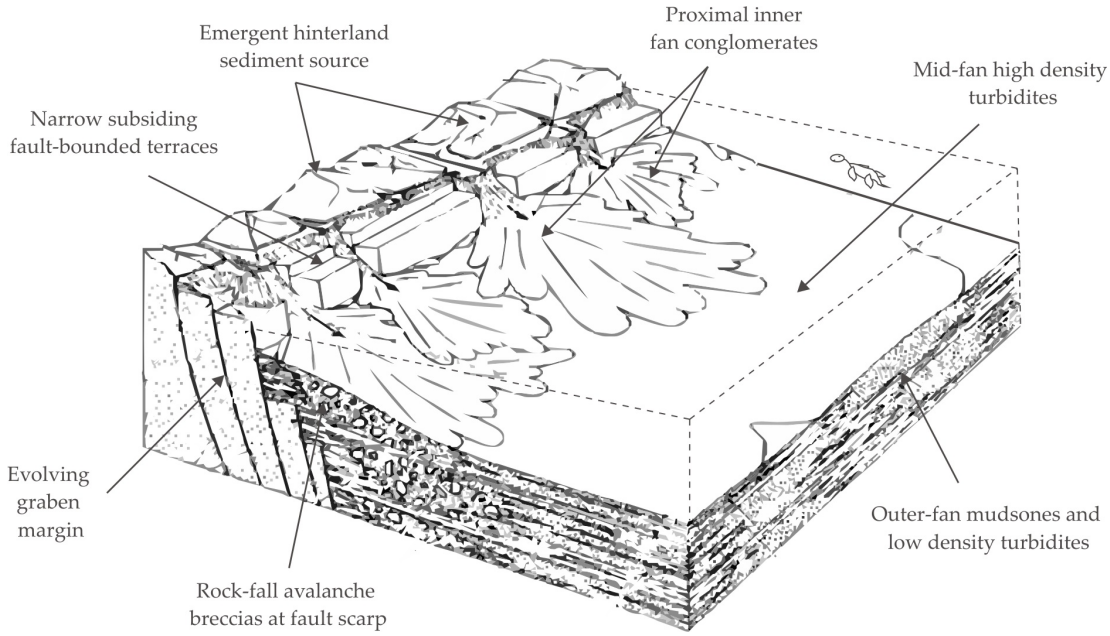

Figure 2.7. Depositional model for the Brae Formation submarine fan system illustrating the facies relationships with proximity to the graben margin fault. Modified from Harris & Fowler (1987).

The Mid-Late Jurassic rifting episode saw the development of a series of normal faults which resulted in the uplift of the basin-bounding East Shetland Platform on the western margin and the Utsira High in the east (Isaksen *et al*., 2002). The intermittent uplift, emergence, and subsequent erosion of the Devonian footwall, the Fladen Ground Spur, served as a source for the submarine fan sediment. Syn-tectonic deposition

throughout the Jurassic resulted in the formation of a pronounced sediment wedge thinning eastwards into the basin, marking the main phase of fault movement along the boundary fault (Roberts, 1991). The fans do show a degree of overlap and differing depositional ages. This is attributed to varying clastic supply along the basin margin due to local tectonism during the Jurassic rifting phase (Turner & Allen, 1991).

The siliciclastic fan deposits adjacent to the graben margin, termed the Brae Formation, comprise conglomerates, sandstones and mudstones derived from the Devonian footwall (Stow & Atkin, 1987). It is this unit which acts as the primary hydrocarbon reservoir for the area, with the abutment of the Brae Formation clastic fans against the impermeable Devonian sandstones of the footwall forming classic hanging wall fault closure traps (Fletcher 2003a). Interdigitated with the Brae Formation, the underlying and overlying Kimmeridge Clay Formation acts as a source and lateral seal for the hydrocarbons (MacKenzie *et al*., 1987).

2.3.2. Brae Formation lithology

The Brae Formation comprises a number of distinct lithofacies which vary vertically and laterally within the fan complexes. A large-scale, overall fining-upward sequence (~600 m thick) is observed within the fans related to fluctuations in sea level, both eustatic and regional due to localised tectonism (Roberts, 1991). A marked variation in lithology occurs laterally (up to 50 km) from the western margin eastward into the basin, with proximal faulted margin influenced deposits consisting of coarse conglomeratic material (e.g. South Brae, Birch) grading into finer distal fan margin sediments (e.g. Miller). Although numerous lithofacies for each of the individual fans have been proposed pending on the field producers (see Turner *et al.* (1987) for detailed South Brae description), these can be simplified to three distinct facies based on distance from the graben margin (Figure. 2.8):

1) *Inner fan conglomerates* – Deposited proximal to the basin bounding fault, the facies predominantly comprises of clast and sand-matrix supported Old Red Sandstone boulders and pebbles, vein quartz, and quartzite derived from the

uplifted Fladen Ground Spur with subordinate sandstone and minimal argillaceous intervals. Analogous to the sub-aerially exposed Helmsdale Boulder Beds (e.g. Pickering, 1984); deposits in contact with the fault surface consisting of angular, very poorly sorted clasts are derived from mass wasting of the fault scarps (Stow & Atkin, 1987; Roberts, 1991; Hook *et al*, 2003).

2) *Mid-fan sandstones* – Consist of massive sandstone units comprising medium to coarse grained material (~2 m thick) interdigitated with conglomeratic material and mud-rich material (<0.5 m) (Harris & Fowler, 1987). Although principally structureless, parallel laminations and current ripples in the sandstone units indicate deposition from high density turbidites forming basinward lobe sequences (e.g. Miller Field) (Rooksby, 1991; Garland, 1993).

3) *Outer-fan - basin plain mudstones* – Interlaminated sandstone and mudstones comprise the distal and marginal facies of the submarine fans. Very fine to fine grained graded sandstones (1 – 10 cm) interbedded with Kimmeridge Clay mudstone (1 – 5 cm) create distinctive 'tiger stripe' bedding, with the sand-rich horizons interpreted as low-density turbidite deposits punctuating an otherwise anoxic marine depositional environment (Harris & Fowler, 1987; Turner *et al*., 1987).

2.3.3. Kimmeridge Clay Formation lithology

Regionally, the Brae Formation is overlain and underlain by the organic-rich Kimmeridge Clay Formation (KCF). The mudrock is the major source rock for virtually all the hydrocarbon accumulations in the South Viking Graben region and beyond (Reitsema, 1983; Justwan *et al*., 2006). In addition, the low permeability KCF serves as the caprock for the Brae Formation reservoirs (Rooksby, 1991; Fletcher, 2003a). Deposition into a deep water anoxic environment during regional rifting and rapid subsidence throughout the latest Jurassic led to the creation of considerable thicknesses (500 – 1000m) of the organic-rich prolific hydrocarbon source rock (Cornford, 1998; Scotchman, 1993).

2.3.4. *Burial history and fluid evolution*

The maturity of the KCF in the region was principally governed by rapid regional burial and resultant heating initiated in the Late Cretaceous – Early Tertiary (Figure 2.9). It is believed that hydrocarbon generation and migration into the Brae Formation reservoirs of the South Brae Field occurred at the earliest from the Late Cretaceous (~70 Ma) onwards (Fletcher 2003a), whereas Marchand *et al*. (2001) concluded that petroleum generation in the adjacent Miller Field started in the Eocene-Oligocene (approximately 40 Ma). Numerous previous studies have examined the diagenetic history of the Brae Formation, evaluating the evolution of the formation waters present within the sandstones (e.g. Greenwood *et al*., 1994; Marchand *et al*., 2002). Such studies concluded that early in the burial history, initial Jurassic marine porewaters were replaced by meteoric re-charge; a phenomenon observed in a host of Late Jurassic Viking Graben fields (Haszeldine *et al*., 1992).

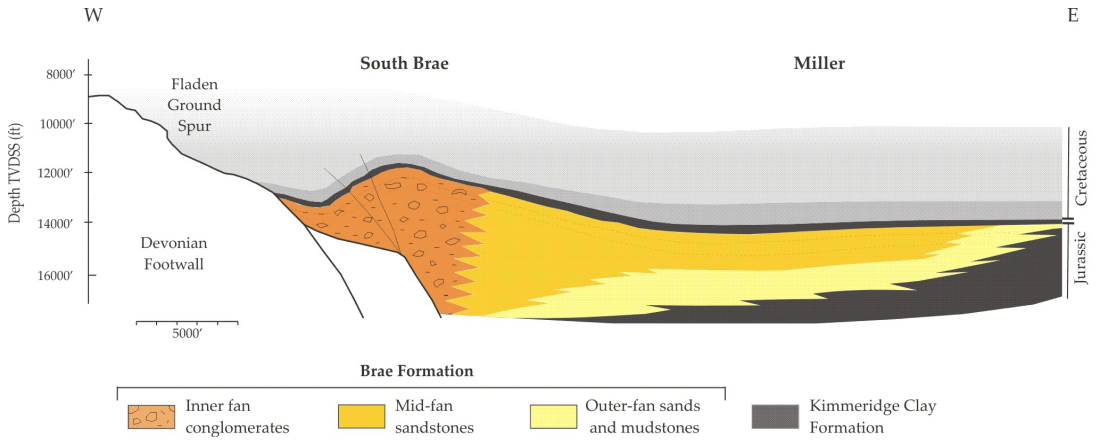

Figure 2.8. Structural cross section through South Brae illustrating the geometry of lithofacies within the Brae Formation and their relationship with the graben margin fault and Kimmeridge Clay Formation. Modified from Fletcher (2003a).

A number of investigators have, however, suggested a later influx of deep basinal fluids into the Brae trend fields. From fluid inclusion studies, Larter *et al*. (1995) concluded that an influx of high salinity water (~25 wt. NaCl eq.) entered the Miller Field ~70 Ma before gradually decreasing due to homogenisation with existing formation waters to present

day salinity values (~8 wt. % NaCl) (Smalley & Warren, 1994); a proposal affirmed by Marchand *et al*. (2002) through stable isotope analysis of diagenetic quartz cements in the Brae Formation reservoirs. Though the exact timing of CO_2 emplacement is unknown, Lu (2008) speculated from carbon isotope evidence that the high salinity input into the fields coincided with the influx of the high CO_2 concentrations observed (~70 – 80 Ma). This suggests that any significant CO_2 influx pre-dated hydrocarbon generation and migration.

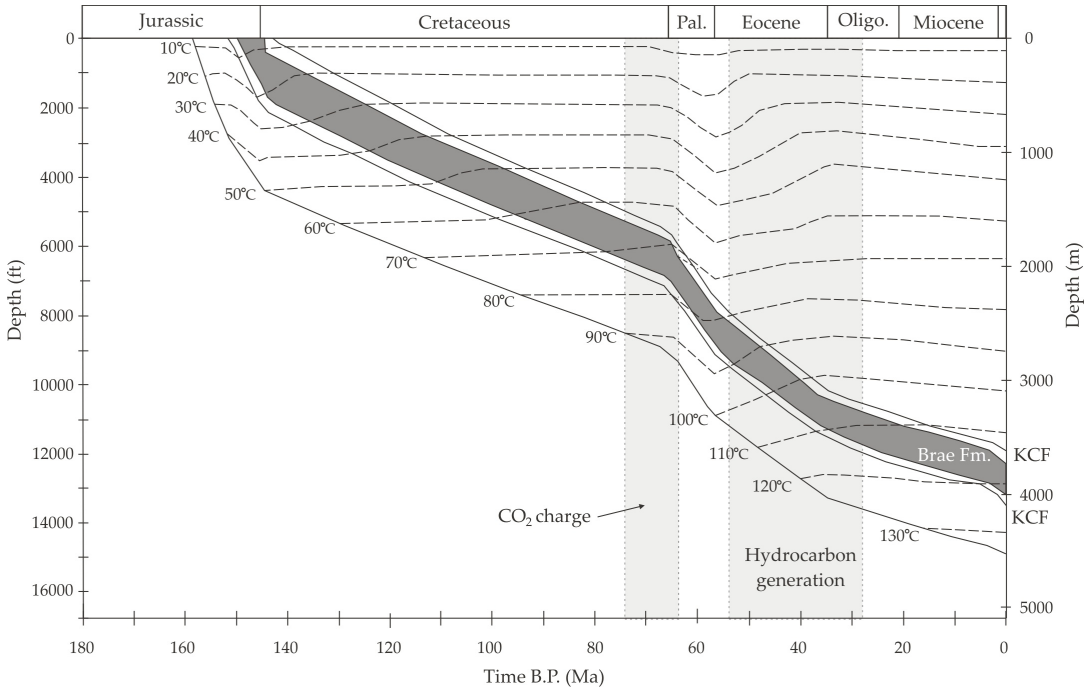

Figure 2.9. Decompacted burial history model with present day isotherms (30°C/km) for the Brae Formation (well 16/7a-30 (North Brae)) showing general petroleum generation and migration window (Marchand *et al*., 2001; Fletcher, 2003a). Timing of estimated CO_2 charge (Lu, 2008) is also shown. However, exact timing is still undetermined, with CO_2 charge potentially contemporaneous with hydrocarbon generation. Burial curve modified from Marchand *et al*. (2001).

2.4. CO_2 in the South Viking Graben

2.4.1. Carbon dioxide distribution

The South Viking Graben forms part of a naturally high CO_2 province, with the hydrocarbon reservoirs in the Brae-Miller region containing abnormally high CO_2

contents. Average concentrations of CO_2 up to 35 mol% within the hydrocarbons present in the South Brae field are observed. Other high-CO_2 fields in the area include; Central Brae (25 – 30 mol%), Miller (28 mol%), Kingfisher (14 mol%), Larch, Birch, and Pine (10 – 20 mol%), Sleipner West (9 mol%), and the T-Block fields (15 – 20 mol%) (James, 1990; Rooksby, 1991; Isaksen *et al*., 2002; Fletcher, 2003a; 2003b; Gambardo & Donagemma, 2003; Baines & Worden, 2004). The majority of South Viking Graben natural gas accumulations, in contrast, typically contain less than 5 % CO_2 (Thrasher & Fleet, 1995). Such low CO_2 concentrations are comparable to analogous clastic reservoirs of a similar age and depositional history in other areas of the northern North Sea. For example, the Upper Jurassic Magnus field is host to gas which exhibits CO_2 concentrations no greater than 2 mol% (Barclay & Worden, 2000).

Carbon dioxide distribution in the region (Figure. 2.10) shows that the highest concentrations of CO_2 are present in the reservoirs adjacent to the basin bounding fault centred around the South Brae field. Eastwards into the basin the levels of CO_2 decrease systematically away from the graben margin. Although Figure 2.10 is constructed using average CO_2 concentrations from the various reservoirs present, the systematic decrease in CO_2 away from the graben margin is also evident within individual fields. Analyses of gas from the Sleipner Vest Field show that samples closest to the western graben margin exhibit CO_2 concentrations greater than 15 %mol. Conversely, gases from the eastern limit of the field on the Utsira High contain CO_2 concentrations below 4 % (James, 1990), with trace levels reported in the more easterly Sleipner Øst Field (Isaksen *et al*., 2002).

Numerous researchers have suggested such a distribution pattern indicates a fluxing of CO_2 from depth up the graben fault system with subsequent migration eastward into the Jurassic reservoirs, mixing with existing formation fluids (James, 1990; Baines & Worden, 2004; Haszeldine *et al*., 2005). Such a suggestion is supported by the observation of the highest CO_2 concentrations being present in the deeper stratigraphic sections of the fields proximal to the graben fault (James, 1990).

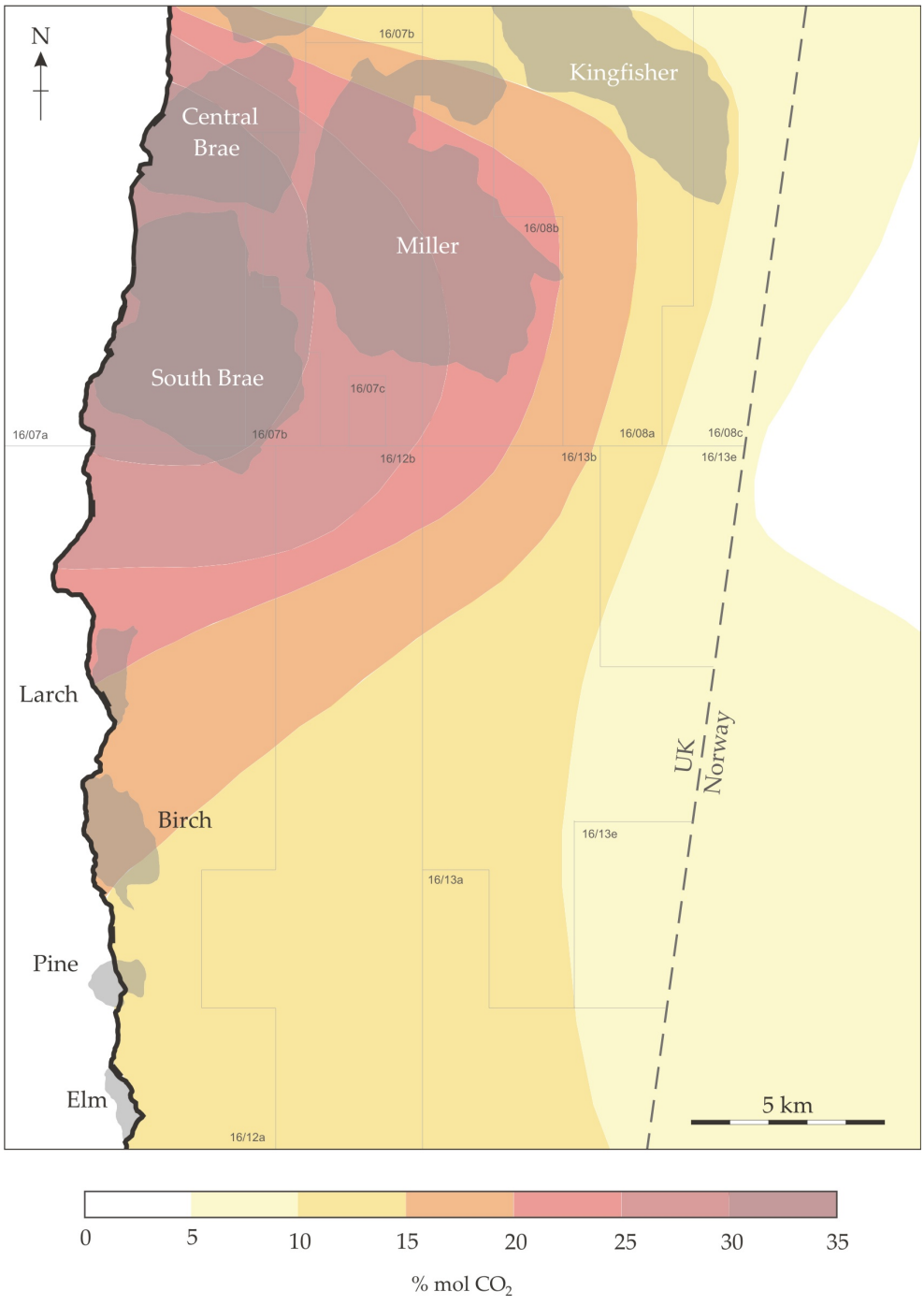

Figure 2.10. Map showing distribution of average CO_2 concentrations within the Upper Jurassic hydrocarbon reservoirs of the Brae trend area adjacent to the western margin fault (adapted from James, 1990; Baines & Worden, 2004; Lu *et al.*, 2009).

2.4.2. Isotopic character of the CO_2

The high-CO_2 gases found deeper in the section and close to the basin bounding fault have carbon isotope ratios of -3 to -5 ‰ (V-PDB). Conversely, carbon dioxide from hydrocarbons further into the basin is isotopically lighter. For example, present day CO_2 in the Miller Field exhibits an average $\delta^{13}C$ value of -8.2 ‰ (Baines & Worden, 2004) and gas in the Sleipner Vest Field contains CO_2 ranging between -8 to -12 ‰ (James, 1990). As a consequence of this variability in content and carbon isotopic composition (-3 to -12 ‰), the CO_2 gas throughout the region is assumed by a number of researchers to be derived from a number of sources, with the graben fault a key control on its distribution. The high concentration (>15 mol%), relatively heavy $\delta^{13}C$ values of CO_2 present deep in the section and adjacent to the graben (-3 to -5 ‰) suggest an inorganic origin for the carbon dioxide present (Thrasher & Fleet, 1995). James (1990) suggested the CO_2 is the product of the thermal degradation of carbonates at depth, with a Zechstein dolomite sequence at depth a potential source (Baines & Worden, 2004). The lighter carbon isotope values witnessed further into the basin are characteristic of those derived from the thermal maturation of organic matter (James, 1990). These gases typically contain less CO_2 (e.g. Sleipner Vest CO_2 exhibiting $\delta^{13}C$ values of -8 to -12 ‰ originate from gases containing < 4% CO_2). These values are comparable to $\delta^{13}C$ values of low CO_2 volumes present in the Magnus Field which were attributed to an organic source (Barclay & Worden, 2000).

It has been suggested that the variability witnessed in CO_2 content and isotopic composition in the region is a product of deep-sourced heavier CO_2 migrating eastwards from the graben into shallower reservoirs and mixing in varying proportions with lighter hydrocarbons derived from the normal maturation of organic matter (James, 1990). Such a migration and mixing process can therefore explain the differentiation and variability witnessed in CO_2 content on a field scale. Carbon dioxide contents within the different Brae Formation units in the Miller Field vary considerably, ranging from 20 – 35 mol% CO_2 in oil phases to 60 – 70 mol% in separator gas during water testing (Figure 2.11). Laterally extensive Kimmeridge Clay horizons interbedded with the sandstone reservoirs therefore probably dictate CO_2 migration pathways,

controlling local CO_2 accumulations within the Brae Formation and equivalent reservoir units.

2.4.3. Possible CO_2 source in the North Sea

The high concentration CO_2 present immediately adjacent to the graben bounding fault has stable carbon isotope ratios between 0 and -6‰, suggesting an inorganic origin (James, 1990; Wycherley *et al*., 1999). A wide range of potential CO_2 sources exist in the northern North Sea: mantle degassing, thermal degradation of carbonates; contact metamorphism, thermal maturation of organic matter (petroleum or coal) (*see Figure 1.2*). However, unequivocal identification of carbon sources is difficult, especially if mixing of components is involved (Jenden *et al*., 1993).

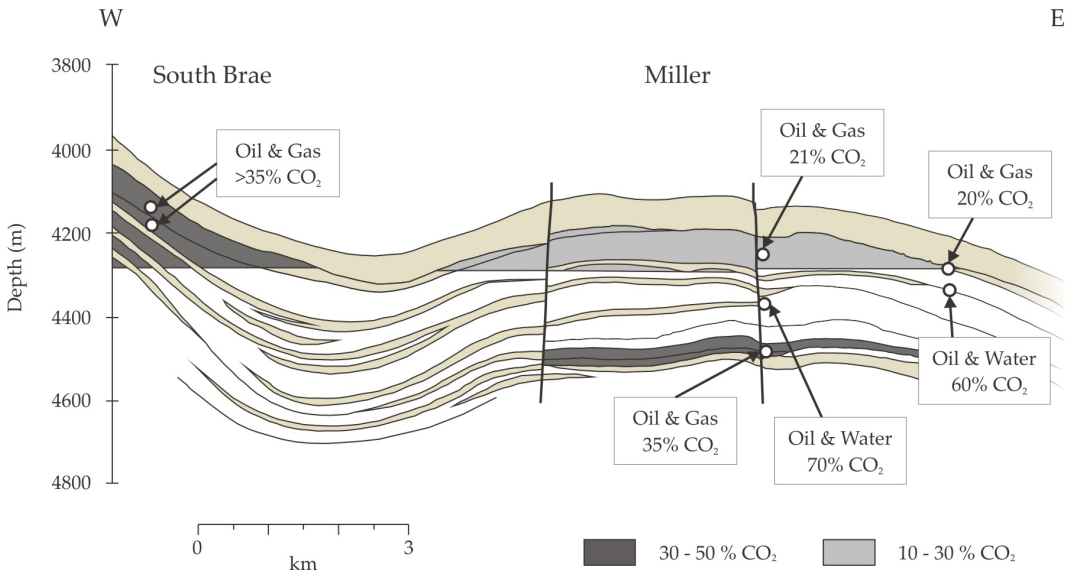

Figure 2.11. Cross section showing compartmentalised nature of the South Brae and Miller fields with respect to CO_2 content in the hydrocarbons present. Units deeper in the Brae Formation and nearer the graben margin fault typically exhibit higher CO_2 content. Modified from Baines & Worden (2004).

Therefore, additional analytical techniques must be employed to differentiate potential sources. For example, noble gas abundances and $^3He/^4He$ isotopic ratios have been used to assess the possibility of mantle-source volatiles in North Sea hydrocarbon

accumulations. Hooker *et al*. (1985) suggested that deep-source contributions are negligible, even in fields close to deep graben faults. Conversely, Oxburgh *et al*. (1986) and Balletine *et al*. (1996) both concluded that a mantle source signature is evident and could have entered the region from depth, with highest noble gas abundances adjacent to major fault structures. However, such isotopic signatures are not restricted to regions of the North Sea with significant CO_2 accumulations. Therefore, it is paramount to understand the geological history of the South Viking Graben with respect to possible CO_2 sources present within the graben fill in addition to the extent and duration of tectonic activity on the graben bounding fault, the inferred conduit for the high CO_2 concentrations in the Jurassic hydrocarbon reservoirs.

2.5. Summary

- The South Viking Graben has experienced a long and complex tectonic history. Basinal extension and sedimentation initiated in the Permian, with rifting patterns during the pronounced Jurassic phase inherited from earlier tectonic signatures. The steeply dipping planar margin fault adjacent to the Brae trend fields is believed to be of Permo-Triassic origin. Movement on Zechstein horizons in the graben fill is also believed to have influenced tectonism in the region.

- Owing to the onset of thermal subsidence following the major Jurassic rifting phase, tectonism in the South Viking Graben has been largely quiescent. However, active tectonism resulting in the reactivation of the western boundary fault has been documented.

- The 'Brae Trend' fields consist of a series of hydrocarbon accumulations located adjacent to the western margin of the South Viking Graben in UKCS blocks 16/-7, -8, -12, and -17. The half graben fault is bounded to the west by the Fladen Ground Spur, with regional Late Jurassic rifting culminating in the deposition of the submarine fan systems on the basin margin.

- The hydrocarbon reservoirs consist of clastic material derived from the erosion of the Devonian footwall, exhibiting overall large scale fining upward sequences in excess of 150 metres (Fletcher, 2003a). Portions of the fields proximal to the faulted margin consist of coarse predominantly conglomeratic material, with units prograding into progressively finer and mud-rich distal fan deposits eastward into the basin.

- The Brae trend reservoirs contain anomalously high CO_2 contents. Fields immediately adjacent to the margin fault contain over 30 %mol. CO_2 (South and Central Brae), with fields further east less than 10 %mol (Sleipner Vest).This suggests that CO_2 may have been introduced to the region via the graben bounding fault before migrating eastward, producing the CO_2 distribution trend. The highest CO_2 concentrations are also witnessed in the deepest portions of the reservoirs, affirming a probable fault related origin.

- The high concentration CO_2 in the Brae region is believed to be of inorganic origin. This differs from low CO_2 concentrations also observed in the region which typically exhibit organically derived CO_2 signatures owing to hydrocarbon generation in the area. Diagenetic reactions and subsequent release of CO_2 enriched fluids in the basin fill are a potential source for the elevated CO_2, with the thermal degradation of Zechstein carbonates at depth also frequently speculated. Subsequent chapters will evaluate possible fluid sources with respect to mineral chemistry (Ch. 3), fluid composition (Ch. 4), and stable isotope signature (Ch. 5).

Chapter 3

Fault zone mineralogy: origin and implications

3.1. Introduction

Based on the apparent relationship between the concentration and distribution of CO_2 in the region and the graben bounding fault (Figure 2.10), the fault zone between the Mesozoic sedimentary basin sequences and the Devonian footwall wereinvestigated for evidence of CO_2-rich fluid flow into the Brae Formation reservoirs. Several previous studies have investigated the passage of fluids upwards along fault zones in the North Sea hydrocarbon province and adjacent areas (e.g. Burley *et al.*, 1989; Macaulay *et al.*, 1997).

This chapter presents the results of petrographic and geochemical analyses of fracture cements in the fault zone. The purpose of the investigation was to establish whether the graben bounding fault zone acts as a conduit for significant volumes of CO_2 ascending

from depth into the adjacent Jurassic reservoirs. The use of scanning electron microscopy allows the high resolution investigation of small scale fracture cements where availability of sample material may be limited. The morphology and composition of the fracture cements provide information on fluid sources, fluid flow, and faulting conditions. The implications of the observations regarding the nature of fluid flow upwards within the fault zone will be discussed and evaluated, elucidating a process whereby the ascent of CO_2 in solution up the fault zone is recorded in the fracture cements. The possible source of the CO_2, based on the chemistry of the fracture cements, will also be considered.

3.2. Methodology

3.2.1. Sampling strategy

To assess whether the fault acted as a conduit for CO_2 flux into the Jurassic reservoirs, sections of the fault zone and immediately overlying reservoir were studied for evidence of fluid movement in the fault zone (i.e. mineral precipitates). Composite logs and geological reports from exploration wells located adjacent to the graben bounding fault were examined to assess the availability and extent of cored material penetrating the fault zone. Although the region has been extensively explored by the hydrocarbon industry, the availability of suitable material for study of the fault zone is limited, with very few cored sections extending below the Brae Formation into the fault zone and overlying Devonian footwall. However, four wells in the high-CO_2 area with sufficient cored sections extending into the fault zone were identified; 16/07a-12 (South Brae Field), 16/12a-19 (Larch Field), 16/12a-17 and 16/12a-16 (both Pine Field) (Figure 3.1). The cored sections investigated in this study are shown in Figure 3.2. All core and sample depths are reported TVDSS.

3.2.2. Analytical approach

Adopting a systematic approach, the focus area of the study was gradually determined using progressively higher resolution methods. The selected cored sections were studied to evaluate the location and morphology of the fault zone, fractures, and

associated cements. In addition to macroscopic observations, transmitted light thin section petrography was employed to investigate the fracture cements in more detail prior to higher resolution analytical methods (i.e. electron microscopy) concentrating on individual fracture cements (Figure 3.3).

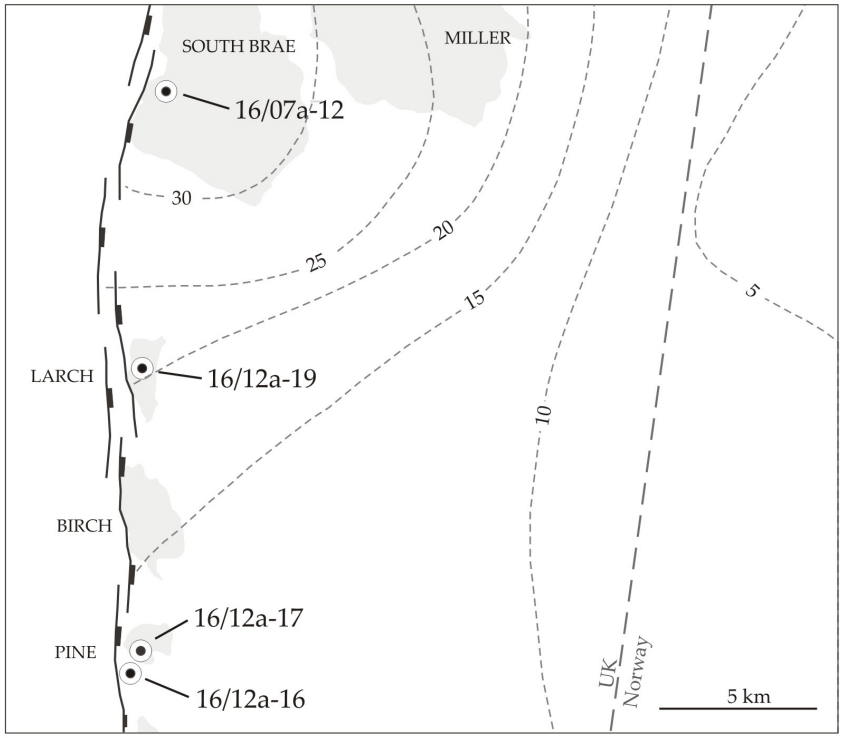

Figure 3.1. Map showing location of wells with available core which transect the faulted contact between the Jurassic hanging wall deposits and Devonian footwall. Contours show CO_2 concentrations (mol%) from Figure 2.10. Note, graben margin fault segmentation shown is purely schematic (see section 3.3.1).

High resolution scanning electron microscopy (SEM) was used to examine the mineralogy and petrographic relationships between the sub-millimetre scale fracture cements present within the sampled fault zone horizons. Core samples were made into polished thin sections and resin blocks. Where possible, the samples were cut perpendicular to the fracture orientation to give the optimum representation of the cement morphology. The samples were subsequently carbon coated for SEM analysis. Back-scattered electron (BSE) and cathodoluminescence (CL) imaging was carried out using a Philips XL30CP SEM fitted with a Philips cathodoluminescence detector.

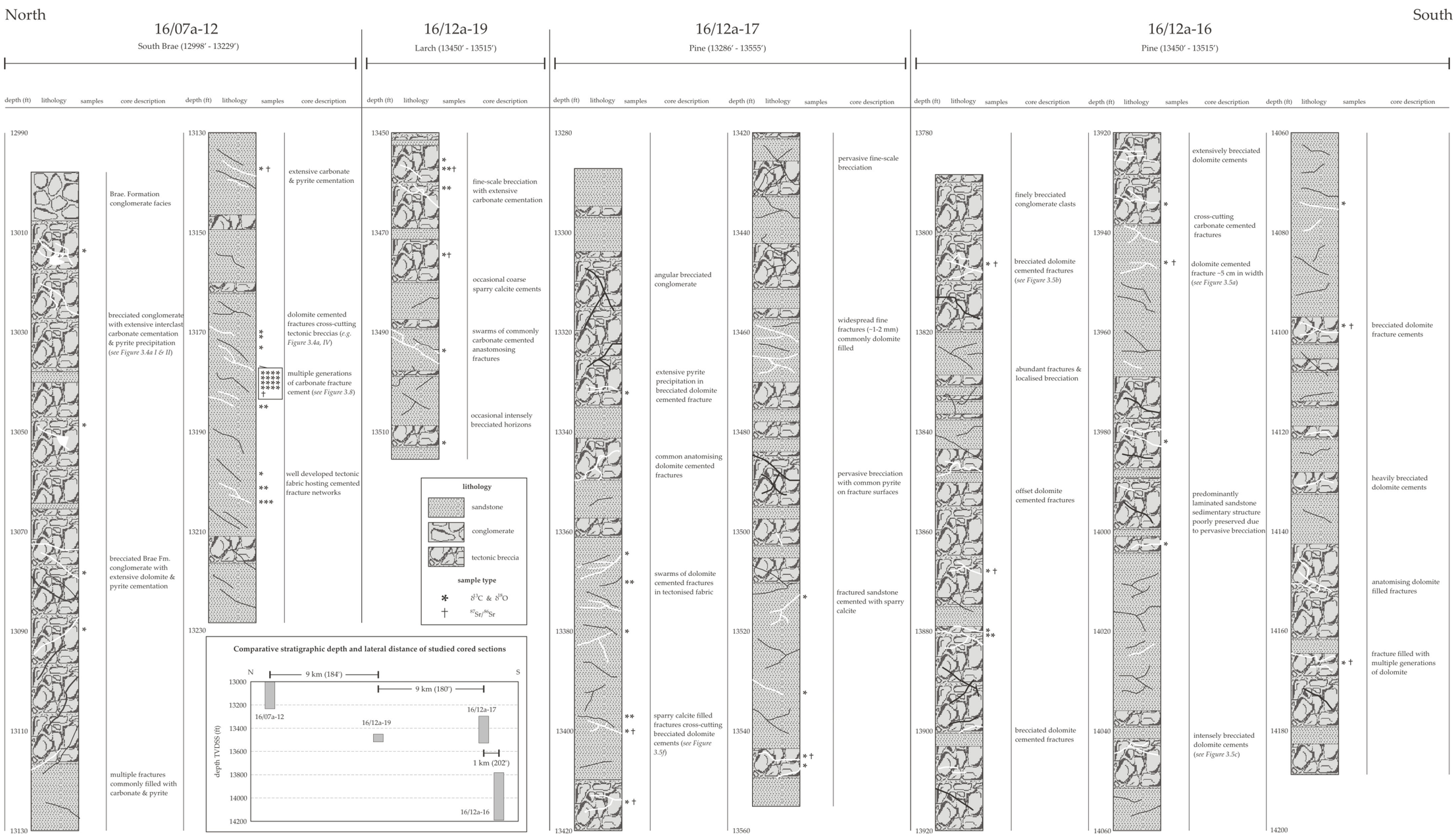

Figure 3.2 Descriptions of the cored intervals investigated in this study. Comparison of the stratigraphic depths of the examined cored sections and distance between the wells in shown. The location of oxygen, carbon, and strontium isotope samples used later in the study are also illustrated. All depths are reported TVDSS.

Working conditions were 20 kV accelerating voltage and 10 mm working distance (15 mm for CL). CL images were obtained by accumulating and integrating the signal of 32 frames using a slow scanning beam raster. Whilst appreciating potential sample damage due to prolonged beam exposure, this method mitigates the effect of prolonged phosphorescence inherent in SEM-CL studies of carbonate minerals (e.g. Lee *et al.*, 2005). Digital image mosaics were obtained over the scale of the samples to create maps used for the determination of cement stratigraphy within the fractures.

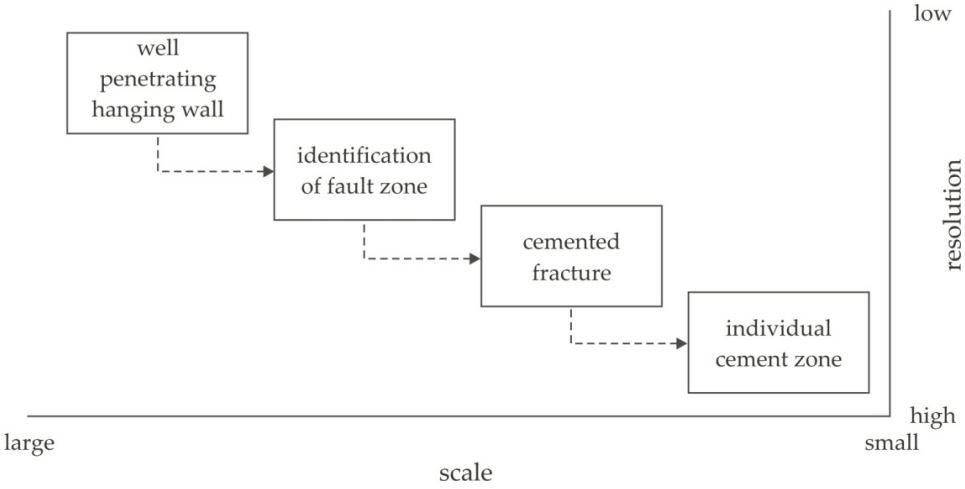

Figure 3.3. Investigative methodology applied in the study of the fault zone showing increasingly smaller sample area at progressively higher resolution, culminating in the study of individual sub-millimetre cements.

Energy dispersive X-ray (EDX) analysis, aiding qualitative spot element analysis (and thus mineral identification), was undertaken using a PGT Spirit X-ray analysis system. Although EDX analysis gives qualitative to semi-quantitative elemental analysis, to assess variation in chemical composition and trace element distribution between the different carbonate facture cements electron microprobe analysis (EMPA) was employed. With a spatial resolution of ~1 μm and detection limits in the order 0.01 to 0.05 wt%, EMPA is able to give more precise and quantitative chemical analysis of the mineral cements. Analysis was carried out using a Cameca SX100 electron microprobe fitted with 5 vertical spectrometers. The cements were analysed for elements common in carbonate minerals (Ca, Mg, Fe, and Mn) and lesser, but potentially significant, trace elements (Na, K, Sr, Ba, and S). Working conditions were 15 μm beam size and 15 kV

accelerating voltage. All analyses were conducted at the School of Geosciences, University of Edinburgh.

3.3. Observations and results

3.3.1. Graben bounding fault extent and geometry

The mapped geometry and strike of the graben bounding fault on a regional scale is limited due to available data limitations and resolution (e.g. Figure 3.1), with higher resolution fault orientations typically only available for specific hydrocarbon fields. However, general trends concerning faulting on the graben margin can be assumed owing to the tectonic framework of the basin. Transfer faults are important structural elements in extensional sedimentary basins, accommodating extension along the basin bounding fault (Gawthorpe & Hurst, 1993). In the T-Block Fields the general north-south lineament of the graben bounding fault is offset by transfer faults, developed during extensional phases during Permo-Triassic rifting (Glennie, 1990). The transfer faults offset the main basin bounding fault creating discrete fault terraces in the region with numerous synthetic faults (typically less than 1km along strike) (Figure 3.4). Similar tectonic features are also observed in the Brae Fields, with the distribution of submarine fans comprising the Brae Formation strongly influenced by fault segmentation along the basin bounding fault (Gawthorpe & Hurst, 1993).

Cherry (1993), suggested that the varying graben margin profile may be indicative of differing footwall geometries, with fault sections exhibiting narrow fault terraces related to steep planar fault geometries (~60°) similar to those noted by Thomas and Coward (1996) on the South Viking Graben margin. Conversely, extended fault terraces typically display low angle listric fault profiles similar to the larger scale Beryl embayment structure witnessed north of the Brae area (Færseth, 1996). Such geometries can have a significant impact on the extent of fault displacement on a relatively small scale, with Cherry (1993) noting throw of the graben margin fault ranging from 500m to 1000m in the T-Block Fields. Example profiles of these contrasting fault plane morphologies on a field scale can be found in Appendix I.a.

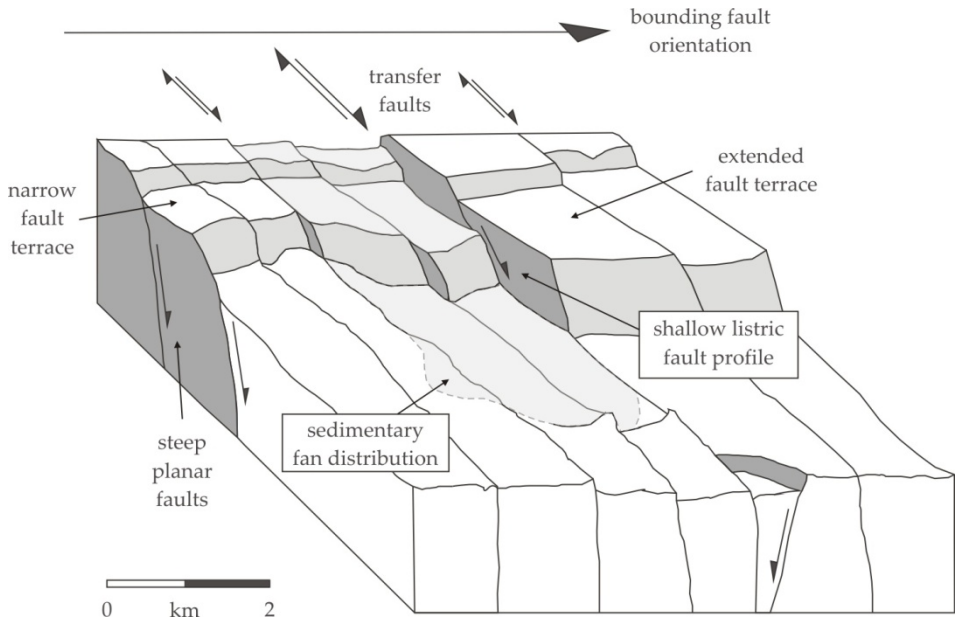

Figure 3.4. Schematic diagram showing fault segmentation and varying morphologies along graben bounding fault in T-Block Fields due to influence of transfer fault oblique to main graben margin orientation. Modified from Cherry (1993).

3.3.2. Fault damage zone morphology

The depth of the fault damage zone in the cored intervals was determined from depths noted in industry reports of the studied wells in conjunction with observations of cored sections. Well 16/07a-12 (South Brae) is the most extensively cored exploration well adjacent to the fault zone identified in the study (13010′ – 13200′ TVDSS). A range of brecciation and cementation styles occur below the archetypal angular slope talus conglomeratic units identified proximal to the graben fault in the Brae Formation (e.g. Turner *et al*., 1987). Shallower cored intervals (13010′ – 13050′) consist of high dilation breccias (e.g. Sibson, 1987) of angular wallrock fragments (5 – >65 mm) cemented by carbonate and iron-sulphide mineralisation (Figure 3.5a , i, ii). At greater depths in the cored sections, the brecciation textures become increasingly tectonised with fracturing of brecciated clasts observed, resulting in the formation of microbreccias adjacent to these clasts. These sections are commonly cross cut by carbonate veins which have been subsequently offset through further faulting (Figure 3.5b, core diagrams iii and v).

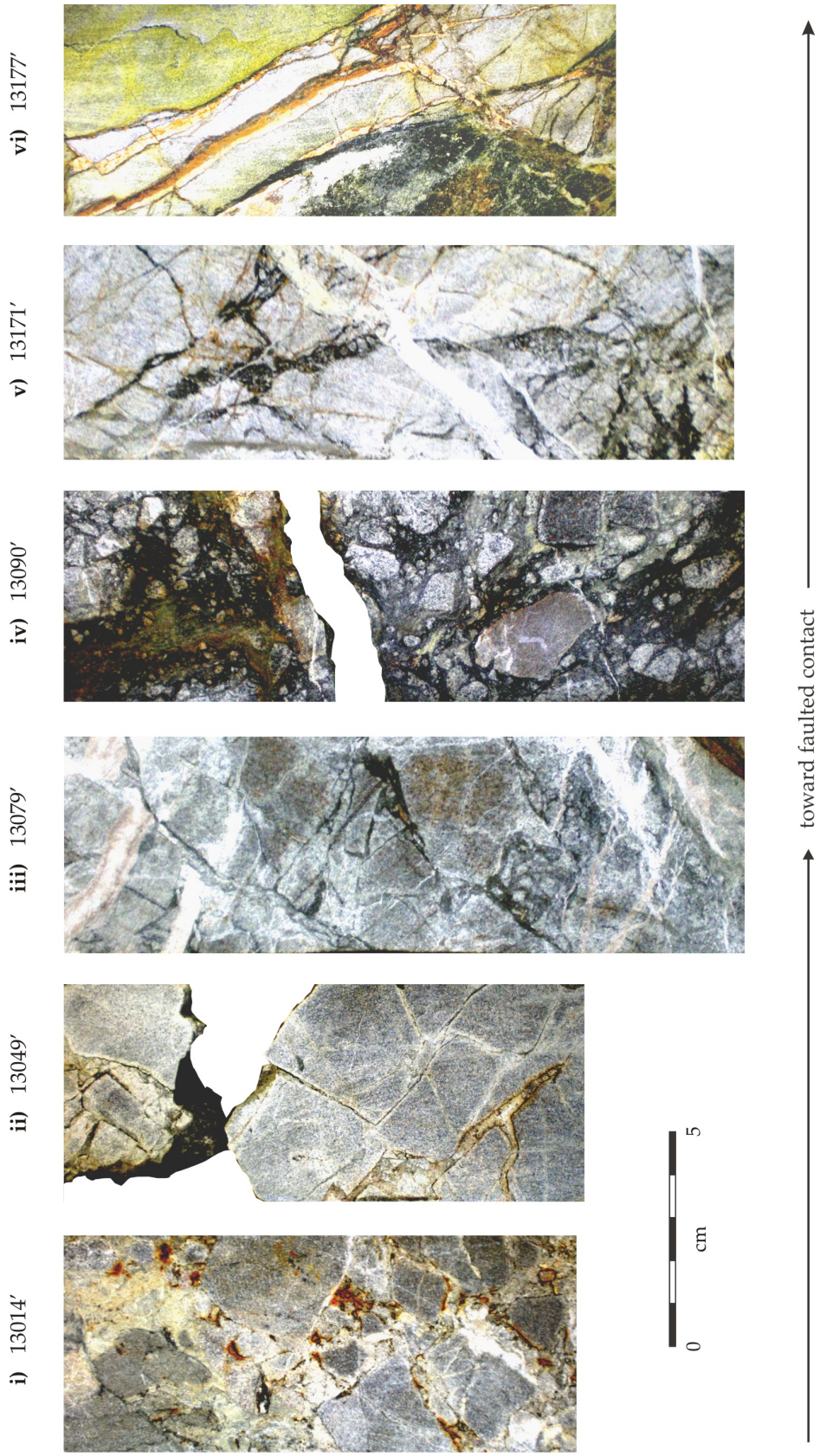

Figure 3.5a. Transect of cored intervals from the postulated fault damaged zone observed in well 16/07a-12 (South Brae) showing the progressive evolution of breccia morphology from sedimentary dominated textures at shallower depths to tectonically influenced breccia at increasingly greater depth.

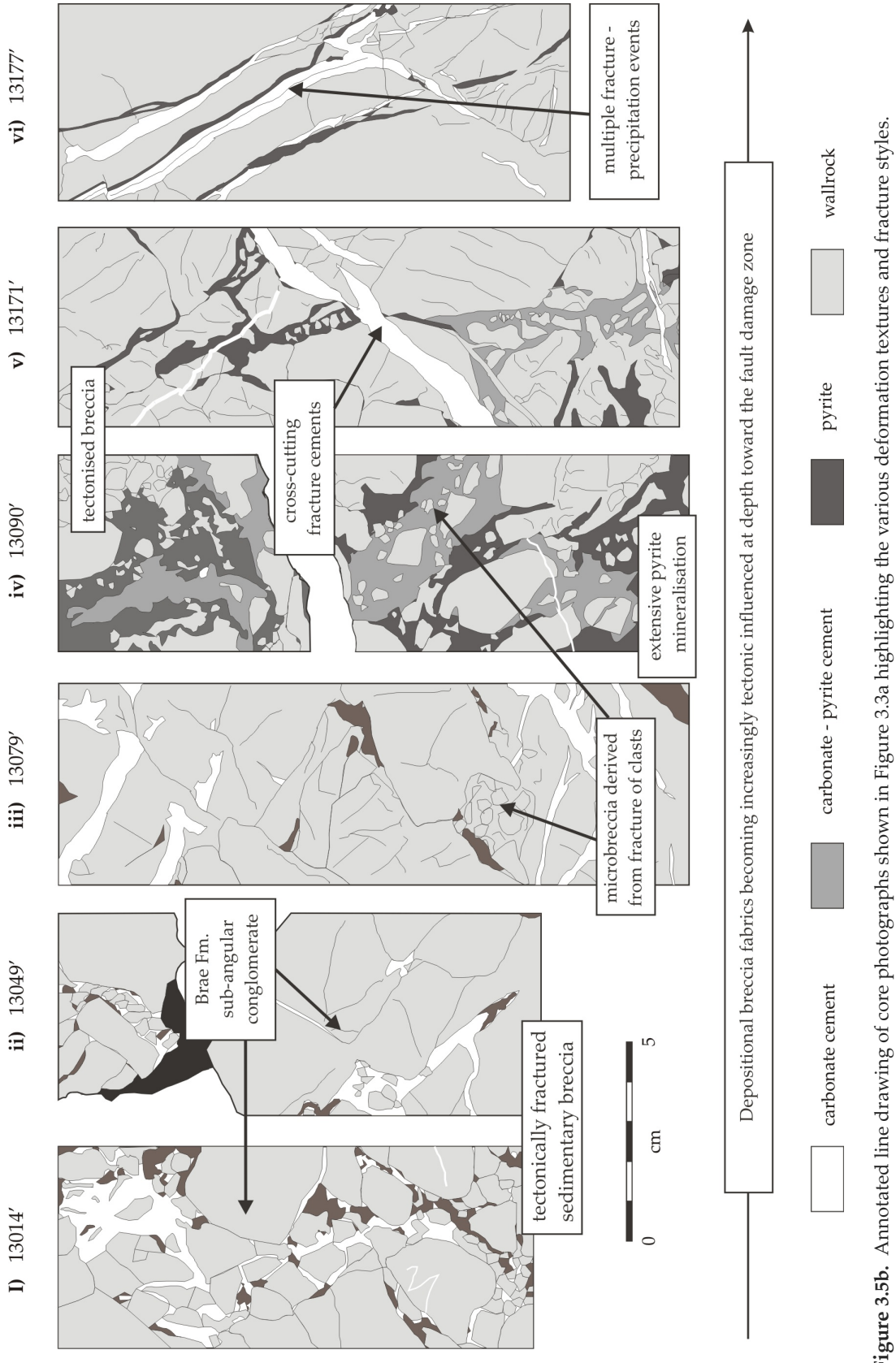

Figure 3.5b. Annotated line drawing of core photographs shown in Figure 3.3a highlighting the various deformation textures and fracture styles.

Breccias hosting extensive pyrite mineralisation are also encountered in number of intervals. These sequences typically show evidence of multiple brecciation episodes, with earlier dolomite and pyrite assemblages disaggregated and subsequently incorporated into a sulphide matrix (e.g. Figure 3.5a, core photograph iv). With increasing depth in the fault zone (>13150'), the fault breccia becomes more clast supported and the tectonised fabric more developed with an absence of the heavily brecciated extensively mineralised fractures witnessed higher in the succession (Figure 3.5a core photograph vi). At greater depth (13175') abundant fracture cements are present within low displacement 'jigsaw' breccias, with the geometry of the fracture arrays less varied.

The exact location of the fault contact *per se* is not determined from the core available; with no standard cataclastic dominated sequences typical of fault contact zones encountered. However, the high density of fractures and tectonic breccias within the cored intervals is indicative of fault damage zones heavily influenced by tectonic and hydraulic activity on the main fault (e.g. Caine *et al*., 1996; Evans *et al*., 1997). The high fracture density coupled with an absence of clay smearing due to low clay content in the fractured horizons suggests fault zone permeability may have been sufficiently high to accommodate appreciable fluid flow through the damage zone upon faulting.

3.3.3. Fault zone hosted fracture cements

Cored sections from horizons identified as the fault zone in all the studied wells exhibit extensive fracturing and pervasive carbonate cementation. The typically anastomosing fracture cements vary in morphology and scale, ranging from sub-millimetre up to ~5 cm width. Dolomite is the volumetrically the most significant mineral present in the fracture cements (>80%), with a distinctive orange hue in cored section. Calcite, typically sparry, cements are also evident with some minor quartz filled fractures, notably in samples from wells 16/12a-17 and 16/12a-19. The dolomite cements exhibit both euhedral and rhombic textures. The largest fracture fills consist of euhedral dolomite (up to 5 cm width) with sandstone wallrock fragments (up to 1 cm diameter) enclosed within the carbonate cement (Figure 3.6 a).

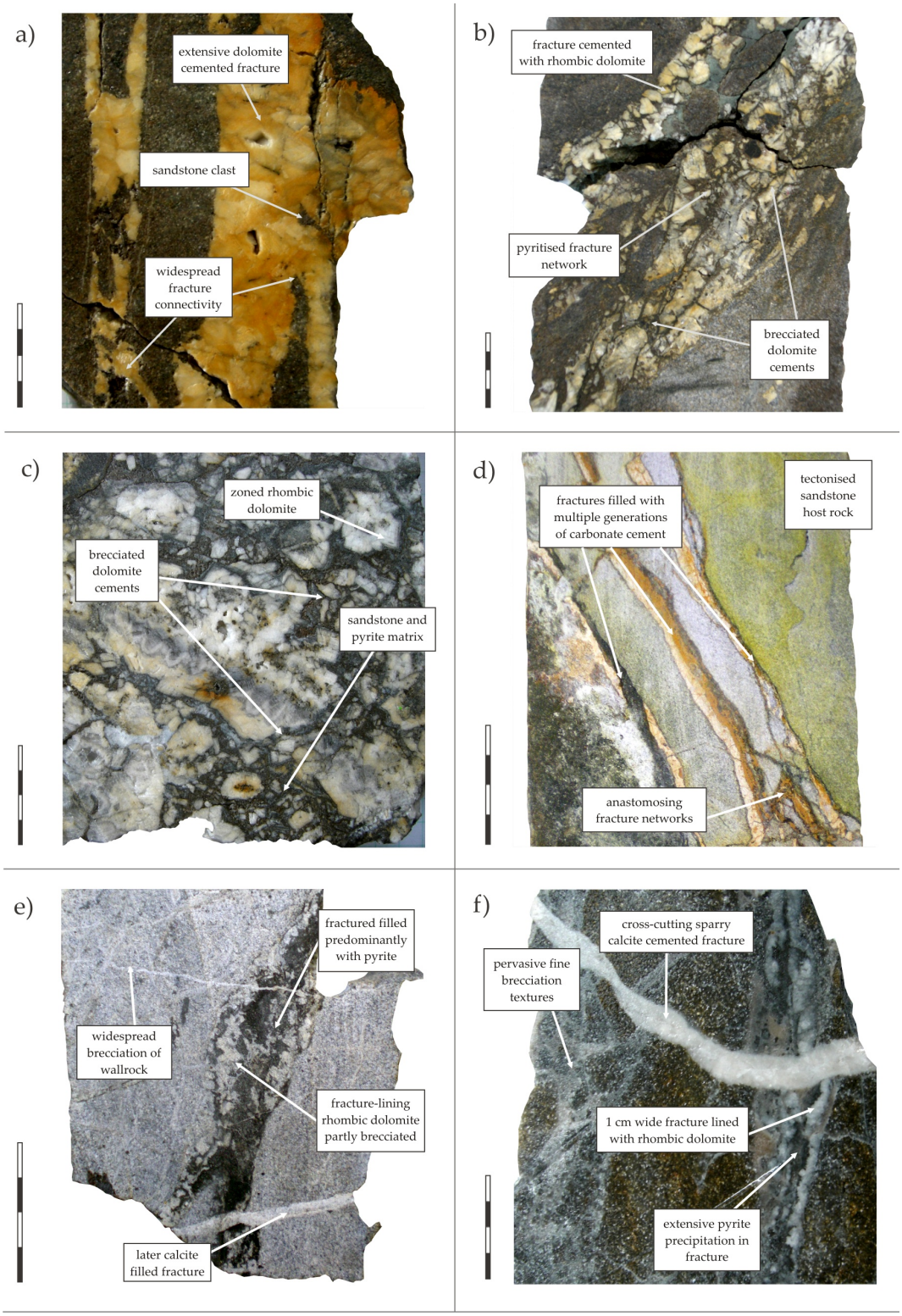

Figure 3.6. Photographs illustrating various fracture morphologies and mineralogical relationships encountered within cored sections of the fault damaged zone along the graben margin fault **a)** 16/12a-16 (13946'), **b)** 16/12a-16 (13803'), **c)** 16/12a-16 (14041'), **d)** 16/07a-12 (13177'), **e)** 16/07a-12 (13026'), **f)** 16/12a-17 (13397') All depths TVDSS. Scale bar 20 mm.

Rhombic dolomite (commonly zoned) is present in a number of fractures, with the individual crystals ranging from millimetre scale to approximately 2 cm in size. In a number of fracture zones, the rhombic dolomite crystals are disaggregated and fragmented (Figure 3.6 b,c). Close examination reveals that many fractures within the tight tectonic breccia of the fault damage zone are composite cement horizons, seemingly formed during a series of individual fracture and cementation episodes (Figure 3.6 d). Most abundant in well 16/07a-12, in core section these are recognised by millimetre scale dolomite cements ranging from pale cream to bright orange in colour on non-freshly cut surfaces. However, in cored section at this macroscopic scale, the number and relative timing of discrete cements cannot be readily identified. There is no dominant orientation of the fractures observed, with the orientation apparently random. However, owing to sample limitations (i.e. essentially a 1D core transect) the orientation of the fracture cements would invariably be ambiguous over the scale of the faulted contact.

Pyrite is observed co-precipitated with rhombic dolomite in a number of fractures, with crustiform banding sequences observed (Figure 3.6 e, f). The extensively pyritised fractures observed are typically no greater than 2 cm in width, with rhombic dolomite crystals less than 5 mm diameter. These fractures are frequently cross cut by later sparry calcite cemented fractures (< 1 cm thick) oblique to the orientation of the pyrite rich fractures. Extensive pyrite mineralisation is notable in the shallower (13010′ – 13050′) brecciated sequences in the cored sections from well 16 / 07a -12 (e.g. Figure 3.4 a, i, ii). The pyrite is present both within the zoned rhombic mineral structure of the dolomite and in the fracture fills coating the syntaxial dolomite rims. Fragmentation and corrosion of the dolomite rhombs is frequently observed and predates pyrite precipitation, suggesting a possible late stage sulphide dominated fluid influx (Figure 3.7). Notably, at macroscopic scale the various morphologies of fractures and range of cementation styles is not confined to any individual well but present across the range of locations studied, and thus over a significant lateral distance along the fault zone (e.g. at least 15 km between wells 16/7a-12 and 16/12a-16).

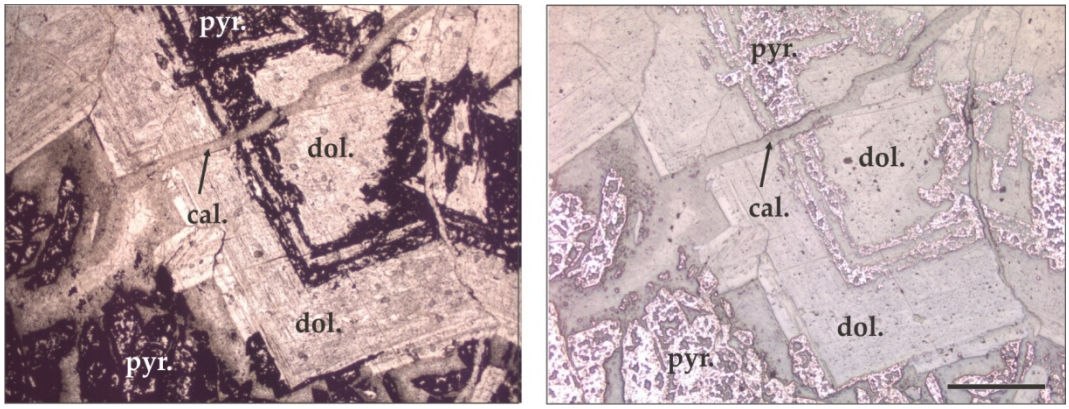

Figure 3.7. Photomicrograph under PPL (left) and reflected light (right) showing corrosion and brecciation of dolomite cements (dol.) in a pyrite matrix (pyr.) Both phases have been subsequently crosscut by calcite filled fracture (cal.) Well 16/07a-12, depth 13026'. Scale bar is 1 mm.

3.3.4. Fracture cement petrography

As noted previously, a number of fracture zones are comprised of multiple cements. On the basis of back-scattered electron microscopy (BSE) analysis, five successive stages of fracturing and cementation (denoted *A* to *E*) are distinguished based on cross cutting relationships within the fracture network (Figure 3.8). This paragenetic sequence is devised from cements observed in well 16/07a-12. The full cement sequence not evident in every sample studied across all the wells studied, with some fracture networks containing only two or three of the cements identified. This suggests some of the fracture zones were not reactivated in each event, creating preferential fluid pathways during some fracture events. However, the cements are correlatable with the more comprehensive composite fractures based on morphology and BSE response coupled with EDX analysis. Figure 3.8 shows a typical transect across a composite vein with all five zones developed. Within the fractures, the cements show varying degrees of crystallinity and symmetry, with earlier cements (*A*, *B*, and *C*) finer and showing unitaxial morphologies, whereas later cements (*D* and *E*) display larger crystals with symmetrically lined distributions. The petrographic and morphological characteristics of the fracture cements are summarised in table 3.1

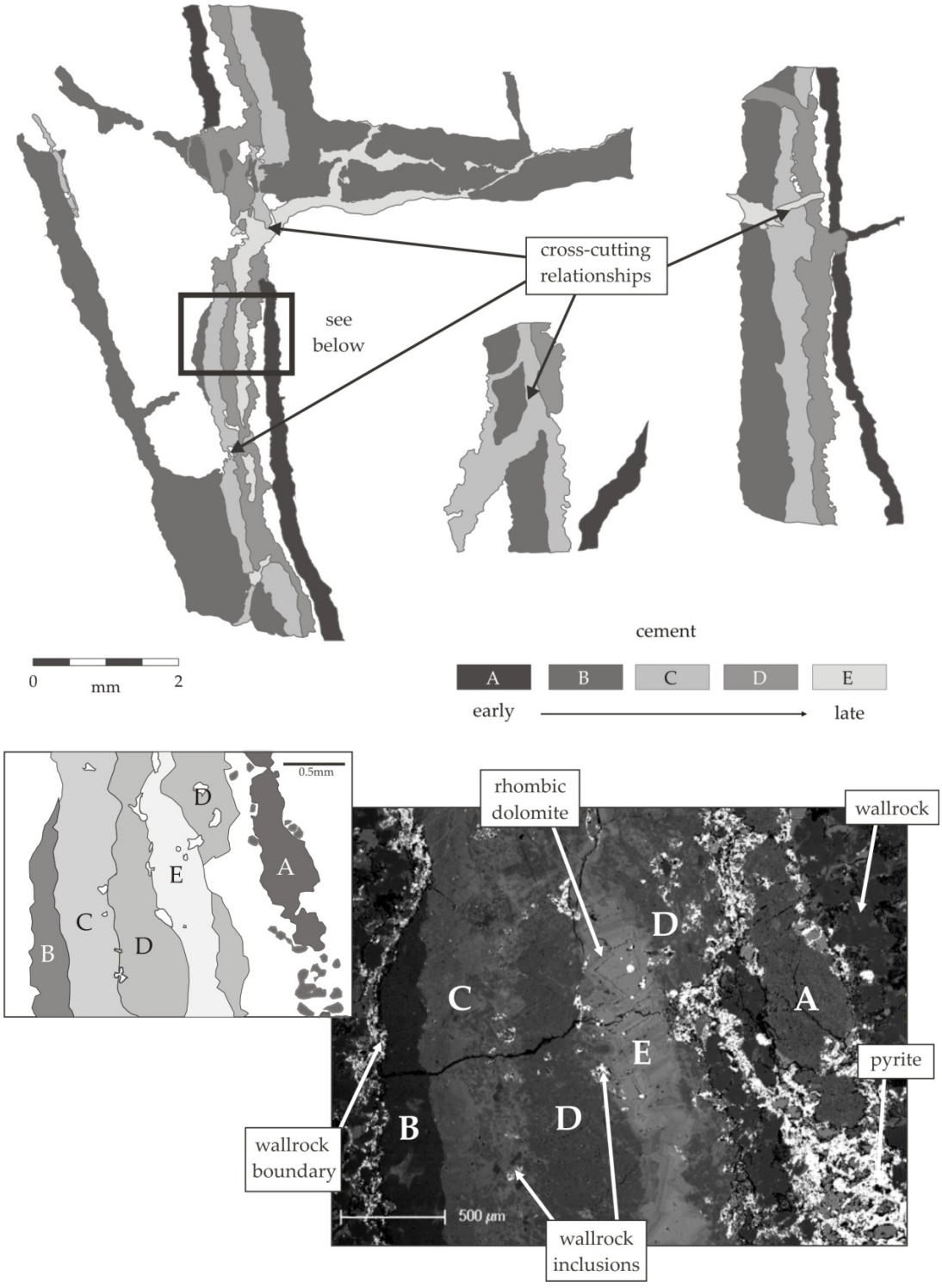

Figure 3.8. Composite image maps of dolomite fracture cement arrays illustrating the paragenetic sequence (A – E) determined from cross-cutting relationships and BSE response. BSE image shows the textural characteristics of the various cement generations. Samples from well 16/07a-12 (South Brae), depth 13177′.

Cement complex *A*

Paragenetically the earliest, this cement is comprised of calcite, dolomite and pyrite. The dolomite exhibits a bright, homogenous BSE response with subhedral crystal morphologies and the darker calcite displays ragged crystal edges adjacent to the dolomite and pyrite (Figure 3.9 a). The observed dolomite and calcite is unlikely to be a primary growth feature which strongly suggests replacement of the calcite by dolomite and pyrite. Previous authors have interpreted similar textures to also cements that have undergone incomplete replacement or recrystallisation (e.g. Montanez & Land, 1994). The replacement is primarily focused on the outer edges of the fracture cements with no dissolution textures or intragranular fracturing of the wallrock observed. From the paragenetic sequence established from cross-cutting relationships the relative timing of calcite to dolomite replacement cannot be determined.

Cement *B*

Cement B comprises subhedral dolomite exhibiting a non-planar anhedral fabric with no apparent preferred mineral growth orientation. The dolomite crystals range between 50 – 300 μm in size and display curved and serrated edges. The cement has grown from a substrate consisting of either the sandstone wallrock or a pyritised margin seemingly created by the oblique fracturing of cement *A*. Under XPL the crystals appear cloudy and exhibit undulose extinction, indicative of saddle dolomite (Radke & Mathis, 1980). The cement exhibits a bright SEM-CL signal, suggesting the dolomite is non-ferroan (Figure 3.9 b). This was confirmed by EDX analysis and EMPA (*see section 3.3.5 and Appendix I.b, c*). No zonation was observed with BSE imaging, indicating there were no significant chemical variations during cement growth.

Cement *C*

Cement C comprises of dolomite. The subhedral crystal morphology and boundaries of the cement are more pronounced using optical microscopy compared to cement *B*. The contact between the two cements is well defined, with some subhedral crystal forms observed radiating from the contact with cement *B*, indicating precipitation nucleated on the previous cement margin after fracturing.

cement generation		mineralogy	composition (Ca:Mg:Fe) [1]	crystal size	morphology	fracture width	additional observations
A	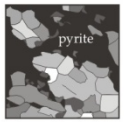	dolomite & calcite	dolomite* Ca: 0.55 - 0.58 Mg: 0.24 - 0.28 Fe: 0.13 - 0.19	100 - 250 µm	anhedral	200 - 500 µm	Calcite replaced by co-precipitated dolomite and pyrite. Remaining calcite displays corrosion textures on crystal edges.
B	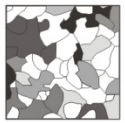	dolomite	Ca: 0.62 - 0.68 Mg: 0.30 - 0.38 Fe: 0.00 - 0.05	50 - 200 µm	anhedral	600 - 1800 µm	Non-planar crystal fabric showing occasional undulose extinction. Fracture cross-cuts cement A obliquely, with subsequent fractures and cements following the trend of cement B.
C		Fe-dolomite	Ca: 0.55 - 0.65 Mg: 0.23 - 0.30 Fe: 0.05 - 0.22	200 - 500 µm	subhedral	300 - 700 µm	Fragments of wallrock (quartz & pyrite) and cement B present in the crystal matrix. Undulose extinction indicative of saddle dolomite commonly observed.
D		Fe-dolomite	Ca: 0.55 - 0.62 Mg: 0.20 - 0.30 Fe: 0.11 - 0.26	100 - 300 µm	subhedral	200 - 500 µm	Compositionally zoned with respect to Fe and Mg distribution. Zonation is poorly defined and diffuse. Crystal boundary with cement C commonly lined with wallrock fragments
E	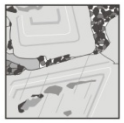	Fe-dolomite	Ca: 0.55 - 0.64 Mg: 0.12 - 0.21 Fe: 0.19 - 0.33	200 - 400 µm	euhedral	200 - 500 µm	Syntaxial cements exhibit bridging textures across fracture. Well defined rhombic crystals display internal compositional zonation.

Ta

Table 3.1. Table illustrating the petrographic, chemical, and textural characteristics of the cement generations (A – E) delineated from cross-cutting relationships.

[1] Chemical data concerning carbonate composition is presented in section 3.3.5. * Composition of dolomite is presented in cement A, calcite typically >0.95 Ca.

The dolomite crystals are larger (crystal size, 200 – 500 μm) and exhibit isolated undulose extinction and cloudy zones indicative of saddle dolomite. The BSE response of the cement is lighter relative to cement B due to a higher Fe content (determined by EMPA; section 3.3.4). Conversely the SEM-CL response is completely quenched due to the presence of Fe (Marshall, 1988). The cement contains quartz and pyrite inclusions probably derived from the wallrock in addition to fragments of cement *B* dolomite, further evidence of the relative age of the cements. Although relatively rare, the inclusions are most frequently present on the inner margins of the cement.

Cement *D*

The margin between cements *C* and *D* shows a more advanced degree of physical deformation compared to that between *B* and *C*. The boundary is irregular and commonly lined with wallrock fragments (quartz, pyrite, clays) which are often cemented together, suggesting disaggregation of the country rock upon fracturing or multiple fracture cementation events (Figure 3.9c). Cement D comprises of subhedral dolomite with a predominantly non-planar fabric, with BSE imaging showing irregular zonation, suggesting non-uniform distribution of Fe and Mg throughout the crystals in the cement.

Cement *E*

The youngest fracture cement identified is characterised by well defined euhedral rhombic dolomite. The rhombic crystals are approximately 300 μm in diameter and exhibit cloudy cores with clear syntaxial rims showing fine internal zoning attributed to compositional variations. The syntaxial rims become progressively more ferroan, as evidenced by a gradually brighter BSE response across transects of the rims. The euhedral nature of the crystals suggests growth of the cements into open fractures as opposed to incremental opening (Hilgers *et al*., 2001).

Figure 3.9d shows wallrock material enclosed by symmetrical dolomite rhombs, indicating that the crystals grew contemporaneously into the interior of the fracture containing wallrock debris. This is also reflected by the increasing incorporation of

disseminated pyrite and wallrock derived quartz subgrains into the rims of the rhombs through time. In the sampled fracture cement assemblages, cement *E* is the first to conclusively show morphologies indicative of symmetrical growth into a void. However, this is potentially due to subsequent fracture and cementation episodes destroying diagnostic textures in previous cements.

3.3.5. Fracture cement chemistry

As observed using BSE imaging, the progressive increase in the brightness of response through cements *B* to *E* (Figure 3.8), indicates variability in dolomite composition throughout the paragenetic sequence. Electron microprobe analysis of the fracture cements shows an overall gradual increase in the percentage of Fe present in the dolomite (Figure 3.10). Cement *B* comprises Ca-enriched dolomite ($Ca_{>0.60}$; $Mg_{>0.30}$; $Fe_{<0.05}$).

Subsequent cements are increasingly ferroan. Fe content of dolomite in cements *C* and *D* ranges from $Fe_{0.05 - 0.23}$ and $Fe_{0.12 - 0.28}$ respectively at the expense of Mg in the mineral lattice. The relatively wide range of Fe:Mg ratios in the cements reflects the degree of heterogeneity observed within the dolomite from BSE response. Cement *E* shows the highest Fe percentage $Fe_{0.20 - 0.35}$), effectively ankerite in composition. Although the cements do exhibit appreciable overlap in their carbonate chemistry, cross-cutting relationships observed between the fracture generations are robust enough categorise them as discrete fracture events.

Fracture cement complex *A* is considered separately owing to the presence of two distinct carbonate minerals present. The original calcite mineralogy prior to replacement is effectively pure ($Ca_{>0.95}$), with the later replacement dolomite observed in the cement *A* sharing a chemical signature similar to that present in cements *C* and *D*, possibly suggesting similar fluids. Although Ca, Mg, and Fe show significant variation between the various cement generations, trace element concentrations are sufficiently low that possible variations between the cements are within the detection and error limits of the technique and are thus not considered (for data see Appendix I.b & c).

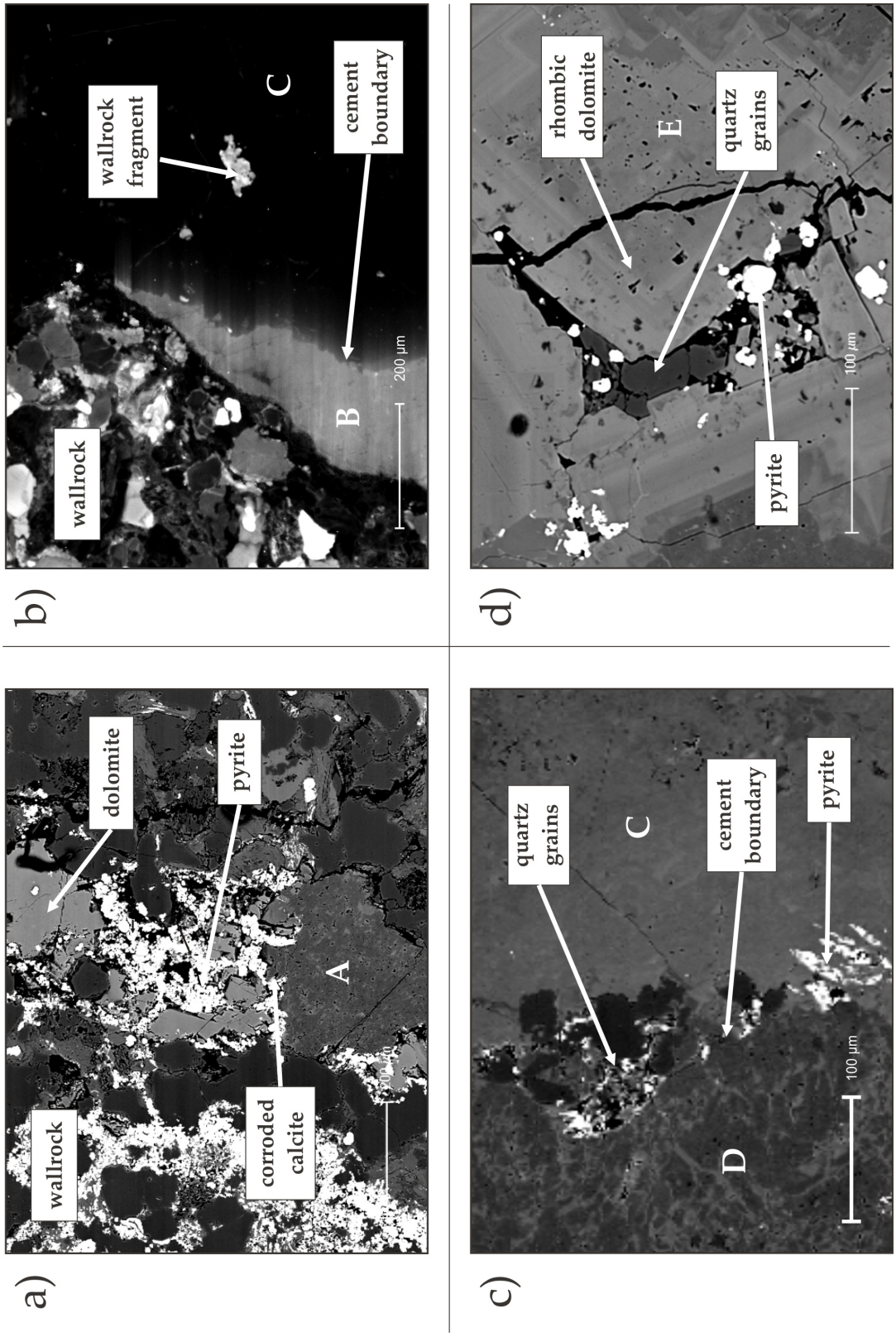
a)
wallrock
dolomite
pyrite
corroded calcite
A
100 µm
b)
wallrock
wallrock fragment
cement boundary
C
B
200 µm
c)
quartz grains
C
cement boundary
pyrite
D
100 µm
d)
rhombic dolomite
E
quartz grains
pyrite
100 µm

Figure 3.9. (previous page). a) BSE image of cement A showing replacement of calcite by dolomite and pyrite **b)** CL image of cements *B* and *C* showing wallrock fragment within cement *C*. Brightness contrast due to negligible Fe content in cement *B* **c)** BSE image showing quartz and pyrite from fractured wallrock contact present on boundary between cements *C* and *D* **d)** BSE image showing symmetrically growing rhombic dolomite of cement E entrapping disaggregated wallrock fragments.

3.3.6. Wallrock petrography

The wallrock hosting the various fracture networks consists of well sorted sub-rounded fine – very fine quartz grains (> 90 %) with ~5 % feldspathic minerals (sublitharenite). Clay content is low, less than 5%. There is no visible porosity in thin section. In XPL the quartz grains exhibit undulose extinction. It is not clear whether this was inherited from the Devonian footwall lithology or is a post-depositional strain-related texture due to later tectonism. The ductile clay minerals are deformed, enveloping the quartz grains. No marked dissolution textures are observed. There is no evidence of carbonate cement or framework grain dissolution in the lithology.

3.4. Discussion

3.4.1. Fault zone evolution and fracture mechanisms

Fracture cement patterns can provide a valuable insight into faulting processes and fluid conditions in fault zones. There are a number of possible mechanisms facilitating fluid movement and subsequent cement precipitation: gravity, compaction, thermal gradients, seismic pumping, and tectonic stresses (e.g. Garven & Raffensberger, 1997). Multiple generations of brecciation and fracture cement attest to a number of tectonic episodes and discrete fluid flow events within the main fault zone respectively. Fault-related fluid flow in sedimentary basins is relatively common, with numerous diagenetic profiles in the Jurassic and Cretaceous attesting to influence of fluids introduced from depth (Burley, 1993). Although the graben margin fault has unquestionably experienced a protracted and diverse tectonic history, the morphology of the brecciation textures and fracture cements does not suggest a predominantly shear influenced genesis as discussed below.

Determination of brecciation and fracturing processes in major fault zones can be problematic given the complex array of breccia types typically observed in such settings (Sibson, 1986). This is further compounded in this study by limited sample horizons. However, the breccias predominantly witnessed in the cores studied share textures similar to episodic breccias observed by Phillips (1972). The author attributed the formation of the angular breccia style to abrupt fluid pressure increases during hydraulic fracturing. Such brecciation styles are frequently observed in sulphide mineralisation deposits arising from the ascent of overpressured fluids (e.g. Gregg, 2004). On a smaller scale, the negligible lateral displacement and absence of typical fault gouge in the fracture cements also suggests an absence of significant tectonic shear in the fracturing process. This is affirmed by the mosaic texture of the earlier cements (i.e. *B* and *C*), and later rhombic dolomite precipitation (cement *E*) which favour mineral growth into dilatant fractures, as suggested by the brecciation process discussed previously

The morphology and cyclic nature of the fracture cements strongly suggests episodic fracturing and precipitation events, with fracture dilation accommodating rapid fracture growth with minimal fault displacement (e.g. Eichhubl & Boles, 2000). Hydraulic fracturing resulting from the build up of formation fluid pressure at depth provides a mechanism accommodating brittle fracturing and the creation of fluid flow pathways. The ascent of over-pressured fluids into lower pressure regimes along the transient permeability of the fault zone facilitates the precipitation of cements in the fractures, promoting repeated cycles of pressure build up and release, termed 'seismic valving' (Sibson, 1981; 1994).

The ascent of overpressured fluids following fracturing results in fluid pressures dropping toward hydrostatic values. Reduction in fluid pressure and/or degassing of the ascending fluid would facilitate precipitation of dolomite in the fractures. The precipitation of the fracture cements would also quickly reduce fault zone permeability, allowing further fluid pressure build-up and initiation of subsequent hydraulic fracturing events, as demonstrated in the multiple cement generations (Figure 3.11).

Disruption of mineral symmetry due to repeated fracturing could account for the variation in the paragenetic sequence witnessed in the cements, with the classical symmetrical profile only preserved in the mineral cements deposited after the last phase of opening (i.e. cement *E*).

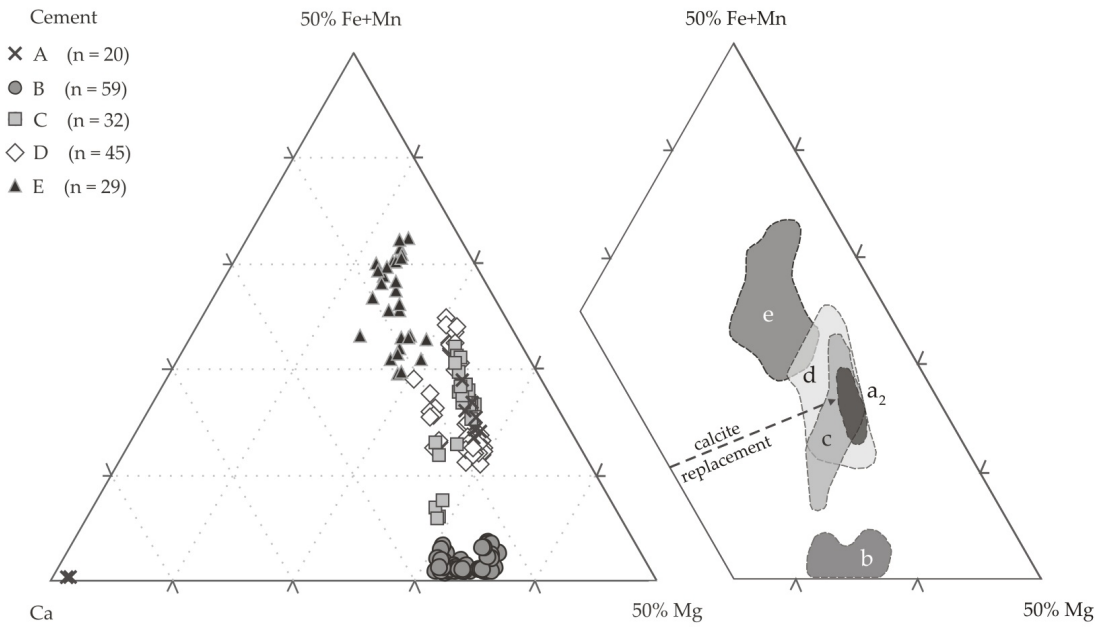

Figure 3.10. Ternary plots showing distribution of Ca, Mg, and Fe (+Mn) present within the carbonate fracture cements (*A* to *E*) determined from EMPA. The data (left) with the interpreted paragenetic sequence (right) shows an overall increase in Fe + Mn content in the Ca-enriched dolomite at the expense of Mg. Replacement dolomite in cement *A* (represented by subscript 2), exhibits a similar composition to cements *C* and *D*, probably reflecting similar precipitation conditions.

Conversely, precipitation of earlier cements may have been sufficiently rapid to inhibit the formation of such mineral textures as evidenced in the finer crystalline nature and less well formed textures of cements *B* and *C*. This may not have been experienced by later fracture cements where elevated pore pressures due to presumably greater burial depths could have increased carbonate solubility in the fluid, thus reducing precipitation rates. The bridging textures observed in the zoned rhombic dolomite in cement *E* alludes to sustained fluid flow and slower precipitation rates in the fracture network.

High fluid pressures present in the precipitation of later cements owing to greater burial may have also maintained high permeability in the fractures. Higher fluid pressures will have also suppressed CO_2 degassing; increasing carbonate solubility and reducing precipitation rates. This could be reflected in the well defined coarsely crystalline texture of the rhombic dolomites in cement E, with the zonation observed in the cements arising from fluctuating fluid composition during the phase of slower precipitation. The mineralogy and implications on fluid source are discussed later.

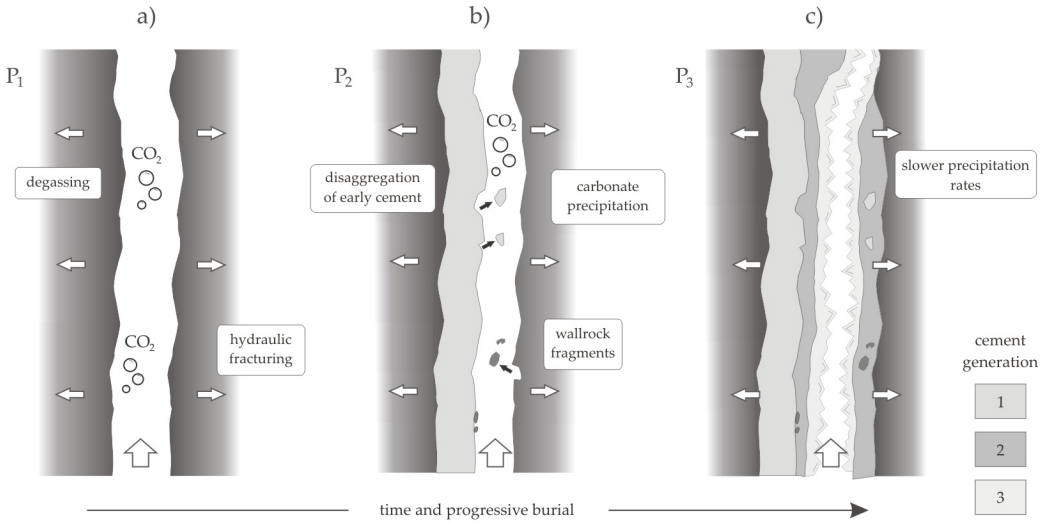

Figure 3.11. Schematic diagram highlighting evolution of fracturing and precipitation styles with progressive burial of the fault influenced zone. **a)** Overpressure build-up culminating in hydraulic fracturing and ascent of overpressured fluid into permeable fracture network. Degassing of fluid entering relatively low pressure environment (P_1) promotes mineral precipitation. **b)** Subsequent fracturing disrupts wallrock and existing cement, with disaggregated fragments incorporated into cement from rapidly precipitating fluid (i.e. cement *C*). **c)** Higher fluid pressures (P_3) may maintain fracture permeability and suppress CO_2 exsolution from the fluid, resulting in slower precipitation rates in later cements, as reflected in the multi-zoned rhombic dolomite observed in the cement generation *E*.

Fluid migration along basin scale faults due to overpressure release in the North Sea has been documented (Carstens & Finstad, 1981), suggesting the phenomenon is not uncommon. The authors observed that Jurassic formations adjacent to Viking Graben faults generally exhibit higher fluid pressures and geothermal gradients than equivalent

units in the nearby East Shetland Platform and Tampen Ground Spur. The authors ascribed this to large scale migration of hot fluids from depth up Jurassic fault block structures and subsequently accumulating within low permeability Cretaceous sequences. The deeper burial late introduction of high salinity fluids into the Fulmar Field, Central Graben, has been attributed to overpressure release (Wilkinson *et al*., 1997), with brittle deformation dolomite and anhydrite fracture cements documenting precipitation from fluids of Zechstein origin in Fulmar Formation sandstones (Macaulay *et al*., 1997). Such cements attest to large scale vertical migration (>2 km) of formation waters up basin margin faults in the North Sea (Cayley, 1987).

It is thus possible that the episodic fracturing and associated mineralogy observed in this study reflects the ascent of overpressured fluids along the fault zone, with cement textures and morphologies comparable to a number of mineral precipitates in basin margin fault localities. However, the degree of influence exerted by tectonic activity on the basin bounding fault in permitting the introduction and distribution of fluids from depth is not obvious.

3.4.2. Significance of fracture cement mineralogy

A number of factors can influence dolomite and calcite solubility. Increasing temperature or pH and decrease in pressure and salinity can all cause carbonate precipitation (Holland & Malinin, 1979). The occurrence of saddle dolomite in the cements *C* and *D* is generally indicative of precipitation from fluids at elevated temperatures (90 – 160°C; Spötl & Pitman, 1998) symptomatic of hydrothermal activity or late stage diagenesis (Radke & Mathis, 1980; Malone *et al*., 1996). The growth of saddle dolomite is considered relatively rapid relative to normal diagenetic carbonates (Searl, 1989), supporting the textural evidence discussed previously. Such precipitation mechanisms could also overcome the kinetic constraints encountered due to increasing carbonate solubility within a cooling ascending solution.

The presence of appreciable concentrations of Fe in the dolomite could attest to anoxic basinal conditions or increased supply of iron in the host fluid (Janssen *et al*., 2007).

Dolomites formed in relatively shallow conditions typically exhibit low Fe (and Mn) levels owing to oxidising conditions. Conversely, reducing conditions evident in deeper basinal waters result in higher levels of Fe and Mn present in solution as reflected in the cements. Therefore, it is possible that the gradual overall Fe increase observed in the paragenetic sequence (Figure 3.10) corresponds to increasing availability of Fe^{2+} in the host solution due to greater reducing conditions as a consequence of increasing fluid temperature arising from progressive burial. As a result, the relative timing of cement precipitation can be determined. For example, cements A_1 (initial calcite) and *B* show negligible Fe content suggesting the fluids were oxidising. Conversely, any available Fe could have been incorporated into another solid phase. However, no Fe dominant minerals (presumably pyrite) are witnessed contemporaneously with these early carbonate fracture cements.

Paragentically later cements (A_2, *C*, and *D)* display similar higher Fe contents (~10 – 20%) suggesting broadly similar reducing conditions for precipitation of all three generations. The introduction of higher temperature reduced fluids is probably manifested in the replacement co-precipitated dolomitisation fabric and pyrite witnessed in cement *A*. The further increase in Fe contents measured within cement *E* suggest further reducing conditions or greater availability of Fe in the precipitating fluids, suggesting appreciable burial and/or fluid evolution since precipitation of the previous cements.

As discussed previously, saddle dolomite is typically associated with base-metal sulphide mineralisation from relatively high temperature basinal fluids in reducing conditions (Radke & Mathis, 1980; Machel, 1987). The ubiquitous association of dolomite and pyrite in the cements (notably in the replacement of cement A_1) is testament to this, with the reduction process raising fluid pH and thus facilitating carbonate precipitation (Surdam *et al*., 1984). At the elevated precipitation temperatures suggested from saddle dolomite in the fractures, thermochemical sulphate reduction (TSR) provides an effective mechanism for the generation of H_2S required for the formation of pyrite present in the fractures and vuggy cements in the overlying

brecciated successions (Machel *et al*., 1995). Hill (1995) showed that in reducing sulphate conditions co-precipitated metal sulphide and higher temperature saddle dolomites can form by replacement of calcite, as observed in cement *A*:

$$H_2S + CO_2 + Fe + Mg + 2CaCO_3 + H_2O \rightarrow FeS + Ca + CaMg(CO_3)_2 + HCO_3^- + 3H^+$$

However, to accommodate the sulphide mineralisation, a source of sulphate and a reducing agent is required in addition to cations present in the cements, notably Mg. In the reservoir units of the Brae Formation, late stage barite and sphalerite cements have also been observed (Greenwood *et al*., 1994), with barite fracture cements also reported in deep reservoir units (Stow & Aktin, 1987). With the sulphate required for the precipitation of these cements unlikely to have been derived from either the sandstone or the mudrock sequences, the source is speculated to the Zechstein Formation (Greenwood *et al*., 1994).

3.4.3. Possible fluid source

Basinal waters produced by the dissolution of evaporitic sequences with interbedded carbonate and sulphate minerals typically contain substantial concentrations of Ca, Mg, and SO_4^{2-} in addition to Na - Cl brine derived from halite dissolution (Hanor, 1994). The carbonate-anhydrite marginal Zechstein facies identified at depth adjacent to the western margin of the South Viking Graben (*see section 2.2.1; Figure 2.2*) provide a probable source for these ions subsequently precipitated in the fault zone carbonate cements. Steep salinity gradients reflecting advective flow of basinal brines in the North Sea is well documented (Bjørlykke & Gran, 1994), while a number of Central Graben fields close to Zechstein sequences contain high salinity formation waters (Osbourne *et al*., 1994). Similarly, comparable late ferroan cementation and base-metal sulphide mineralisation reported adjacent to significant faults in the North Sea (Witch Ground, Central Graben) have been attributed to large scale fluid movement along faults from Zechstein anhydrite sequences (Burley *et al*., 1989; Baines *et al*., 1991).

Organic acids produced from the generation of CO_2 during the thermal maturation (peak 80 – 120°C) of the Kimmeridge Clay Formation (KCF) source rock provide a suitable reducing agent for sulphate though are shown to reduce the pH of the surrounding porewater, potentially increasing carbonate solubility (Surdam *et al*., 1989). However, the buffering capacity of carbonate systems has been demonstrated to be significantly greater than that exerted by organic acids (Hutcheon & Abercrombie, 1990). As such, pH buffering by the carbonate-rich basinal fluid may actually promote carbonate precipitation.

The Fe present in the pyrite and carbonates of the fracture cements is probably sourced from porewaters influenced by diagenesis of the KCF during burial (Irwin, 1980). This is also witnessed in the incidence of diagenetic Fe-rich carbonate cements adjacent to and within the KCF in a number of Jurassic oilfields (Macaulay *et al*., 1998). Such a proposal can account for the extensive carbonate and sulphide precipitation observed in the heavily brecciated sequences overlying the fault damaged zone where cross-formational flow would be expected to be more pronounced (Figure 3.12). Aggressive formation fluids influenced by the onset of thermal decarboxylation in the KCF are also probably responsible for the corroded textures observed in a number of late-stage dolomite cements which are subsequently post-dated by pyrite mineralisation (Figure 3.6).

The timing of cementation influenced by these iron-rich fluids predates the onset of hydrocarbon migration in the region (~55 – 40 Ma), and thus may be contemporaneous with proposed basinal influx into the Brae Formation reservoirs approximately 70 Ma (Larter *et al*., 1995). The precipitation of late diagenetic sulphate minerals present in the Brae reservoirs can also be accounted for with mixing between SO_4^{2-}-rich basinal fluids and formation waters. Due to the very low solubility of sulphate and Ba in the same solution, differing fluid sources containing dissolved Ba and SO_4^{2-} are required (Hanor, 2000). The influx of Zechstein sourced SO_4 into the high concentration Ba formation waters prevalent in the region (Warren & Smalley, 1994) would thus permit the precipitation of $BaSO_4$ (e.g. McNeil *et al*., 1998). Similar mixing processes are responsible

for the extensive scaling problems encountered during the development of the Brae fields (Hardy *et al.*, 1994).

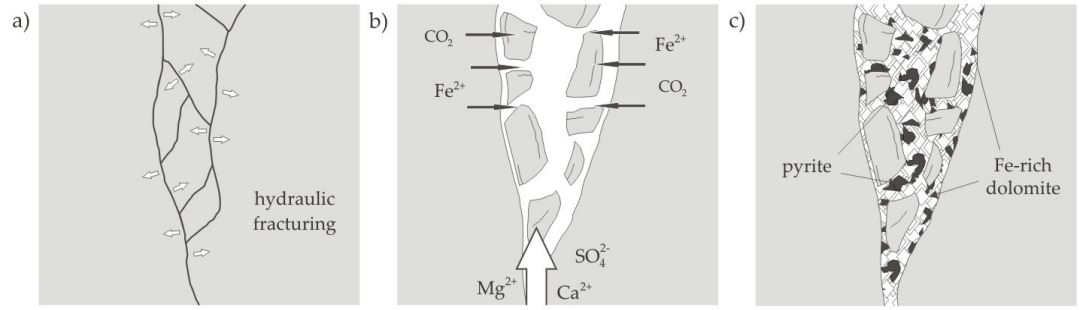

Figure 3.12. Schematic diagram illustrating pyrite and dolomite precipitation mechanism. **a)** build-up of fluid overpressure at depth culminates in hydraulic fracturing and brecciation of wallrock **b)** Ascending Zechstein derived basinal fluid mixes with in situ KCF influenced porewater, resulting in TSR of introduced sulphate **c)** pH buffering by the carbonate derived fluid and mixing of the two fluids promotes precipitation of pyrite and dolomite in the fracture network (e.g. Figure 3.7).

The variation in cementation styles along the fault zone and with depth in cored sections could thus be attributed to formation water heterogeneity during thermal maturation owing to proximity to organic-rich Kimmeridge Clay units. This could be further compounded by the distribution of permeable fluid pathways within both the fault zone and adjacent formations.

3.4.4. Summary

From the various aspects of the fault zone mineralogy, fracture mechanisms, and possible fluid sources discussed, the fault zone brecciation textures provide strong evidence for hydraulic fracturing as the principal mechanism for fracture generation. The ascent of overpressured fluids is a probable driver for both the fracturing and introduction of fluids into the fault zone from depth. Multiple generations of carbonate cement attest to discrete episodic fluid influxes into the permeable fracture network.

Mineral chemistry of the fracture cements requires a fluid dominated by Mg, Ca, Fe, SO_4^{2-}, and CO_2. Dissolution of Zechstein facies present in the graben fill underlying the Brae area at depth provides a plausible source. The ascent of overpressured deep-sourced fluids along basin bounding faults in the North Sea is well documented (e.g. Carstens & Finstad, 1981), with abnormal geothermal gradients and formation pressures adjacent to the western margin of the Viking Graben attesting to similar processes in the Brae region. The ascent of Zechstein derived fluids into the Jurassic reservoirs via the fault could also be responsible for the introduction of CO_2 into the region.

However, the possible influence of fluids derived from diagenetic reactions in the Kimmeridge Clay Formation cannot be neglected as evidenced in the supply of Fe and providing a reducing agent to permit the precipitation of late stage pyrite. It is therefore probable that components of both evolved basinal fluids and organic influenced formation waters are responsible for the observed mineralogy in the fracture cements.

To evaluate the respective influences of these two probable fluid types in the precipitation of the fracture cements, a number of methods can be utilised. Fluid inclusion microthermometry (Ch. 4), isotopic analysis (Ch. 5, 6), and geochemical modelling (Ch. 7) are used to help delineate a fluid source for the cements. Employing such techniques will also assist in evaluating the precipitation mechanism and environments suggested for the cements and thus test the hypothesis that basinal fluid was introduced into the Brae Formation by overpressure release from Zechstein Formation sequences at depth.

3.5. Conclusions

- Investigation of cored sections adjacent to the graben margin reveals extensive fault related deformation. Fracturing is predominantly manifested as brecciated sequences displaying extensive carbonate and pyrite mineralisation. Petrographic examination shows the brecciation style is characteristic of hydraulic fracturing, with disaggregation of previous mineral and breccia assemblages indicative of episodic refracturing and precipitation behaviour. The

style of fracturing and brecciation encountered is probably governed by fluid and local pressures within the fault zone through time.

- Electron microscopy allows the determination of at least five discrete fracturing and related fluid flow episodes. The overall degree of crystallinity and crystal size in the cements increases through time, with the evolution of the precipitation fluid traced in the gradual Fe-enrichment observed in the carbonate cements. Later cement generations comprising of Fe-rich euhedral dolomites are interpreted to have precipitated relatively slowly in open fracture networks.

- Cements consisting of saddle dolomite indicate precipitation from relatively high temperature fluids (90 – 160°C) in the fault zone. Affirmed by geothermal anomalies observed adjacent to the Viking Graben (Carstens & Finstad, 1981), fluid flux from depth is a possible source for the higher temperature precipitating fluids. Brecciation styles in the cored sections which suggest possible fracturing due to overpressure rupturing provide support for this hypothesis. Fault valving of overpressured fluids from depths provides a potential mechanism to account for the observed fracture morphology, mineral textures, and cyclic nature of the cements. Overpressure development within the North Sea basin is well documented and provides an ideal catalyst for fluid ascent up the graben margin.

- Dissolution of underlying marginal Zechstein carbonate-anhydrite facies provides a source for the Mg, Ca and CO_2 precipitated in the carbonate cements. Resident formation waters influenced by the diagenesis and thermal maturation of the Kimmeridge Clay Formation (KCF) are probably responsible for the reduction of SO_4^{2-} in the ascending basinal fluid, promoting the extensive iron sulphide mineralisation observed in late-stage fracture fills. The aggressive porewaters generated in the KCF are probably responsible for the corrosion observed on the rims of late-stage dolomites.

Chapter 4

Fluid Inclusion Microthermometry

4.1. Introduction

As determined from petrographic analysis, the fracture cement networks hosted in the fault zone infer episodic (potentially CO_2-rich) fluid flux up the fault zone. Although inferences have been made regarding a probable mechanism for fracture genesis and subsequent fluid transfer up the fault zone from depth, additional evidence from the cements is required to validate such proposals. Fluid inclusions can give an invaluable insight into fluid flow histories within fault zones, providing information on P-T conditions and composition of fluids from which minerals precipitated.

When crystals grow or recrystallise in a fluid, growth irregularities can result in the trapping of small portions of the fluid in the solid crystal. Irregularities that are sealed off during the growth of the host crystal yield primary fluid inclusions. Healing of

fractures during or after crystal growth gives rise to pseudo-secondary and secondary fluid inclusions respectively (Roedder, 1984). Primary inclusions provide a record of the fluid composition and temperature at the time of crystal formation enabling a greater understanding of the fluid source (e.g. salinity, volatile content) and formation conditions (e.g. temperature, pressure) for a host of diagenetic cements and fracture veins (e.g. Parry, 1998; Goldstein, 2001; Wilkinson, 2001).

Measuring entrapment temperatures of the fluid inclusions in the fracture zone gives the temperature at which the cements were precipitated. Formation temperatures for the cements are pivotal in establishing the timing of fluid movement up the fault zone. If CO_2 was emplaced into the Jurassic reservoirs ~70 – 80 Ma, as proposed by Lu (2008), and sourced from fluids ascending the fault zone then fluid inclusion homogenisation temperatures can potentially be related to existing burial profiles for the area (e.g. Greenwood *et al.*, 1994; Marchand *et al.*, 2001). However, if the transfer of fluid up the fault zone was rapid, with coincident rapid carbonate cement precipitation (as suggested by petrographic analysis), then high temperature anomalies might be recorded, with subsequent implications for the rate of the ascending fluid from depth.

The mass transport of fluids derived from the Zechstein Formation up basin bounding faults into stratigraphically higher regions in the northern North Sea has been extensively documented (e.g. Burley *et al.*, 1989; Macaulay *et al.*, 1997) and heavily implied for the South Viking Graben (James, 1990). Therefore, if saline deep basinal fluids have been imported into the Brae Formation reservoirs, the composition of the fluids trapped in the inclusions should reflect this (e.g. Banks *et al.*, 2002; Gleeson & Turner, 2006). Trace gases present in vapour phases (e.g. CO_2, CH_4) could also act as tracers for the origin of the fluids present.

Using the paragenetic sequence determined in the previous chapter, microthermometric analysis was used to assess the evolution of the P-T conditions and fluid from which the carbonate cements precipitated. The homogenisation temperature results are discussed with respect to the nature of fluid flow up the fault zone, with the

applicability and significance of the data evaluated. Measurements regarding the composition of the fluid inclusions are addressed, assessing a potential source for the fluid in the fault zone and the presence of CO_2 in the fluid.

4.2. Methodology

4.2.1. Microthermometry

Microthermometry is the measurement of temperatures of phase changes within fluid inclusions during the heating and cooling of samples. The determination of homogenisation temperature (T_h) and final melting temperature (T_m) of fluid inclusions provides information on the minimum formation temperature of the inclusion and salinity of the precipitating fluid respectively (Roedder, 1984).

Two phase inclusions (liquid and vapour) result from the differential shrinkage of the host mineral and trapped fluid upon cooling from the formation temperature. Upon cooling to present ambient observation temperature, the internal pressure of the inclusion drops below the saturation vapour pressure as the entrapped fluid contracts, leading to the development of a vapour phase within the inclusion. Heating of the inclusion until the vapour disappears into the liquid component gives the minimum temperature at which the inclusion was formed. This is termed the homogenisation temperature (T_h) (Figure 4.1) (Roedder, 1984).

The homogenisation temperature only represents a minimum estimate for the entrapment temperature (T_t) for the inclusion as the homogenisation of a liquid-vapour inclusion is a function of both the density of the fluid and pressure at the time of formation. As the density of the fluid in the inclusion essentially remains constant, pressure is the primary control, with higher pressures resulting in higher T_t. The difference between T_t and T_h due to these factors is referred to as the 'pressure correction' (Roedder, 1984). Realistically, only if the pressure at trapping is known can T_t be established. However, in methane bearing inclusions, Hanor (1980) concluded that T_h is very similar to T_t and as such no pressure correction is required.

Although density is assumed to be constant for application of pressure corrections, the determination of fluid density is essential to accurately estimate T_t using T_h. The salinity of fluids can have a profound effect on the determined pressure correction; with higher salinity fluids increasing measured T_t compared to non-saline fluids (Shepherd *et al*., 1985). As basinal fluids trapped in fluid inclusions exhibit a wide of salinities, determination of fluid composition is pivotal. By freezing and reheating aqueous inclusions, compositional information and the salinity of the trapped fluid can be obtained. The temperature at which a solid phase melts is termed the final melting temperature (T_m). Assuming the solid is ice, T_m is controlled by the salinity of the fluid, with increased salinity depressing the T_m.

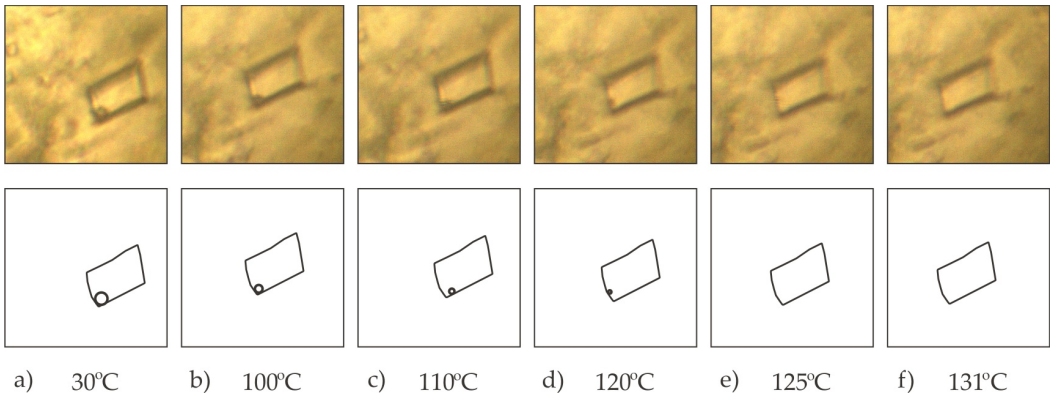

Figure 4.1. Photomicrographs and accompanying schematic showing gradual disappearance of vapour bubble within fluid inclusion during heating from room temperature (a to f). Homogenisation temperature (T_h) was reached at 131°C (f). Well 16/07a-12, depth 13177′ (field of view 25μm).

Although the relationship between T_m and salinity varies slightly depending on the species dominant in the solution (e.g. NaCl, $CaCl_2$, etc.), results are typically reported as % NaCl equivalent (Bodnar, 1992). In diagenetic systems this yields realistic salinity values. The effect of volatiles typically present in fluid inclusions, specifically CO_2 in this study, has a negligible effect upon T_m as only a small fraction exists in the liquid phase in the range of temperatures experienced in NaCl fluid melting. Frantz *et al*. (1992) found that up to ~43 mol% CO_2 within fluid inclusions had minimal effect on observed final melting temperatures.

4.2.2. Analytical methods

Polished wafers for fluid inclusion analysis were made from composite fracture cement arrays present in the fault zone. In total 25 wafers were used from well 16/07a-12 owing to the wide range of fracture cement generations observed in cored samples from the well. The depth range sampled is the same as in chapter 3, with wafers made as duplicates of previous thin sections and polished blocks.

Fluid inclusions in the wafers were identified using transmitted light microscopy. Photomicrograph maps of fluid inclusion distribution within the samples were constructed at a range of magnifications to facilitate rediscovery for microthermometric analyses. Well defined primary two-phase inclusions were collated prior to microthermometric analysis, with the dimensions, morphology and degree of fill of each inclusion was recorded. Due to the monomineralic nature of the composite fractures, the potential difficulty in determining the relative time of formation of the inclusions in the fractures was resolved using the paragenetic relationship between the various fracture cements determined using BSE response (e.g. Wilkinson *et al*., 1999). This approach allows the creation of a paragenetic history relating to formation temperature and solution composition to be constructed for the fracture cements using fluid inclusions from specific cement horizons.

As the samples potentially record numerous temperature and composition regimes within the cement phases, care was taken to avoid damaging inclusions in adjacent cements by carefully breaking the wafers or rastering across the sample during heating and cooling, assessing the change in the inclusions across a number of cements. Three heating cycles and two freezing cycles were applied to the sample inclusions. Repeatability of homogenisation temperature measurements was generally good, with T_h decreases less than 3°C in 66 of 81 of the T_h measurements taken.

The majority of samples exhibited subsequent Th drops following the second measurement. Transmitted light microscopy and microthermometric measurements were conducted on a LINKAM heating and freezing stage equipped with a Leitz

Metallux 3 microscope. The stage and associated microprocessor allowed heating and cooling rates to be controlled in a step-by-step manner, facilitating accurate measurement of phase transitions observable in fluid inclusions. Precision varied between temperature intervals; ±1.0°C below -30°C, ±0.2°C recorded between -20 and 80°C, ±0.5°C between 80°C and 150°C and ±1.0°C over 151°C. All measurements were conducted at the University of Edinburgh.

Inclusion volumes were calculated using the method of Bodnar (1983). The method uses the diameter of the vapour phase bubble in L+V inclusions in conjunction with the homogenisation temperature, salinity, and volumetric properties of the trapped fluids to determine fluid inclusion volumes. For H_2O-NaCl inclusions the volume is calculated by:

$$V_l = \frac{(v_2^{25°C})(d_l^{25°C})}{d_l^{25°C} - D_l}$$

whereby: V_1 = total volume of fluid inclusion
v_2^T = volume of vapour phase at given temperature
d_1^T = density of liquid at given temperature
D_1 = total density of inclusion

Vapour bubble volume was calculated using the diameter assuming a sphere. This was determined optically using a calibrated graticule. Error was estimated to be ±1 μm given the size (~2 μm) and resolution of the vapour bubbles at the magnification required. Fluid densities of the vapour saturated H_2O-NaCl inclusions were calculated using the equation applied by Bodnar (1983). This can be found in Appendix II.a.

4.3. Results

4.3.1. Fluid inclusion morphology and distribution

Fluid inclusions occur in all five of the fracture cements generations. Liquid and liquid-vapour (L+V) inclusions were chosen for investigation owing to their desirable properties for microthermometric analysis. All the inclusions are thought to be of

primary origin and typically sparsely and randomly distributed with no obvious growth zoning within each cement generation. Due to the differing crystal morphologies of the various fractures cements and resultant optical clarity of the inclusions present, the frequency and size of observable inclusions in each fracture cement varies (table 4.1).

Most inclusions exhibit sub- and euhedral negative crystal morphologies, with a number of well-defined inclusions exhibiting the rhombohedral form of the host dolomite (Figure 4.2. a to c). For microthermometric analysis, particular attention was paid to such inclusions owing to their perceived integrity. No evidence of hydrocarbons was observed in the inclusions under UV light. Numerous very small secondary inclusions where observed in planar arrays in a number of samples. However, these were too far below the resolution of the microscope to allow accurate measurement. Obvious necking-down and stretching of inclusions was also observed but avoided due to possible leakage; a problem inherent in soft, easily cleavable carbonate minerals (Shepherd *et al*., 1985).

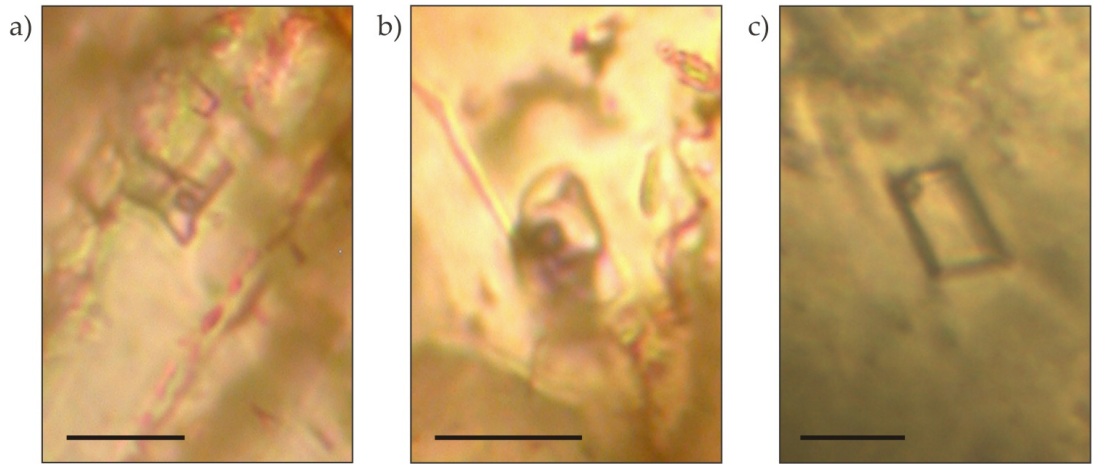

Figure 4.2. Photomicrographs of typical negative crystal morphology liquid + vapour fluid inclusions in dolomite at 25°C viewed under transmitted light (well 16/7a-12, 13177'). Scale bar 10 μm.

4.3.2. Microthermometry

In total 84 T_h measurements were obtained from the inclusions analysed and 71 measurements for T_m (table 4.1). All the fluid inclusions for microthermometric analysis were two-phase inclusions with liquid and vapour present at room temperature. Due to the kinetics of vapour nucleation, acknowledgement of a temperature lag upon cooling was required to confirm homogenisaton of the liquid and vapour phases (Samson *et al*., 2003).

Homogenisation temperature measurements from the inclusions exhibit a slightly asymmetric profile across a wide temperature range (87 to 182°C), with two notable peaks between 115 – 120°C and 125 – 130°C, with an overall mean of 120.5°C. Histogram plots of homogenisation temperatures from fluid inclusion populations within the cements show a tentative trend toward increasing average T_h through the successive cement generations (Figure 4.3; table 4.1). Statistical analysis and the significance of the apparent trend are discussed subsequently (*see 4.4.4*).

The T_m of the inclusions in the cements is variable, ranging between -2.8 and -9.3°C. Using the conversion of Bodnar (1992), these T_m values give salinity estimates between 4.3 and 12.6 wt. % NaCl equivalent respectively with a mean of 8.5 wt. % NaCl. There is no apparent difference in the salinity values determined from fluid inclusion populations in each fracture cement generation, with salinity ranges typically between 5 and 10 wt. % NaCl equivalent (Figure 4.4). A number of inclusions failed to freeze upon cooling down to -155°C. This was probably due to decrepitation on cooling, creating the disparity between the number of T_h and T_m measurements acquired. No evidence of appreciable quantities of CO_2 in the inclusions was observed in the form of discrete liquid and vapour phases upon cooling.

Cement zone	T_h (°C)	T_m (°C)	Salinity (wt. % NaCl)	Shape factor	Vapour vol. (μm^3)	Inclusion density @ T_h	Inclusion density @ 25°C	Inclusion vol. (μm^3)
A	94	-5.1	7.7	6	59	1.016	1.051	1759
	97	-6.8	9.8	9	73	1.029	1.068	1981
	101	-5.5	8.1	7	88	1.014	1.054	2310

	99	-4.1	6.3	8	70	1.003	1.040	1973
	104	-6.3	9.2	6	81	1.020	1.063	1984
	113	●	-	9	71	-	-	-
	118	-7.3	10.7	4	75	1.020	1.075	1468
	127	-5.8	6.5	7	63	0.984	1.041	1142
B	87	-5.8	7.1	4	119	1.016	1.046	4141
	93	●	-	8	91	-	-	-
	98	-6.1	9	2	103	1.023	1.062	2810
	103	-5.2	7.8	6	113	1.011	1.052	2888
	105	-4.4	6.8	6	130	1.002	1.044	3271
	106	-2.8	4.3	5	94	0.985	1.024	2456
	106	-5.6	8.2	7	91	1.011	1.055	2190
	107	-6	8.9	7	163	1.016	1.061	3834
	112	●	-	6	92	-	-	-
	117	●	-	3	101	-	-	-
	117	-6.1	9	9	154	1.009	1.062	3098
	118	-3.3	5.1	8	77	0.982	1.030	1628
	118	-3.8	9.2	5	84	1.010	1.063	1661
	121	-5.9	8.9	8	94	1.005	1.061	1786
	124	-4.7	7.4	6	115	0.993	1.049	2141
	126	-3.8	5.9	4	91	0.981	1.037	1687
	131	●	-	4	123	-	-	-
	137	-6.5	9.4	7	133	0.996	1.065	2050
C	97	-5.9	8.9	6	87	1.023	1.061	2400
	104	-3.8	5.9	7	78	0.997	1.037	2043
	107	-6.3	9.2	5	98	1.018	1.063	2283
	108	-6.6	9.6	4	105	1.020	1.066	2394
	108	-7.1	10.3	8	113	1.025	1.072	2559
	112	-4.5	6.9	7	184	0.998	1.045	4140
	114	-6.3	8.9	10	117	1.010	1.061	2474
	115	●	-	6	126	-	-	-
	116	-3.9	6	7	53	0.989	1.037	1140
	116	-7.2	7.3	8	91	0.998	1.048	1906
	119	-5	7.5	7	91	0.997	1.049	1818
	120	-6.8	9.8	9	105	1.012	1.068	1975
	122	-5.3	7.9	7	106	0.998	1.053	2025
	124	-7.9	7	7	113	0.990	1.045	2127
	126	-6.2	9.1	6	71	1.003	1.062	1268
	127	-6.7	9.6	8	87	1.005	1.066	1513
	127	-4.8	7.4	6	130	0.990	1.049	2330
	130	-5.5	8	6	98	0.992	1.053	1673
	131	●	-	4	77	-	-	-
	133	-3.5	5.5	3	116	0.973	1.033	1969

	137	-4.4	10.7	7	73	1.005	1.075	1109
	144	-5.9	8.9	5	115	0.987	1.061	1637
	156	●	-	8	63	-	-	-
	161	-3.3	9.2	6	108	0.974	1.063	1275
D	99	-5	7.5	7	80	1.011	1.049	2190
	104	-4.8	7.4	6	91	1.007	1.049	2297
	107	-2.8	4.3	7	133	0.984	1.024	3422
	111	-3.5	5.5	8	103	0.989	1.033	2424
	114	-6.3	9.2	7	108	1.013	1.063	2258
	116	-9.1	12.6	5	123	1.035	1.091	2409
	118	-7.4	10.7	9	126	1.020	1.075	2451
	122	-6.6	9.5	6	156	1.009	1.066	2923
	123	-7.1	10.3	8	159	1.013	1.072	2910
	124	-3.2	6.2	7	120	0.984	1.039	2285
	125	-6.7	9.6	8	99	1.007	1.066	1778
	125	-5.5	8	7	130	0.996	1.053	2375
	126	-6.1	9	5	119	1.002	1.062	2116
	127	-7.5	10.8	10	140	1.014	1.076	2409
	130	-7.8	11.1	6	119	1.014	1.079	1966
	130	-8.4	11.7	8	115	1.018	1.084	1886
	131	●	-	4	113	-	-	-
	135	-5.8	8.8	8	131	0.993	1.060	2091
	135	-5.7	9.4	7	101	0.998	1.065	1592
	140	●	-	5	119	-	-	-
	146	-4.6	9.9	9	128	0.992	1.069	1781
	182	●	-	8	115	-	-	-
E	109	-4.8	7.4	6	89	1.004	1.049	2085
	114	-7	10.1	9	78	1.019	1.071	1613
	118	-5.8	8.8	6	128	1.007	1.060	2561
	119	-3.7	9.6	7	84	1.012	1.066	1630
	123	-5.7	8.5	4	126	1.001	1.058	2353
	127	-5.5	8	5	94	0.994	1.053	1666
	127	-6.5	9.4	7	119	1.004	1.065	2079
	128	-3.6	9.8	7	115	1.006	1.068	1971
	130	●	-	8	105	-	-	-
	133	-7.3	10.6	6	101	1.008	1.075	1613
	143	●	-	8	95	-	-	-
	145	-4.2	11.2	7	109	1.002	1.080	1513

● no T_m measured (see text for detail)

Table 4.1. Microthermometric results (T_h and T_m), shape factors (See Appendix II.b.), and fluid inclusion volumes (calculated using the method of Bodnar, 1983) for fluid inclusions measured in cement zones A to E.

4.4. Discussion

4.4.1. Evaluation of the trapping temperatures

The trapping temperature (T_t) of the fluid inclusions is estimated from the measured homogenisation temperature (T_h) through the application of a pressure correction assuming prior knowledge of pressure conditions at the time of trapping. As the inclusions are from fracture cements with no accurate constraint on pressure conditions owing to limited knowledge of precipitation timing relative to burial (further complicated by differential tectonism in the region) or potentially variable fluid pressures within ascending fluids, pressure corrections are thus difficult to apply. However, pressure corrections can be omitted if methane saturation of the aqueous phase is assumed (Hanor, 1980). Although no petroleum inclusions were observed, the assumption of methane saturation is reasonable given the pervasive influence of Kimmeridge Clay maturation on the resident pore fluids, with negligible CH_4 required to saturate relatively saline fluids (Haas, 1978). Therefore, in the following discussion, T_h is used as a reasonable approximation to the trapping temperature T_t.

4.4.2. Did the fluid precipitating the cements transport CO_2?

Lu (2008) observed that the CO_2 content of H_2O – CO_2 inclusions postdating the influx of CO_2 in the Miller Field (~28 mol % CO_2) was minor (< 10 mol %), with relatively few inclusions trapping gas species observed in the field. This suggests that the volatile content of the inclusions studied may not necessarily reflect the volatile content of the overall host solution. Therefore it is perhaps not unexpected that no evidence of CO_2 is observed within the inclusions in the fracture cements. Although no direct microthermometric evidence of appreciable volumes of CO_2 (or other volatile gas components) was observed in the fluid inclusions of the fracture cements (e.g. in the form of clathrates), the precipitation of appreciable volumes of carbonate material implies that dissolved carbon was undoubtedly present in the fluid circulating within the fracture system (e.g. Craw *et al*., 1992). The apparently low concentrations of CO_2 may be due to a number of factors. The solubility of CO_2 in formation waters of similar composition (>4 wt. % NaCl eq.) and temperature (~90 – 160°C) to reservoir conditions

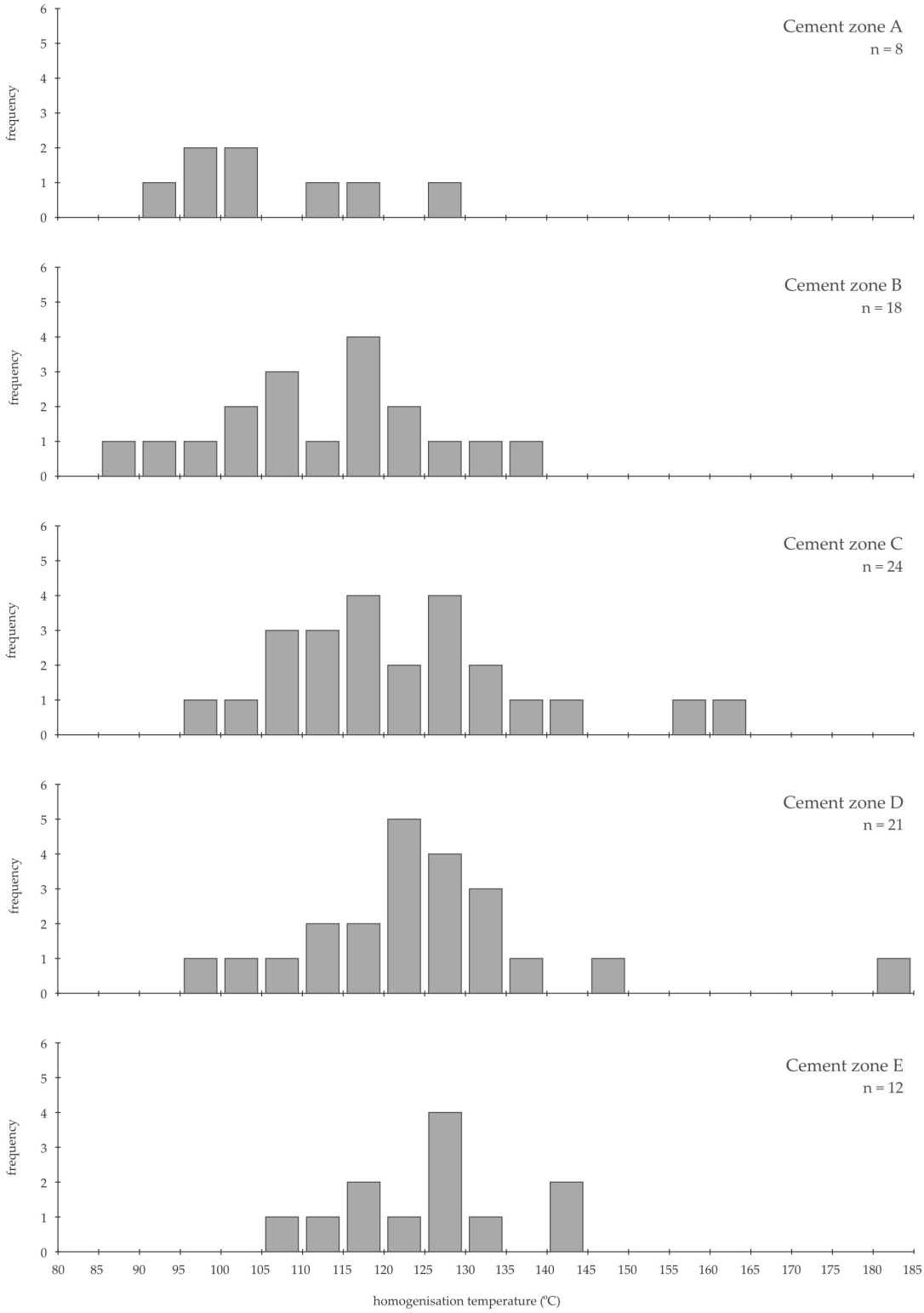

Figure 4.3. Histograms of homogenisation temperatures (T_h) measured in fluid inclusions from each of the five observed fracture cement generations (A to E). Detailed data are shown in table 4.1.

up to the present-day (500 bar) is less than 5 wt. % (<1.2 mol kg^{-1} H_2O) (Enick & Klara, 1990; Duan & Sun, 2003).

Therefore, under such conditions it is probable that any CO_2 concentrations in the host fluid would be relatively minor. However, with no realistic constraint on fluid pressure in the fault zone such estimates are tentative. It is plausible that the absence of CO_2 in the fluid inclusions may be due to exsolution from the fluid during decompression (Bowers, 1991). In addition, the absence of monophase (liquid or vapour) inclusions homogenising to both liquid *and* vapour phases upon heating suggests effervescence of CO_2 from the host fluid was not contemporaneous with precipitation of the cements at the sampled horizons (Roedder, 1984).

4.4.3. Comparison with existing T_h values in the Brae Formation

Previous published studies utilising fluid inclusion analysis in the Brae area primarily focus on reservoir quality (Osborne & Haszeldine, 1993; Larter *et al*., 1995; Marchand *et al*., 2002). Homogenisation measurements from these studies typically exhibit a relatively broad distribution (~80 to 130°C) with skew toward higher temperatures (Figure 4.5). These temperature distributions are attributed to late-stage cementation at burial depths and reservoir temperatures similar to the present day (120 - 125°C; Marchand *et al*., 2002) and partial or full resetting of initially lower temperature inclusions to present-day reservoir conditions (Osborne & Haszeldine, 1993).

Comparing T_h values from the fracture cements with the previous reservoir studies, there is significant overlap of the data (Figure 4.6). This suggests that the fracture cements have possibly shared a similar thermal history or have been subsequently reset (e.g. Goldstein, 1986). However, ~30 % of the inclusions exhibit T_h values greater than the present day formation temperature. These higher T_h inclusions are present in the paragenetically later cement generations *C* to *E* (Figure 4.3, Appendix II.d). Therefore it is apparent that the inclusions in these fracture cements may represent precipitation from fluids with temperatures greater than those currently observed at the maximum burial depth of the region.

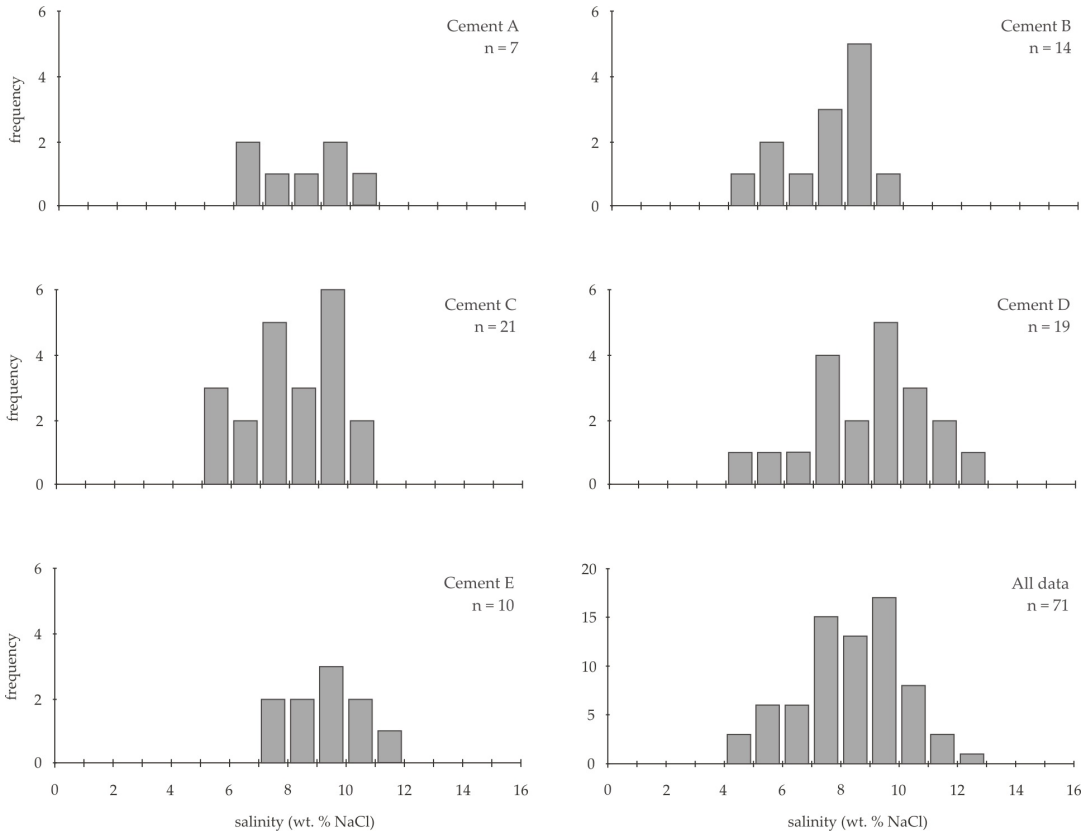

Figure 4.4. Histograms showing relatively uniform salinity values (~4 to 12 NaCl wt.% eq.) in fluid inclusions measured across all the cement generations (A to E).

Possible higher temperature sources include a greater geothermal gradient in the past or circulation of warmer fluids from depth up the fault zone. Due to prolonged extensional tectonic activity on the graben margin since the Jurassic, geothermal gradients greater than the present post-rift gradient (~30°C km^{-1}) would be expected. Elevated heat flows of 80 mW m^{-2} have been proposed during active rifting periods in the region before subsiding to present-day rates (55 mW m^{-2}; Schroeder & Sylta, 1993). Assuming the thermal conductivity range for North Sea sediments of Evans (1977), this equates to geothermal gradients up to ~ 45°C km^{-1}. However, burial depths of the Brae Formation encountered during the pronounced extensional episodes on the graben margin during the Jurassic and Late Cretaceous are ~1000m and ~3000 m respectively (see Figure 2.9, p. 27). Even accounting for elevated geothermal gradients during this period (~40°C/km), encountered formation temperatures at these burial depths (up to ~110°C) (Figure 4.5)

are still not sufficient to explain the elevated homogenisation temperatures above present day maximum reservoir temperature recorded in a number of cements. The significance of these higher temperature inclusions is discussed later in section 4.4.5.

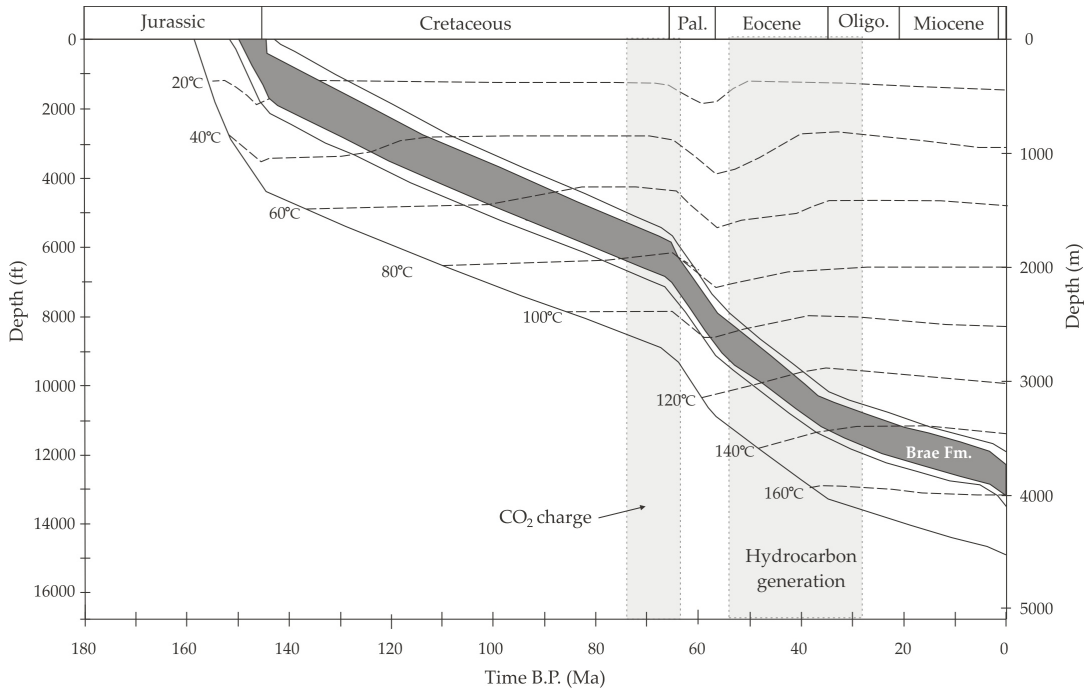

Figure 4.5. Burial curve constructed for Brae Formation displaying elevated geothermal gradient (40°C km^{-1}) indicative of Jurassic-Cretaceous extensional phase in the South Viking Graben. Diagram shows that for suggested time of CO_2 influx and fracture cementation (~70Ma), regional temperatures are not sufficient to explain elevated homogenisation temperatures recorded in a number of inclusions studied. Burial curve modified from Marchand *et al*. (2001)

Accounting for increased geothermal gradients at these depths, temperatures are still not sufficiently high to account for the higher end T_h values observed in the fluid inclusions of the fracture cements. Therefore it is possible that the observed higher homogenisation temperatures seen predominantly in the later cements could reflect periods of fluid flow up the graben bounding fault from a relatively higher temperature source at depth (e.g. Krebs & Macqueen, 1984) when burial of the region was more advanced than earlier cement generations. With the ascent of over-pressured formation

waters proposed as the fracture mechanism, the introduction of relatively higher temperature fluids into the fault zone is plausible.

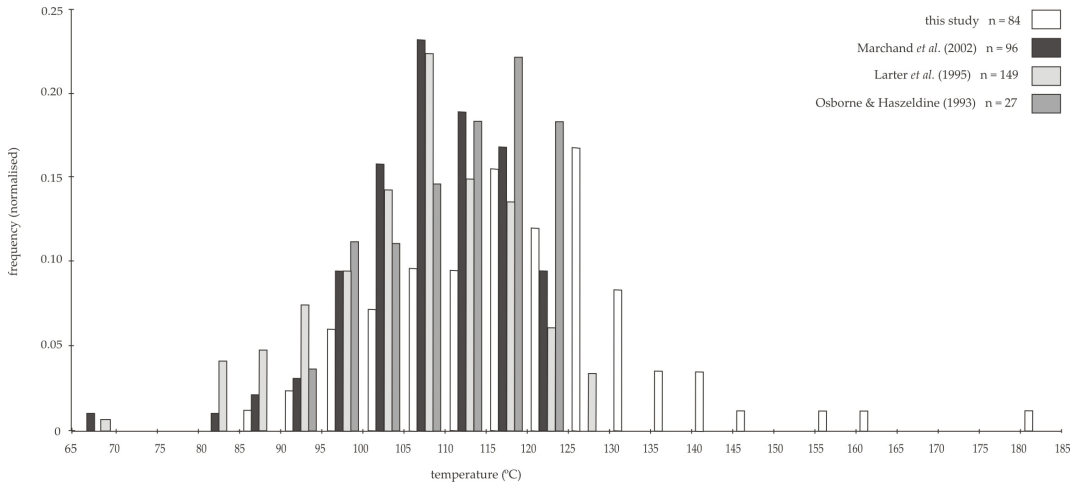

Figure 4.6. Normalised distribution plot of homogenisation temperatures from all fractures in this study (A to E) and previous reservoir studies from South Brae (Osborne & Haszeldine, 1993) and the Miller Field (Larter *et al*., 1995; Marchand *et al*., 2002). Note the absence of T_h values greater than present day formation temperature from the reservoir temperatures.

4.4.4. Temperature evolution in the fracture cements

According to Goldstein and Reynolds (1994), large T_h ranges in a fluid inclusion population can result from heterogeneous trapping, necking-down, leakage and trapping of inclusions or trapping over a large temperature range. Statistical analysis was employed to assess the possible differences between the fluid inclusion populations between each cement generation with respect to their measured homogenisation temperatures with view to determining whether each cement generation constitutes a discrete temperature precipitation event through time or represents an artefact of the aspect mentioned above. The T_h results from each cement generation were compared using unpaired Student's T-test analysis with the results of the tests shown in Figure 4.7. Assuming a null hypothesis whereby all the inclusions belong to the same population (i.e. fluid source temperature), then it is apparent that

this hypothesis can be rejected in a number of pairings. For example, the largest disparity between the earliest and latest cement generations, A and E, is very statistically significant (p = 0.002) at the 0.05 level, showing the two populations bear little similarity. This therefore suggests the fluid inclusion assemblages in cements A and E formed in two distinctly different temperature regimes (Figure. 4.7).

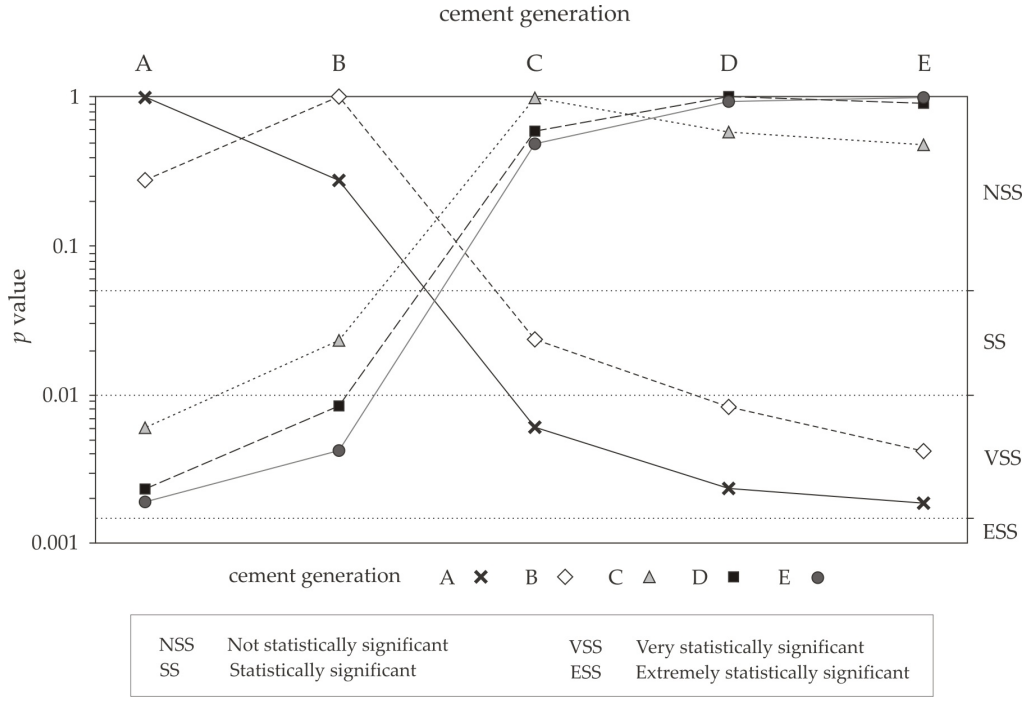

Figure 4.7. Relative p-value and subsequent statistical significance (at 0.05 level) from unpaired Student T-tests of T_h values between cement generations showing evident disparity between grouping of cements A & B and cements C, D, & E, suggesting at least two separate temperature events.

The relationship between cement A and subsequent cements shows an overall decrease in p-value. The statistical variations between T_h values for cements C, D, and E are not significant enough to reject the null hypothesis at the 0.05 significance level (p = 0.470 to 0.930). A similar relationship is observed between cements A and B also (p = 0.265). As a result distinct precipitation temperatures for each discrete cement cannot be invoked. However, sufficient statistical variation between cement B (and earlier A) and cement C (and later *D* and *E*), exists in which the null hypothesis can be rejected. This suggests

that at least two discrete precipitation temperature regimes are observed in the T_h data, with a marked temperature increase between earlier cements (A and B) and the later cements (C, D, and E). However, although the analysis proves there is both variation and similarity in the T_h values between a number of the cement generations, the method cannot prove why the variations are observed.

Petrographic and geochemical analysis suggests discrete precipitation events from compositionally different fluids for each cement generation (Figure 3.10, p. 54). Figure 4.8 shows that temperature ranges for the different cement generations show a degree of overlap, compositionally some vary. Cements A_2 (later dolomite), C, and D share similar T_h ranges and chemical composition. However, cements A_1, B, and E also exhibit similar T_h ranges but are compositionally distinct from each other and the aforementioned cements. This suggests that the precipitating fluids were derived from different sources at similar temperatures or the original fluids trapped in the inclusions have been subsequently reset, thus sharing a common temperature regime.

4.4.5. Evidence for resetting of fluid inclusions

An important assumption in fluid inclusion microthermometry is that aqueous inclusions are resistant to re-equilibration upon progressive burial and subsequent increasing temperature. In studies of more resistant quartz, Osborne and Haszeldine (1993) proposed that resetting of inclusions to higher temperatures readily occurs in diagenetic environments; with consistent correlations between measured homogenisation temperatures and present-day reservoir temperatures as key evidence.

The occurrence of resetting in the diagenetic realm has been widely debated, with numerous authors arguing against the concept (e.g. Robinson *et al*., 1992; Worden *et al*., 1995). Bodnar *et al*. (1989) found the degree of resetting of fluid inclusions to be partially dependent on size, with small inclusions typically more resistant than larger inclusions. Thus, a reset inclusion population should yield a specific distribution of inclusion characteristics with large inclusions exhibiting higher T_h values than small inclusions in a scenario of increasing temperature after inclusion formation. The T_h values from the

fracture cements do encompass the present-day formation temperature for the Brae Formation in the South Brae oilfield at similar depths (~125°C).

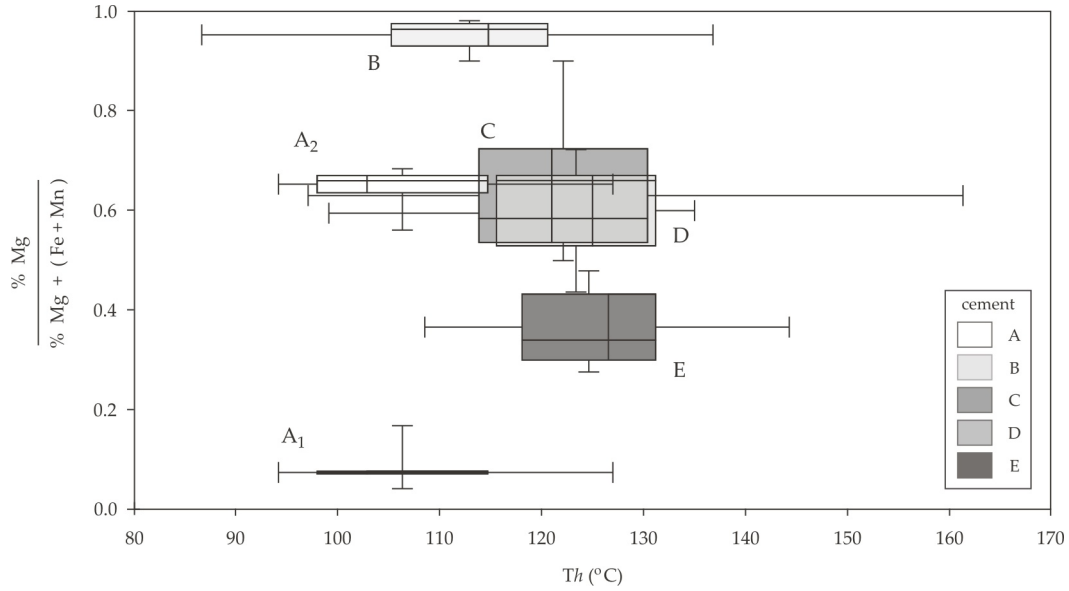

Figure 4.8. Box and whisker plot of composition (Mg relative to Fe + Mn) and measured T_h ranges of the carbonate fracture cement generations (A to E) showing the T_h ranges of the individual cement generations show appreciable overlap. However, four distinct mineral compositions are evident, suggesting probable inclusion resetting (see text for details). Subscripts 1 and 2 on cement A denote the earlier calcite and later dolomite phases respectively. Note: outlying 182°C T_h measurement from cement D omitted. Boxes represent the median and 25th and 75th percentiles in the x and y plane (see table 4.1 and appendix I.b for data).

All inclusions with T_h greater than maximum present-day formation temperature (>125°C) have volumes below ~2200 μm^3 and are present in the later fracture cements (*C* to *E*). Conversely, inclusions with T_h similar to and below the present day formation temperature exhibit a larger volume range (~1000 - 4000 μm^3) and encompass all the interpreted cement generations (Figure 4.9). Therefore, it is plausible that the larger inclusions in the population have been reset (e.g. Osborne & Haszeldine, 1993). Therefore, the smaller inclusions may have been overall more resistant to re-equilibration and thus maintained their initial trapping temperatures or conversely, the

larger inclusions may have been more susceptible to resetting early in during burial, reflected in their lower T_h, with the smaller, more resilient inclusions resetting later after further burial at higher temperatures similar to those encountered in present day within the Brae Formation. Osborne and Haszeldine (1995) noted that to accurately assess the relationship between inclusion size and resetting, inclusions formed at the same P-T conditions (i.e. cement generations) should be evaluated. The data from individual cement generations show similar trends as the complete dataset; with the smaller inclusions in each cement generation exhibiting higher homogenisation temperatures (see Appendix II.c).

However, resetting cannot be readily invoked for the smaller inclusions which do exhibit homogenisation temperatures greater than both the current formation temperature (Figure 2.9) and elevated regional temperature gradients encountered during periods of extension in the graben at the suggested time of precipitation (Figure 4.5). The data therefore suggests the trapping of fluids with temperatures greater than those experienced in ambient formation temperatures throughout the burial of the graben. A possible source for the higher temperature fluids recorded in the cements is the introduction of heated fluids into the fault zone from depth. Burley *et al*. (1989) interpreted homogenisation temperatures significantly higher than regional geothermal gradients within cements proximal to the faulted margin of the Tartan Field (UK, North Sea) as deriving from the influx of heated fluids from depth. Large scale vertical fluid migration in excess of 2km reported in North Sea fault systems (Cayley, 1987) suggests that fluids with elevated temperatures ascending from deep in the graben are not inconceivable. Therefore it is possible that the fluid inclusions exhibiting homogenisation temperatures greater than those observed in the present day represent similar ascending heated fluids up the fault zone.

Carstens and Finstad (1981) attributed elevated temperature anomalies along the basin margin of the South Viking Graben to fluid flow up the bounding fault arising from overpressure release. Fracturing and cementation styles observed from cored sections in this study which appear to attest to overpressure release support this proposal.

However, caution must be expressed in the neglecting the potential resetting of carbonate minerals irrespective of their morphology and size owing to their inherent structural weakness compared to quartz. Although previous studies have accepted the validity of microthermometric data attained from similar calcite cements (e.g. Burley *et al*., 1989), fluid inclusions in carbonate minerals have been known to re-equilibrate to temperatures higher than those at which the host mineral originally grew due to stretching and leakage (Goldstein, 1986).

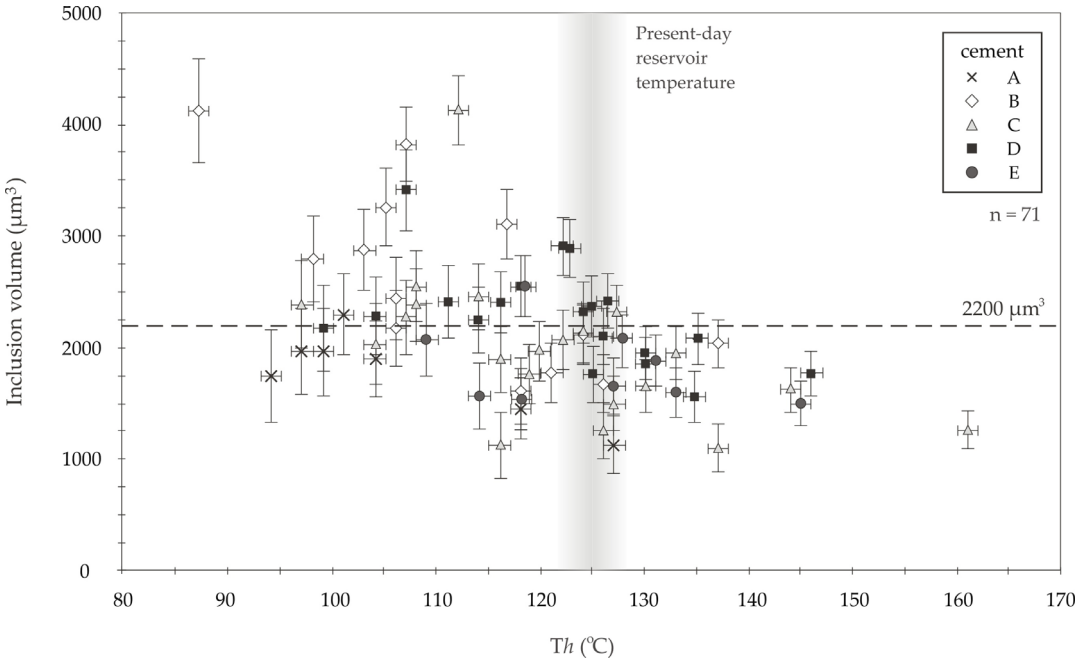

Figure 4.9. Relationship between inclusion volume and T_h from fracture cement inclusions. Homogenisation temperatures higher than present-day South Brae reservoir temperature are recorded in the smaller inclusions (<2200 µm^3), with larger inclusions typically exhibiting T_h values and ranges comparable to existing South Brae reservoir studies (e.g. Osborne & Haszeldine, 1993). Inclusion volumes calculated using the method of Bodnar (1983) (*see 4.2.2*). Error bars represent ±1 µm variability in vapour bubble diameter measurement and ±1.0 °C error in T_h based on analytical error in calibration of the heating stage over the temperature interval and not variation in T_h measurement of individual inclusions.

4.4.6. Evaluation of fluid composition

Inclusions reset by stretching due to overpressure shift the T_h to values contemporaneous to those of the formation at that time but do not alter the composition of the fluid contained (Osborne & Haszeldine, 1993; Goldstein & Reynolds, 1994). However, inclusions which have experienced leakage and refilling alter T_h and composition. The contrasting mineralogy of the fracture cements suggests an evolving or different fluid source. Therefore, such fluid compositional changes should be observed in the trapped fluids (e.g. O'Hara, 1995). Present day pore waters from the Brae Formation reservoirs in the South Brae field exhibit salinity values ranging from 6.6 to 9.9 wt. % NaCl eq. (Hardy & Hart, 1994). These values are within the estimated salinity range determined from the T_m of the fluid inclusions present in the fault zone fracture cements (4.3 to 12.6 wt. % NaCl eq.). This suggests that either the inclusions have leaked and subsequently refilled with fluids similar to the present day formation waters, or that the fluid in the reservoir has experienced minimal compositional variation since precipitation of the fracture cements (and estimated time of CO_2 emplacement).

High salinity fluids, up to 26 wt. % NaCl eq., have been reported in fluid inclusions within quartz cements of the Miller Field (Larter *et al.*, 1995; Marchand, 2001). These cements exhibit homogenisation temperatures of ~70 - 90°C before decreasing in salinity and increasing in T_h with progressive burial to the present day (Figure 4.10). The distribution in Figure 4.10 is attributed to an influx of deep basinal high salinity water at ~70°C, which, according to Lu (2008), coincides with estimated CO_2 charge into the reservoir ~70 Ma as suggested by stable isotope data.

Assuming similar fluids fluxed into both the Brae Fields and the Miller Field, this implies that if the carbonate fracture cements in the fault zone do represent the influx of CO_2 into the Brae reservoirs then they have leaked and thus do not contain the higher salinity fluids originally trapped upon precipitation. Given the periodic stress applied to

the cements through numerous stages of tectonic activity on the fault zone since the Late Cretaceous, impairment of the structural integrity of inherently weak carbonate hosted inclusions is not unexpected. However, the fluid inclusions in the fracture cements with homogenisation temperatures greater than current reservoir temperatures (Figure 4.9) predominantly exhibit salinities greater than 8 wt. % NaCl (see Appendix II.d). With estimated salinities between 10 and 12 wt. % NaCl, and elevated T_h values, these smaller inclusions have seemingly not been re-equilibrated and thus probably reflect the original salinity of the fluid during precipitation of the later cement generations which exhibit homogenisation temperatures higher than the palaeogeothermal gradient shown in Figure 4.5.

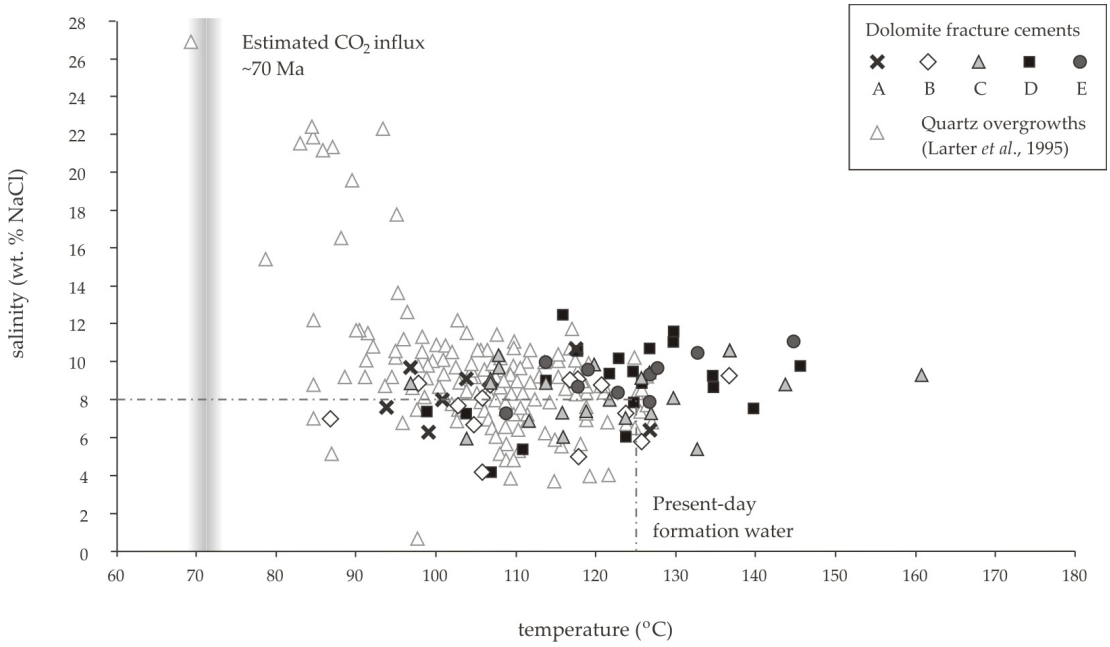

Figure 4.10. Salinity vs. T_h measurements from the fault zone fracture cements superimposed upon microthermometric data of Larter *et al*. (1995) from the Miller Field. Data from this study exhibits similar T_h and salinity values to present day formation water and late stage quartz cements, with no inclusions containing the high salinity fluids (26 wt. % NaCl) attributed to Zechstein fluids (see text for detail).

Numerous authors have proposed the underlying Zechstein evaporites as a possible source for the highly saline fluids reported in cements of the Brae region (e.g. Larter *et al*., 1995; Baines & Worden, 2004) and analogous reservoir settings (e.g. Macaulay *et al*., 1997; Scotchman *et al*., 2000), with the basin bounding fault serving as a conduit for both the high salinity basinal fluids and contemporaneous CO_2 in the former (Wycherley *et al*., 1999). However, the presence of CO_2 in fluid inclusions (attributed to have precipitated from Zechstein derived fluids) can cause an overestimate of salinities (Hedenquist & Henley, 1985; McNeil *et al*., 1995), with estimates potentially in error by 50 % (Collins, 1979). Therefore, salinity values attributed to Zechstein fluids from previous inclusions studies may potentially lie at the lower end of their salinity estimate. Therefore, a Zechstein origin for a CO_2-rich fluid flux should not be accepted or dismissed purely on microthermometrically determined salinity estimates.

Although fluid inclusion microthermometry can undoubtedly provide key evidence regarding the nature of fluid from which cements precipitated, as witnessed in this study, sometimes the availability and validity of data collected can be limited. Therefore, additional techniques can be employed to further analyse the cements. Stable oxygen and carbon isotopes (Ch. 5) and $^{87}Sr/^{86}Sr$ isotopic analysis (Ch. 6) can help elucidate the source of the precipitating fluid and thus assist in verifying the suggested high temperature fluid influx proposal inferred from the data acquired from the fluid inclusions in the fracture cements.

4.5. Conclusions

- Fluid inclusion populations from the fault zone fracture cements predominantly exhibit T_h values ranging from ~85°C to temperatures comparable to current reservoir conditions (~125°C). Although there is apparent variability in the range of T_h values within each cement generation, evidence suggests the inclusions have been reset and do not represent original trapping temperatures in the fault zone.

- Salinity values determined from T_m of fluid inclusions in the fracture cements range between 4.3 to 12.6 wt. % NaCl, with minimal variability between each cement generation. These relatively low values are similar to present-day formation waters, suggesting leakage and refilling of the inclusions relatively recently.

- A number of inclusions exhibit T_h above present day reservoir conditions (>125°C) (Figure 4.9). These inclusions are evident in later stage cement generations (*C*, *D*, and *E*) and are typically smaller than average (i.e. potentially more resistant to resetting). The fluids in these inclusions are typically more saline and could potentially reflect original trapping conditions during the precipitation of the cements at elevated temperatures, possibly deriving from overpressure release of a heated basinal fluid ascending the fault zone from depth.

- The absence of detectable CO_2 in the inclusions cannot disprove the graben bounding fault served as the conduit for CO_2 flux into the Brae reservoirs. Although low concentrations of CO_2 are not readily detected during routine heating and cooling experiments (Sasada, 1985), appreciable quantities (e.g. 10 mol%) should be noticeable during microthermometric analysis. Given the solubility of CO_2 at reservoir conditions and possible mechanisms for precipitating the fracture cements, it is probable that quantities of dissolved CO_2 in the solution upon precipitation would be negligible irrespective of the volumes of CO_2 ascending the fault.

Chapter 5

Carbon and Oxygen Stable Isotope Analysis and Modelling

5.1. Introduction

Interpretation of fluid evolution from isotopic signatures of fracture cements can lead to a better understanding of the interaction between deep sourced fluids and fault zones. Stable isotope analysis of carbonate material is widely applied to diagenetic and ore-forming studies. The carbon and oxygen isotopic signature is widely used to constrain the origin of fluids and the carbon source from which the carbonate precipitated in diagenetic (e.g. Haszeldine *et al*., 1992; Marchand *et al*., 2002) and hydrothermal regimes (e.g. Winter & Knauth, 1992; Kopf *et al*., 2003; Sacchi *et al*., 2003). Such an approach requires knowledge of the precipitation temperature of the studied carbonate. This can be determined independently from fluid inclusion analysis. However, when microthermometric data proves inconclusive or unreliable, as witnessed in the investigation of the fracture cements (*see chapter 4*), estimates on probable precipitation

conditions are required, with isotopic compositions dependent on temperature and origin of the fluid (e.g. marine, meteoric, and basinal). With a range of potential CO_2 sources existing in the subsurface (Figure 1.2: p. 7), the $\delta^{13}C$ isotopic signature of CO_2 can be used to constrain a possible source (table 5.1).

Extensive stable isotope investigations of carbonate cements have been conducted in the northern North Sea with a view to elucidate diagenetic histories of Jurassic hydrocarbon bearing reservoir formations (e.g. Brent, Piper, Magnus) (e.g. Haszeldine *et al*., 1992; Macaulay *et al*., 1998). Carbon isotope ratios of CO_2 gas from these low volume accumulations (< 10 %vol.) typically exhibit $\delta^{13}C$ values less than -10 ‰, suggesting a predominantly organic origin for the CO_2. Carbonate cements from reservoir units in the fields also exhibit stable isotope signatures indicative of a significant influence of organic carbon. This is also reflected in similar diagenetic profiles and fluid evolution patterns owing to their ubiquitous association with hydrocarbon generation and retention (e.g. McLaughlin *et al*., 1994). Naturally occurring large accumulations of CO_2 gas (> 15 %vol.) typically exhibit $\delta^{13}C$ ratios between 0 – 10 ‰ indicative of an inorganic origin (Thrasher & Fleet, 1995). Although a significant hydrocarbon province, CO_2 gases analysed from the South Viking Graben fault fall into this latter category, with the heaviest $\delta^{13}C$ values (-3‰) observed in the deeper portions of the graben immediately adjacent to the western fault also exhibiting the highest concentrations (~35 mol%) (James, 1990).

Through analysing the $\delta^{13}O$ and $\delta^{18}O$ isotopic ratios of the carbonate cements from the fault zone, it is possible to examine the influence of the isotopically heavier CO_2 encountered in the region, eliminating and constraining possible sources for the precipitating fluid and associated CO_2. This chapter presents the results of stable isotope analysis of the fracture cements in the four wells studied. Incorporating conclusions from earlier chapters and previous studies in the region, a fluid evolution history for the region is constructed. A number of models are proposed to account for the isotope data with respect to a flux of CO_2-rich basinal water ascending the graben bounding fault from an inorganic carbon source. The spatial distribution of the isotope data are also

discussed, with implications for fluid flow mechanisms and flux sites on the graben margin fault.

CO_2 source	$\delta^{13}C$ range (PDB)	Occurrence
Magmatic origin/deep crust	-4 to -7 ‰	Near deep fault systems
Atmospheric CO_2 exsolved from meteoric waters	Variable approx -6 ‰	Aquifer sandstones
Burial diagenesis of impure limestones	-2 to +3 ‰	Most sedimentary basins in clastic sequences
Burial diagenesis of carbonate cemented sandstones	Dependent on $\delta^{13}C$ of cement	
Thermal metamorphism of carbonates	-2 to +3 ‰	Contact metamorphism (i.e. intrusive events)
Methanogenesis of organic matter	-20 to +20 ‰	Early burial of organic-rich sediments
Thermal decarboxylation of organic matter	~ 20 ‰	Petroleum source rocks and coal sequences
Sulphate reduction of petroleum	-20 to -40 ‰	Near surface bacterial; and deeper thermochemical (TSR)

Table 5.1. Geological sources of CO_2 and their typical $\delta^{13}C$ isotope signatures. Data from Irwin *et al*. (1977); Jenden *et al*. (1993); Thrasher & Fleet (1995); Wycherley *et al*. (1999).

5.2. Methodology

5.2.1. Sampling method

Samples of the carbonate fracture cements previously identified and studied in the cored sections of fault zone were extracted for isotopic analysis. Powder samples were collected using an electric drill with a 2mm tungsten carbide drill bit. These samples consist of a range of cement phases as identified in chapter 3. Where possible, different generations of cements were collected individually using a microscope mounted MicroMill, allowing high resolution microsampling (~200 μm) of specific fracture cement horizons. The data acquired by each method is discussed later. All samples were taken from polished blocks or clean unweathered core section.

Sixty-five samples were collected in total from the four wells studied. In the highest CO_2 level well, 16/07a-12 (South Brae), 32 samples were taken from the fault zone depth ranges between 13014' and 13204'. From wells 16/12a-19, 16/12a-17, and 16/12a-16, 8, 13, and 12 samples were taken respectively at depths between 13332' and 14166'.

5.2.2. Analytical methods

Oxygen and carbon isotope analyses were performed at the Scottish Universities Environmental Research Centre (SUERC), East Kilbride, and the School of Geosciences, University of Edinburgh. Carbon and oxygen isotope ratios of the carbonate material were measured using conventional procedures. Owing to the differing treatment of calcite and dolomite in stable isotope analysis, the powder samples were analysed using XRD prior to ingestion to differentiate between which carbonate phase was present. Samples in which the carbonate mineral present was conclusively determined were analysed in bulk, with the CO_2 gas extracted from rock powder by overnight reaction with 100% phosphoric acid at 70°C.

In samples where both calcite and dolomite were present and could not be physically separated, sequential extraction was employed. The CO_2 gas was extracted by three hours reaction at 25°C and overnight at 100°C for calcite and dolomite respectively, with yields measured for each gas release. It must be noted that after the first sequential extraction stage (3 hours at 25°C), continued gas release was noted, suggesting separation of calcite from dolomite was not completely clean, possibly due to the non-stoichiometric nature of the dolomite, with calcium-rich dolomite more liable to react with acid than stoichiometric dolomite (Yui & Gong, 2003). This stoichiometry effect compromises the differential acid extraction method used to measure reliable stable isotope measurements from the mixed dolomite and as such should be interpreted with caution.

The extracted CO_2 gas was dried and purified, with the gas run over a Ag_3PO_4 trap to remove possible H_2S contamination from possible trace sulphides present in the powdered fracture cements, prior to analysis on Analytical Precision AP2003 (SUERC)

and VG PRISMIII (Edinburgh) mass spectrometers. Carbon isotopic ratios are reported as ‰ relative to V-PDB (Vienna Standard Pee Dee Belemnite). Oxygen is reported relative to V-PDB and V-SMOW (Vienna Standard Mean Ocean Water), with accuracy better than ±0.2 ‰ at 1σ.

5.3. Results

Table 5.2 (see rear of chapter) displays the carbonate $\delta^{13}C$ and $\delta^{18}O$ isotopic compositions of the fracture cement samples analysed (48 dolomite, 17 calcite), showing the well, depth, and carbonate phase attributed to each sample. The majority of the samples represent bulk analyses of a range of fracture cement generations owing to sample limitations and scale of individual cements. Fifteen samples consist of individual cement zones and noted accordingly.

The $\delta^{13}C$ values from all the wells range from -1.08 to -17.86 ‰ V-PDB, while $\delta^{18}O$ range between -4.24 and -15.45 ‰ V-PDB (26.54 and 14.99 SMOW). Fracture cements from well 16/07a-12 exhibit a $\delta^{18}O$ range between -4.24 and -15.68 ‰ V-PDB (26.54 and 14.75 SMOW) and a relatively narrow $\delta^{13}C$ range between -2.94 and -6.23 V-PDB (ave. -4.12). In addition, microdrilled samples of individual fracture cements from well 16/07a-12 show no apparent systematic variation in $\delta^{13}C$ or $\delta^{18}O$ isotopic compositions through the paragenetic sequence (Figure 5.1 a). The similarity of both $\delta^{13}C$ and $\delta^{18}O$ values determined from bulk powder samples with discrete cement generations suggests the bulk data is a suitable representation of the cements in the fault zone.

Cements from well 16/12a-16 have $\delta^{18}O$ compositions between -7.29 and -15.45 ‰ V-PDB (23.40 to 14.99 SMOW), and relatively heavier $\delta^{13}C$ values between -1.08 and -4.57 ‰ V-PDB (ave. -2.69). The data exhibit a curved trend with $\delta^{13}C$ decreasing with increasing $\delta^{18}O$ values (Figure 5.2 b), a pattern also broadly reflected in well 16/07a-12. Isotope data from well 16/12a-19 exhibits ranges of $\delta^{18}O$ and $\delta^{13}C$, from -4.51 to -7.45 (26.26 to 23.23 SMOW) and -4.85 to -17.86 ‰ V-PDB (ave. 9.67) respectively (Figure 5.2 c). The $\delta^{13}C$ compositions of the fracture cements from the well are significantly lighter than wells 16/07a12 and 16/12a-16 and exhibit a markedly narrower $\delta^{18}O$ range.

In well 16/12a-17, $\delta^{18}O$ values range from -5.74 to -8.25 ‰ V-PDB (24.99 to 22.40 SMOW) and $\delta^{13}C$ values from -7.33 to -15.10 ‰ V-PDB (ave. -10.90) (Figure 5.2 d). There is no evident correlation between $\delta^{13}C$ or $\delta^{18}O$ isotopic compositions with depth within each individual well sampled or between the four investigated fault zone horizons (Figure 5.3).

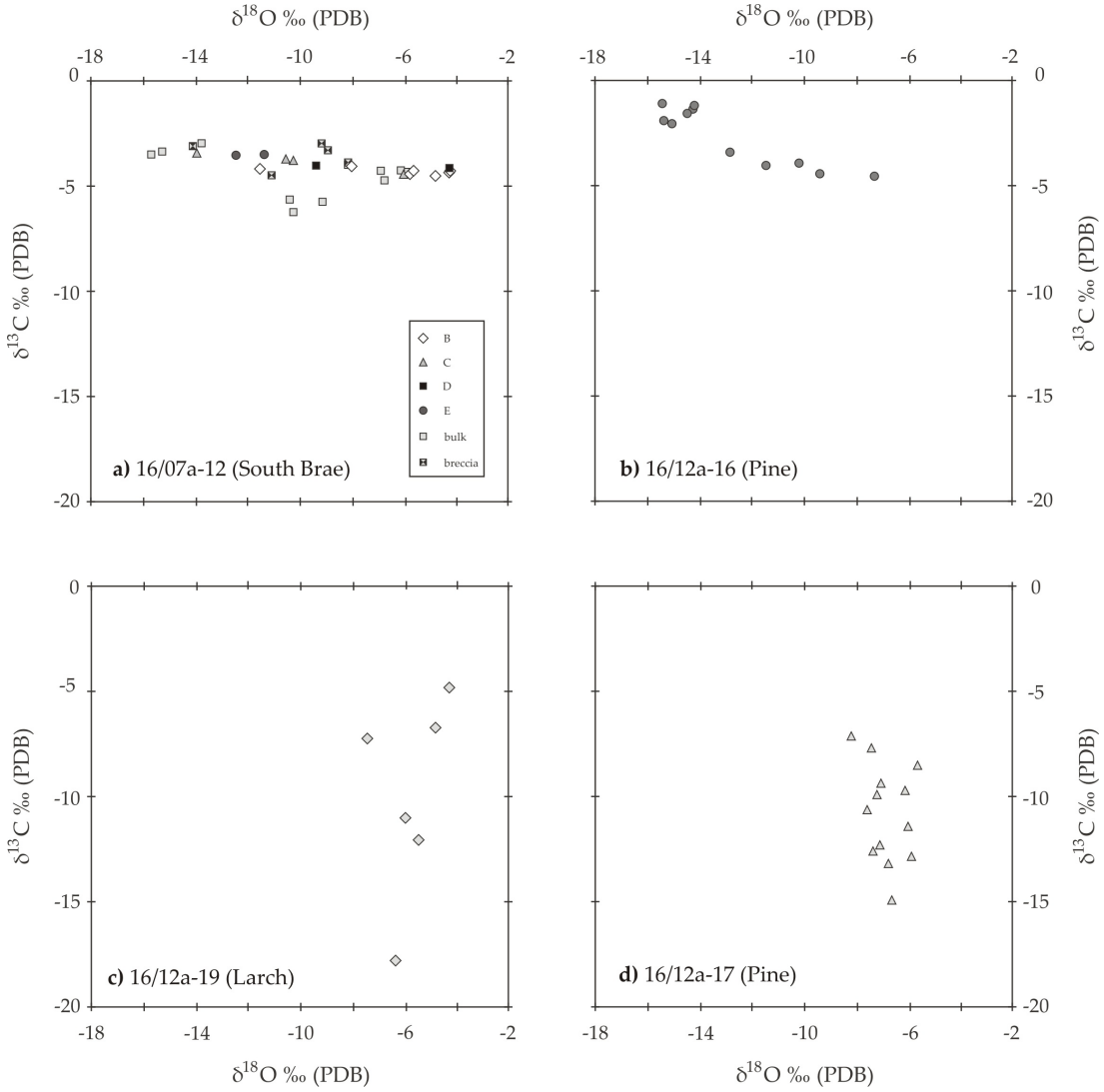

Figure 5.1. $\delta^{18}O$ vs. $\delta^{13}C$ plots of analyses carbonate fracture cements from the four wells studied (see Figure 3.1 for well locations). Wells 16/07a-12 and 16/12a-16 exhibit similar narrow $\delta^{13}C$ ranges (~-1 to -7 ‰ V-PDB) with wide distribution of $\delta^{18}O$ ratios (~-4 to -15 ‰ V-PDB). Conversely, cements from wells 16/12a-19 and 16/12a-17 show wide $\delta^{13}C$ ratios (~-18 to -5 ‰ V-PDB) and narrow $\delta^{18}O$ signatures (~-4 to -8 ‰ V-PDB). Key appended to chart a) relates to fracture cement generations observed in well 16/07a-12.

5.4. Discussion

From the $\delta^{13}C$ and $\delta^{18}O$ data of the four studied wells (Figure 5.1) there are two apparent distinct isotopic trends; a narrow $\delta^{18}O$ (-4.5 to -8.2 ‰ V-PDB), broad $\delta^{13}C$ (-4.8 to -15.1 ‰ V-PDB) distribution, and a wider range $\delta^{18}O$ (-4.2 to -15.7 ‰ V-PDB), narrow $\delta^{13}C$ trend (-1.1 to -6.2 ‰ V-PDB). Samples from the fault zone in wells 16/07a-12 and 16/12a-16 exhibit the latter distribution, with wells 16/12a-19 and 16/12a-17 the former. This suggests that there may be at least two distinct fluid types or fluid evolution trends to account for the observed isotopic trends encountered in the fracture cements. The isotopic signatures from the fault zone fracture cements are compared with previous stable isotope studies of diagenetic cements in the Brae Formation to assess the evolution of the precipitating fluids.

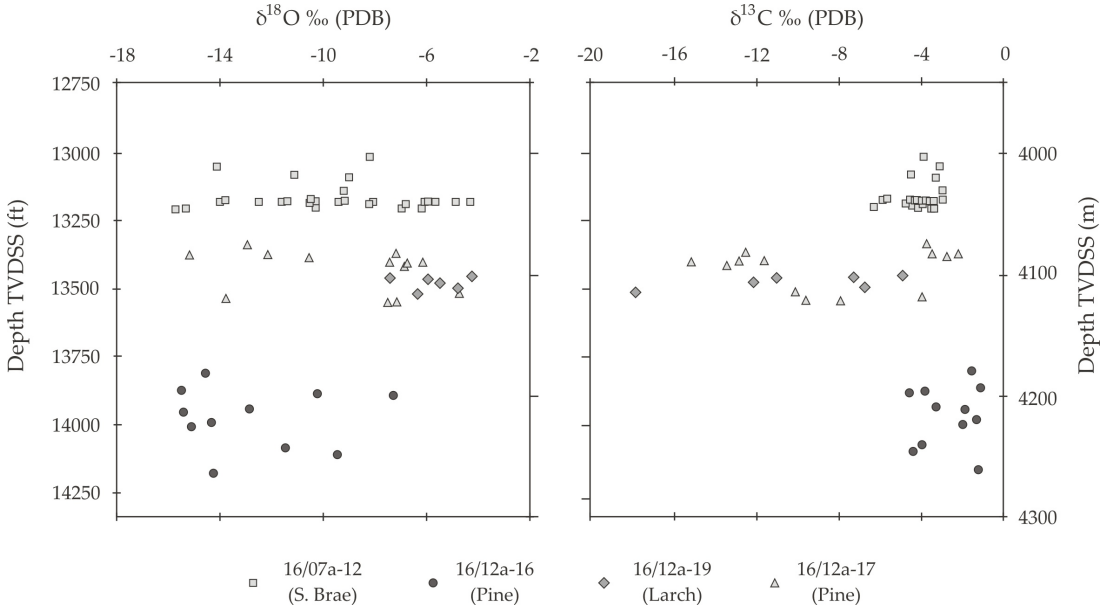

Figure 5.2. Plots of $\delta^{18}O$ and $\delta^{13}C$ vs. present-day depth for the fracture cements in the four wells. No discernable trend reflected in the data regarding possible temperature-depth related isotope fractionation in the cements is witnessed.

5.4.1. Carbon isotopes

The $\delta^{13}C$ signature of carbonate cements is strongly controlled by the source of the carbon, with temperature effects on carbon isotopic fractionation smaller compared to

those witnessed in oxygen isotope fractionation. The $\delta^{13}C$ composition of the CO_2 source from which the carbonate precipitated can be calculated from the measured $\delta^{13}C$ value of the carbonate and precipitation temperature using the carbon isotope fractionation equations; calcite, Bottinga, (1968); dolomite, Sheppard & Schwarz (1970):

$$1000ln\alpha_{calcite-CO2(gas)} = 2.78\ (10^6\ T^{-2}) - 2.89 \quad (5.1\ a)$$

$$1000ln\alpha_{dolomite-CO2(gas)} = 0.18\ (10^6\ T^{-2}) + 0.17 + 1000ln\alpha_{calcite-CO2(gas)} \quad (5.1\ b)$$

Where $1000ln\alpha_{carbonate-water} \approx (\alpha - 1)\ 1000 \approx \delta^{13}C_{carbonate} - \delta^{13}C_{CO2(gas)}$

$\delta^{13}C_{carbonate}$ = the measured carbon isotopic composition of the carbonate

$\delta^{13}C_{CO2(gas)}$ = isotopic composition of the CO_2 source

T = precipitation temperature in °K

This section compares the two observed isotopic trends in the fracture cements with respect to their $\delta^{13}C$ signatures, discussing possible carbon sources and implications for the distribution of CO_2 in the region.

Wells 16/12a-17 and 16/12a-19

The wide $\delta^{13}C$ ranges measured in the predominantly calcite cemented fracture cements of wells 16/12a-17 and 16/12a-19 (-7.33 to -15.10 ‰ V-PDB, and -4.85 to -17.86 ‰ V-PDB respectively) require a temperature variation of up to 200°C if the distribution in $\delta^{13}C$ values is attributed to a single source solely dependent on temperature; a prospect that is extremely unlikely. This is further compounded by the narrow $\delta^{18}O$ range which, assuming a constant porewater, suggests a temperature range no greater than 40°C. Therefore, it is likely that a mixture of carbon sources with varying $\delta^{13}C$ signatures is responsible for the observed trend. Fluid mixing may also alter the $\delta^{18}O$ composition of the porewater, potentially increasing the measured $\delta^{18}O$ range. However, given the relatively small quantity of carbon in the porewater, the $\delta^{13}C$ signal is much more sensitive to mixing.

The carbonate fracture cements present in the Brae Formation in wells 16/12a-17 and 16/12a-19 exhibit relatively light $\delta^{13}C$ (< -7 ‰) values comparable to $\delta^{13}C$ ratios of carbonate cements in the Brae Formation units (e.g. McLaughlin, 1994), and other similar Upper Jurassic hydrocarbon reservoir formations (Macaulay *et al*., 1998). These cements contrast with the relatively isotopically heavy $\delta^{13}C$ values of CO_2 encountered proximal to the fault zone in the Brae area (James, 1990). Although, unequivocal identification of specific carbon sources in the diagenetic realm is difficult, in hydrocarbon provinces such negative $\delta^{13}C$ ratios are typically attributed to the contribution of isotopically light carbon (-25 ‰) from the maturation and thermal decarboxylation of organic matter (Irwin *et al*., 1977). The oxidation of organic matter is a significant carbon source during burial diagenesis, with burial depth a major control on the diagenetic reactions within mudrock sequences and the evolution of formation waters (Curtis 1978; Scotchman *et al*., 2002).

It is widely acknowledged that reservoir units adjacent to significant organic-rich mudrock accumulations receive fluids rich in carboxylic acids which influence subsequent carbonate cementation (Surdam *et al*., 1989; Worden & Barclay, 2000). Therefore, given the proximity of organic rich Kimmeridge Clay below and overlying the Brae Formation reservoirs, the influence of organic matter on the isotopic signature of carbonate cementation in the area is expected. The reactions affecting the organic matter are subsequently reflected in the $\delta^{13}C$ signature of carbonate cements precipitated during burial, with carbonate cements in the Brae Formation exhibiting highly variable $\delta^{13}C$ compositions (McLaughlin, 1994; McLaughlin *et al*., 1994; Lu, 2008) (Figure 5.3).

Typically, early carbonate cements display relatively positive $\delta^{13}C$ values. This is attributed to incorporation of carbon derived from the methanogenesis of organic matter ($\delta^{13}C$ = 0 to 15 ‰) occurring at shallow burial depths (<1 km), with later cements precipitated at greater depths (>1 km) influenced by carbon released from thermal decarboxylation ($\delta^{13}C$ = -25 ‰) (Irwin *et al*., 1977; Curtis, 1978). Progressive $\delta^{13}C$ depletion during concretion growth in the Brae Formation has been observed in the

Miller Field (Lu, 2008) and South Brae (McLaughlin *et al*., 1994), with the isotopic trend attributed to porewater evolution resulting from depth-related diagenesis of the KCF. Such depth related $\delta^{13}C$ evolution profiles are not observed in the wells studied or within the paragenetic sequence of individual cements (Figure 5.1).

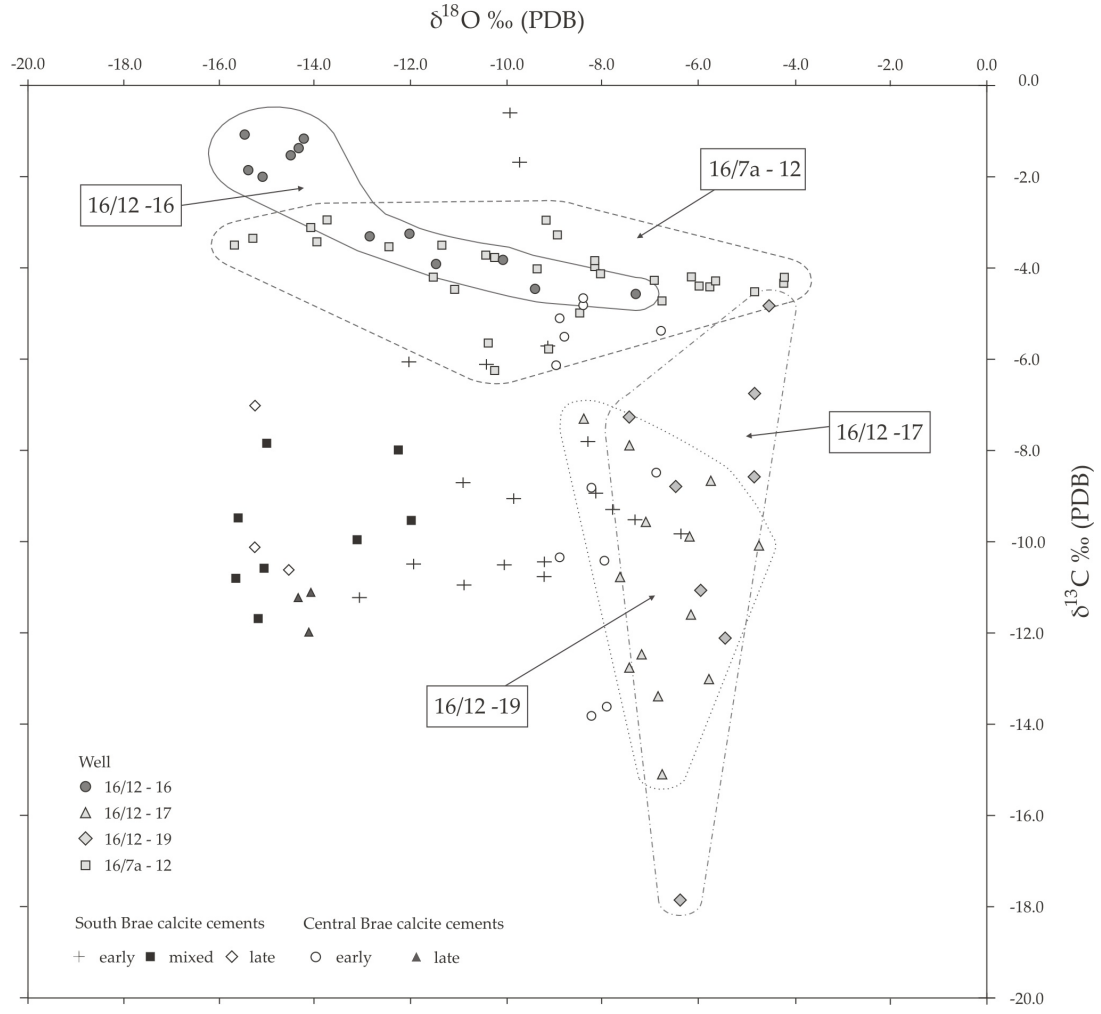

Figure 5.3. $\delta^{18}O$ vs. $\delta^{13}C$ plot of data from wells 16/07a-12. 16/12a-16, 16/12a-17, and 16/12a-19 with early and late diagenetic carbonate cements from South and Central Brae (*McLaughlin., 1994; McLaughlin et al., 1994*). Diagenetic cements show typical overall gradual decrease in $\delta^{13}C$ and $\delta^{18}O$ inherent in progressively buried North Sea sequences. Calcite fracture cements from wells 16/12a-17 and -19 exhibit isotopic ratios comparable to early diagenetic cements observed in the Brae Formation (McLaughlin *et al*., 1994).

Therefore, it is feasible that in wells where markedly negative $\delta^{13}C$ ratios are encountered in the fracture cements (i.e. well 16/07a-17), there has been an appreciable input of carbon derived from the thermal maturation of organic matter into the precipitating fluid. The influence of organic-rich fluids on the formation of the fracture cements has been suggested previously in the supply of reducing agents permitting sulphide mineralisation. However, given the apparent later age of fracture cement precipitation from petrographic evidence in the fault zone, the influence of $\delta^{13}C$ signatures derived from methanogenesis during early burial stages on the precipitation of the fracture cements can be largely neglected.

Wells 16/07a-12 and 16/12a-16

Fracture cements from wells 16/07a-12 and 16/12-16 produced significantly heavier $\delta^{13}C$ ratios between -1.08 and -6.23 ‰ V-PDB (ave. -3.72 ‰). These ratios, and their narrow range, differ with carbon isotope values of later carbonate cements in the South and Central Brae Fields (McLaughlin *et al*., 1994). A possible explanation for the more positive $\delta^{13}C$ ratios could be a greater incorporation of carbon from methanogenesis or marine carbonates through the dissolution of fossiliferrous material ($\delta^{13}C$ = ~0 %). Secondary porosity created through the dissolution of carbonate cements and bioclasts is observed in the Brae and Kimmeridge Clay Formations (Greenwood *et al*., 1994; McLaughlin *et al*., 1994). However, such diagenetic reactions were relatively early in the burial history of the units (Shaw & Primmer, 1991) and thus do not corroborate with the apparent advanced burial depth suggested for the time of fracture generation.

Significantly, the values from the fracture cements in the two wells are comparable to the $\delta^{13}C$ signatures of the high concentration CO_2 gases observed in the region (-3 to -8 ‰) (James, 1990). Assuming typical late stage diagenetic temperature ranges observed in the region (70 – 130°C), carbonate cements precipitated from fluids containing such CO_2 exhibit $\delta^{13}C$ ratios similar to those observed in the data set. Therefore, it is possible that the lighter isotopic signatures in the fracture cements from fault zones in wells 16/07a-12 and 16/12a-16 reflect the presence of inorganic CO_2 in the precipitating fluid,

introduced to the region via the fault as postulated by numerous researchers (James, 1990; Wycherley *et al*., 1999).

These authors advocate the influx of a CO_2-rich basinal water as providing a mechanism for introducing the high concentrations of CO_2 into the Jurassic reservoirs. To assess the viability of such a proposal, understanding the nature and temperature of the fluid responsible for precipitating the fracture cements is pivotal.

5.4.2. Oxygen isotopes

Variations in oxygen isotope ratios in carbonate cements are indicative of precipitation from differing temperatures or sourced from differing formation fluids. For example, at a given temperature, evolved basinal brines typically exhibit heavier $\delta^{18}O$ values compared to meteoric water and seawater due to increased fluid-rock interaction and diagenetic reactions during burial (Clayton *et al*., 1966; Sheppard, 1986). Conversely, with no independent temperature determination (e.g. microthermometry), and assuming a constant fluid isotopic composition, $\delta^{18}O$ values for carbonates will progressively deplete if precipitated at progressively higher temperatures. The measured $\delta^{18}O$ values of carbonate (calcite and dolomite) can be used to estimate the $\delta^{18}O$ composition of the host pore water if the precipitation temperature is known, or vice versa. The fractionation equations for calcite (Friedman & O'Neil, 1977) and dolomite (Matthews & Katz, 1977) are:

$$1000 ln\alpha_{calcite - water} = 2.78 (10^6 T^{-2}) - 2.89 \quad (5.2\ a)$$

$$1000 ln\alpha_{dolomite - water} = 3.06 (10^6 T^{-2}) - 3.24 \quad (5.2\ b)$$

Where $1000 ln\alpha_{carbonate - water} \approx (\alpha - 1)\ 1000 \approx \delta^{18}O_{carbonate} - \delta^{18}O_{water}$

$\delta^{18}O_{carbonate}$ = the measured oxygen isotopic composition of the carbonate

$\delta^{18}O_{water}$ = composition of pore water from which the carbonate precipitated

T = precipitation temperature in °K

The fracture cements exhibit $\delta^{18}O$ values ranging from -4.24 to -15.45 ‰ V-PDB (26.54 to 14.99 SMOW)). Plotted against $\delta^{13}C$, the results do not show a typical decreasing $\delta^{18}O$ vs. decreasing $\delta^{13}C$ trend indicative of temperature controlled precipitation from a single pore water type or carbon source in any of the wells studied (Figures 5.1 and 5.3). The two $\delta^{13}C$ vs. $\delta^{18}O$ trends observed in the data potentially represent two different fluid types; as interpreted through evaluation of the $\delta^{13}C$ signatures. The narrow $\delta^{18}O$ range, -4.51 to -7.68 ‰ V-PDB (26.26 to 22.99 ‰ SMOW), evident in fracture cements seemingly precipitated from fluids with appreciable organic carbon input (*see section 5.4.1*).

Conversely, the cements exhibiting $\delta^{13}C$ signatures interpreted to be indicative of inorganic carbon input show a broad $\delta^{18}O$ range (-4.26 to -15.68 ‰ V-PDB (26.52 to 14.75 ‰ SMOW)). Estimation of the $\delta^{18}O$ composition and temperature of the fluids resulting in the two isotopic trends present in the data is pivotal in understanding the source and timing of the fluid present in the fault zone and its relationship with formation waters in the overlying Brae Formation reservoirs. Using homogenisation temperatures measured from fluid inclusion analysis in chapter four, a wide range of $\delta^{18}O$ compositions for the precipitating fluids in well 16/07a-12 are suggested (Figure 5.4). Accounting for all the cement generations in which inclusions were analysed (B to E), applying the oxygen isotope fractionation equation of Matthews and Katz (1977) for dolomite, possible fluid compositions range between approximately -3 to +10 ‰ SMOW.

With the $\delta^{18}O$ ratio intrinsically governed by the fluid temperature, this wide range represents the upper and lower limit of possible $\delta^{18}O$ compositions; a factor exacerbated by the wide T_h ranges recorded within the individual cement generations (e.g. T_h range in cement generation C ~ 65°C). As a result, the $\delta^{18}O$ range estimated from the microthermometric data provides no reliable constraint on the isotopic composition, and thus possible source, of the precipitating fluid. This is further compounded by the probable leakage and re-setting of the fluid inclusions during burial as discussed previously, overprinting the original precipitation temperature. There is no apparent

trend regarding evolution of the $\delta^{18}O$ signature with the paragenetic sequence of the fracture cements and their respective T_h ranges (Figure 5.4).

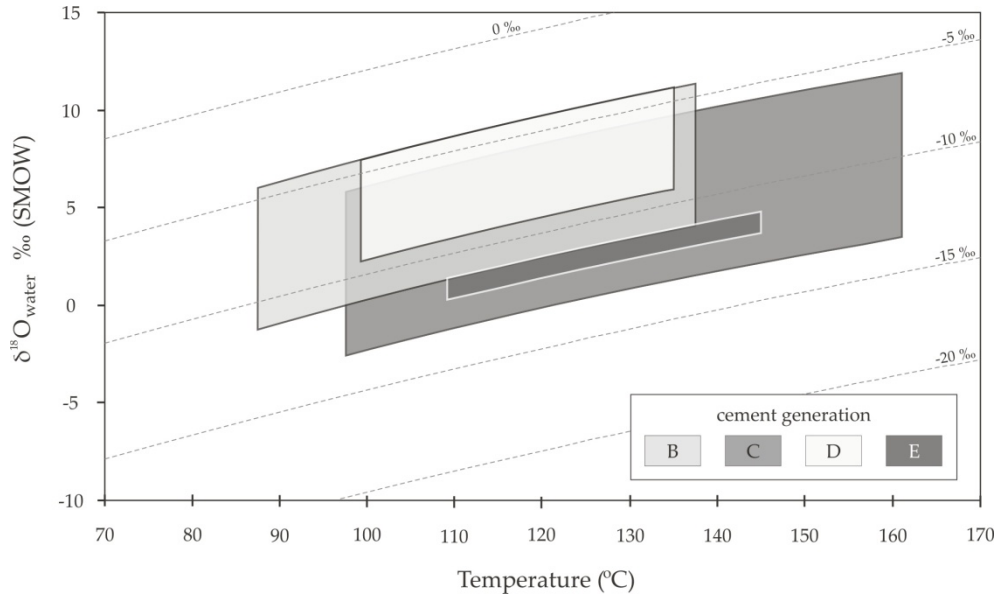

Figure 5.4. Estimated $\delta^{18}O$ ratio of porewaters from measured $\delta^{18}O$ ratios of dolomite fracture cements in well 16/07a-12 using homogenisation temperatures determined from fluid inclusion analysis. Possible $\delta^{18}O$ compositions encompass fluids ranging from evolved meteoric waters (-3 ‰), to heavily evolved basinal brines (+10 ‰). No fluid or temperature evolution pattern in the paragenetic sequence of the cements is observed from the data presented. Dolomite curves are calculated from Matthews and Katz (1977) and shown with respect to V-PDB.

Previous diagenetic studies have concluded that early in the burial history of a number of Jurassic reservoirs in the Viking Graben, the original Jurassic marine porewater ($\delta^{18}O$ = -1 ‰ SMOW) was replaced by meteoric re-charge (e.g. Bjørlykke, 1989; Haszeldine *et al*., 1992), with $\delta^{18}O$ of Upper Jurassic meteoric water = -7 ‰ SMOW (Hamilton *et al*., 1987). Isotopic signatures attesting to this have been recognised in early diagenetic cements in both South Brae (McLaughlin *et al*., 1994), and the Miller Field (Marchand *et al*., 2002). The role of basinal fluids in the evolution of formation waters in Jurassic reservoirs present in the Viking Graben region has been discussed extensively (Egeberg & Aagaard, 1989; Warren & Smalley, 1994), with a number of fields showing evidence for the influence of isotopically evolved fluids during diagenesis. Girard *et al*. (2002)

suggested evolved basinal waters with $\delta^{18}O$ values up to +3 ‰ SMOW were responsible for late diagenetic carbonate cements in the Hild Field, with the fluids derived from deep in the Viking Graben. Similar fluids have also speculated during the precipitation of late stage quartz cements in the Miller Field (Marchand *et al*., 2002). Using equations 5.2a and 5.2b, possible precipitation temperatures for the fracture cements were considered assuming a host of possible fluid types; meteoric, marine, and basinal (table 5.3). The fluid evolution implications for the two $\delta^{18}O$ isotopic trends are considered separately.

fluid source (SMOW)	16/12a-17 & 16/12a-19		16/07a12 & 16/12a-16	
	min temp (°C)	max. temp (°C)	min temp (°C)	max. temp (°C)
meteoric (-7 ‰)	5	30	16	76
marine (-1 ‰)	31	62	43	127
basinal (+4 ‰)	60	98	72	192

Table 5.3. Calculated precipitation temperatures for carbonate cements using the maximum and minimum $\delta^{18}O$ ratios for the two identified isotopic trends assuming precipitation from meteoric, marine, and basinal waters. Isotopic ratios for dolomite and calcite calculated using the equations of Matthews and Katz (1977) and Friedman and O'Neil (1977) respectively.

Wells 16/12a-17 and 16/12a-19

The predicted precipitation temperatures assuming fluids predominantly influenced by the influx of meteoric water from the $\delta^{18}O$ signatures of cements in wells 16/12a-17 and 16/12a-19 are relatively low (<30°C). This would suggest fracture cement precipitation very early in the burial history of the unit at depths <1 km (see Figure 2.9, p. 27). Such a proposal is not supported by petrographic evidence which suggests fracturing due to overpressure rupturing, a process not attainable in a meteoric influenced open system. The relatively negative $\delta^{13}C$ ratios attest to the probable presence of organically derived carbon from thermal decarboxylation; a process significant at higher temperatures (80 - 90°C) attained later during burial (~70 Ma). Such precipitation temperatures invoke a heavier $\delta^{18}O$ source fluid (+4 ‰ SMOW) than meteoric waters. Diagenesis of the

adjacent KCF, releasing light $\delta^{13}C$ during early maturation and heavy $\delta^{18}O$ through clay mineral diagenesis provides a probable source for these isotopic signatures. Late stage quartz cements in the Miller Field also suggest the influx of an isotopically heavier basinal fluid around 90°C, with earlier lower temperature diagenetic minerals precipitating from isotopically lighter marine and meteoric waters (Marchand *et al*., 2002).

Interestingly, precipitation temperatures of approximately 90°C correspond to burial temperatures around the time of the suggested high salinity influx into the Brae trend fields around 80 – 70 Ma (Larter *et al*., 1995). Marchand (2001) also observed fluid inclusions in this temperature interval (70 – 90°C) exhibiting high salinities (15 – 25 wt%. NaCl eq.) in the Miller Field. The introduction of evolved basinal water from depth would invariably increase both the salinity and $\delta^{18}O$ content of the existing formation water; a trend evidently recorded within cements present in the region. Therefore, it is possible that the fracture cements displaying these narrow $\delta^{18}O$ ratios precipitated from such a basinal fluid, with the suggested precipitation temperatures similar (~70 to 90°C) formation water temperatures at the assumed time of basinal influx (~70 Ma). With the influx of high salinity basinal fluids suggested as the method of charging the Brae trend fields with CO_2 (Wycherley *et al*., 1999; Lu, 2008), the absence of definitive inorganic CO_2 isotope tracers in these fault cements poses a potential problem, especially given the faults suspected role in serving as the conduit for CO_2 flux into the region.

The proposed basinal fluid composition of ~ +4 ‰ SMOW could be isotopically lighter than the actual fluid which initially ascended the fault due to mixing with the meteoric influenced isotopically lighter resident formation water present in the reservoir. A number of modern day formation waters are a mix of heavy evaporitic sources and depleted meteoric waters (Egeberg & Aagaard, 1989). Both Macaulay *et al*. (1997) and Smalley *et al*. (1992) recorded porewater compositions of +8 ‰ (SMOW) for the Fulmar and Ekofisk Fields respectively. The authors attributed the fluids to the vertical migration of saline basinal waters derived from the Zechstein. Such positive $\delta^{18}O$ ‰

(SMOW) values are typical of evolved basinal fluids, with brines up to +10 ‰ (SMOW) reported from evaporitic successions (Knauth & Beeunas, 1986).

As concluded previously, the $\delta^{13}C$ signatures of the fracture cements in wells 16/12a-17 and 16/12a-19 suggest the incorporation of organically derived lighter carbon, as witnessed in diagenetic cements throughout the Brae Formation sandstones. Therefore, a possible explanation accounting for the wide $\delta^{13}C$ and narrow $\delta^{18}O$ range encountered in these fracture cements could be due to mixing of an ascending isotopically heavier $\delta^{13}C$ and $\delta^{18}O$ CO_2-rich basinal fluid with the isotopically lighter existing formation water in the fracture network. The probable influence of cross-formational flow from the KCF in the formation and chemistry of the fracture cements has been discussed previously (*see section 3.4.3*). Consequently, the precipitation of the carbonate cements would thus reflect the mixed fluid composition; with the fluid attaining near thermal equilibrium with the existing formation water temperature due to conductive heat loss from the basinal fluid following mixing (~70 - 90°C).

Wells 16/07a-12 and 16/12a-16

The interpreted inorganic $\delta^{13}C$ signature of the carbonate fracture cements in wells 16/07a12 and 16/12a-16 appears to suggest the strong influence of the fluid responsible for introducing the significant volumes of heavy $\delta^{13}C$ CO_2 into the region with seemingly minimal mixing with the resident Brae Formation porewater prior to precipitation. If the basinal influx at ~70 Ma reflects the precipitation of the fracture cements from an evolved fluid (> +4 ‰ SMOW) the $\delta^{18}O$ range of the cements in wells 16/07a-12 and 16/12a-16 suggests precipitation temperatures ranging from ~70°C to 190°C assuming a uniform $\delta^{18}O$ fluid ratio. These temperatures are higher than those encountered by the Brae Formation at the time of assumed influx, even accounting for elevated heatflow during extension (~70 Ma, 100°C; Figure 4.5). With seismic pumping or release of over-pressured fluids from depth along the fault zone providing a suitable mechanism for transferring heated fluids from depth (e.g. Burley *et al*., 1989), the host fluids may have been significantly hotter than the resident formation waters in the surrounding fractured country rock, thus reflecting the isotopic composition of the

fluid. This is supported by microthermometric evidence recorded in later fracture cement generations which exhibit elevated T_h values greater than any formation water temperatures experienced by the Brae Formation during burial.

Assuming a relatively uniform $\delta^{18}O$ composition for the ascending basinal fluid, the $\delta^{18}O$ of the carbonate fracture cements in the paragenetic sequence do not indicate precipitation from increasingly warmer fluids as could be expected through progressive burial (i.e. enrichment in $\delta^{18}O$ with respect to PDB). However, this could be readily attributed to fluctuating fluid overpressures and fault permeability affecting the flux rate, and thus temperature distribution, of the basinal fluids ascending the fault zone. Conversely, the precipitating fluids may become more isotopically evolved than in previous generations owing to progressive fluid-mineral interaction at source; potentially concealing any temperature increase in the resultant isotopic signature of the precipitated mineral (e.g. 100°C, $\delta^{18}O_{fluid}$ +2 ‰ = $\delta^{18}O_{dolomite}$ = -10 ‰ (PDB); 150°C, $\delta^{18}O_{fluid}$ +6 ‰ = $\delta^{18}O_{dolomite}$ = -10 ‰ (PDB)). The presence of saddle dolomite in the fracture cements of well 16/07a-12 indicates precipitation temperatures relatively high in the context of diagenetic studies (>90°C; Radke & Mathis, 1980). As discussed previously, although caution must be taken with the microthermometry results in this study, a number of inclusions did also produce homogenisation temperatures greater than those experienced at current deepest burial depth, suggesting such elevated temperatures may be recorded in the cements.

5.4.3. Fluid Evolution

Assuming a basinal fluid influx contemporaneous with overpressure fracturing along the graben margin, a fluid evolution model (Figure 5.5) can be developed, accommodating both the observed $\delta^{18}O$ compositions of the fracture cements and the oxygen isotope compositions of diagenetic cements previously studied in the Brae Formation. McLaughlin et al. (1994) proposed that early diagenetic calcite cements in South and Central Brae precipitated at relatively low temperatures (<35°C) following meteoric recharge during early burial; a process commonly observed in the Late Jurassic rifting phase of the Viking Graben (e.g. Haszeldine *et al.*, 1992).

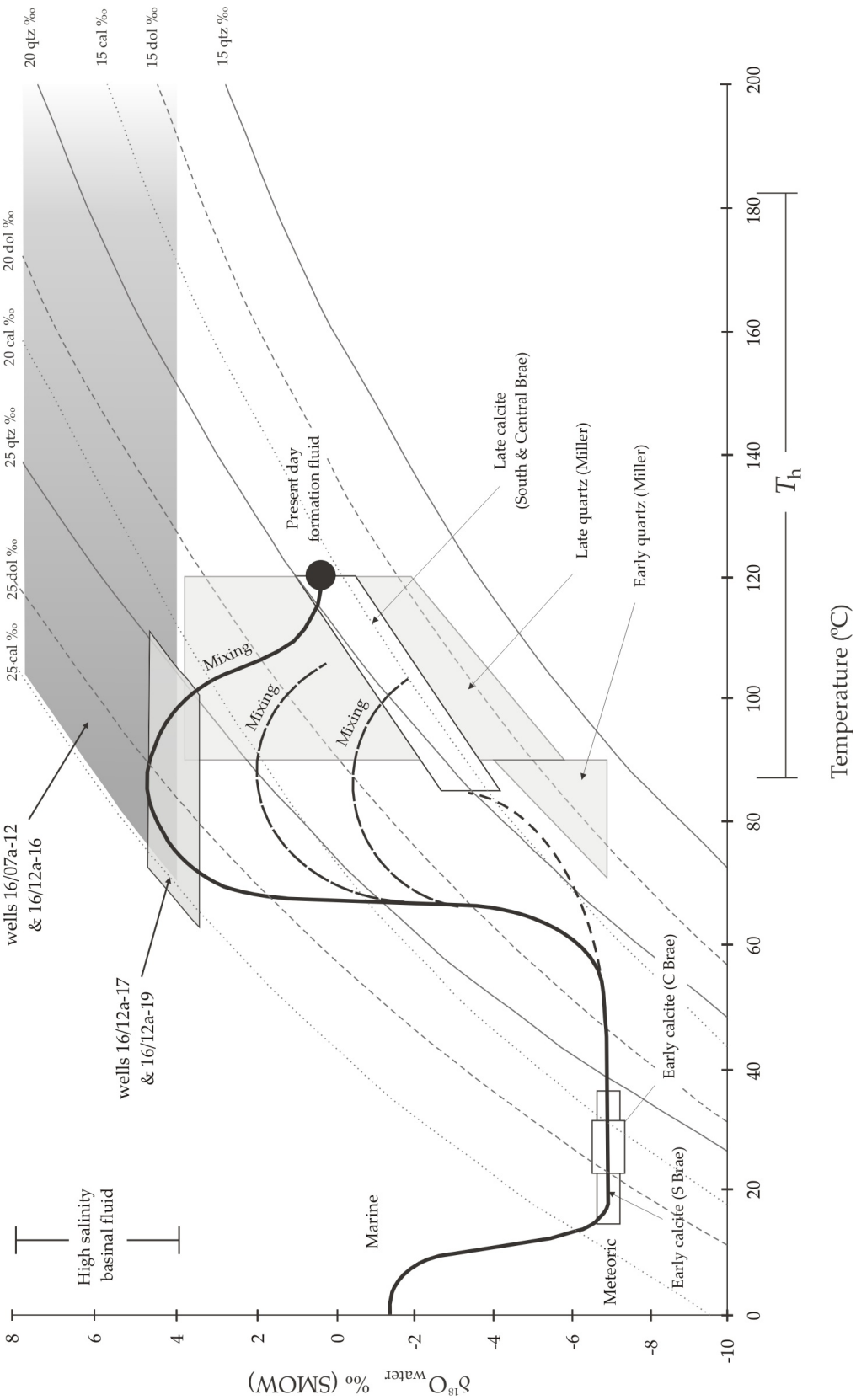
20 qtz ‰
15 cal ‰
15 dol ‰
15 qtz ‰
25 cal ‰
25 dol ‰
25 qtz ‰
20 cal ‰
20 dol ‰
wells 16/07a-12
& 16/12a-16
wells 16/12a-17
& 16/12a-19
Mixing
Mixing
Mixing
Present day
formation fluid
Late calcite
(South & Central Brae)
Late quartz (Miller)
Early quartz (Miller)
Early calcite (C Brae)
Early calcite (S Brae)
Meteoric
Marine
High salinity
basinal fluid
$\delta^{18}O_{water}$ ‰ (SMOW)
8
6
4
2
0
-2
-4
-6
-8
-10
0
20
40
60
80
100
120
140
160
180
200
T_h
Temperature (°C)

Figure 5.5. (Previous page). Formation water $\delta^{18}O$ evolution models for the fault zone fracture cements and Brae Formation reservoirs in the South Brae, Central Brae, and Miller Field. High salinity ^{18}O enriched fluids (>+4 ‰) introduced ~70 Ma (70 – 90°C) as reported by Larter *et al*. (1995) and Marchand *et al*. (2001), precipitating the fracture cements; with the $\delta^{18}O$ signature and temperature of the fluid dictated by the degree of mixing with the *in situ* lighter formational fluid (see Figures 5.7, 5.8, and text for details). The $\delta^{18}O$ of the fluid from which the late stage calcite and quartz precipitated is suggested to be isotopically lighter (Marchand *et al*., 2002). The wide $\delta^{18}O$ variability witnessed in the Miller quartz cements may be a product of variable homogenisation with the resident formation water with ascending basinal fluids for the fault zone, resulting in the porewater value observed in the present day. Shaded areas denote measured $\delta^{18}O$ compositions and inferred fluid compositions of calcite and quartz cements from the Brae Fields and Miller Field respectively (McLaughlin *et al*., 1994; McLaughlin, 1994; Marchand *et al*., 2000; Marchand *et al*., 2002). $\delta^{18}O$ fractionation curves for calcite, dolomite and quartz are shown relative to SMOW. Homogenisation temperature (T_h) range shown is for inclusions from fracture cements in well 16/07a-12.

Continual ^{18}O enrichment of the resident formation water following early meteoric influx is assumed due to ongoing fluid-mineral interactions during progressive burial of the Brae Formation sandstones, as reflected in interpreted porewater compositions for early authigenic quartz cements in the Miller Field (Marchand *et al*., 2002). However, as discussed in the previous section and determined from observed fracture textures and microthermometric results, a basinal influx approximately 70 Ma can be invoked whereby the $\delta^{18}O$ ratio of the carbonate cements correspond to precipitation temperatures greater than the formation water at the time (>70°C) and from fluids significantly more isotopically evolved than those previously encountered in the Brae Formation reservoirs.

A relatively high temperature basinal influx model is plausible for the following reasons: 1) the introduction of a possible Zechstein derived fluid can account for high salinity fluid inclusions corresponding to ~70 Ma; 2) such a fluid provides an otherwise locally absent source of Mg, facilitating the precipitation of dolomite in the fractures and overlying heavily cemented portions of the Brae Formation.; 3) $\delta^{13}C$ compositions of

cements precipitated from the higher temperature more evolved fluids ($\delta^{13}C$ = -2 to -4 ‰) are indicative of inorganically sourced carbon, possibly from the exsolution of CO_2 following the dissolution of carbonates at depth in the Zechstein Formation. As discussed previously, the difference in $\delta^{18}O_{fluid}$ and temperature ranges estimated between cements studied from wells 16/07a-12 and 16/12a-16 with wells 16/12a-17 and 16/12a-19 can be attributed to the degree of fluid mixing with the *in situ* formation water as speculated from their $\delta^{13}C$ signatures and estimated precipitation temperatures. The degree of fluid mixing experienced may be a function of the distance the sampled wells are from the main basinal flux point on the graben margin.

Elevated temperatures as proposed in the basinal influx model have been recorded and observed in a number of analogous extensional tectonic settings (e.g. Rhine Graben, East Africa Rift). High heat flows comparable to those predicted for the South Viking Graben during the extensional phase (80 mW m^{-2}) have been observed in the present-day Rhine Graben (Clauser & Villinger, 1990). In addition to elevated regional geothermal gradients, the margin of the Rhine Graben is punctuated with numerous localised thermal anomalies, with temperatures in excess of 140°C reported at relatively shallow depths (<1 km) (Rybach, 2007). Lampe and Person (2000) attributed the thermal anomalies to episodic faulting events introducing hot fluids to shallower depths up selected fault zones and fracture networks along the graben. Similar deep sourced fault networks have been implicated as conduits for high temperature fluid flow resulting in localised near-surface thermal anomalies in the present-day Central Ethiopian Rift (Abiye & Haile, 2008). Such anomalies demonstrate the circulation of deep-sourced fluids up fault zones in active extensional regimes and provide a suitable analogue for ancient fault hosted fluid flow in this study and previous investigations (e.g. Burley *et al*., 1989; Smith *et al*., 1998).

Marchand *et al*. (2002) ultimately discounted a discrete basinal-type fluid influx in their porewater evolution model of the Miller Field, as they could not reconcile a decrease in $\delta^{18}O_{fluid}$ to present day formation water values following basinal influx. The authors instead opted for a continual fluid evolution model to accommodate the increase in $\delta^{18}O$

signatures in the cements studied. However, the model fails to fully account for the introduction of high salinity inclusions within the quartz cements at 70 - 90°C. Assuming a continual fluid evolution model, one would expect the formation water to become further enriched in dissolved solids; a trend not evident in later higher temperature inclusions from the field typically exhibit lower salinities (~8 ±2 wt.% NaCl) (Larter *et al*., 1995), suggesting a cessation in the supply of high salinity fluids into the field. Lu (2008) proposed that a decrease of $\delta^{18}O$ in the formation water in the field may due to the CO_2 charge into the reservoir, with the ascending CO_2 consisting of isotopically light oxygen. However, CO_2 present in solution contributes minimal oxygen compared to the host solution, especially in higher salinity fluids with reduced CO_2 solubility (Duan & Sun, 2003).

Therefore, the possibility of the $\delta^{18}O_{fluid}$ signature being influenced by the introduction on CO_2 into the reservoir is questionable. However, mixing between the high salinity basinal fluid influxes and the existing formation water could be used to explain the apparent decrease in salinity and can thus be invoked to explain the decrease in $\delta^{18}O$ of the formation water in the Miller Field to the present day values; ~7.8 wt.% NaCl and +0.6 ‰ respectively (Smalley & Warren, 1994).

5.5. Isotope modelling

Isotope modelling was employed to evaluate the relative importance of fluid mixing (between ascending basinal fluids and *in situ* formation waters) and CO_2 degassing from an ascending fluid on the isotopic signatures recorded in the fracture cements.

5.5.1. Modelling parameters

The co-variations in the $\delta^{13}C$ and $\delta^{18}O$ values witnessed in the fracture cements between the four studied wells were modelled using fluid mixing and Rayleigh fractionation equations accounting for the possible fluids, CO_2 sources, and precipitation temperatures. For the temperature range suitable for the fluids in question the carbonate – $CO_{2(g)}$ fractionation factors of Bottinga (1968) and Sheppard and Schwarz (1970) were

selected (equations 5.1 a, 5.2 b). The carbon isotope composition of a fluid is controlled by the concentrations of the different carbon species (e.g. H_2CO_3, aqueous CO_2, HCO_3^-, CO_3^{2-} and CH_4) present within it. The differing isotopic fractionation factors between the various carbon species results in $\delta^{13}C$ variations in the subsequently precipitated carbonate minerals. The relative distribution of the carbon species and which is dominant is strongly dependent on changes in pH. The oxidised carbon species in fluids below 350°C are: H_2CO_3, HCO_3^-, and CO_3^{2-} (Ohmoto & Rye, 1979).

In fluids with low pH, H_2CO_3 is the most important carbon species, with CO_2 the principle component of the fluid having being dissolved into the solution from its gaseous phase at high pressures. Although a number of studies have shown that under equilibrium conditions a small but distinct fractionation of carbon isotopes occurs between gaseous carbon dioxide and an aqueous solution of the gas (Vogel *et al*., 1970, Zhang *et al*., 1995), in this study H_2CO_3 and aqueous CO_2 are often considered together as $H_2CO_{3(app)}$ as advocated by Ohmoto and Goldhaber, (1997). In addition, at the temperatures suggested in this study the fractionation between them above 100°C is considered negligible, so the fractionation factors for CO_2 is used to account for both species (Ohmoto, 1972).

With increasing pH, decreasing temperature, and lowering partial pressure of the CO_2, the dominant carbon species present should be HCO_3^-. Additionally, in fluids buffered by carbonate rocks, the most important dissolved carbon species is HCO_3^- (Spangenberg *et al*., 1996). In such a system, the fractionation factor of Ohmoto and Rye (1979) was applied. The fractionation factors for the carbon species and carbonates used in this study are presented in Figure 5.6. Although isotopic fractionation between carbonates and water decreases with increasing salinity, a consideration in this study owing to the influence of basinal brines, at the temperatures suggested (<200°C) the effect can be neglected (Horita *et al*., 1995).

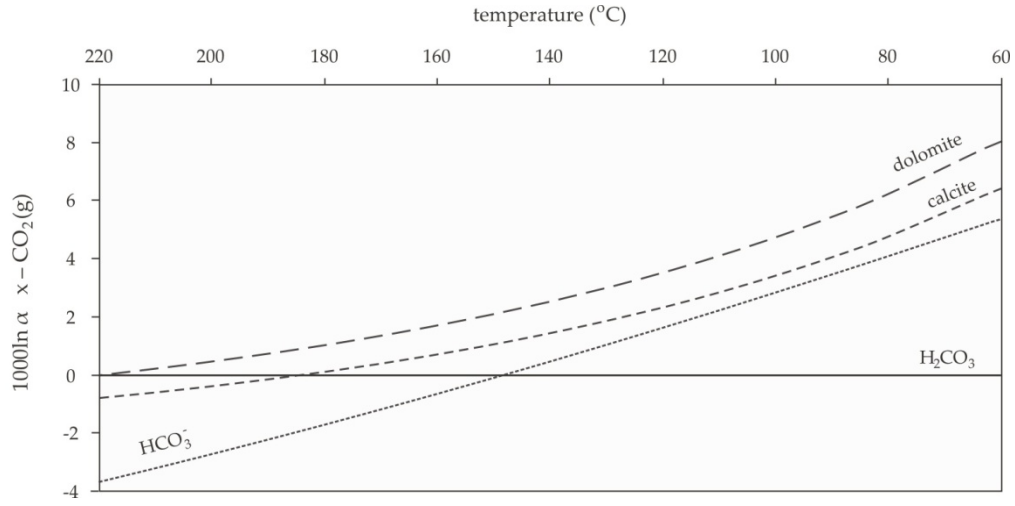

Figure 5.6. Fractionation factors for various carbon species relative to gaseous CO_2 used in the modelling for the temperature range appropriate for the potential precipitating fluids (60 – 220°C). Dolomite (Sheppard & Schwarcz, 1970); calcite (Bottinga, 1968); HCO_3^- (Ohmoto, 1979). The fractionation factors used are in good agreement with similar factors for the temperature range.

5.5.2. Fluid mixing

The mixing of fluids provides an effective mechanism for the precipitation of carbonate minerals, with the dilution of saturated fluids from mixing with poorly saturated fluids resulting in precipitation (Holland & Malinin, 1979). The mixing of two differing fluids produces compositions dictated by the initial $\delta^{18}O$ and $\delta^{13}C$ values of each fluid and the proportion of each in the mixture. Due to dominance of water in the fluids, the mixing of $\delta^{18}O$ is effectively uniform between two any given fluids. However, fluids can invariably exhibit varying carbon contents, with a profound impact on the resultant $\delta^{13}C$ signature of the mixed fluid. Zheng and Hoefs (1993) defined the proportions of carbon contents (P) is as:

$$P = C_b / C_a \sim {}^{12}C_b / {}^{12}C_a$$

where subscripts *a* and *b* denote the two fluids. Using the fluid mixing equation of Zheng and Hoefs (1993), the isotopic composition of calcite precipitated from the mixing

of two fluids with differing $\delta^{18}O$, $\delta^{13}C$ signatures, and carbon content for given temperatures can thus be calculated:

$$d^{13}C_{calcite} = \frac{X_a\,(d^{13}C_a + 10^3 \ln a_{calcite - HCO_3^-}) + P\,(1 - X_a)\,(d^{13}C_b + 10^3 \ln a_{calcite - HCO_3^-})}{P + X_a - P\,X_a}$$

$$d^{18}O_{calcite} = d^{18}O_b + 10^3 \ln a_{calcite - H_2O} + X_a\,(d^{18}O_a - d^{18}O_b)$$

where *X* represents the fraction of ascribed fluid present in the mixture. Other terms are explained previously.

The two observed $\delta^{13}C$ vs. $\delta^{18}O$ isotope trends were simulated using the above mass-balance equations for fluid mixing. The method was adopted to test whether the composition of the carbonate cements can be explained by a model invoking the mixing of two end-member fluids; isotopically light resident formation water and a hypothetical ascending basinal brine (Figure 5.7). The *in situ* formation water is assumed to be influenced by thermal degradation of organic matter ($\delta^{13}C$ = -25 ‰ V-PDB (e.g. Irwin *et al*., 1977)) and consists of a compositionally evolved meteoric water influenced by progressive diagenesis during burial ($\delta^{18}O$ = -2 ‰ SMOW) (c.f. Marchand *et al*., 2002). The basinal fluid was assumed to have a $\delta^{18}O$ composition similar to typical heavily evolved formation waters (+7 ‰ SMOW), with $\delta^{13}C$ values representative of inorganically derived CO_2; -4 ‰ V-PDB (e.g. James, 1990). The dominant dissolved carbon species present in the fluid is assumed to be HCO_3^- owing to the inferred dissolution of carbonate sequences at depth prior to the ascent of the fluid (see section 3.4.5); a factor potentially reflected in the relatively high HCO_3^- (>2000 mg/l) and Ca (~2250 mg/l) values observed in the formation waters of the Brae trend fields in the present day (Hardy *et al*., 1994; Smalley & Warren, 1994).

Conversely, the resident formation water is assumed to be dominated by H_2CO_3 due to the dissolution of CO_2 released through the breakdown of organic matter and the pH decrease resulting from this. The temperature of *in situ* porewater in the Brae Formation

(60 – 90°C) corresponds to formation conditions at the time of suggested basinal influx of CO_2 (~70 Ma) based on burial depths of ~2 km accounting for both a normal geothermal gradient (35°C km^{-1}; Figure 2.9) and elevated heat flow due to extensional tectonism at the time of precipitation (40°C km^{-1}; Figure 4.5). The temperature of the ascending solution is discussed subsequently in the context of the two observed $\delta^{18}O$ vs. $\delta^{13}C$ trends.

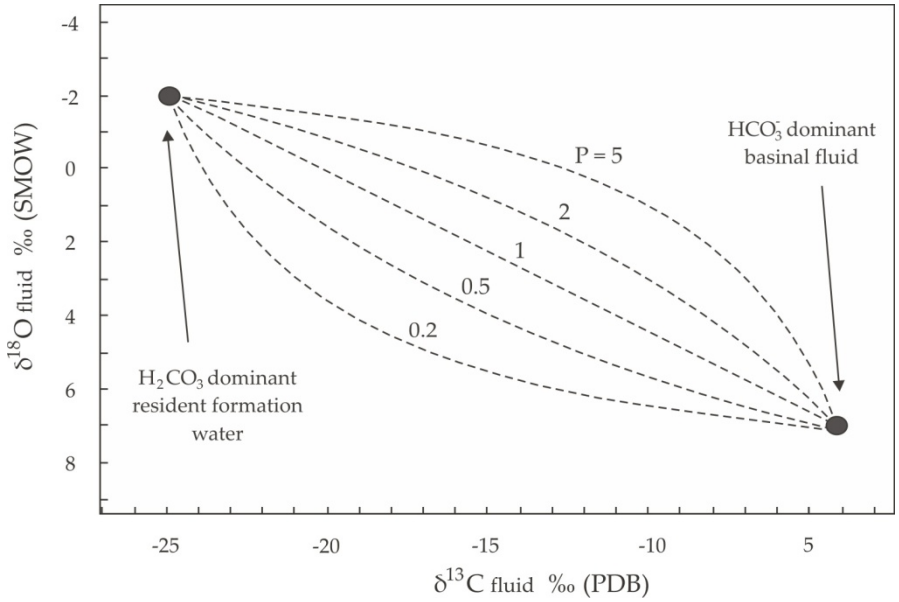

Figure 5.7. Mixing curves of fluid compositions from mixing of isotopically lighter meteoric and decarboxylation influenced resident formation water ($\delta^{18}O$ = -2 ‰ (SMOW), $\delta^{13}C$ = -25 ‰ (PDB)) with evolved basinal water with heavier dissolved CO_2 (c.f. James, 1990) ($\delta^{18}O$ = +7 ‰ (SMOW), $\delta^{13}C$ = -2 ‰ (PDB)). P is the concentration ratio of dissolved carbon in the basinal fluid to the existing formation water. The fluid mixing line relates to the model presented in Figure 5.8. The absolute quantity of carbon is not inferred.

Wells 16/12a-17 & 16/12a-19

In this mixing model calcite is considered instead of dolomite as it is the predominant mineralogy observed in the fracture cements from these wells and due to the calcite displaying the largest isotopic variation in the $\delta^{18}O$ vs. $\delta^{13}C$ space. In this model a temperature range of 60 – 90°C is used for the basinal fluid based on the assumption of conductive heat loss following mixing with the relatively cooler resident formation The

model provides a suitable fit to the measured isotopic compositions of the cements in the wells, with the majority of the data points representing the calcite fracture cements enclosed by curves representing mixing of the basinal brine with up to 40 % of the existing formation water in a HCO_3^- dominated system (Figure 5.8).

The resultant precipitation temperatures derived from mixing between the two end member fluids are consistent with those encountered by Larter *et al*. (1995) and Marchand (2001) for high salinity inclusions in the Miller Field (70 – 90°C; salinity 15 – 25 wt.% NaCl). The $\delta^{18}O$ composition of approximately +4 ‰ for the fluids resulting from mixing is in agreement with those suggested in the formation water evolution model in Figure 5.5 for wells 16/12a-17 and 16/12a-19, suggesting precipitation occurred under relatively homogenous conditions. The observed decrease in carbon content ratio with greater mixing as witnessed in the model can be reconciled by the increasing influence of carbon in the resident formation water.

Wells 16/07a-12 & 16/12a-16

Similar mixing models can also be applied to explain the $\delta^{18}O$ vs. $\delta^{13}C$ trends witnessed in data acquired from wells 16/07a-12 and 16/12a-16 (Figure 5.3). Higher fluid temperatures (up to ~200°C) and a greater temperature range (~120°C) are invoked for these wells as per the fluid evolution model presented in section 5.4.3 (Figure 5.5). The model assumes basinal influxes of relatively high temperature fluids from depth based on the fluid inclusion homogenisation temperatures measured in well 16/07a-12 and the $\delta^{18}O$ compositions of the analysed fracture cements. Basinal fluid $\delta^{18}O$ ratios range between +8 and +6 ‰ (SMOW); values comparable to typical heavily evolved formation fluids (Egeberg & Aagaard, 1989). *In situ* Brae Formation water isotopic signatures are those used in previous mixing models ($\delta^{13}C$ = -25 ‰ PDB, $\delta^{18}O$ = -2 ‰ SMOW at 80°C) based on formation temperatures at the time of assumed fluid influx (~70Ma) in an elevated geothermal gradient temperature regime (see Figure 4.5).

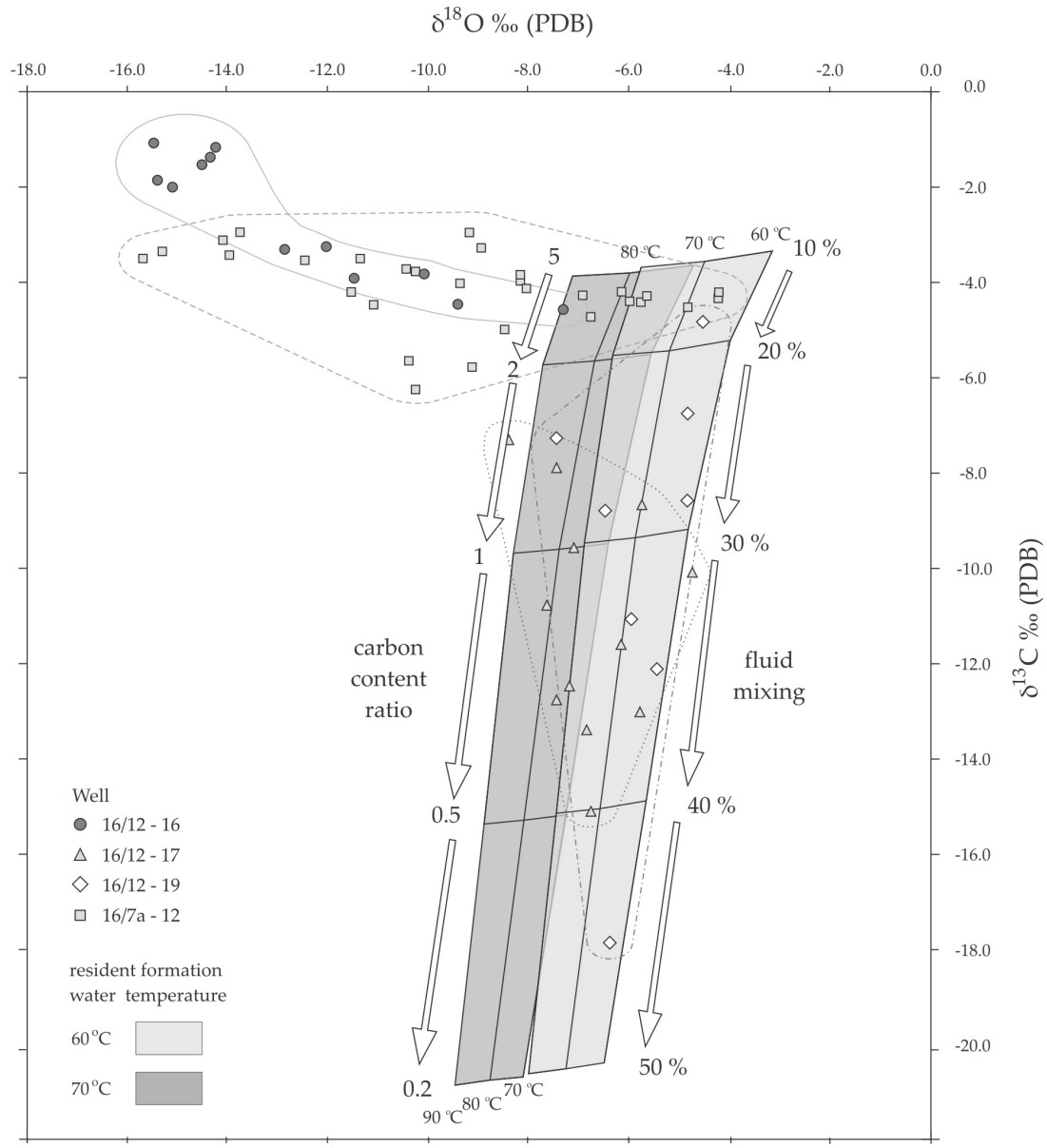

Figure 5.8. Range of potential $\delta^{13}C$ and $\delta^{18}O$ ratios of calcite precipitated from the mixing of basinal and formation waters. Less than 50% mixing with the formation water is required to produce the observed isotopic ratios, with the degree of mixing required less at higher temperatures (see text for detail). The model assumes mixing of ascending HCO_3^- dominant basinal fluid ($\delta^{13}C$ = -4 (PDB), $\delta^{18}O$ = +7 (SMOW)) at temperatures of 90, 80, and 70°C mixing with resident formation water ($\delta^{13}C$ = -25 (PDB), $\delta^{18}O$ = -2 (SMOW)) at 60 - 90°C; the temperature at time of influx ~70 Ma.

A range of potential mixing scenarios result from variations in the isotopic composition of the ascending fluid and the degree of fluid mixing. Most data points for the dolomite cements in the two wells are enclosed by curves applying the fluid temperatures and evolved formation water oxygen isotope signatures assumed above (Figure 5.9 a). In high-CO_2 concentration basinal fluids dominated by inorganically sourced carbon ($\delta^{13}C$ = -4 ‰ PDB; James, 1990), even a relatively large degree of fluid mixing with the resident formation fluid (>20%) results in a limited negative $\delta^{13}C$ shift less than 1.0 ‰ at lower temperatures (~80°C) and no greater than 2 ‰ at higher temperatures (200°C) (Figure 5.9 b).

From the model this suggests that in such CO_2-rich fluids, the carbon isotope signature of the hydrocarbon dominated formation water is overwhelmed by the ^{13}C signature imposed by the ascending inorganic fluid. The magnitude of the carbon content ratio in the ascending fluid is intrinsically governed by the solubility of CO_2 in the host solution. Carbon dioxide solubility in high salinity fluids (~22 wt. % NaCl) at temperatures up to 200°C and relatively elevated pressures (1000 bar) is approximately 1.6 mol kg^{-1} H_2O (~7 wt. %) (Duan & Sun, 2003). With CO_2 solubility reducing with decreasing pressure but increasing at a greater rate with decreasing ionic strength, the potential for ^{13}C signatures from dissolved CO_2 in the ascending fluid to extensively overwhelm those in the presumably lower salinity resident formation water is arguably limited.

Therefore, the degree of fluid mixing or, more likely, natural variability in the isotopic signature of the carbon source possibly provides a more plausible explanation for the variability in $\delta^{13}C$ ratios witnessed in the fracture cements. However, from the data points alone, the respective influence of the degree of fluid mixing or carbon concentration cannot be readily surmised. A number of comparable previous fluid mixing models regarding carbonate ore genesis commonly consider additional fluid-wallrock interaction and isotopic exchange with carbonate country rock (e.g. Spangenberg *et al*., 1996). Owing to the siliciclastic composition of the fractured wallrock hosting the carbonate cements, this approach was not adopted in this study. Additionally, potential alteration of previous carbonate isotope signatures from

subsequent fluid influxes (e.g. Taylor, 1977) is not considered as mixing between fluids of different origins is of much more significance than mixing between fluids of broadly similar origin.

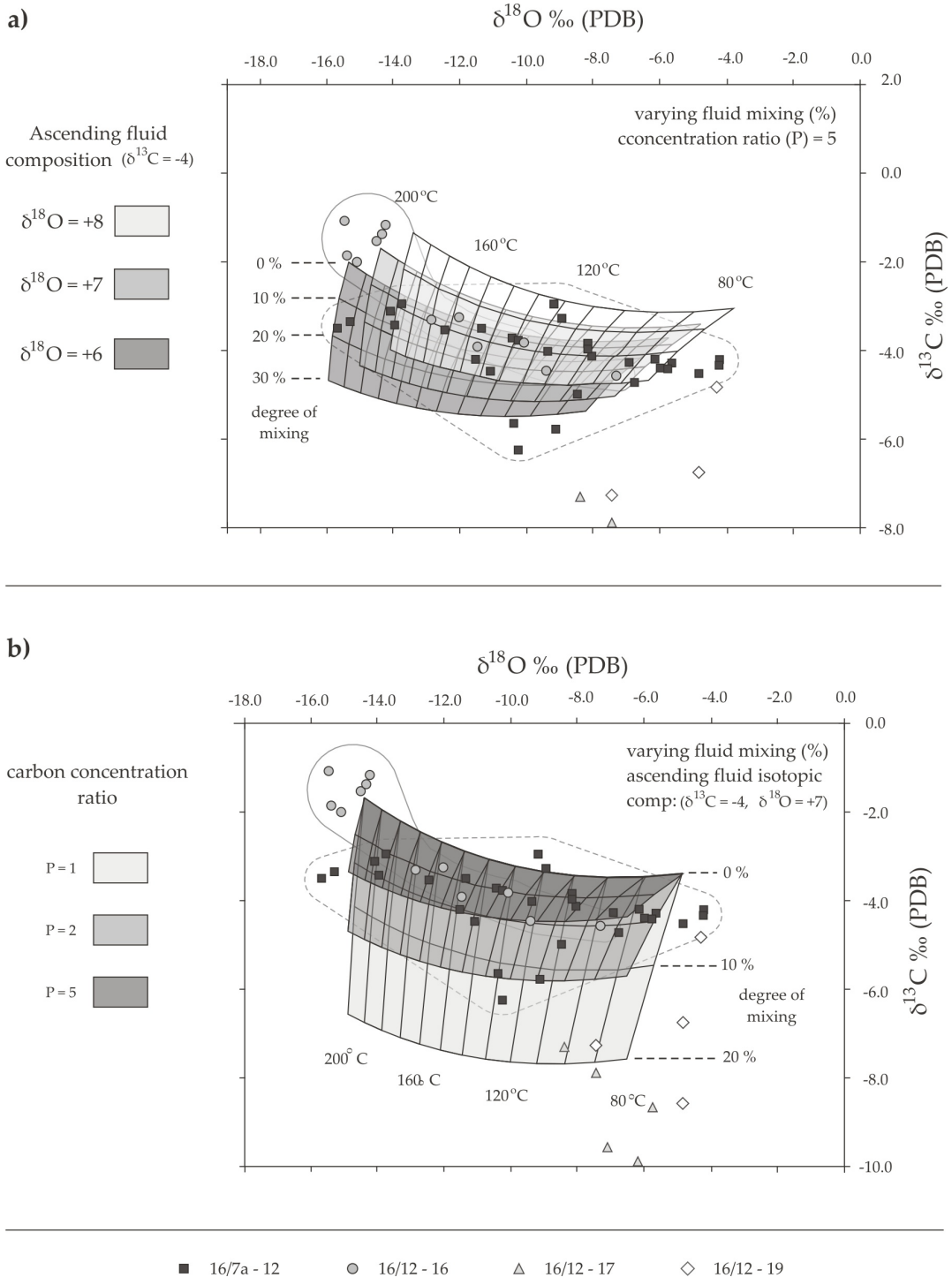

Figure 5.9. (previous page) Plots showing the range of possible $\delta^{13}C$ vs. $\delta^{18}O$ compositions of dolomite precipitated from postulated high temperature basinal influxes (80°C – 200°C) through fluid mixing with resident formation water. Potential variations in the isotopic composition fields are shown with respect to **a)** the $\delta^{18}O$ composition of the basinal fluid and **b)** the carbon concentration ratio between the ascending fluid and pre-existing formation water. See text for details.

However, the $\delta^{18}O$ composition of the fracture cements may have been influenced by mixing with the resident formation water. Cross-formational flow, principally with the adjacent KCF, has been discussed previously to account for the influx of lighter carbon isotope signatures witnessed in a number of cements and the increasing iron content and pyrite observed in later cement generations. Clay diagenesis in the KCF has been proposed as a driver for evolving $\delta^{18}O$ signatures in diagenetic cements in the Brae Formation reservoirs (*see section 5.4.3*) and these evolved formation waters could thus have an influence on the isotopic composition of the carbonate fracture cements. However, with fluid mixing assumed to be relatively limited in the model (≤30%), the impact of $\delta^{18}O$ from formational fluids on the isotopic signatures of the fracture cements is probably accommodated for in the variability of basinal fluid composition used in the model (e.g. 5.9a).

5.5.3. Rayleigh fractionation – CO_2 degassing-precipitation model

The solubility of carbonates in fluids increases with decreasing temperature, and decreases with decreasing pressure. As such, ascending solutions should become undersaturated with respect to carbonates upon cooling (Holland & Malinin, 1979). Therefore, theoretically carbonates cannot be precipitated from a relatively hot ascending fluid by simple cooling. Degassing of CO_2 from the host fluid is one mechanism facilitating carbonate precipitation, with CO_2 exsolution a common factor in the deposition of hydrothermal carbonates and associated sulphides in southeast Missouri, U.S.A. (Leach *et al.*, 1991).

With carbonate solubility dependent on fluid pressure, ascending fluids migrating in fault systems suffer a drop in fluid pressure, reducing CO_2 solubility in water, resulting

in degassing and subsequent carbonate mineral precipitation (Segnit *et al*., 1962). As such, Rayleigh fractionation models can be used to describe the variation in carbon isotopic compositions during both CO_2 degassing and subsequent carbonate precipitation from an aqueous fluid without the need to invoke fluid mixing. Zheng (1990) showed that using the relationship defined by Rayleigh (1902), the effect of CO_2 degassing on the isotopic signature of the vein calcite can be approximated to:

$$\delta^{f}_{fluid} = \delta^{i}_{fluid} + \ln (1 - X_{CO2}) \times 10^3 \ln \alpha_{CO2(g) - CO2 (aq)}$$

where *f* and *i* are the final and initial values with respect to degassing. X_{CO2} is the mol fraction of carbon remaining in the fluid after degassing and $\alpha_{CO2(g) - CO2 (aq)}$ is the isotopic fractionation factor between CO_2 and fluid. Similarly, the isotopic composition of carbonate precipitated from the fluid due to CO_2 degassing is defined by:

$$\delta^{f''}_{fluid} = \delta^{i''}_{fluid} + \ln (1 - 2X_{CO2}) \times 10^3 \ln \alpha_{carbonate - CO2 (aq)}$$

where f'' and i'' refer to the final and initial fluid values with respect to carbonate precipitation (i.e. after degassing) and $\alpha_{calcite - CO2 (aq)}$ is the isotopic fractionation factor between carbonate and $CO_{2(aq)}$. The model assumes the mol fraction of carbon lost from the fluid through carbonate precipitation is identical is to that released during CO_2 degassing. The isotopic composition of carbonate precipitated from fluid due to Rayleigh degassing – precipitation is represented by:

$$\delta_{carbonate} = \delta^{i}_{fluid} + \ln (1 - X_{CO2}) \times 10^3 \ln \alpha_{CO2(g) - CO2 (aq)}$$

$$+ (1 + \ln (1 - 2X_{CO2})) \times 10^3 \ln \alpha_{carbonate - CO2(aq)}$$

$\delta_{carbonate}$ = $\delta^{13}C$ ‰ of precipitated carbonate

δ^{i}_{fluid} = $\delta^{13}C$ ‰ of the initial fluid prior to CO_2 degassing/precipitation

X_{CO2} = mol fraction C in solution after degassing

The model only considers the carbon dissolved in the solution and its $\delta^{13}C$ signature, thus neglecting any fluid mixing with externally sourced fluids (i.e. section 5.5.2). The

effect of CO_2 degassing and carbonate precipitation on the oxygen isotope composition of the host fluid is negligible compared to that for carbon and is thus not accounted for.

Owing to the proposed rapid fluid ascent up the fault zone from the data in wells 16/07a-12 (South Brae) and 16/12a-16 (Pine), only the $\delta^{18}O$ vs. $\delta^{13}C$ trends from these wells are considered in this modelling approach. A Rayleigh fractionation model was developed to simulate an ascending HCO_3^--dominant fluid accommodating the isotopic evolution of the initial fluid due to continual degassing of CO_2 and precipitation of carbonate (Figure 5.10). Bicarbonate dominated fluids were selected due to the probable dissolution Zechstein carbonate sequences providing the source of the ascending fluid in the fault zone. Cooling of the hot fluid ascending the fault can be accommodated via conductive heat loss with the surrounding cooler country rock and formation waters whose temperature is controlled by the regional geothermal gradient at the time of fluid ascent (~70 Ma ≈ 80°C; see figure 4.5). However, the rate of cooling in the ascending fluid is not purely dependent on burial depth and vertical distance of fluid flow, with fault zone permeability an important factor governing the distribution and cooling rate of the basinal fluid in the fault zone. This will be explored further in chapter seven. As such, in the model shown here, fluid temperatures used are based on fluid inclusion homogenisation temperatures and $\delta^{18}O$ isotope signatures from the fracture cements and are not related to a specific burial depth.

The isotope curves are calculated assuming that the isotopic composition of carbon in the fluid progressively evolves due to removal of CO_2 through degassing and carbonate precipitation. The oxygen composition of the fluid remains unaltered from its initial value. Figure 5.10a illustrates that calculated models for CO_2 losses between 1 and 10 % provide an excellent correlation for the measured isotopic ratios of the dolomite cements for a fluid cooling from 200°C to 80°C. However, the model assumes a constant fraction of CO_2 (expressed as a percentage) is removed from the fluid at a given degassing-precipitation step. Assuming a finite amount of dissolved CO_2 per litre is ascending up the fault zone, the actual fraction of CO_2 removed through degassing and precipitation would gradually decrease given a specific percentage loss.

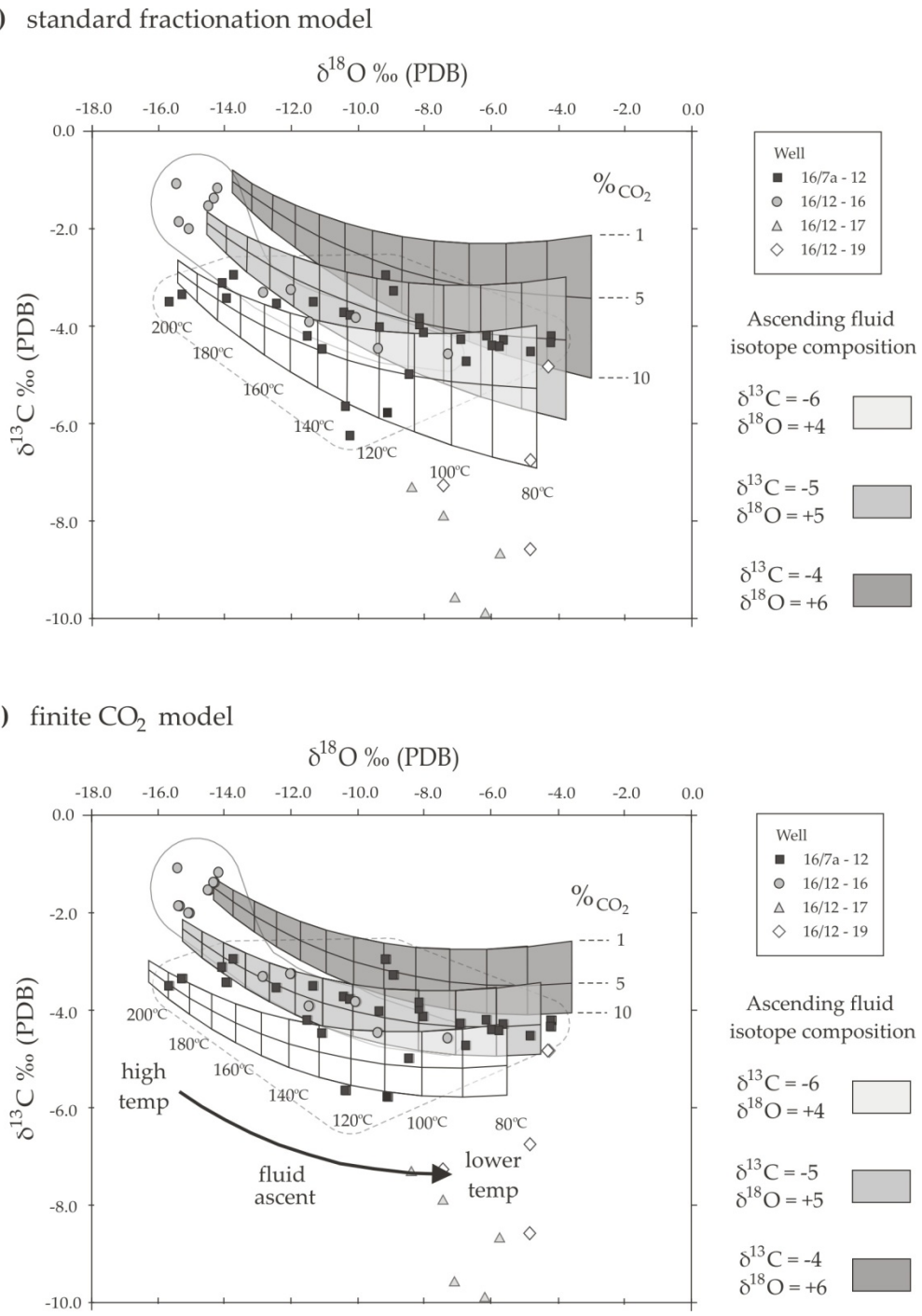

Figure 5.10. $\delta^{13}C$ vs. $\delta^{18}O$ plots of Rayleigh degassing-precipitation using (**a**) the standard molar fractionation approach, and (b) the finite CO_2 model. The model does not account for pressure fluctuations and the resultant effect of CO_2 solubility.

Accounting for this, Figure 5.10b highlights that Rayleigh degassing-precipitation fractionation from a finite quantity of CO_2 produces a decreased $\delta^{13}C$ shift for a given percentage CO_2 loss compared to the previous model (assuming the same isotopic composition of the host fluid). No suggestion as to the amount of CO_2 ascending the fault zone in solution is inferred. A relatively small amount of CO_2 loss (1 – 10%) is required to account for the isotopic co-variation witnessed in the dolomite fracture cements in both of the models assuming a degree of inherent natural variability (±1 ‰) in the $\delta^{18}O$ and $\delta^{13}C$ composition of the fluid and carbon source. The results of the model offer a possible explanation for the isotopic profile of the dolomites in wells 16/07a-12 and 16/12a-16 whilst providing a plausible precipitation mechanism through the degassing of CO_2 from an ascending basinal fluid.

Additionally, the $\delta^{13}C$ composition of the degassed CO_2 in the model is comparable to gases encountered in the Brae region. Figure 5.11 illustrates that the $\delta^{13}C$ signature of exsolved CO_2 from the model ranges between approximately -2 and -10 ‰ (PDB). The range of isotopic ratios is similar to those measured by James (1990) for the South Viking Graben. Moreover, CO_2 degassed at relatively high temperatures (200 – 140°C) exhibits heavier $\delta^{13}C$ ratios (-2 to -6 ‰) similar to those reported deeper in the graben close to the basin bounding fault (-3 to -5 ‰; James 1990) and speculated to be of inorganic origin (Thrasher & Fleet, 1995). It is thus plausible that during fluid ascent, early degassing from relative hotter basinal fluid could produce CO_2 gas with $\delta^{13}C$ compositions similar to those estimated from the model. This CO_2 could have subsequently accumulated in the deeper portions of the graben, maintaining the characteristic $\delta^{13}C$ signature of the CO_2 gas witnessed in these horizons today (James, 1990). On the other hand, CO_2 exsolved at lower temperatures exhibits more depleted carbon isotope profiles (-6 to -10 ‰). These values are comparable to $\delta^{13}C$ ratios present in CO_2 throughout the region, notably the Miller Field ($\delta^{13}C$ = 8.2 ‰). James (1990) attributed the depleted carbon isotope signature of these gases to the pervasive influence of organically derived CO_2 present in the region. However, Rayleigh fractionation highlights that similar isotopic profiles are achievable without the addition of external carbon sources.

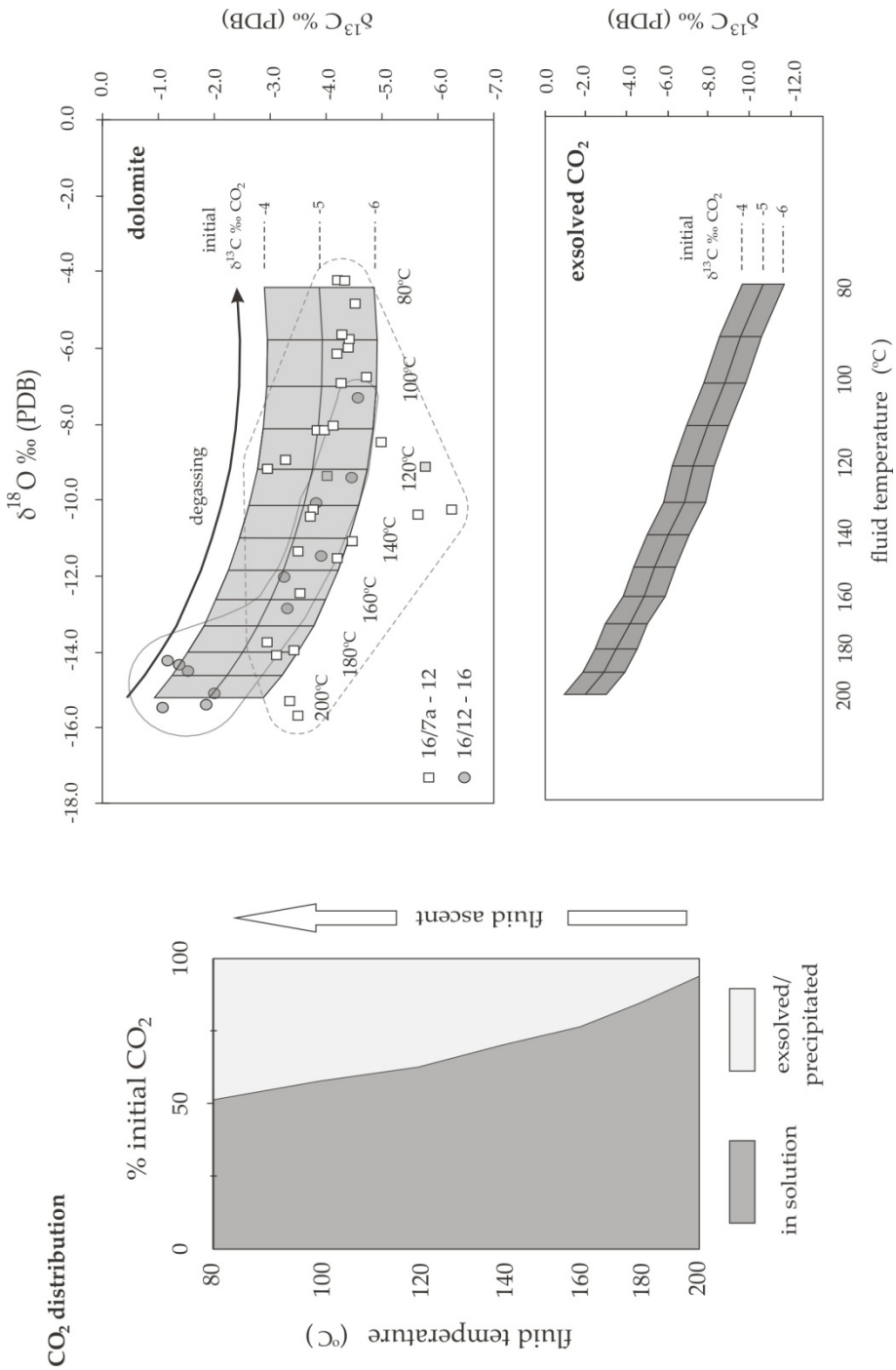

Figure 5.11. Finite CO_2 Rayleigh degassing-precipitation model illustrating the cumulative amount of CO_2 removed from the initial solution during ascent (left) and the resulting $\delta^{13}C$ composition of dolomite cements (centre), and exsolved CO_2 (right). 5 % CO_2 loss at each temperature iteration. Fluid composition, $\delta^{18}O$ = +5 ‰ SMOW; initial CO_2, $\delta^{13}C$ = -5±1 ‰ PDB.

5.4.4. Is fluid mixing or CO_2 degassing the most viable approach?

Both mixing and degassing modelling approaches provide a method accommodating the observed stable oxygen and carbon isotope trends witnessed in the data acquired. Rayleigh fractionation provides an eloquent explanation for the observed $\delta^{18}O$ vs. $\delta^{13}C$ trends witnessed in wells 16/07a-12 and 16/12a-16 assuming a high temperature basinal influx. Additionally, the model also provides a viable mechanism to account for the introduction of gaseous CO_2 into the region. This is affirmed by the $\delta^{13}C$ composition of the exsolved CO_2 which corresponds to the spatial variation witnessed in carbon isotope ratios of CO_2 gas recorded in the South Viking Graben (e.g. James, 1990).

As discussed, fluid mixing can also be invoked to account for the $\delta^{18}O$ vs. $\delta^{13}C$ co-variations, providing a method which can be used to describe the proposed contrasting precipitation scenarios between the two isotopic trends. Fluid mixing provides a feasible explanation for the incorporation of lighter carbon isotope signatures into otherwise inorganic $\delta^{13}C$ dominated fluids derived from depth, notably present in the cements from wells 16/12a-17 and 16/12a-19. Mixing fluids of differing source is also seen to be crucial in permitting the precipitation of the fracture cements, with formation fluids influenced by the diagenesis and thermal decarboxylation of the KCF the likely source of pyrite precipitation witnessed in late-stage fracture cements (e.g. Figure 3.12) in addition to the organic $\delta^{13}C$ signatures recorded in the cements.

Both isotope modelling approaches propose a method to account for the isotopic composition of the fracture cements. It is apparent that no exclusive process accounting for the $\delta^{18}O$ vs. $\delta^{13}C$ trends witnessed is viable. Both fluid mixing and CO_2 degassing processes would be most likely required to produce the observed mineralogy (i.e. sulphide precipitation) and accumulation of CO_2 gas in the region respectively. The potential impact of CO_2 degassing on fracture cementation will be tested by geochemical modelling (Ch. 7). To evaluate the extent of fluid mixing strontium isotope analysis ($^{87}Sr/^{86}Sr$) will be utilised to further assess the impact of KCF-influenced *in situ* formation waters on the precipitation of the fracture cements (Ch. 6).

5.5. Conclusions

- Two distinct $\delta^{13}C$ vs. $\delta^{18}O$ trends are observed from 65 samples taken of the fracture cement carbonates; a narrow $\delta^{13}C$ (-2 to -5 ‰), wide $\delta^{18}O$ (-4 to -15 ‰) trend, and a wide $\delta^{13}C$ (-5 to -17 ‰), narrow $\delta^{18}O$ (-4 to -8 ‰) distribution. The trends are restricted to wells; 16/07a-12 and 16/12a-16, and 16/12a-17 and 16/12a-19 respectively; suggesting the two pairings share similar precipitation regimes. No systematic variation in $\delta^{13}C$ vs. $\delta^{18}O$ is witnessed between the various fracture cement generations or with depth.

- Isotopically heavy $\delta^{13}C$ signatures from fracture cements in wells 16/07a-12 and 16/12a-16 reflect the presence of inorganic carbon sources in the precipitating fluid. These ratios are comparable to CO_2 recorded in the region (-3 to -8 ‰) which is assumed to have been introduced via the fault as postulated by numerous researchers (James, 1990; Wycherley *et al*., 1999). Conversely, more depleted $\delta^{13}C$ ratios of cements from wells 16/12a-17 and 16/12a-19 suggest the influence of an isotopically lighter organic carbon. The onset of thermal decarboxylation in Kimmeridge Clay Formation mudrocks provides a likely source for both isotopically light carbon and evolved $\delta^{18}O$ signatures resulting from burial diagenesis, with the migration of porewaters from the KCF to adjacent sandstones well documented.

- Using the $\delta^{18}O$ signature of the fracture cements and existing isotope analyses of diagenetic cements in the Brae-Miller region, a fluid evolution model was constructed. The introduction of a basinal fluid dominated by dissolved inorganic CO_2 from depth up the fault zone is used to account for the observed isotope trends (Figure 5.5). A high salinity influx ~70 – 80 Ma as reported by Larter *et al*. (1995) is incorporated, explaining both the high precipitation temperatures from fluid inclusion homogenisation temperatures (90 - 180°C) and evolved fluid (>+4 ‰ SMOW) calculated from the $\delta^{18}O$ ratios of the cements.

- The difference between the two isotope trends in the data is explained by variations in fluid mixing between the wells studied. Reduced flow rates culminating in enhanced mixing of the basinal fluid with *in situ* formation waters dominated by organically derived carbon are inferred to account for lower precipitation temperatures and depleted $\delta^{13}C$ isotopic signatures of cements (wells 16/12a-17 and 16/12a-19). With the postulated influx suggested as been responsible for the introduction of CO_2 into the region (Lu, 2008), the basinal influx model proposed (Figure 5.5) thus accommodates both the $\delta^{13}C$ and $\delta^{18}O$ ratios recorded in the fracture cements of wells 16/07a-12 and 16/12a-16.

- A Rayleigh fractionation model of an ascending overpressured CO_2-rich fluid provides an excellent match to the $\delta^{13}C$ vs. $\delta^{18}O$ co-variations witnessed in the speculated rapid fluid flux wells (16/07a-12 & 16/12a-16). $\delta^{13}C$ values of degassed CO_2 are comparable to those reported adjacent to the graben margin fault. Degassing provides an effective mechanism to overcome carbonate solubility constraints encountered in a cooling solution.

Table 5.2. Carbon and oxygen isotope ratios of dolomite and calcite fracture cements and sample type used from four wells investigated. The data for each individual well are displayed in Figure 5.1 and collectively in Figure 5.3 (● denotes samples from the heavily brecciated cemented horizons overlying the fault damage zone).

Well	Depth (TVDSS)		$\delta^{13}C$ ‰ (V-PDB)	$\delta^{18}O$ ‰ (V-PDB)	$\delta^{18}O$ ‰ (V-SMOW)	Mineral	Sample type
	ft	m					
16/7a - 12	13014	3966.7	-3.86	-8.16	22.49	dolomite	bulk ●
	13049	3977.3	-3.09	-14.08	16.39	dolomite	bulk ●
	13079	3986.5	-4.46	-11.08	19.48	dolomite	bulk ●
	13090	3989.8	-3.27	-8.94	21.69	dolomite	bulk ●
	13137	4004.2	-2.94	-13.75	16.74	dolomite	bulk ●
	13170	4014.2	-5.63	-10.39	20.20	dolomite	bulk
	13171	4014.5	-2.95	-9.17	21.45	dolomite	bulk
	13173	4015.1	-5.76	-9.13	21.50	calcite	bulk
	13177	4016.3	-4.36	-5.95	24.78	dolomite	bulk
	13177	4016.3	-4.27	-4.24	26.54	dolomite	zone B
	13177	4016.3	-4.31	-4.28	26.50	dolomite	zone B
	13177	4016.3	-3.71	-10.44	20.14	dolomite	zone C
	13177	4016.3	-4.22	-4.26	26.52	dolomite	zone D
	13177	4016.3	-4.51	-4.84	25.92	dolomite	zone B
	13177	4016.3	-3.76	-10.26	20.34	dolomite	zone C
	13177	4016.3	-4.27	-5.65	25.08	dolomite	zone B
	13177	4016.3	-4.39	-6.00	24.73	dolomite	zone C
	13177	4016.3	-3.42	-13.96	16.52	dolomite	zone C
	13177	4016.3	-3.49	-11.36	19.20	dolomite	zone E
	13177	4016.3	-3.53	-12.46	18.07	dolomite	zone E
	13177	4016.3	-4.40	-5.75	24.98	dolomite	zone B
	13177	4016.3	-4.19	-11.54	19.02	dolomite	zone B
	13177	4016.3	-4.04	-8.03	22.63	dolomite	zone B
	13177	4016.3	-4.01	-9.37	21.25	dolomite	zone D
	13185	4018.8	-4.71	-6.77	23.93	dolomite	bulk
	13185	4018.8	-3.93	-8.19	22.47	dolomite	bulk
	13198	4022.8	-6.23	-10.26	20.34	dolomite	bulk
	13201	4023.7	-4.26	-6.93	23.76	dolomite	bulk
	13201	4023.7	-4.24	-6.16	24.56	dolomite	bulk
	13204	4024.6	-3.49	-15.68	14.75	dolomite	bulk
	13204	4024.6	-4.91	-8.38	22.27	dolomite	bulk
	13204	4024.6	-3.35	-15.28	15.16	dolomite	bulk

16/12a - 16	13806	4208.1	-1.54	-14.49	15.98	dolomite	bulk
	13868	4227.0	-1.08	-15.45	14.99	dolomite	bulk
	13880	4230.6	-3.81	-10.18	20.42	dolomite	bulk
	13881	4230.9	-4.57	-7.29	23.40	dolomite	bulk
	13881	4230.9	-3.21	-12.02	18.52	dolomite	bulk
	13934	4247.1	-3.31	-12.84	17.68	dolomite	bulk
	13946	4250.7	-1.86	-15.39	15.05	dolomite	bulk
	13982	4261.7	-1.34	-14.26	16.21	dolomite	bulk
	14002	4267.8	-2.01	-15.07	15.37	dolomite	bulk
	14074	4289.8	-3.92	-11.45	19.10	dolomite	bulk
	14099	4297.4	-4.46	-9.39	21.23	dolomite	bulk
	14166	4317.8	-1.17	-14.21	16.26	dolomite	bulk
16/12a - 17	13332	4063.6	-10.82	-7.68	22.99	dolomite	bulk
	13364	4073.3	-12.47	-7.18	23.51	calcite	bulk
	13370	4075.2	-8.72	-5.74	24.50	dolomite	bulk
	13370	4075.2	-9.90	-6.21	24.51	dolomite	bulk
	13380	4078.2	-13.03	-5.98	24.75	dolomite	bulk
	13397	4083.4	-11.55	-6.14	24.58	calcite	bulk
	13397	4083.4	-12.79	-7.42	23.26	calcite	bulk
	13400	4084.3	-15.10	-6.74	23.96	calcite	bulk
	13414	4088.6	-13.38	-6.85	23.85	calcite	bulk
	13513	4118.8	-10.09	-7.29	23.39	calcite	bulk
	13532	4124.6	-7.33	-8.25	22.40	dolomite	bulk
	13545	4128.5	-9.57	-7.15	23.54	calcite	bulk
	13547	4129.1	-7.90	-7.50	23.18	calcite	bulk
16/12a - 19	13455	4101.1	-4.85	-4.51	26.26	calcite	bulk
	13457	4101.7	-7.28	-7.45	23.23	calcite	bulk
	13457	4101.7	-8.77	-6.39	24.52	calcite	bulk
	13461	4102.9	-11.07	-5.98	24.75	calcite	bulk
	13461	4102.9	-8.68	-4.81	25.95	calcite	bulk
	13474	4106.9	-12.11	-5.46	25.28	calcite	bulk
	13493	4112.7	-6.77	-4.82	25.94	calcite	bulk
	13512	4118.5	-17.86	-6.35	24.36	calcite	bulk

Chapter 6

$^{87}Sr/^{86}Sr$ isotope analysis

6.1. Introduction

The use of strontium isotope ratios ($^{87}Sr/^{86}Sr$) can be used to elucidate the source and evolution of formation waters in diagenetic systems and their cements. Unlike stable $\delta^{13}O$ and $\delta^{18}O$ isotopes, $^{87}Sr/^{86}Sr$ ratios are unaffected by kinetic, equilibrium, or temperature dependent fractionations during carbonate precipitation (Veizer, 1983). In studies like this one where constraining of precipitation temperature can prove problematic, Sr ratios can thus be used as an important tracer for fluid genesis, with the isotopic composition of Sr in carbonate cements providing a record of the pore-water chemistry from which they precipitated (Faure, 1986).

Fluctuations in $^{87}Sr/^{86}Sr$ are caused by the relative fluxes of strontium sources exhibiting dissimilar Sr isotopic compositions. The $^{87}Sr/^{86}Sr$ ratio of seawater has evolved over time owing to the relative input of high Sr ratios from continental weathering of silicates (e.g. feldspars) and lower radiogenic strontium from hydrothermal circulation (e.g. Burke *et*

al., 1982). Strontium ratios of seawater from the Late Carboniferous to the present-day range between ~0.706 to ~0.709 (Burke *et al*., 1982; Veizer *et al*., 1999). Identification of the origin of interstitial water can prove invaluable for establishing the source and evolution of fluids in diagenetic environments. In the diagenetic realm, reactions with silicate minerals exhibiting high Sr ratios (average 0.720 (Faure, 1986)) result in many formation waters and cements invariably exhibiting $^{87}Sr/^{86}Sr$ ratios appreciably higher than any seawater observed through time. Numerous investigations of North Sea hydrocarbon reservoirs have employed $^{87}Sr/^{86}Sr$ analysis to evaluate the extent and timing of diagenetic reactions involving detrital silicates on subsequent carbonate cements owing to their characteristic $^{87}Sr/^{86}Sr$ signatures (e.g. McLaughlin *et al*., 1994; Girard *et al*., 2002).

This chapter presents results of $^{87}Sr/^{86}Sr$ analysis undertaken on the carbonate fracture cements from the four wells studied. The results are discussed with respect to the possible origin of the precipitating fluid and the compatibility with a proposed Zechstein source and the influence of *in situ* diagenetically evolved formation waters.

6.2. Methodology

6.2.1. Sampling

Carbonate fracture cements were identified and sampled as described in chapter five, with powdered samples collected by methods illustrated previously in section 5.2.1. Where possible, discrete cement generations were sampled with considerable care to avoid contamination with wallrock material which could contain relatively radiogenic Sr within clay minerals present in the sandstone. In total 12 samples were analysed for $^{87}Sr/^{86}Sr$ from the four wells studied, with $\delta^{13}O$ and $\delta^{18}O$ isotope ratios also determined from the samples (*see chapter 5*).

6.2.2. Chemistry

Powdered samples were weighed and placed in Teflon beakers. Any residual clay with potential contaminant Sr was then removed from the samples by adding 1 ml of 1 molar ammonium acetate (CH_3COONH_4) and allowed to stand for 2 hours. The liquid and

samples were then centrifuged and the liquid and any dispersed non-carbonate material carefully pipetted-off, preserving the test material. The remaining carbonate powders were then rinsed twice with 1 ml Milli-Q water to remove any residual ammonium acetate and dried. The dried samples were then each digested in 1 ml of 8 molar HNO_3 and left to stand for at least 2 hours to ensure complete dissolution. Strontium was then extracted using a Sr specific resin using the following method, a modification of the method described in Henderson *et al*. (1994). The resin was initially pipetted into cation exchange columns and cleaned with 0.01 molar HNO_3 to remove any Sr residue prior to conditioning with 1ml of 8 molar HNO_3. The dissolved samples were then loaded into the columns and each eluted with 1ml 8 molar HNO_3 to ensure all the sample was washed into the resin.

The removal of Ca and Ba was achieved by eluting a further 5 ml of 8 molar HNO_3 into the sample. This was followed by the addition of 10ml of 3 molar HNO_3 to ensure that all Ca was flushed from the sample. The Sr that had adhered to the resin was then extracted from the columns by eluting 5ml 0.01 HNO_3 and collected in Teflon beakers. The samples were then dried on a hot plate. The Sr samples were subsequently loaded onto single Ta filaments with 1 N of phosphoric acid and analysed on a VG Sector 54–30 multiple collector mass spectrometer. Accuracy is better than ±0.2 ‰ at 1σ, using the standard NIST SRM987. All analyses were undertaken at SUERC, East Kilbride.

6.3. Results

Table 6.1 shows the $^{87}Sr/^{86}Sr$ composition of the 12 carbonate cement samples analysed with their accompanying $\delta^{13}O$ and $\delta^{18}O$ ratios. The data shows the $^{87}Sr/^{86}Sr$ ratios between the four studied wells range between 0.7109 and 0.7133, with an average of 0.7116. The $^{87}Sr/^{86}Sr$ ratios across the wells is relatively uniform (Figure 6.1a), with one analysis from well 16/12a-17 exhibiting a notably higher Sr ratio (0.7133). The uniformity is also reflected in the type of carbonate mineralogy, with no apparent variation in $^{87}Sr/^{86}Sr$ between sampled calcite and dolomite fracture cements. In addition, no systematic variation in $^{87}Sr/^{86}Sr$ is observed between the fracture cement generation(s)

analysed (Figure 6.1b), with samples from single cement zones typically exhibiting Sr ratios similar to those from multiple generations.

Well	Depth (TVDSS) (ft)	Depth (TVDSS) (m)	$^{87}Sr/^{86}Sr$	$\delta^{13}C$ ‰ (‰ V-PDB)	$\delta^{18}O$ ‰ (‰ V-PDB)	Mineralogy
16/07a-12	13137	4004.2	0.71093	-2.94	-13.75	dolomite
	13177	4016.3	0.71139	-4.40	-5.75	dolomite
16/12a-19	13457	4101.7	0.71188	-7.28	-7.45	calcite
	13474	4106.9	0.71178	-12.11	-5.46	calcite
16/12a-17	13400	4084.3	0.71163	-15.10	-6.74	calcite
	13414	4088.6	0.71150	-13.38	-6.85	calcite
	13545	4128.5	0.71157	-9.57	-7.15	calcite
16/12a-16	13806	4208.1	0.71329	-1.54	-14.49	dolomite
	13868	4227.0	0.71109	-1.08	-15.45	dolomite
	13946	4250.7	0.71094	-1.86	-15.39	dolomite
	14099	4297.4	0.71198	-4.46	-9.39	dolomite
	14166	4317.8	0.71113	-1.17	-14.21	dolomite

Table 6.1. $^{87}Sr/^{86}Sr$ ratios and stable isotope compositions ($\delta^{13}O$ and $\delta^{18}O$) of carbonate fracture cements.

6.4. Discussion

6.4.1. Origin of $^{87}Sr/^{86}Sr$ ratios recorded in the fracture cements

The results show that the analysed fracture cement samples exhibit Sr ratios significantly higher than any Phanerozoic seawater (Figure 6.1a). The highest Sr ratios are observed in the present day, rising from 0.7076 to 0.7090 from the Mid-Tertiary (Burke *et al.*, 1982). Mesozoic $^{87}Sr/^{86}Sr$ values are ~0.707, with relatively minor fluctuations (Veizer *et al.*, 1999). All formation waters show more radiogenic Sr isotope ratios than contemporaneous seawater, suggesting the evolution of fluids throughout burial (Egeberg & Aagaard, 1989). Increases in $^{87}Sr/^{86}Sr$ are accounted for by incorporation of radiogenic Sr from detrital silicate minerals (e.g. muscovite = 0.790 (Hamilton *et al.*, 1987)) or pre- and post-dating carbonate sources through fluid-mineral interaction during diagenesis.

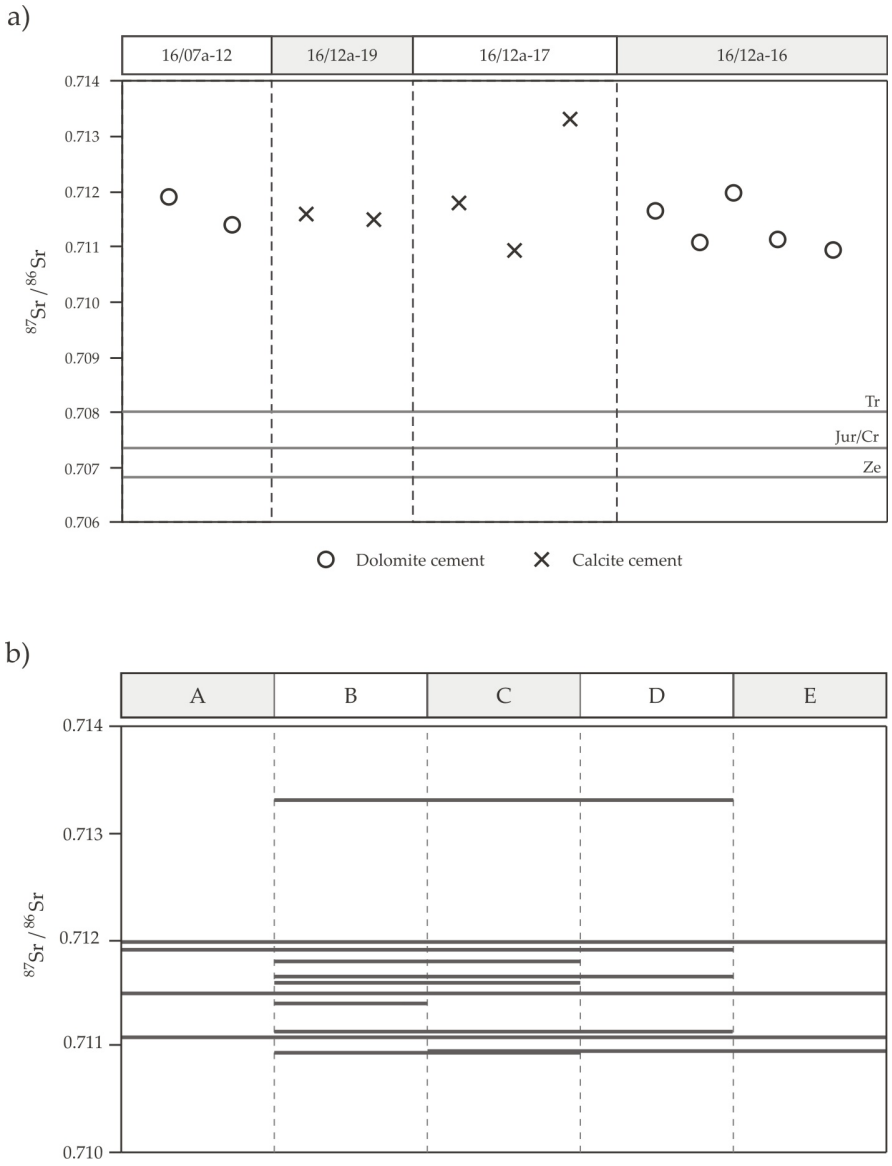

Figure 6.1. a) $^{87}Sr/^{86}Sr$ ratios of sampled carbonate cements from the four wells studied showing minimal variation between the wells and between dolomite and calcite. Data is compared to typical seawater values in the Triassic (Tr), Zechstein (Ze), Jurassic (Jur), and Cretaceous (Cr) (Burke *et al*., 1982; Veizer *et al*., 1999; Korte *et al*., 2006). **b)** $^{87}Sr/^{86}Sr$ ratios of samples showing cement generations present in each sample (A – E) owing to sample limitations due to required yield for analysis. Note minimal variation irrespective of number of generations sampled, suggesting relatively uniform fluid composition.

The relative uniformity between the Sr ratio of the samples between the cement generations suggests the cements precipitated from roughly similar composition waters with respect to Sr. This implies the formation fluid from which the cements precipitated may not have altered appreciably with respect to Sr in the period during which the cements precipitated. It is thus possible that the precipitating fluid was derived predominantly from a single discrete source.

6.4.2. $^{87}Sr/^{86}Sr$ evolution of Brae Field formation waters

The present day $^{87}Sr/^{86}Sr$ composition of formation water in South Brae is significantly higher than values determined from the fracture cements at 0.7247 (Hardy & Hart, 1994). Such elevated Sr ratios can be explained by the greater incorporation of radiogenic strontium into the formation water through time due to greater mineral interaction (e.g. albitization of plagioclase); a phenomenon witnessed in most present-day North Sea formation waters (e.g. Egeberg & Aagaard, 1989). Late stage dissolution of earlier calcite cements and feldspathic minerals creating extensive secondary porosity is readily observed in the Brae Formation sandstones of South Brae (Greenwood *et al*., 1994). Elevated dissolved CO_2 in the porewaters has been ascribed as a potential driver for the observed feldspar dissolution and subsequent late-stage calcite precipitation (Baines & Worden, 2004). However, no definitive source of the CO_2 in these studies is determined, with decarboxylation of adjacent organic units and influx of inorganic CO_2 both possible catalysts.

All late stage calcite cements reported by McLaughlin *et al*. (1994) exhibit $^{87}Sr/^{86}Sr$ compositions higher than 0.720 (Figure 6.2). Data from mixed early and late diagenetic cements is also reported, but typically show Sr ratios below 0.720 owing to probable sample homogenisation with earlier, relatively lower $^{87}Sr/^{86}Sr$ cements. A similar progressive radiogenic Sr enrichment trend is also observed in carbonate concretions in the study. Fracture cements in this study exhibit Sr ratios similar to early carbonate cements observed in the Brae Formation. McLaughlin *et al*. (1994) attributed the $^{87}Sr/^{86}Sr$ signatures of early calcite cements to meteoric flushing, with the dissolution of detrital silicates and bioclastic marine debris resulting in cements exhibiting higher Sr ratios

than the initial Jurassic seawater owing to the formation water becoming progressively evolved due to prolonged mineral interaction.

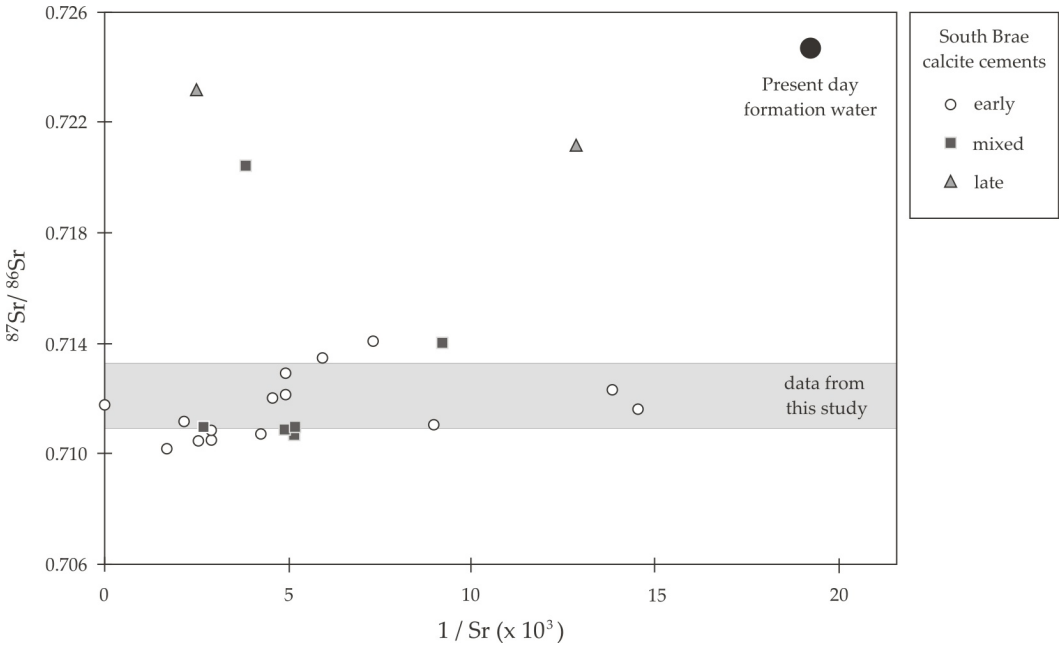

Figure 6.2. Plot of $^{87}Sr/^{86}Sr$ from the fracture cements compared with calcite cements from South Brae (data from McLaughlin *et al*., 1994) showing Sr ratios from the fractures similar to early diagenetic cements from the Brae Formation. However, petrographic and stable isotopic evidence suggests the two cement types did not precipitate from the same fluid *per se* (see text for details). Late authigenic cements exhibit Sr ratios comparable to present day formation water $^{87}Sr/^{86}Sr$ ratios representative of radiogenic strontium input from silicate dissolution (Hardy & Hart, 1994). No Sr concentration data is available for the fracture cements, hence only the range of $^{87}Sr/^{86}Sr$ data is represented.

Although a degree of ambiguity exists as to the absolute timing and source of the fluids responsible for the precipitation of the fracture cements with respect to their $^{87}Sr/^{86}Sr$ signature, it suggests the appreciable enrichment of Sr in the Brae Formation porewaters post-dated the precipitation of the fracture cements. However, the extent of influence exerted by the fluids present in the fault zone on the subsequent composition of the in situ formation water is largely unknown given the number of possible drivers for late-

stage diagenesis which could control the porewater chemistry and Sr content (e.g. burial diagenesis, hydrocarbon maturation).

6.4.3. Strontium sources and fluid mixing

The $^{87}Sr/^{86}Sr$ ratio of the cements can potentially provide an insight into the evolution of interstitial fluids circulating in the fault zone and into adjacent high permeability regions with respect to two aforementioned fluid origin possibilities; locally sourced and derived from depth. A local source for elevated Sr ratios has been identified as resulting from early diagenetic silicate dissolution possibly controlled by meteoric influx. The similarity in Sr ratios exhibited by the carbonate fracture cements and early South Brae calcite cements suggests they may share a common fluid source prior to the appreciable radiogenic Sr input observed in later diagenetic calcite cements and present-day formation water is testament to this (Figure 6.3a). However, as discussed previously, the fracture cements present in the faulted cored sections do not seemingly represent products of meteoric influenced early diagenesis due to hydraulic fracturing textures which attest to overpressure release from a closed system.

Additionally, the extent of meteoric flushing in the Brae trend fields has been questioned by Burley (1993), who argued that the rapid rate of subsidence during the deposition of the reservoirs was sufficient to inhibit meteoric influence on early diagenetic precipitation. This view is shared by Girard *et al*. (2002) who suggested diagenetic reactions in the Hild Brent sandstones proximal to the Viking Graben were related to the influence of higher temperature basinal brines and not a meteoric water influx. Although relatively early precipitation from meteoric influenced Late Jurassic formation waters cannot be unequivocally discounted owing to the $^{87}Sr/^{86}Sr$ signatures of the cements, fluid mixing can also be inferred, accommodating later precipitation from more evolved basinal fluids.

Subsurface fluid flow may cause waters of differing composition to become mixed on a range of scales, causing variation in the Sr isotopic ratio (Mearns & McBride, 1999). Migration of formation waters from depth can be facilitated by a number of

mechanisms: sediment compaction, fluid overpressure, thermal gradients, fluid density contrasts. A number of these methods have previously been considered regarding the formation and propagation of the fault zone fractures and the subsequent cementation witnessed (*see section3.4.1*). Therefore, the influence exerted by deep sourced basinal fluids on the Sr signature of the fracture cements needs to be considered. Formation waters in deeply buried clastic sequences typically exhibit high $^{87}Sr/^{86}Sr$ ratios owing to appreciable radiogenic Sr input during numerous phases of burial diagenesis.

Smalley *et al*. (1992) argued that depth increases in $^{87}Sr/^{86}Sr$ and salinity in the Ekofisk Field were testament that the two components were related; suggesting that higher Sr ratio fluids were derived from evaporitic sequences underlying the field. However, dissolution of Zechstein sequences in a closed system (i.e. overpressured cell) would not necessarily produce fluids with markedly different $^{87}Sr/^{86}Sr$ ratios to the original seawater upon deposition (~0.707) given the evaporitic nature of the sediments in which a large continental influx of radiogenic Sr is very unlikely (Korte *et al*., 2006). Numerous authors have reported the migration of brines over considerable distances in the subsurface. Thus it seems reasonable to assume brines in the North Sea may have migrated in response to overpressure release from deep within the Viking Graben into the fault blocks and to the flank (Egeberg & Aagaard, 1989). However, if the Zechstein did provide the source of the fluids from which the fracture cements precipitated, the higher $^{87}Sr/^{86}Sr$ ratio of the cements suggests the basinal waters were modified, possibly through interaction with radiogenic Sr-rich siliciclastic lithologies during basinal flux ~70 Ma (e.g. Winter *et al*., 1995), or through mixing with more evolved formation waters prior to carbonate precipitation (Figure 6.3b). The potential dissolution of evaporitic sequences through the subsurface circulation of relatively radiogenic Sr-enriched meteoric waters must also be acknowledged.

Marine limestones and anhydrites typically have high Sr concentrations (>500 ppm) and ratios that reflect contemporaneous seawater. Conversely clay and feldspathic minerals exhibit high Sr ratios but low concentrations (<100 ppm) (Faure, 1986), with $^{87}Sr/^{86}Sr$ data that defines a positive slope in Sr ratio and 1/Sr are indicative of brines interacting with

siliciclastic lithologies. Using EMPA, no or negligible Sr was reported in the carbonate fracture cements using this analysis, possibly suggesting Sr concentrations within the fracture cements were in the magnitude of the detection limit (~250 ppm) and thus their $^{87}Sr/^{86}Sr$ signature was predominantly influenced by radiogenic Sr derived from silicate interaction (see Appendix I.b). Such values are typical for the majority of formation waters in the Central and Northern North Sea (0 – 500 ppm) where predominantly evaporitic formation waters are largely absent.

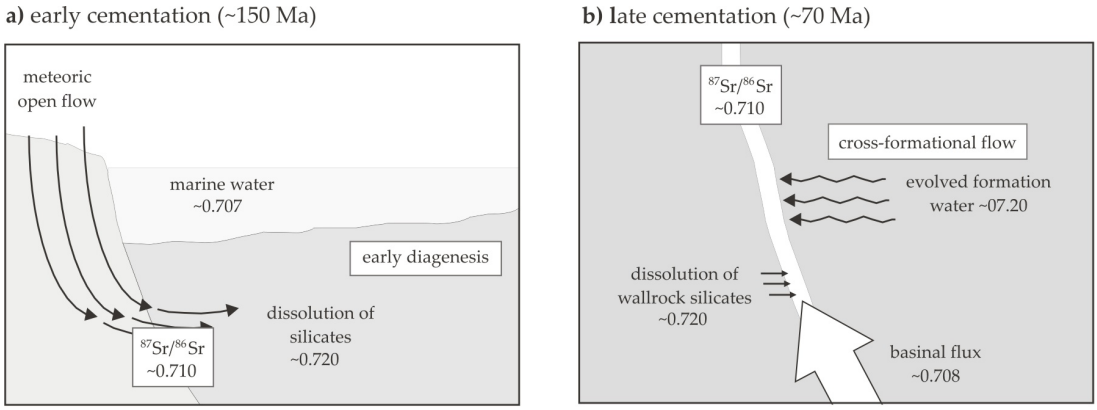

Figure 6.3. Schematic diagram showing the possible origin of $^{87}Sr/^{86}Sr$ ratios measured in the fracture cements of the fault zone. **a)** early meteoric influx promotes dissolution of silicates, leading to radiogenic Sr enrichment of the resident formation water and reflected in early cemented fractures. **b)** later influx of predominantly evaporitic basinal fluid from depth interacting with wallrock minerals upon ascent and mixing with evolved KCF and Brae Fm. waters. Due to the inherent variability in the $^{87}Sr/^{86}Sr$ ratio of both hypothetical fluids, the extent of mixing between them is not quantified. No scale implied.

The problem arising from either of the two models proposed above is the apparent discrepancy between the age of precipitation and $^{87}Sr/^{86}Sr$ ratio of formation water in that time interval. For example, the measured Sr ratios and concentrations of the fracture cements allude to Late Jurassic precipitation from diagenetically influenced formation waters. This is in direct conflict with the previously discussed hydrodynamic constraints which suggest later episodic fracturing. It is not usually possible to identify the source of radiogenic Sr in subsurface fluids (e.g. McNutt *et al*., 1987); therefore the

$^{87}Sr/^{86}Sr$ ratio of the cements must be evaluated with respect to other isotopic parameters to assess the applicability of the two possible fluid source scenarios outlined above.

6.4.4. Evaluation of $^{87}Sr/^{86}Sr$ with respect to $\delta^{13}C$ and $\delta^{18}O$ stable isotopes

As discussed in the previous chapter, stable $\delta^{13}C$ and $\delta^{18}O$ isotopic signatures of carbonate cements can be used to facilitate the identification of carbon sources and elucidate fluid evolution histories in sedimentary basins. Comparing stable isotope measurements with $^{87}Sr/^{86}Sr$ analysis allows further inferences to be made regarding the extent of diagenetic reactions on the chemistry of formation waters from which the cements precipitated. Mixing of subsurface waters can cause variation in the Sr isotopic ratio with respect to other factors in an open system. For example, Sullivan *et al*. (1990) observed coupling between Sr and $\delta^{13}C$ isotopic ratios in the Rotliegend sandstones of the Southern North Sea; a trend attributed to cross-formational flow and subsequent mixing of *in situ* marine porewater with evolved, diagenetically-influenced, formation water. There is no such linear correlation observed between $^{87}Sr/^{86}Sr$ and $\delta^{13}C$ isotopic compositions within the authigenic calcite cements studied by McLaughlin *et al*. (1994) in South Brae, suggesting the sources of carbon and strontium are mutually exclusive and not linked to the mixing of fluids of differing provenance.

A slight correlation can possibly be inferred between $^{87}Sr/^{86}Sr$ and $\delta^{13}C$ from the fracture cements in this study, with isotopically heavier carbon (0 to -5 ‰) samples typically exhibiting relatively lower Sr ratios (~0.711). Conversely, lighter $\delta^{13}C$ carbonates cements exhibit more radiogenic Sr signatures (>0.715) (Figure 6.4a). However, owing to the absence of a comprehensive dataset any inferences regarding possible mixing of fluid sources must be made with extreme caution. A more noticeable variation is witnessed between $^{87}Sr/^{86}Sr$ and $\delta^{18}O$, with two distinct groupings observed; low Sr – "light" $\delta^{18}O$ and higher Sr – "heavy" $\delta^{18}O$ (Figure 6.4b). The less radiogenic $^{87}Sr/^{86}Sr$ grouping (~0.711) is associated with samples taken from wells 16/07a-12 and 16.12a-16 which exhibit depleted $\delta^{18}O$ values. As discussed in the previous chapter, the oxygen isotope signatures from these wells were speculated to be the consequence of precipitation from higher temperature evolved basinal fluids (>+4 ‰ $\delta^{18}O$ SMOW) with

limited homogenisation with the in situ porewaters. As a result, the relatively lower Sr ratios measured in these samples could also be attributed to limited mixing with the resident more radiogenic formation water.

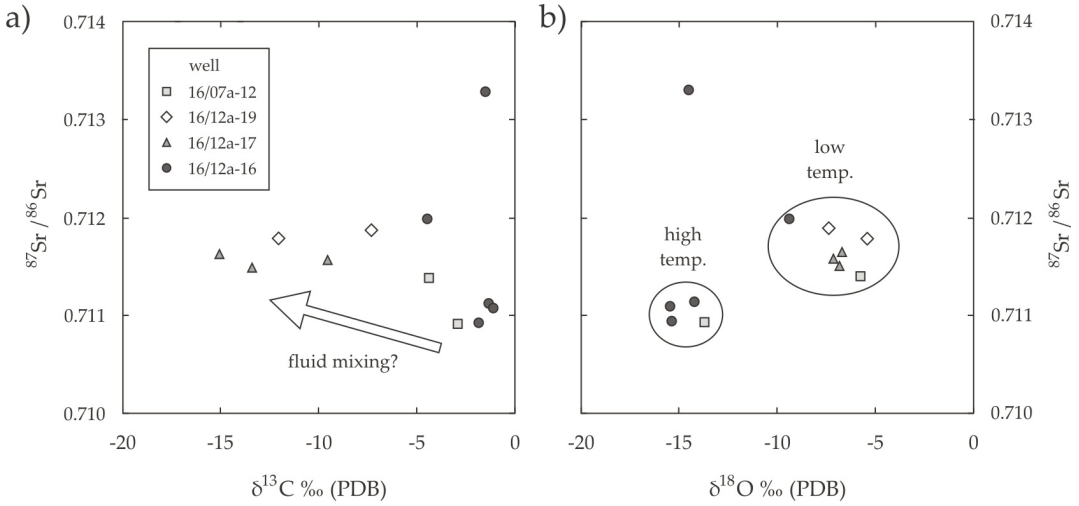

Figure 6.4. Plots of $^{87}Sr/^{86}Sr$ vs. corresponding stable carbon and oxygen isotope ratios. **a)** relatively depleted $\delta^{13}C$ ratios from carbonate fracture cements (notably in wells 16/12a-17 and 16/12a-19) typically exhibit more radiogenic $^{87}Sr/^{86}Sr$ signatures. **b)** $\delta^{18}O$ vs. $^{87}Sr/^{86}Sr$ illustrates two groupings; a more radiogenic, ^{18}O enriched group and a ^{18}O depleted group exhibiting lower $^{87}Sr/^{86}Sr$ ratios. These two isotopic trends can be explained by variable fluid mixing of resident formation water with a relatively hotter ascending basinal fluid (see text for details).

Conversely, the more radiogenic Sr signatures are predominantly present in cements from wells 16/12a-17 and 16/12a-19. These cements exhibit more enriched $\delta^{18}O$ signatures (-10 to -5 ‰) and depleted $\delta^{13}C$ ratios. The higher $^{87}Sr/^{86}Sr$ ratio measured in these cements could be linked to fluid mixing with resident formation waters enriched with radiogenic Sr due to diagenetic reactions in both the Brae Formation and the Kimmeridge Clay Formation (*see section 6.4.2*). Enhanced mixing between fluids in the fault zone and the *in situ* formation waters was also inferred to account for the lower precipitation temperatures (70 - 90°C) from meteoric influenced porewaters and incorporation of depleted $\delta^{13}C$ in the carbonate cement isotope signatures. Although this fluid mixing model can also be applied to account for the variation between $^{87}Sr/^{86}Sr$

signatures between the two well groupings, the absolute difference in $^{87}Sr/^{86}Sr$ ratio (~0.001) is arguably not significant enough to prove or disprove such a hypothesis.

However, irrespective of the variation in Sr isotopic composition with respect to $\delta^{13}C$ and $\delta^{18}O$ signatures in the fracture cements, the apparent radiogenic Sr signature of the fracture cement carbonate attests to probable fluid mixing between a low $^{87}Sr/^{86}Sr$ basinal source and a more radiogenic fluid. Fluids derived during the diagenesis of the Kimmeridge Clay Formation have been attributed as the probable source for the increased iron content and corrosion textures witnessed in the late-stage fracture cements (*section 3.4.3*). Additionally, organic carbon isotope signatures recorded in the cements are also probably the product of early thermal maturation of the KCF (*section 5.4.1*). Extensive silicate dissolution, notably K-feldspar, following the onset of thermal maturation has been widely documented in the KCF and adjacent Brae Formation sequences (McLaughlin *et al*., 1994; Lu, 2008). Therefore, it is plausible that the $^{87}Sr/^{86}Sr$ ratio (0.711 – 0.713) of the fracture cements can be attributed to mixing between evolved radiogenic KCF-influenced formation waters and a high salinity Zechstein derived basinal brine.

6.5. Conclusions

- All the samples analysed from the fracture cements exhibit $^{87}Sr/^{86}Sr$ ratios indicative of evolved formation waters (>0.710). The uniformity of Sr ratios possibly suggests a discrete source or appreciable homogenisation of the precipitating fluid.

- The $^{87}Sr/^{86}Sr$ ratios are similar to those in calcite cements reported to have precipitated in the Brae Formation during early diagenesis following meteoric charge. Potential precipitation of the fracture cements in such an environment seemingly contradicts the overpressured basinal fluid origin inferred from petrographic and stable isotope analysis. Comparing Sr with $\delta^{13}C$ and $\delta^{18}O$ isotopic signatures across the wells to potentially define a less radiogenic basinal source proved inconclusive.

- Although Zechstein Fm. derived fluids are believed to provide the principal source for the fracture cements, the $^{87}Sr/^{86}Sr$ ratio of the sampled cements cannot be confidently used to elucidate a discrete Sr source due to a plethora of potential Sr sources in the subsurface. The Sr signature reflected in the cements is probably dependent on the extent of fluid circulation and mixing in the fault zone (e.g. Baumann & Hofmann, 1988); a factor not readily quantifiable with respect to Sr isotopes given their sensitivity to additional radiogenic Sr input (e.g. products of silicate diagenesis).

- Elevated radiogenic signatures in the fracture cements relative to those derived purely from a Zechstein source suggest that a degree of fluid mixing between proposed a basinal flux and resident formation waters will have occurred prior to carbonate cementation.

Chapter 7

Modelling CO_2-rich fluid flux

7.1. Introduction

The application of geochemical modelling to understand the behaviour of CO_2 in the subsurface is a relatively new technique principally utilised to aid in understanding the long-term effects of CO_2 storage upon geological formations (e.g. Gaus *et al*., 2005; Kaszuba *et al*., 2005). However, a number of previous studies have employed similar techniques to simulate the behaviour of CO_2 in a dynamic system, modelling the amount of CO_2 removed from solution due to decompression (Becker *et al*., 2008), and through the precipitation of carbonate minerals (May, 2005), as a consequence of fluid flux to the surface in faulted terranes.

Carbon dioxide present in subsurface waters evolves through a number of stages prior to release on The Earth's surface: 1) initial release of CO_2 (e.g. thermal degradation of

carbonates or decarboxylation of organic matter), 2) dissolution of gaseous CO_2 into formation water, forming carbonic acid (H_2CO_3), and 3) degassing of CO_2 from solution during ascent to the surface due to decompression. Based on the proposition of a flux of CO_2-rich fluid up the basin bounding fault accounting for the high CO_2 levels observed in the Brae Fields, such a modelling process can provide a mechanism for the observed carbonate fracture cements and anomalously high CO_2 levels present in the reservoirs.

In this chapter a geochemical evolution model of CO_2-rich solutions ascending up the basin bounding fault is developed based on data and conclusions in the previous chapters and published studies . Geochemical modelling is used to estimate the fraction of CO_2 that is 1) exsolved from solution, 2) maintained in solution, and 3) incorporated into carbonate minerals during fluid ascent from relatively high P-T conditions present at source to increasingly low P-T environments up the fault and in the reservoirs. The model is calibrated for a number of parameters (e.g. pressure, temperature, fluid flow rate, fluid-rock interaction, etc.) related to the nature of the ascending fluid. By varying such parameters, the behaviour of dissolved CO_2 and resultant geochemical and mineralogical reactions in a host of hydrodynamic simulations is evaluated.

7.2. Methodology

The PHREEQC program (Parkhurst & Appelo, 1999) has been used for the reaction process simulation. PHREEQC can be used as a speciation program to calculate saturation indices, distribution of aqueous species, and precipitation of solid mineral phases. The PHREEQC code was chosen due to this capability in modelling reactions between multiple phases (i.e. solution, mineral, gas) as opposed to other models designed exclusively for estimating CO_2 solubility (Soong *et al*., 2003). It is assumed that partial pressure of CO_2 is equal to the total pressure of the system; with PHREEQC assuming carbon dioxide behaves as an ideal gas whereby partial pressure is equivalent to fugacity. Therefore, when the partial pressure of CO_2 is elevated, the pressure of the system must also be increased to reflect this. However, PHREEQC was principally designed for relatively low temperature natural water systems, with speciation calculated only at fixed pressures (1 atm.) using the default database (phreeqc.dat). As

such, the model does not have a built in method to adjust the equilibrium constants as a function of pressure and temperature. At the elevated pressures and temperatures employed in the modelling of the ascending fluid, the thermodynamic properties of the fluid species are very sensitive. Therefore, equilibrium constants for all gases, aqueous species, and minerals was calculated using the SUPCRT92 code and the dprons96.dat database (Johnson *et al*., 1992) for the range of P-T conditions used in the simulations to reflect an initially "hot" fluid decompressing and cooling upon ascent.

7.2.1. Modelling process

The conditions of the modelling are determined by the nature of the software employed. Using PHREEQC, gaseous CO_2 was initially dissolved into 1 kg water (with associated ions) at a set temperature and depth (related to pressure regime). As a result, this represents the highest potential concentration of CO_2 in solution in the ascribed P-T regime. The CO_2-rich solution was then incrementally shifted to decreasing P-T conditions so to simulate the ascension of the fluid up the basin margin fault. At each increment the properties of the fluid (e.g. pH, molar concentrations, speciation, saturation indices) following reaction (e.g. CO_2 exsolution, carbonate precipitate, fluid-rock interaction) were recorded (i.e. P-T_1). This data was then inputted to comprise of the solution for the subsequent increment as the solution was reacted at a lower pressure and temperature condition (i.e. P-T_2). Gaseous CO_2 exsolved from the solution during fluid ascent was removed from the model and unable to react with the subsequent solution.

7.2.2. Formation water chemistry

Present-day formation waters within Brae Formation reservoirs exhibit moderate salinity, ranging from 65 900 to 122 368 mg/l total dissolved solids (TDS), with an average of 95 851 mg/l (Warren & Smalley, 1994). Fifteen analyses of formation water produced from 11 wells in the Brae, Miller, and T-Block Fields are presented in table 7.1. The relatively high concentrations of dissolved ions in the present day formation water suggest significant fluid evolution, resulting in chemical signatures distinct from marine

or meteoric sources. This differs from most Viking Graben reservoirs which exhibit reduced salinities due to meteoric influence (Egeberg & Aagaard, 1989) and thus probably reflects a pronounced influx of saline basinal fluids from depth. As previously discussed, this can be inferred from stable isotope analysis in this study and previous fluid inclusion investigations in the region (e.g. Larter *et al*., 1995).

Sample	Well	Field	Depth (m)	T(°C)	pH	TDS (mg l^{-1})
1	16/07a-A08	South Brae	4045	123	7.50	80 890
2a	16/07a-A27	South Brae	4000	123	7.83	65 900
2b	16/07a-A27	South Brae	4108	123	7.90	99 630
3	16/07a-B09	North Brae	3904	120	6.53	79 790
4	16/07a-C04	Central Brae	4118	123	6.39	128 060
5	16/17-4	Toni	3981	-	6.40	95 808
6	16/17-13	Tiffany	4270	-	7.03	115 170
7a	16/17-7	Thelma	3738	137	5.97	99 100
7b	16/17-7	Thelma	4097	143	6.24	122 368
7c	16/17-7	Thelma	4107	149	6.25	117 003
7d	16/17-7	Thelma	4121	-	7.70	118 520
8	16/08b-2Z	Miller	4159	120	6.95	82 700
9	16/08b3	Miller	4103	120	8.05	77 270
10	16/07b-24	Miller	4099	120	7.50	76 560
11	16/07b-25	Miller	4099	120	7.50	79 000

Sample	cations (mg l^{-1})							anions (mg l^{-1})		
	Na	K	Mg	Ca	Sr	Ba	Fe	Cl	SO_4	HCO_3
1	29 410	1390	67	335	52	890	1	46 620	7	2180
2a	23 700	920	33	345	19	490	1	36 730	17	3620
2b	35 220	1490	77	705	145	1610	1	58 680	14	1620
3	26 810	1230	210	1860	140	790	29	47 390	3	1330
4	44 270	1470	73	1380	69	2520	19	77 040	7	1140
5	33 377	-	370	2737	-	679	178	57 256	-	1211
6	40 320	2010	370	3790	355	1190	145	68 380	3	1100
7a	35 581	-	338	2561	166	508	-	59 946	-	1196
7b	40 227	-	404	5968	683	783	-	74 303	-	634
7c	38 732	-	377	5647	640	494	-	71 113	-	756
7d	38 740	-	390	5760	660	740	69	71 620	<10	610
8	28 780	1830	115	1060	110	1050	14	47 660	8	2090
9	27 650	1280	105	645	72	780	47	44 260	5	2470
10	27 400	1480	87	325	41	680	1	44 190	4	2350
11	28 100	1630	113	615	65	770	3	46 050	4	1655

Table 7.1. Present reservoir conditions and composition of waters from the Brae Formation in the Brae, Miller, and T-Block fields. Data from Warren and Smalley (1994) and references therein.

Warren and Smalley (1993) observed that formation waters of Zechstein origin typically exhibit characteristically high Ca/Cl ratios (>0.06) compared to other North Sea formation waters. A number of water samples from the T-Block Fields exhibit high Ca/Cl ratios (~0.08) which are invariably coincident with high salinity waters (90, 000 – 100, 000 mg l^{-1}). These fluids attest to a Zechstein influence on the water composition in the fields. However, the majority of similar Brae trend fields show ratios significantly lower (<0.02) (Warren & Smalley, 1994). Evidence of high salinity Zechstein Formation derived fluids has been reported in the Brae Formation of the Brae fan complex (e.g. Larter *et al*., 1995). Therefore, why do formation waters in the present day Brae Fields not reflect the apparent high salinity influx as witnessed in the T-Block Fields?

Zechstein deposits are notably present at a relatively shallower depth below the T-Block Fields compared to the more northerly Brae Field counterparts (Cherry, 1993). Therefore, the influence of the Zechstein deposits may be more pervasive and prolonged in the T-Block Fields, with homogenisation of formation waters more realised in the more northerly Brae Fields owing to limited connectivity to high salinity sources at depth. Another possible explanation could be the incorporation of Ca into late carbonate cements notably evident in the Brae Formation sandstones (e.g. Lu, 2008), reducing the Ca/Cl ratio of the formation water present. However, insufficient chemical data is available to truly delineate a possible evaporitic source of the Brae Field formation waters due to a lack of conservative aqueous component analyses (e.g. Br).

Another conspicuous chemical signature of the formation waters present in the Brae Trend fields is the very high barium content, up to 2520 mg l^{-1} (average 931), the highest witnessed in the North Sea. The Gyda Field (Central Graben) also exhibits very high Ba (up to 563 mg l^{-1}), with barite scaling problems as encountered in the Brae Fields (Oxtoby, 1994). Interestingly, the Gyda Field is dominated by Zechstein derived fluids which could have transported Ba into the field; a scenario that could be applicable to the Brae Trend fields. However, the source of the high Ba remains enigmatic though and though shown to be not related to salinity (Warren & Smalley, 1993), a deep graben (possibly Zechstein) source cannot be discounted.

In a number of the T-Block Fields direct juxtaposition of the reservoirs against Zechstein successions is observed (Cherry, 1993). Permian Zechstein formation waters typically exhibit significantly higher salinities than those currently observed in the Brae Formation reservoirs (in excess of 200 000 mg/l) (Warren & Smalley, 1994), with the formation waters of a number of hydrocarbon fields immediately over- and under-lying Zechstein sequences also largely controlled by the evaporitic succession (Bjorlykke & Gran, 1994). Salinity of formation waters in the Brae region is stratified, with higher salinity fluids present at greater depth in the reservoir (see table 7.1). This is notable in Ba and Ca concentrations, which display significantly higher values in the deeper sections of the Brae Formation. The present-day waters determined in the Brae reservoirs may reflect a degree of homogenisation between the host porewaters and the saline influx alluded to in a number of studies and discussed in section 5.4.3. For the models employed in this study, a range of fluids with varying degrees of salinity were used as input, as shown in table 7.2.

Salinity (%wt)	ions mg l^{-1}						
	Na	K	Mg	Ca	Cl	SO_4	TDS
1	3 080	114	368	118	5 531	774	9 983
2	6 161	228	734	236	11 061	1 548	19 968
5	11 540	570	1 834	590	27 653	3 870	49 920
10	30 806	1 140	3 668	1 179	55 307	7 740	99 840

Table 7.2. Initial composition of fluid sources with varying %wt salinities used in the model.

7.2.3. Pressure-temperature parameters

It is assumed the fluid flow up the graben bounding fault is relatively rapid, with the fault zone acting a conduit for fluid flow. From the petrographic data (see *chapter 3*) episodic fluid flux has been determined in the fault zone, probably due to overpressure in the basin, with the graben bounding fault functioning as valve, periodically releasing fluid from depth (e.g. Cathles & Smith, 1983; Eichhubl & Boles, 2000). Sibson (2000) noted that fault systems related to relay ramps and transfer zones, as evident on the graben margin (*see section 3.3.1.*), can act as high permeability networks serving as

conduits for heated fluids from depth. Such high flow rates are manifested in the anomalously high temperatures determined using microthermometry recorded in the fracture cements (see *chapter 4*). To simulate the conditions under which a fluid would ascend up the fault zone, a series of pressure-temperature scenarios have been proposed.

The model was constructed assuming an initial fluid derived from the Zechstein Formation at approximately 70 Ma when CO_2 and basinal fluid influx up the fault zone into the Brae Formation reservoirs has been proposed. Given the degree of ambiguity at what depth Permian successions are present adjacent to the graben margin, a depth of ~6 km depth is estimated (c.f. Hospers & Ediriweera, 1991). Assuming a typical North Sea geothermal gradient in the Fladen Ground Spur region of ~40°C/km during the proposed time of basinal influx (Figure 4.5) (Evans & Coleman, 1974), this corresponds to a temperature of 240°C.

Figure 7.1a shows a schematic temperature profile of the model assuming a slowly ascending fluid incapable of producing significant temperature anomalies due to thermal equilibrium with the surrounding country rock. These temperatures are higher than expected from the palaeogeothermal gradient at the time of precipitation (see Figure 4.5) and are thus indicative of hot ascending fluids up the graben margin (c.f. Burley *et al.*, 1989). Such a scenario is plausible in a slowly subsiding basin with fluid expulsion related to compaction driven flow (e.g. Bethke, 1985). Reduced temperature loss in rapidly ascending fluids in high permeability fault zones results in anomalously high fluid temperatures at discrete localities. Such temperature anomalies (in excess of 40°C) associated with large scale fluid flow in steep major basin bounding fault zones have been documented in the South Viking Graben (Carstens & Finstad, 1981).

Similar high temperature localised thermal anomalies due to rapid ascension of fluids are also witnessed in a number of present-day analogous fault zones (e.g. the Rhinegraben (Clauser & Villinger, 1990), and the Great Basin fault zone (Fairley & Hinds, 2004a)). Figures 7.1b and 7.1c show the temperature profiles of the rapidly

ascending fluids adopted in this study, with increased permeability and subsequent heat flow in the upper regions of the fault zone as purported by Fleming *et al*. (1998) for similar graben margin fault configurations. Temperature anomalies of ~20°C and ~45°C respectively are observed at the proposed depth of the Brae Formation reservoirs assuming the source depth and temperature conditions outlined above.

In rapidly subsiding basins such as the Viking Graben overpressure is commonly observed (Harris & Fowler, 1987). Therefore, with faulting (episodic pumping or tectonic), expulsion of fluids with differing thermal and pressure properties compared to the regime into which they are ascending is not uncommon. As such, a range of fluid pressure gradients are modelled in this study; lithostatic (223bar/km) representative of fracturing and subsequent fluid expulsion due to overpressure and lithostatic failure (e.g. episodic seismic pumping), intermediate (154bar/km) representative of a moderately overpressured system undergoing fluid expulsion due to tectonism, and hydrostatic (100bar/km).

The P-T regimes in this study accommodate the highest possible fluid pressure gradient (lithostatic) at the point of rupture in the fault zone at depth, falling coseismically to hydrostatic as the fluid ascends. Pressure-temperature variations with depth used as conditions for the models are illustrated in Appendix IIIa.

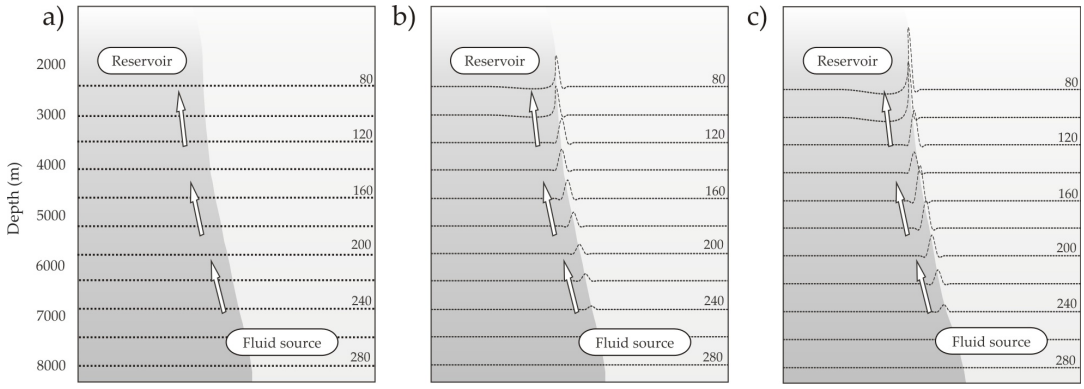

Figure 7.1. Schematic diagram showing theoretical isotherm profiles of the basin bounding fault for differing fluid flow rates (a – c) discussed in the text.

7.2.4. Mineral and CO_2 input

The nature of the PHREEQC program dictates that the user defines the reactant phases within the model. In addition to those minerals evident from petrographic study of the fracture cements (i.e. dolomite and calcite), other carbonate minerals (siderite, anhydrite, etc) were permitted to precipitate in the model to allow comparison with observed mineral assemblages in the fractures with the modelling outcomes. Wall-rock interaction simulations were conducted using three hypothetical wall-rock mineralogical compositions accounting for fluid ascending into fractures bound by earlier carbonate phases and typical mineral assemblages present in sedimentary basins (table 7.3). In the model the products of the reactions between the fluid and wallrock were added incrementally to the solution and permitted to equilibrate with secondary mineral phases. The program assumes the fugacity of CO_2 is equal to its partial pressure. In the model, the CO_2 partial pressure is assumed equal to the total pressure of the system. Therefore, when the pressure and temperature of the system are varied the partial pressure of CO_2 is adjusted accordingly to account for this.

wallrock	mol mineral per litre of ascending water			
carbonate	dolomite	0.5	calcite	0.5
sandstone #1	quartz	0.5	illite	0.01
sandstone #2	quartz	0.5	K-feldspar	0.01

Table 7.3. Composition of hypothetical wallrock permitted to react at P-T each increment in the model.

7.3. Modelling results

A number of simulations were run varying the range of parameters (pressure, temperature, salinity) to determine the relative significance of each factor contributing to CO_2 solubility and carbonate precipitation upon ascension of a solution up the hypothetical fault zone. Tabulated results of the simulations are presented in Appendix III.

Modelling predicts that rapidly ascending hot CO_2-rich fluids in thermal disequilibrium with the surrounding cooler regional geothermal regime undergo greater CO_2 degassing. Figure 7.2 illustrates that in a moderately overpressured ascending fluid in thermal equilibrium with the regional geothermal gradient 2.81 mol/l CO_2 is degassed in total. This equates to 50% of CO_2 initially in solution. Conversely, higher temperature ascending fluids profiles, b and c, exsolve 3.16 (56%) and 3.38 mol/l CO_2 (60%) respectively. As expected, this is in agreement with the retrograde solubility of CO_2. The model indicates the effect of temperature on solubility becomes more telling at pressures less than 600 bar when the differing quantity of degassed CO_2 from the three temperature regimes becomes more marked. The model predicts that varying temperature gradients have a minimal impact on the amount of carbonate precipitated; ranging from 282 mg/l from rapidly ascending higher temperature fluids to 314 mg/l from fluids in thermal equilibrium with the regional geothermal gradient.

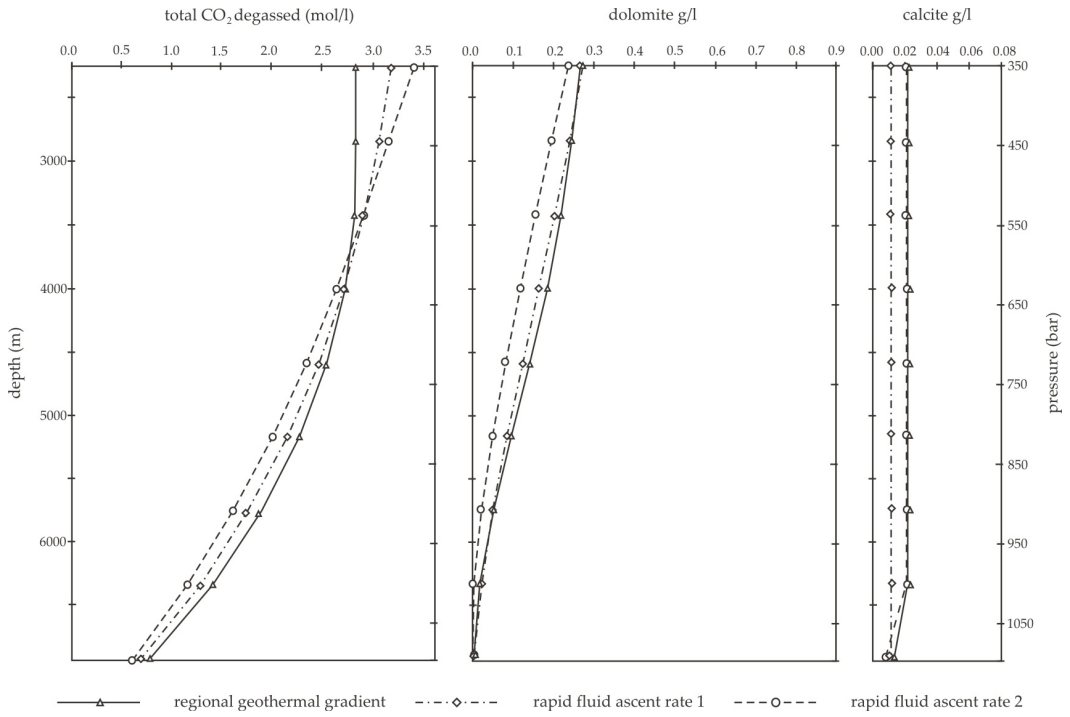

Figure 7.2. Cumulative degassing of CO_2 and carbonate precipitation from an ascending solution with intermediate fluid pressure and a range of temperature profiles (see Figure 7.1). Initial solution: 1 %wt salinity water saturated with CO_2 at 260°C and 1143 bar pCO_2.

Simulating the effect of pressure on the extent of degassing and precipitation from an ascending fluid, the model predicts that lower pressure regimes result in the largest amount of carbonate precipitation (Figure 7.3). Given that the original carbon content of the initial solutions was greater in the lithostatic pressure simulation (5.51 mol/l) than hydrostatic (4.97 mol/l), the actual percentage carbon thus incorporated into carbonate phases in the hydrostatic pressure model is notably higher. However, the actual quantity of carbon precipitated in carbonate phases is typically two magnitudes less than that lost through degassing. Although similar quantities of degassed CO_2 are witnessed between hydrostatic and intermediate pressures, the actual fraction lost in each simulation is 56.5% and 50.2% respectively (Figure 7.3). Lithostatic pressures predict the smallest volume of CO_2 degassing (2.35 mol/l). This represents 42.6% of carbon originally in solution.

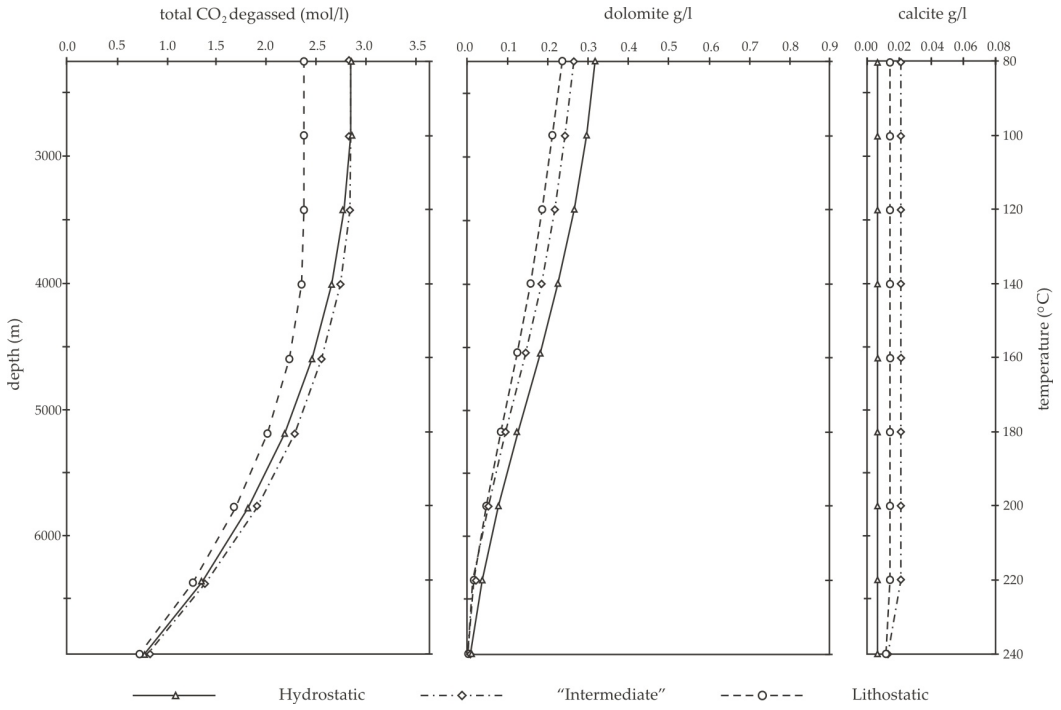

Figure 7.3. Cumulative CO_2 degassing and carbonate precipitation totals from an ascending CO_2 saturated low salinity fluid (1 wt%) at hydrostatic, lithostatic, and an intermediate fluid pressures assuming equilibrium with the regional geothermal gradient (37°C/km).

Figure 7.4 shows that with increasing salinity, the amount of CO_2 exsolved from an ascending fluid decreases from 3.31 mol/l in a zero salinity fluid to 2.67 mol/l in a 5 % salinity fluid. The reduced solubility of CO_2 in higher salinity fluids is reflected in the decreasing amount of overall CO_2 exsolution from the various solutions upon decompression. The model predicts that approximately 55 % of the initial carbon introduced into the system by CO_2 dissolution is degassed regardless of fluid salinity. However, the modelling output shows that greater amounts of carbonate are precipitated from higher salinity fluids owing to the greater availability of applicable cations, with the amount of dolomite precipitation predicted to be at least a magnitude greater than that of calcite.

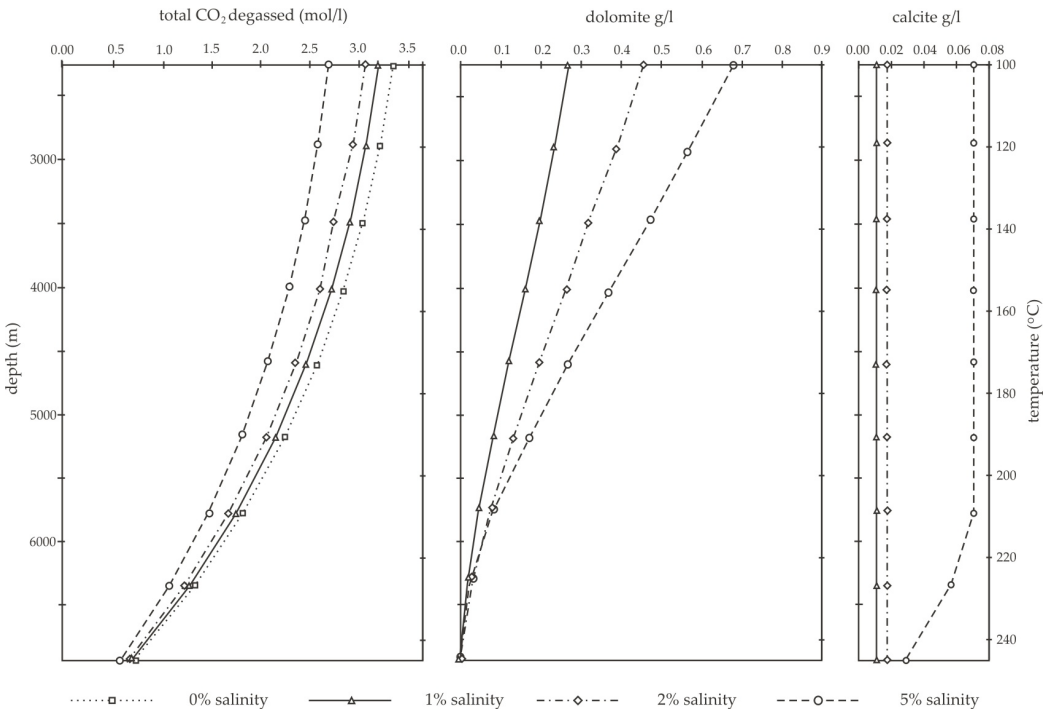

Figure 7.4. Cumulative CO_2 degassed and carbonate precipitated from ascending solutions of varying salinity (0, 1, 2, and 5 %wt (see table 7.1.)). The model assumes relatively rapidly ascending fluids at intermediate pressure (Figure 7.1. thermal regime c) that maintain elevated pressure and temperature relative to regional pressure and temperature conditions. Initial solutions saturated with CO_2 at 260°C and 1143 bar pCO_2.

In higher salinity fluids with more available Ca and Mg ions in solution, the model calculates a greater fraction of the initial carbon in solution is consumed in precipitating carbonate from such solutions (Figure 7.5). For example, in the 5 %wt salinity solution, approximately 0.20 % of the carbon initially in solution is incorporated into the precipitated carbonate (~0.8 mol). In a 1 %wt solution, 0.06 % carbon is used (~0.3 mol). Modelling fluids with salinities in excess of 6 wt% resulted in a breakdown of the increasing precipitation trend observed in fluids with salinities between 1 and 5 %wt. The significance of this with respect to the limitations of the modelling approach is discussed later (see section 7.4.4).

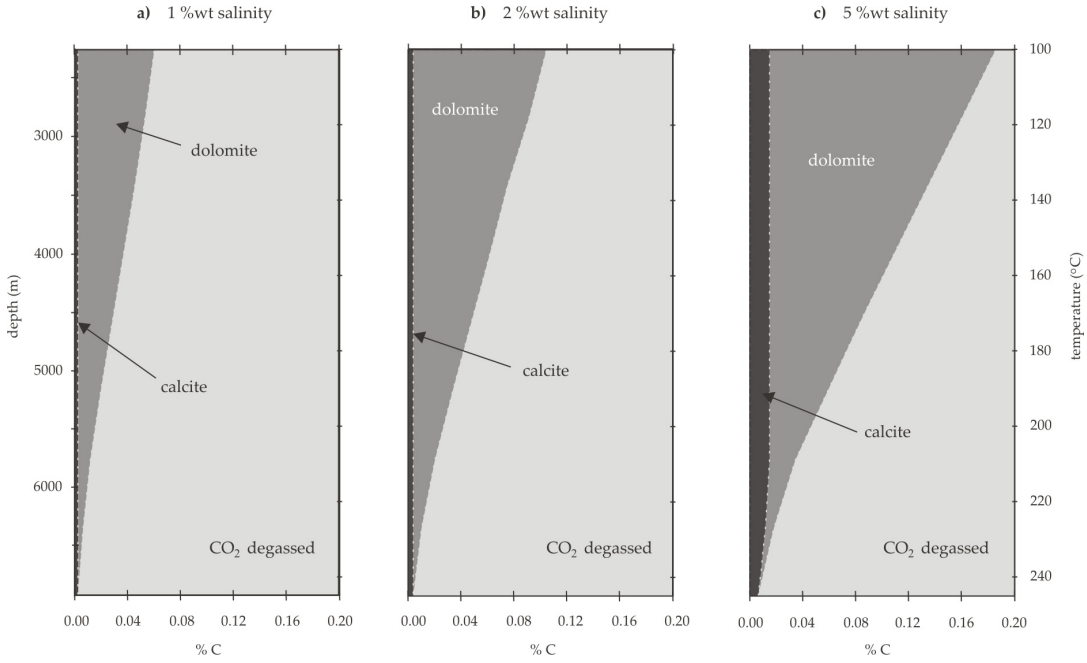

Figure 7.5. Carbon balance diagrams showing the cumulative fraction of carbon from the initial solution used in precipitation of dolomite and calcite in ascending 1, 2, and 5 %wt salinity fluids. See Figure 7.4 for model conditions.

In Figure 7.6 the cumulative amount of CO_2 degassing and carbonate precipitation following interaction with various hypothetical wallrock compositions is shown. A control simulation with no wallrock reactants produces cumulative totals of dolomite and calcite of 350 mg/l and 6.45 mg/l respectively upon cessation of the simulation at 80°C and 230 bar. Corresponding simulations permitting interaction with quartz and

clay wallrock (sandstone #1) precipitates 347 mg/l dolomite and 8.5 mg/l calcite. Substituting illite for K-feldspar (wallrock; sandstone #2), no calcite is precipitated and dolomite precipitation increases to 429 mg/l. Negligible variation in the overall quantity of CO_2 degassed apparent regardless of the wallrock composition (~2.8 CO_2 mol/l).

7.4. Discussion

7.4.1. Fluid flow effects on CO_2 degassing and carbonate precipitation

The modelling approach clearly illustrates simultaneous CO_2 degassing and carbonate precipitation from ascending CO_2-rich fluids. The quantity of CO_2 degassed and carbonates precipitated from solution is dependent on a number of factors. The modelling predicts that higher fluid temperature profiles assuming rapid fluid flux in the higher permeability tip of the fault zone produces more degassed CO_2 than lower temperature reduced flux rates (Figure 7.2). This effect can be readily attributed to the retrograde nature of CO_2 solubility in higher temperature fluids, suggesting that rapid fluid flux from depth is thus more likely to generate larger volumes of gaseous CO_2 in the immediate area (i.e. Brae reservoirs). In the absence of rapid high temperature flux the model predicts that rates of CO_2 degassing on shallower portions of the fault are relatively low compared to those predicted at greater depths were pressure predominantly controls CO_2 solubility

Irrespective of the pressure regime applied, modelling indicates that CO_2-saturated solutions rapidly undergo degassing due to fluid decompression upon ascent, with ~75% of all CO_2 lost through degassing removed above ~180°C. Similar trends are observed in all the simulations run. This suggests that free phase CO_2 should be concomitant with the ascending fluid. Buoyant ascent of gaseous CO_2 up the fault provides a suitable mechanism to account for the high concentration accumulation of CO_2 present in the Brae Formation and sealed by the KCF. However, the incremental nature of the model does not account for previously exsolved CO_2 dissolving back into solution; a factor which could decrease fluid pH and subsequent carbonate precipitation.

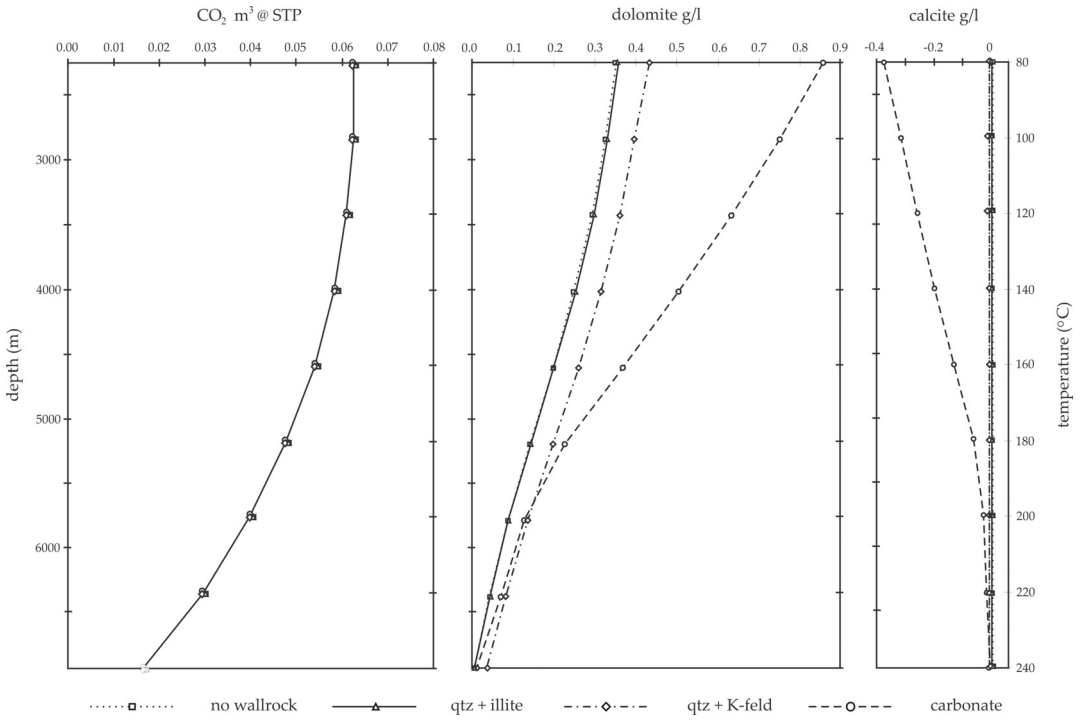

Figure 7.6. Cumulative CO_2 degassing and carbonate precipitation/dissolution totals from an ascending solution from interaction with a host of hypothetical wallrock compositions. The model assumes hydrostatic fluid pressure and thermal equilibrium with the regional geothermal gradient (37°C/km). Initial solution: 1 %wt salinity water saturated with CO_2 at 260°C and 743 bar pCO_2.

Volumes of carbonate precipitated from the ascending solutions are relatively minor, with typically less than 0.1% of carbon initially in the fluid subsequently trapped in minerals. Dolomite is the predominant carbonate phase predicted by the model, with calcite accounting for less than 10% of the carbonates precipitated. The ratio of dolomite to calcite predicted from the models is similar to that observed in the fracture cements. The preference towards dolomite precipitation in the model can be attributed to higher concentrations of Mg in the initial fluid. However, Mg/Ca ratios of the fluids in the simulation (~3:1) are lower than those suggested by Folk and Land (1975) to permit "pure" dolomite precipitation (10 – 5:1). Zechstein derived brines exhibiting high Mg/Ca ratios appear the likely source for the dolomite cements witnessed in the fractures, with the degree of fluid salinity the key influence on precipitation volumes (Figure 7.4).

7.4.2. Stable isotope modelling – Rayleigh fractionation

The previous Rayleigh degassing-precipitation model used to explain the carbon and oxygen isotope trends in wells 16/07a-12 and 16/12a-16 (section 5.5.3) was based on two assumptions regarding carbon removal from the ascending fluid; constant % mol loss at a given temperature iteration and 1:1 ratio carbon distribution between degassed CO_2 and precipitated carbonate.

The PHREEQC modelling shows that the fraction of carbon loss through CO_2 degassing and carbonate precipitation is highly variable and dependent on the pressure and temperature profiles of the ascending fluid with carbon loss through degassing typically reducing progressively with fluid ascent. As discussed previously, carbon incorporated into mineral phases is only a fraction of that removed from the fluid through CO_2 degassing (<< 1%). The Rayleigh fractionation equation presented in section 5.5.3 (p.118) can be amended to account for differing carbon fraction loss though degassing and precipitation:

$$\delta_{carbonate} = \delta^{i}_{fluid} + \ln F_1 \times 10^3 \ln \alpha_{CO2(g)\,-\,CO2\,(aq)} + (1 + \ln F_2) \times 10^3 \ln \alpha_{carbonate\,-\,CO2(aq)}$$

where F_1 and F_2 represent the fraction of carbon removed through degassing and precipitation respectively. Differing pressure regimes produced the largest relative difference in fraction of CO_2 removed from solution in the modelling process (Figure 7.5). Applying the results of these simulations to a Rayleigh fractionation model suggests that CO_2 degassing and precipitation has a very limited effect on the degree of isotopic variation, with differences in $\delta^{13}C$ signatures between hydrostatic and lithostatic pressures less than 1 ‰ (Figure 7.7). Although, the PHREEQC models predict a similar overall fraction of carbon is lost from the fluid as the theoretical model in Figure 5.13 (~50 %), the larger quantities degassed at higher temperatures when isotopic fractionation between CO_2 and HCO_3^- is relatively small, producing overall minimal $\delta^{13}C$ variation in the cements. The results of this model suggest that fluid mixing or variability in the isotopic signature of the original carbon source has much more

profound effect on the $\delta^{13}C$ composition of cements precipitated from a fluid undergoing active CO_2 degassing.

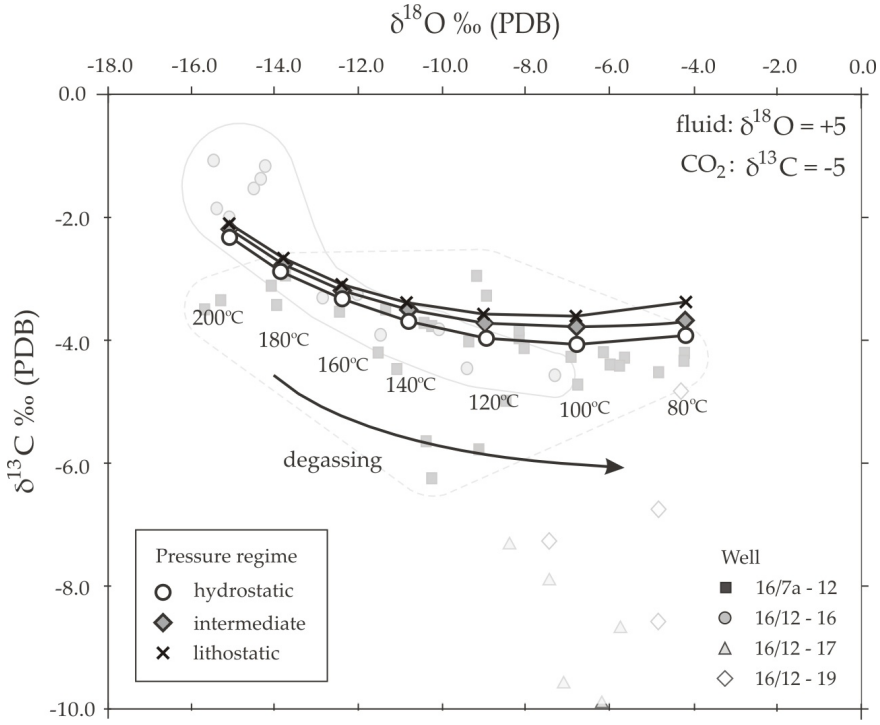

Figure 7.7. Rayleigh fractionation model showing minimal variation in $\delta^{13}C$ ratio of dolomite precipitated from CO_2 flux simulations in various pressure regimes. Fluid: $\delta^{18}O$ = +5 ‰ SMOW; initial CO_2, $\delta^{13}C$ = -5 ‰ PDB.

7.4.3. Mineral reactions

All minerals in a sedimentary system have different abilities to buffer pH, which is related to the amount of CO_2 in formation. It is often assumed that an increase of pCO_2 will cause dissolution of carbonate, a process implicated in many situations as creating secondary porosity (Surdam,*et al*., 1989), whereby:

$$CaCO_3 + CO_{2(aq)} + H_2O \rightarrow Ca^{2+} + 2HCO_3^-$$

In the absence of some other control of pH, this is correct. However, if pH is buffered, the addition of CO_2 may the cause precipitation of carbonate. The modelling shows calcite dissolution is observed following reaction between the CO_2-rich fluid and the

carbonate wallrock (Figure 7.6). The model predicts coincident dolomite precipitation following the reaction. This could result from sufficient buffering of the fluid pH following dissolution of the calcite. The resultant dolomite may be the preferred carbonate phase precipitated due to the Mg-rich nature of the waters.

Lithologies rich in calcium and magnesium silicate minerals can reduce the acidity of the host solution by providing such cations as Ca_2^+, Mg_2^+ and Fe_2^+ that can form stable carbonate phases in the presence of CO_2 (Baines & Worden, 2004; Matter *et al*., 2007). Numerous thermodynamic models have shown the destabilisation of feldspar minerals a key aspect of increased CO_2 levels in reservoir sandstones (Barclay & Worden, 2000). The ability of K-feldspar dissolution to act as a buffer in high CO_2 situations was shown by Raistrick *et al*. (2009), who observed that CO_2 injection in an EOR program at the Weyburn oilfield (Canada) resulted in dissolution and buffering of the formation fluid pH, potentially leading to carbonate precipitation.

Extensive secondary porosity resulting from feldspar dissolution has been widely reported in the Brae Formation (McLaughlin *et al*., 1994). The dissolution of feldspar (up to 15 % secondary porosity generation) has been suggested as strong evidence for the pervasive influence of high CO_2 concentrations on the mineralogical and diagenetic patterns observed in the Brae Formation sandstone reservoirs (Baines & Worden, 2004). The modelling approach used in this study suggests that dissolution of K-feldspar ($KAlSi_3O_8$) increases the overall quantity of carbonate precipitated, notably dolomite, by approximately 25% relative to the precipitation with no fluid-mineral interaction with the country rock. The pH buffering reaction of CO_2 with K-feldspar culminating in the precipitation of carbonate and other mineral phases can be expressed as:

$$\text{feldspar + clay minerals + } H_2O + CO_{2(aq)} \rightarrow \text{ carbonate + kaolinite + quartz}$$

The model also predicts coincident precipitation of quartz in addition to carbonate at a ratio of approximately 10:1. However, negligible volumes of quartz are observed in the fracture cement mineralogy.

7.4.4. Modelling limitations

Almost any geochemical modelling approach is inherently limited due to the complexity in assuming a range of input parameters. When modelling complex natural systems, reasoned approximations inevitably have to be made. For example, given the sparse available data (i.e. cored section) and general poor resolution of the fault on a regional scale, the fault zone represented in the model exhibits homogeneous properties, essentially acting as a simple 1D high permeability conduit for fluid flow. As a result the modelling approach underestimates the complexity and heterogeneity inherent in active fault systems (e.g. Fairley & Hinds, 2004b). However, the crude approximation for the fault morphology used by the model is sufficiently applicable to the large steep angle planar faults present on the graben margin (Færseth, 1996), with the geometry and flow paths typically less complex and tortuous than shallow angle listric fault morphologies. Additionally, the model neglects lateral fluid flow (c.f. Magara, 1976), focusing on rapid carbonate precipitation with negligible mixing between the ascending fluid and *in situ* formation waters. However, as discussed throughout this thesis, fluid mixing provides an important mechanism in the precipitation of the fracture cements and its role can be qualified from observations in both the petrography and stable isotope analysis.

The PHREEQC code uses Debye-Hückel expressions to account for the non-ideality within aqueous solutions caused by the incorporation of dissolved solids. Such models are accurate for low ionic strength solutions (< 0.1M). However, the composition of the solutions ideally used to replicate a basinal influx consist of higher ionic strength saline fluids (e.g. 10 %wt. NaCl = ~1.7 M). As such, in these solutions, the activity coefficient may actually increase rather than decrease with ionic strength, thus decreasing solubility. Such a phenomena was observed in simulations with solutions of greater than 6 %wt salinity. As a result, for solutions with higher salinities and greater ionic strengths, the Pitzer equations would be more applicable. Given that the salinities suggested for fluids introduced into the Brae Formation are typically higher than those accommodated by the simulation (e.g. 22 wt. % NaCl; Larter *et al*., 1995), the model can only serve as a rough estimate for the amount of carbonate precipitation, with the amount of CO_2 degassed probably over-estimated due to the decreased solubility of CO_2

in higher salinity solutions not achievable using the PHREEQC program and presently available databases.

However, even considering low salinity fluids in the model, CO_2 solubility is most likely overestimated. The calculations of Duan and Sun (2003) have been shown to produce estimates of CO_2 solubility over a wide range of pressures, temperatures, and salinities consistent with experimental data. Comparing CO_2 solubility values determined using the model in this study and those using the calculations of Duan and Sun (2003) show CO_2 solubility is appreciably overestimated using the model adopted here (Figure 7.8). In modelling CO_2 storage options in saline aquifers, Allen *et al*. (2005) also noted this limitation in the PHREEQC code to successfully replicate CO_2 solubilities at elevated pressures even when utilising appropriate databases to account for P-T conditions.

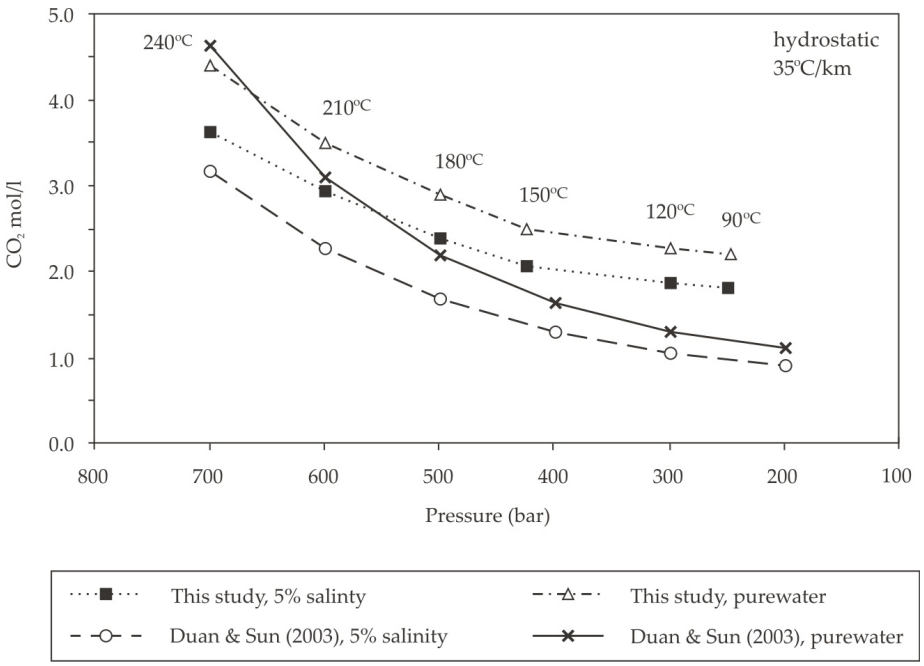

Figure 7. 8. Results of carbon dioxide solubility estimates from the model adopted in this study and those calculated by Duan and Sun (2003). The results show that the PHREEQC model typically overestimates CO2 solubility.

Although all CO_2 solubility estimates are overestimated, the most profound variation in CO_2 solubility overestimation is witnessed at lower temperatures and pressures where

estimates from this model are roughly twice those calculated by Duan and Sun (2003). This suggests that the reduction in CO_2 degassing rate witnessed in the simulations at lower pressures and temperatures is not representative of CO_2 behaviour in solution at these conditions and hence appreciable CO_2 degassing would not be restricted to deeper, higher temperature regions of the fault as predicted from the models. Given the modelling approach here assumes CO_2 saturated fluids, such overestimation could have profound repercussions on predicted fluid chemistries. For example, due to CO_2 solubility overestimation carbon speciation in fluids produced in the model is typically dominated by H_2CO_3, with fluid acidity approximately pH = 4. The resulting higher acidity waters increases carbonate solubility which in turn may underestimate overall potential precipitation volumes.

7.5. Conclusions

- Varying pressure and temperature regimes used to simulate the ascent of overpressured CO_2-saturated fluids are shown to have minimal impact of the amount of carbonate precipitated. It is demonstrated that volumes of carbonate precipitated are very low, typically consuming less than 0.1% of carbon initially in the fluid. As observed in the fractures, dolomite is shown to be the predominant carbonate phase precipitated from Mg-rich Zechstein type fluids in the models, with greater volumes of carbonate precipitation predicted from higher salinity fluids.

- Rates of CO_2 degassing are predicted to be relatively low at depth horizons comparable to those suggested for the fault adjacent to the Brae fields (<3.5 km), with the majority of CO_2 loss is predicted at greater depth in the simulations. Applying the largest relative difference in CO_2 loss predicted from the simulations (between hydrostatic and lithostatic pressure regimes), the impact on $\delta^{13}C$ variation in a Rayleigh fractionation modelling is limited, suggesting CO_2 degassing alone cannot account for the isotope variations observed in the fracture cements.

- The present-day formation water chemistry of the Brae Fields cannot be readily reconciled with a postulated high salinity basinal influx as evidence in previous microthermometric studies. This suggests significant formation water homogenisation and evolution within the Brae Formation during the last ~70 Ma since the proposed influx of high salinity fluids.

- Modelling suggests that fluid-mineral interaction exerts the largest control on carbonate precipitation of the parameters evaluated, with increased volumes of carbonate precipitated attributed to pH buffering of the solution. The results indicate that CO_2 promotes K-feldspar dissolution and subsequent carbonate precipitation. Dissolution of carbonate wallrock is shown to produce the largest volumes of dolomite. However, net carbonate precipitation is less than seen in silicate reactions.

- Although permitting the simulation of water-mineral-gas interactions, the PHREEQC model is shown to significantly overestimate CO_2 solubility compared to models constructed exclusively for CO_2 solubility (e.g. Duan & Sun. 2003). This can result in a number of errors in the simulation of CO_2 ascent by potentially underestimating rates of degassing and carbonate precipitation.

Chapter 8

Synthesis and summary

8.1. Introduction

The Brae area consists of a linear trend of hydrocarbon accumulations situated adjacent to the western margin at the southern end of the South Viking Graben in blocks 16/07a, 16/12, and 16/17 of the UK North Sea (Figures 2.1 and 2.6). The area forms a naturally high-CO_2 province, with hydrocarbons present in the reservoirs containing up to 35 mol% CO_2 (Baines & Worden, 2004). Accumulations elsewhere in the South Viking Graben region typically contain less than 5 % CO_2 (Thrasher & Fleet, 1995). An investigation was conducted in order to determine the genesis and subsequent emplacement process resulting in the large volume accumulation of CO_2 in the oilfields.

The reservoirs in the Brae trend fields comprise Late Jurassic submarine fan sandstone deposits termed the Brae Formation. The reservoirs consist of clastic material derived

from the erosion of the Devonian footwall on the graben margin and exhibit overall large scale fining up trends. Fields proximal to the faulted margin consist of coarse predominantly conglomeratic material (e.g. South Brae), with units prograding into progressively finer grained and mud-rich distal fan deposits eastward into the basin (e.g. Miller-Kingfisher) (Figures 2.7 and 2.8). The sandstones are overlain and underlain by the Kimmeridge Clay Formation. The mudrock provides the source and seal for the reservoirs; with hydrocarbon migration pathways relatively short (Reitsema, 1983; Rooksby, 1991). The fields have undergone continuous burial since deposition, with a present day depth of ~4km and formation temperatures between ~125°C.

Carbon dioxide concentrations in the region show a gradual decrease eastward into the basin away from the western bounding fault of the South Viking Graben (Figure 2.10), with highest concentrations present in the deepest sections adjacent to the fault (James, 1990). The distribution of the CO_2 indicates that it was initially introduced up the graben bounding fault into the oilfields adjacent to basin margin (e.g. South Brae Field) before migrating laterally into the surrounding basinward fields (e.g. Miller Field). The South Viking Graben has experienced a long and complex tectonic history punctuated by two extensive rifting phases in the Permian and Mid-Late Jurassic. The earlier rifting phase is characterised by Zechstein Formation deposits in the basin fill, with marginal carbonate-rich facies present at depth adjacent to the Fladen Ground Spur (Cherry, 1993). Rapid subsidence on the western margin half graben during the Late Jurassic rifting event culminated in the deposition of a series of overlapping syn-tectonic wedges defining the Brae trend fields (e.g. Stow *et al*., 1982). The steeply dipping fault planes present in the Brae area are believed to be inherited from earlier Permo-Triassic fault configurations and may provide conduits for fluid transfer from deep in the graben fill (Figure 2.3).

Four exploration wells which penetrate the fault zone along the graben margin were investigated for evidence of CO_2 rich fluid flow which would suggest possible influx from depth. Cored sections from these wells in the fault damage zone show evidence of fracturing and extensive carbonate (calcite and dolomite) cementation with subordinate

pyrite. The style of fracturing evolves with depth, with brecciation textures becoming increasingly more tectonised with depth (Figure 3.5). SEM analyses reveal at least five generations of dolomite cement in composite fractures in well 16/07a-12 (Figure 3.8 and Table 3.1).

8.2. Synthesis

8.2.1. Fracturing and overpressure generation

The morphology and cyclic nature of the fracture cements strongly suggests episodic fracturing and precipitation events (e.g. Eichhubl & Boles, 2000). Hydraulic fracturing resulting from the ascent of overpressured fluids facilitates the precipitation of cements in the fractures, promoting repeated cycles of pressure build up and release (Sibson, 1981). Homogenisation temperatures from inclusions in late-stage fracture cements attest to fluid temperatures significantly higher than those expected from the palaeogeothermal gradients throughout the burial history of the Brae Formation (Figure 4.9). This microthermometric evidence coupled with the fracturing and cementation styles observed suggests that hot fluids were introduced into the Brae Formation up the graben margin fault through the release of overpressured fluids at depth in the graben fill. Saddle dolomite present in the fracture cements suggests precipitation from relatively high temperature fluids (90 – 160°C) in the fault zone (Radke & Mathis, 1980); suggesting flux of heated fluids up the graben bounding fault from depth.

The rapid subsidence experienced by the South Viking Graben provides a likely contributor to fluid overpressure, with elevated geothermal gradients and fluid pressures in Jurassic formations of the Viking Graben attributed to the migration of heated fluids from depth (Carstens & Finstad, 1981). Complex diagenetic sequences similar to those in the fracture cements have been encountered adjacent to a number of major faults in the North Sea (Burley *et al*., 1989; Burley, 1993), with the cements attributed to periodic release of over-pressured basinal fluids up the faults in situations analogous to the formation of Mississippi Valley-Type (MVT) deposits (Cathles & Smith, 1983; Malone *et al*., 1996).

However, the role of tectonism in the generation of the fractures accommodating fluid flow cannot be neglected. Glassman (1992) speculated that the influx of basinal fluids reflected in diagenetic assemblages observed in deep sections of a number of Viking Graben fields was initiated by movement on bounding faults during the Late Cretaceous tectonic event. Some cemented horizons do exhibit brecciated (e.g. Figure 3.6 b, c) and offset dolomite cements possibly indicative of shear-related faulting processes. As such, fracture propagation resulting from movement on the basin bounding fault could be dependent on both fluid overpressure and tectonic shear stress, with the timing of fracturing controlled by the cycling of the two factors during inter-seismic periods (Figure 8.1) (Sibson, 1992). In such circumstances, faulting initiated by tectonic loading could induce the ascent of overpressured fluids into the fault damage zone; with the flow rate and volume of fluid dictated by the degree of overpressure build-up in the periods of tectonic quiescence (Sibson, 1994).

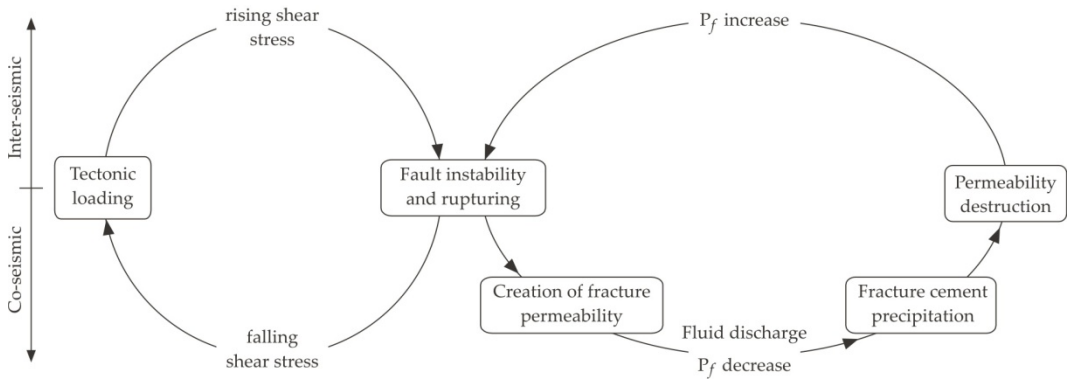

Figure 8.1. Schematic representation of seismic valving, illustrating the relationship between fluid pressure (P_f) and tectonic shear stress on fault activity (modified from Sibson, 1992).

The generation of fluid overpressure has been interpreted to provide a driving force for vertical migration of hydrothermal fluids along the fault zone, with a number of possible sources for the generation of overpressure exist in sedimentary basins (e.g. Osborne & Swarbrick, 1997). In the North Sea basin, overpressuring of formation fluids in stratigraphic sequences is common (Buhrig, 1989), and typically attributed to compaction disequilibrium due to rapid basin subsidence during pronounced rifting

periods (Mudford *et al*., 1991, Holm, 1998). Overpressure in Zechstein sequences is well documented owing to retention of formation fluids and gas within the very low permeability and near isotropic salt-rich sealing lithologies (Warren, 2000b; Nollet *et al*., 2005); as demonstrated in difficulties encountered in the exploration of a number of Zechstein sequences in the Southern North Sea (e.g. Finnie, 2001). Fluid overpressures could also be further increased in the Zechstein through *in situ* gas generation and pervasive dehydration of gypsum to anhydrite during burial (Jowett *et al*., 1993).

8.2.2. Fluid source – Zechstein basinal waters

Due to their chemistry, the carbonate cements are interpreted to be partly derived from Mg-rich basinal fluids. Zechstein Formation carbonate-rich marginal facies present deep in the South Viking Graben fill (Figure 2.2) provide a probable source for the cations present in the carbonate mineralogy observed. Previous fluid inclusion studies of quartz cements in the Brae Formation (Larter *et el*., 1995; Marchand, 2001) indicate a high salinity basinal influx (up to 26 wt. % NaCl) approximately ~70 Ma (Figure 4.9), thus attesting to the influx of basinal fluids during the burial history of the Brae Formation. Although the high temperature fluid inclusions in this study do not exhibit such high salinities, their values are higher than present-day formation waters which suggests they may contain an evolved basinal fluid component to their composition (Figure 4.10).

Geochemical elemental analysis of the various cement generations attests that they precipitated from in discrete fracture events as suggested from the multi-stage fracture morphologies witnessed. This further supports the interpretation of cyclic fracture-precipitation events suggested from the fracture cements textures and relationships. The proposed basinal fluid is interpreted as evolving over time, as evidenced in gradual Fe enrichment of the dolomite cements in the paragenetic sequence (Figure 3.10).

A number of analogous carbonate cemented MVT type deposits also infer the derivation of high salinity brines from subsurface dissolution of thick salt sequences as providing the source for precipitating fluids (Warren, 2000a). Episodic release of highly salinity overpressured formation waters seems the viable mass fluid transport mechanism (e.g.

Burley *et al*., 1989; Macaulay *et al*., 1997). The steep reactivated Permo-Triassic graben bounding fault in the Brae region (Figure 2. 3) facilitates the rapid transfer of fluids from the Zechstein to the shallower Jurassic reservoirs, with the fracture cements observed in the fault zone testament to this.

Assuming high temperature fluids (90 - 180°C), as suggested from fluid inclusion homogenisation temperatures, and supported by probable overpressure fluid ascent from depth, $\delta^{18}O$ isotope signatures of the fracture cements (notably in wells 16/07a-12 and 16/12a-16) can be interpreted as precipitating from evolved basinal fluids (>+4 ‰ SMOW) (Figure 5.5). Heavy $\delta^{13}C$ isotope ratios also present in these cements suggest a probable inorganic carbon source, with ascending Zechstein waters rich in dissolved carbonate accommodating the distinctive stable isotope signatures, elevated fluid temperatures, and cement mineralogy. However, stable isotope signatures from fracture cements in wells 16/12a-17 and 16/12a-19 attests to the influence organic carbon in the precipitating fluid, suggesting mixing between the proposed basinal fluid and the *in situ* formation water in the Brae reservoirs. The variation in $\delta^{13}C$ vs. $\delta^{18}O$ trends witnessed between the wells (Figure 5.3) with respect to the graben margin is considered later (*see section 8.2.6*).

8.2.3. Fluid mixing – influence of KCF porewaters

The evolution of the fluid seen in the EMPA data is interpreted as the increasing influence of resident *in situ* formation waters on the precipitation of the cements. The impact of burial diagenesis and the onset of thermal decarboxylation in the adjacent Kimmeridge Clay Formation (KCF) on the fracture cements is evident throughout the study. The increasing iron content in the cements and pyrite precipitation is probably due to mixing with porewaters influenced by the diagenesis of the KCF during burial, as observed in diagenetic Fe-rich carbonate cements adjacent to the KCF in a number of North Sea reservoirs (Macaulay *et al*., 1998). Corrosion textures post-dating dolomite precipitation attest to the presence of aggressive acidic porewaters produced during thermal maturation in the KCF (Figure 3.7). The absence of hydrocarbons in the fluid inclusions analysed suggests cement precipitation pre-dated petroleum generation in

the region (~50 – 40 Ma) but post-dated the onset of thermal decarboxylation in the KCF, as suggested from cement textures and $\delta^{13}C$ signatures. This timeframe coincides with the suggested time of basinal influx approximately 70 Ma (Larter *et al*., 1995). Strontium isotope analysis of the carbonate fracture cements does indicate the input of radiogenic Sr compared to Zechstein Fm. water $^{87}Sr/^{86}Sr$ ratios, with extensive silicate dissolution observed in the KCF the probable source (Figure 6.1a).

Organic $\delta^{13}C$ signatures (principally in wells 16/12a-17 and 16/12a-19) presumably related to the generation of CO_2 at the onset of thermal decarboxylation are also observed in the cements. The distribution of the contrasting $\delta^{13}C$ and $\delta^{18}O$ signatures between the studied wells and the graben margin is discussed later. Therefore, based on the available data, it is apparent that the influence of mixing between a proposed Zechstein derived basinal fluid with Kimmeridge Clay influenced formation waters in the fault zone cannot be neglected and may in fact have assisted in precipitation of the fracture cements due to pH buffering between the contrasting fluids.

Present-day formation waters in the Brae trend fields exhibit salinities between ~65,000 and 122,000 mg/l (Table 7.1) (Warren & Smalley, 1994). These values are greater than those typically encountered in other Jurassic reservoirs in the Viking Graben. Although elevated, the salinities currently reported in the Brae Formation are appreciably lower than the high salinity waters (26 wt. % NaCl) measured in fluid inclusions estimated to have trapped fluids ~70 Ma (e.g. Larter *et al*., 1995). Coupled with a subsequent decrease in reported fluid inclusion salinities in the region, this suggests that porewaters in the Brae Formation have become progressively mixed following the input of basinal fluids, as reflected in the salinities observed in the present-day.

8.2.4. Controls on cement precipitation and isotopic signatures

Fluid mixing and CO_2 degassing models have been applied to account for the $\delta^{13}C$ and $\delta^{18}O$ trends witnessed in the fracture cements. Both of these mechanisms facilitate carbonate precipitation, overcoming carbonate and CO_2 solubility constraints encountered in an ascending progressively cooling fluid. Carbonates precipitated from a

cooling basinal-type fluid undergoing CO_2 degassing upon ascent fit the observed $\delta^{13}C$ vs. $\delta^{18}O$ trends in wells 16/07a-12 and 16/12a-16 very convincingly (Figure 5.10). The distribution and calculated $\delta^{13}C$ ratios of $CO_{2(g)}$ exsolved from the fluid in the model are in good agreement with those reported in the region. Theoretical modelling estimates isotopically heavier CO_2 (-2 to -5 ‰) degassing at higher temperatures and lighter CO_2 (-8 to -12 ‰) present at lower formation temperatures (80 – 100°C) (Figure 5.11).

James (1990) reported similar heavy $\delta^{13}C_{CO2}$ values at depth adjacent to the graben margin fault. Although the author attributed the variability of $\delta^{13}C_{CO2}$ observed in the South Viking Graben to mixing between ascending inorganic CO_2 and resident organically derived CO_2 from hydrocarbon maturation in the reservoirs, the possible contribution of CO_2 with lighter $\delta^{13}C$ signatures derived purely from the isotopic fractionation of a degassing ascending solution cannot be totally neglected. However, geochemical modelling of fluid ascending from depth up the fault suggests CO_2 degassing alone is not sufficient to produce the variation in stable isotope signatures witnessed. Therefore a degree mixing between a basinal fluid and resident formation waters is probable, as reflected in the organic carbon signatures and radiogenic $^{87}Sr/^{86}Sr$ ratios recorded in a number of samples.

In addition, geochemical modelling suggests CO_2 degassing has limited impact on precipitation volumes, with fluid-rock reactions and solution composition having a much greater influence carbonate precipitation volumes (section 7.3). Cross-formational flow with KCF influenced porewaters is the most likely driver for extensive carbonate mineralisation witnessed in the fractures as suggested from the incorporation of KCF diagenesis related products (e.g. increasing iron) and radiogenic Sr signatures into the fracture cements. Although the role of CO_2 on controlling the precipitation volumes of the fracture cements appears to be limited, the potential impact of elevated CO_2 levels in the Brae reservoirs has been considered. Both Baines and Worden (2004) and Lu (2008) attributed enhanced dissolution textures in the Brae Formation and KCF respectively to the reactions resulting from the input of CO_2–rich fluids into the region.

8.2.5. Implications for CO_2 source

With the graben margin and associated fault zone intimately linked with the high CO_2 concentrations present in the Brae trend reservoirs, the predominantly carbonate cemented fractures provide reasonable evidence of the movement of CO_2-rich fluids up the fault zone. Formation waters influenced by the onset of thermal decarboxylation within the Kimmeridge Clay Formation have been shown to have an impact on both the stable isotope signatures and mineralogy of the fracture cements. However, organic CO_2 generated during maturation of the KCF does not exhibit the distinctly heavy $\delta^{13}C$ signatures interpreted from the stable isotopes of cements in this study or those reported by James (1990) in locations adjacent to the graben margin. In addition, if thermal decarboxylation was responsible for the high CO_2 concentrations observed in the Brae type fields, why are significantly elevated CO_2 levels not also reported in other oilfields juxtaposed with the KCF?

This suggests that fluids ascending the fault zone and precipitated in the fractures as are probably responsible for the large-scale influx of CO_2 into the region. Stable isotope data from this study suggest basinal fluids exhibiting inorganic CO_2 isotopic signatures have been imported into the region, with the Zechstein Formation underlying the fields at depth proposed as the source of the high salinity fluids. Diagenetic reactions in the Zechstein carbonate-rich sequences provide a plausible source for the CO_2, with the dissolved CO_2 present in the high salinity fluids periodically released due to overpressure rupture up the graben margin. However, the ascent of Zechstein fluids along fault zones in the North Sea is not unique to the South Viking Graben (e.g. Macaulay *et al*., 1997). Therefore, if the high CO_2 in the Brae fields is derived from the Zechstein Formation, why are similar concentrations not observed in the other localities?

High concentrations of CO_2 (up to 90%) have been encountered in a number of Zechstein sequences in the Permian Basin across Western Europe (Fischer *et al*., 2006). The authors speculated the CO_2 was probably generated from the thermal degradation of the host carbonates rather than biochemical processes at the high late diagenetic

temperature of formation. More convincingly, $\delta^{13}C$ isotopic signatures have shown that the breakdown of carbonates deep within basin fill was responsible for the high-CO_2 concentrations present in hydrocarbon accumulations of the Békés Basin, Hungary (Clayton *et al*., 1990). Like James (1990) in the South Viking Graben, both of these studies noted the highest CO_2 concentrations (>20%) were coincident with isotopically heavy $\delta^{13}C$ ratios (>-7‰) and vice versa, suggesting a similar source is certainly plausible. This is echoed by Farmer (1965) who concluded that high concentration CO_2 accumulations in the subsurface predominantly originate from the degradation of carbonate minerals.

Although a number of researchers have postulated that the high-CO_2 observed in the Brae area is derived from the thermal destruction of Zechstein carbonates (Wycherley *et al*., 1999; Baines & Worden, 2004), there is no immediate source of localised high temperature anomalies sufficient to invoke thermal degradation of carbonates (>250°C; Brown, 1999). Although understanding of the deep basin fill in the South Viking Graben is very limited (due to poor seismic resolution below the major Jurassic exploration horizons), given the wide geographic distribution of Cenozoic age igneous activity in the North Sea, emplacement proximal to Zechstein sequences in the region cannot be unequivocally rejected. A number of magnetic anomalies identified in the East Shetland Platform adjacent to the western margin of the Viking Graben have been ascribed to igneous bodies (e.g. Donato & Tully, 1982; Holloway *et al*., 1991). However, the timing of emplacement is unconstrained.

Therefore, although thermal degradation cannot be conclusively rejected, it is plausible the availability of overpressured, carbonate rich Zechstein sequences deep within the graben adjacent to the boundary fault may provide a suitable source for CO_2. The steep, Permo-Triassic portion of the graben margin fault in the Brae area (Figure 2.3) would likely provide a suitable conduit for the flux of the CO_2-rich fluid from depth. The proposed fracture-precipitation mechanism and the contributing factors interpreted from the integrated approach adopted in this study are shown in Figure 8.2.

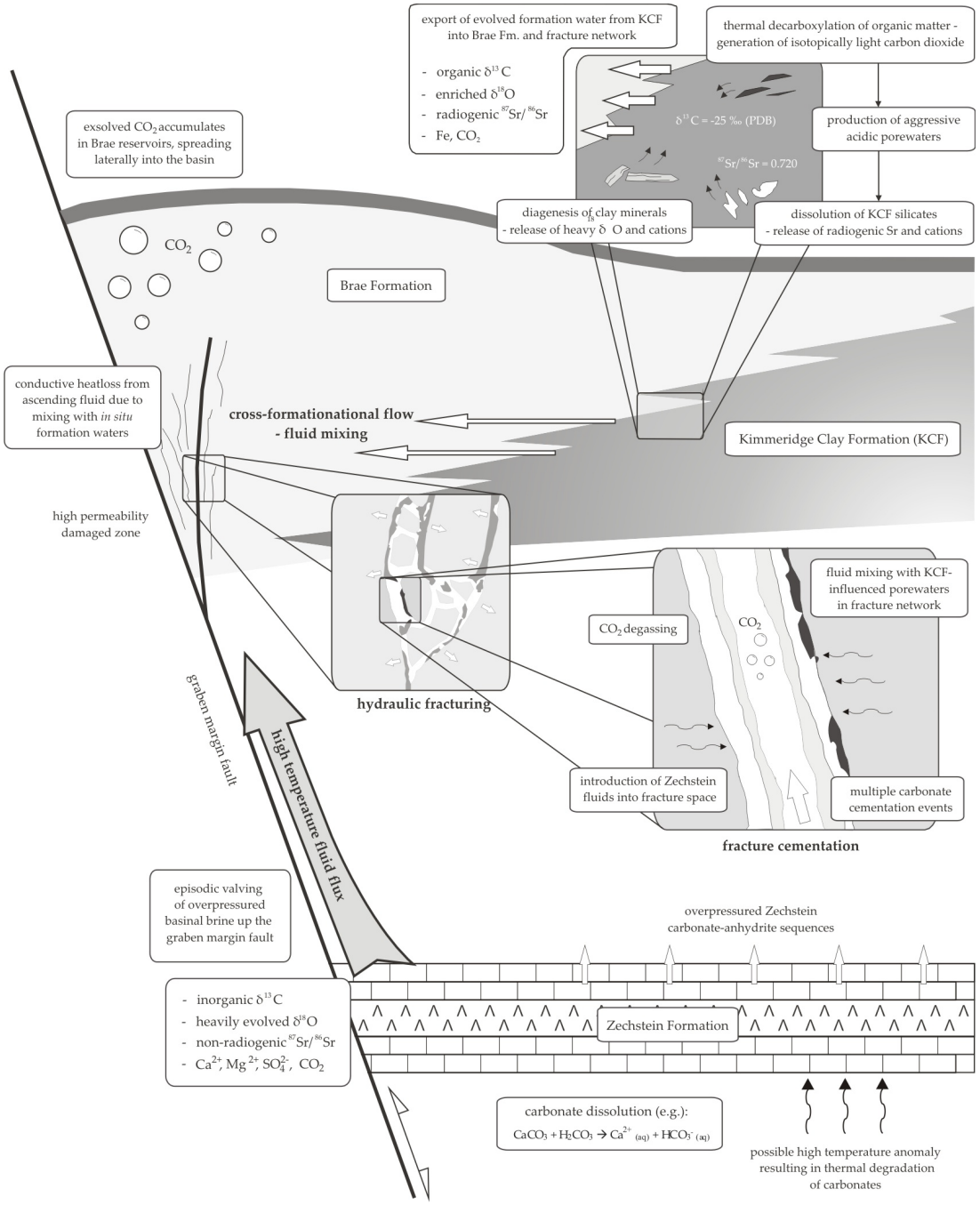

Figure 8.2. Schematic diagram illustrating the processes and drivers invoked for fracture generation (i.e. ascent of overpressured basinal fluids) and carbonate precipitation (i.e. fluid mixing) in relation to CO_2 influx into the Brae type fields proposed from evidence gathered in this study. Note: no scale implied.

8.2.6 Graben margin controls on fluid flux distribution

The fluid evolution model proposed in section 5.4.3 (Figure 5.5) attributes the two distinct $\delta^{13}C$ vs. $\delta^{18}O$ isotope trends observed in the four studied wells to the degree of fluid mixing between the proposed basinal fluid influx and the resident formation water. There is no apparent depth control on the degree of fluid with the shallowest (16/07a-12) and deepest (16/12a-16) cored sections studied (see Figure 3.2) interpreted to have experienced high temperature fluid input. Therefore it is possible that fluid flux distribution (and related heat transfer) is controlled by permeability variations and the degree of fault connectivity on the graben margin.

The speculated higher temperature basinal influxes in wells 16/07a-12 and 16/12a-16 (80 – 200°C) interpreted from cement $\delta^{18}O$ signatures (and T_h values in 16/07a-12) may thus correspond to higher permeability portions of the fault zone where fluid mixing with resident formation waters may be limited. Permeable high fluid flux conduits along fault planes are well documented, with many studies showing that structural and fluid properties of large fault systems not only vary in time, but also in space, particularly along strike of a fault system (Caine *et al*., 1996).

Conversely, fracture cements with depleted $\delta^{13}C$ isotope signatures in wells 16/12a-17 and 16/12a-19 are interpreted to have precipitated from fluids with temperatures similar to the resident formation water (70 – 90°C) due to conductive heat loss from the ascending fluid following mixing proposed for the stable isotope trends in wells 16/12a-19 and 16/12a-17. These potentially more mixed fluid compositions may have arisen due to increasing distance away from the main basinal flux site on the fault or reduced flow rates in lower permeability fractures arrays (Clennell, 1997).

The heterogeneous distribution of high fluid flux locations along the fault could potentially be accounted for by fluid flow variations along the fault zone. As noted previously with reference to the Rhine Graben, discrete high temperature fluid flux sites present along large graben bounding fault systems is not uncommon (Lampe & Person, 2000; Pribnow & Schellschmidt, 2000). The complexity of fault distribution, morphology,

and segmentation in the Brae trend fields discussed previously (*see section 3.3.1*). Transfer zones developed along major basinal faults as seen on the western margin of the South Viking Graben are commonly areas of high fracture density and subsequently increased fluid flow focus sites (e.g. Eichhubl *et al*., 2009). Therefore, it is plausible that the proposed introduction of basinal fluids into the Brae Formation reservoirs may have been focused at such higher permeability locations on the graben margin. Such a process may thus be able to explain the apparent contrasting fluid-temperature regimes interpreted from the stable isotope data acquired from the two neighbouring wells studied in the Pine Field (16/12a-16 and 16/12a-17).

Figure 8.3 highlights the effect of fluid flow variations in the fault zone which may affect fluid mixing rates and thus the resultant fracture cement compositions. With limited data concerning in distribution of fault patterns with respect to well locations in the oilfields studied commercially available, the fault arrangements shown in Figure 8.3 are purely representative of the fault distribution and morphologies commonly encountered in fault segments of the graben margin (*see Figure 3.4*).

Episodic faulting would greatly increase the permeability of selected fault zones, with low permeability sections potentially related to sites of tectonic weakness inherited from the Permo-Triassic fault configurations on the graben margin. These re-activated ancient faults typically exhibit planar surfaces with dips of ~60° (Thomas & Coward, 1996) and are possible conduits for high temperature fluid flow originating from overpressured Zechstein sequences. Conversely, shallow low angle faults on the graben margin may exhibit lower flow rates or have reduced connectivity with the flux of basinal fluid ascending the graben margin. As a result, fracture cements in these locations may show evidence of greater fluid interaction with the resident formation water (i.e. organic $\delta^{13}C$ signatures). See Appendix I.a for representative fault plane morphologies.

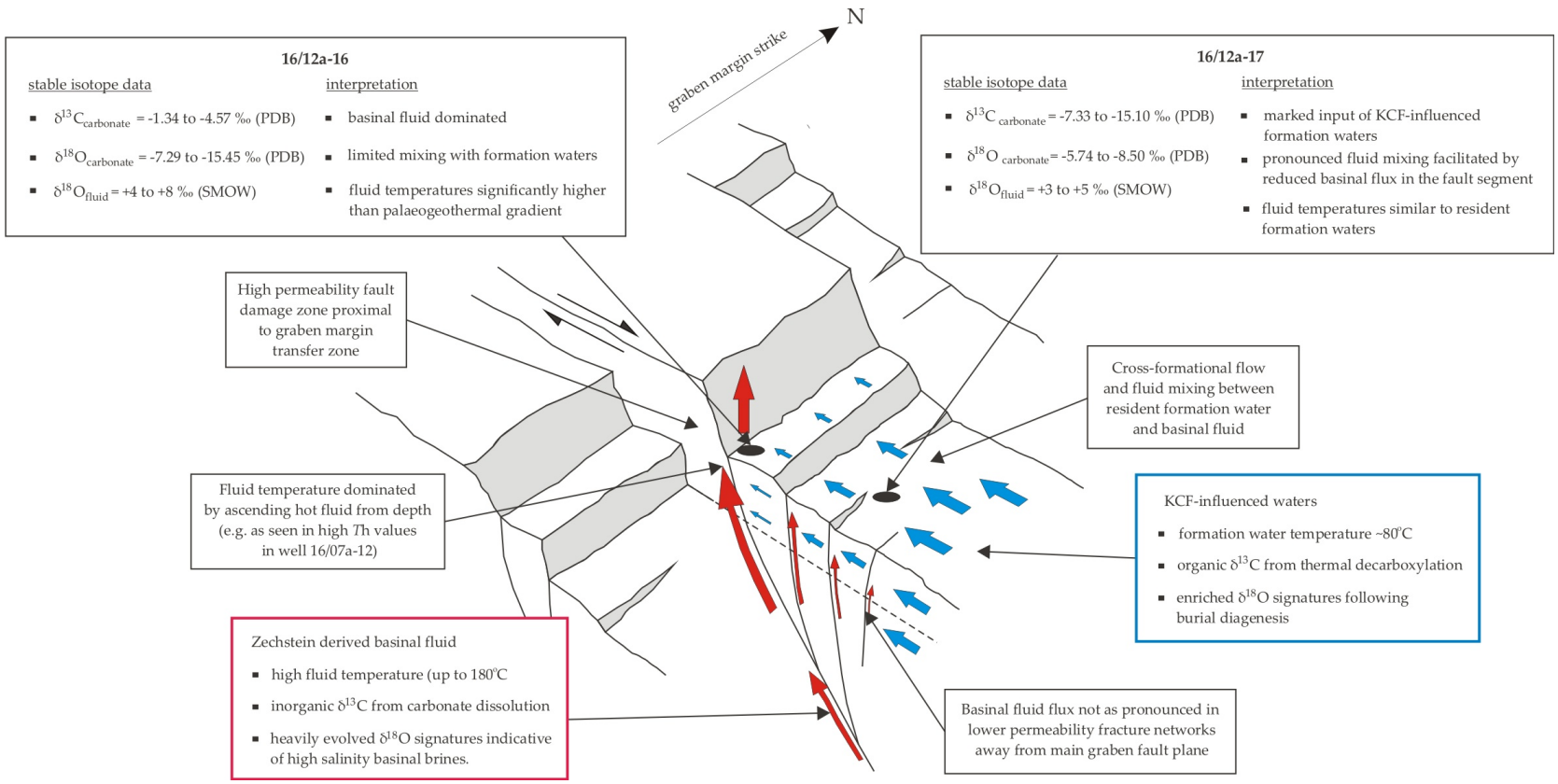

Figure 8.3. Schematic cut-away diagram showing the possible controls imposed by the graben margin fault morphology on the distribution of basinal flux and fluid mixing in the in the Pine Field. Stable isotope data and the conditions of the fluid evolution model proposed in chapter 5 are incorporated to highlight the contrasting fluid-temperature regimes observed on an oilfield scale. Note: the size of arrow indicates the magnitude of fluid flow and input.

The implications of the varying distribution of CO_2-rich basinal fluid flux sites on the margin does not seemingly correlate with the CO_2 concentration contours estimated for the region (Figure 2.10). With the stable isotope characteristics of cements studied in well 16/12a-16 (Pine) seemingly attesting to inorganic CO_2 compositions similar to those in 16/07a-12 (South Brae), this suggests that the distribution of CO_2 flux sites from deep in the graben fill may be more complex than initially proposed by previous studies (e.g. James, 1990; Baines & Worden, 2004). It is therefore probable that numerous foci for CO_2-rich fluid ascent along the graben are present as opposed to a specific CO_2 flux locus in the proximity of the South Brae Field.

However, it must be noted that this variable flow rate model for the graben margin shown in Figure 8.3 is based principally on the stable isotope data acquired in this study. No apparent variations in fracturing and cementation styles are observed between the wells; therefore additional evidence (e.g. fluid inclusion microthermometry) would be required to further validate the proposal regarding degrees of fluid mixing (*see section 8.5*).

8.3. Concluding remarks

The observations and results presented in this thesis provide an insight into the source of the elevated CO_2 concentrations witnessed in the Brae trend oilfields. Applying an integrated approach, this study has demonstrated overpressured CO_2-rich fluids are likely to have flowed through the graben margin fault zone, as manifested in the carbonate fracture cements observed. Dissolution of Zechstein Formation marginal carbonates at depth provides a likely source for the fluids and accompanying CO_2. This conclusion adds credence to the proposals of Wycherley *et al*. (1999) and Baines and Worden (2004) regarding the genesis of CO_2 into this region of the South Viking Graben. Coupled with previous investigations concerning fault hosted cements (e.g .Burley *et al*., 1989), the study provides a greater understanding into the nature of fluid flow and

fault-controlled diagenesis along basin margins frequently encountered in the North Sea.

The results of this study provide a good natural analogue case study for evaluating the movement of CO_2-rich fluids in the subsurface, a key factor when evaluating potential storage sites for CO_2 as part of the carbon capture and storage (CCS) process. Investigation of the boundary fault of the South Viking Graben has demonstrated that CO_2 can migrate considerable distances in the subsurface from an initial source location. With potential leakage from faults a pivotal factor in selecting storage sites, the study highlights the need to fully consider and evaluate fault characteristics and their response to increasing fluid overpressures, a likely consequence of CO_2 subsurface injection (e.g. van Ruth *et al*., 2006; Cappa & Rutqvist, 2011).

8.4. Summary

- The Brae area of the South Viking Graben is host to oilfields containing naturally high-CO_2 contents (up to 35 mol %), with the adjacent graben bounding fault providing a conduit for the introduction of CO_2 from deep in the graben fill ~70 Ma.

- Carbonate fracture cements present in fault damage zones attest to flow of CO_2-rich fluid up the graben bounding fault. Faulting patterns provide evidence of hydraulic fracturing in the fault zone, with the release of overpressured fluids generated from the rapid subsidence of the basin the probable cause. The cement morphology highlights the episodic nature of fluid release up the fault, with mineral precipitation resulting from CO_2 degassing of the ascending fluid inferred.

- Fluid inclusions in the cements exhibit homogenisation temperatures significantly greater than the regional palaeogeothermal gradient during burial of the graben, suggesting the graben margin fault acted as a conduit for hot fluids from depth.

- A high salinity basinal influx from depth concomitant with CO_2 charge into the region provides a probable source for the heated fluids and dissolved solids precipitated as carbonate in the fracture networks. The inorganic $\delta^{13}C$ signatures of CO_2 gas reported in the region attributed to the dissolution of Zechstein carbonates at depth underlying the Brae area suggests the two are inextricably linked.

- Stable oxygen and carbon isotope signatures of the carbonate cements reflect the influence of evolved basinal type fluids. Differing $\delta^{13}C$ vs. $\delta^{18}O$ trends between wells suggest varying degrees of fluid mixing with the resident formation water, a factor potentially governed by fault zone permeability variations related to the morphology of the graben margin.

- Degassing of CO_2 and fluid mixing can be used to account for carbon and oxygen isotopic co-variations in the carbonate cements. Geochemical simulations show CO_2 exsolution in an ascending fluid is controlled by a number of parameters (e.g. flow rate, fluid pressure, and salinity) and resultant carbonate precipitation strongly influenced by fluid-wallrock interaction and solution concentrations rather than CO_2 degassing.

8.5. Possible future work

- The general trend for the distribution of CO_2 in the Brae area established by James (1990) demonstrates decreasing concentrations eastward into the basin coincident with an overall decrease in $\delta^{13}C_{CO2}$. This pattern is attributed to inorganic CO_2 introduced up the basin margin source mixing with resident hydrocarbon influenced sources as it migrates. However, the resolution and quantity of the existing data, notably with regard to $\delta^{13}C$ signatures of CO_2 throughout the region, is limited. This study has highlighted the possibility of multiple conduits for CO_2 flux along the graben bounding fault. Higher resolution sampling and analysis of CO_2 accumulations from well to well on an oilfield scale would thus provide a greater understanding of possible CO_2

sources and migration pathways with respect to morphology of the graben margin.

- Although there is a wide body of evidence suggesting the large volumes of CO_2 in the Brae area are derived from Zechstein Formation carbonate sequences in the basin fill, conclusive $\delta^{13}C$ signatures for CO_2 generated from the Zechstein are not available. Therefore, future investigation could focus on analysing $\delta^{13}C$ ratios of CO_2 released following the dissolution of analogous marginal-carbonate facies lithologies identified underlying the region.

- The study highlighted the need for a greater understanding of the distribution and morphology of the fault arrangements on the western margin of the South Viking Graben. With fault characteristics pivotal in controlling fluid flow up the graben margin, determination of fault traces (2D and 3D) adjacent to the margin would be invaluable, allowing comparison of isotopic or microthermometric trends in particular wells to specific fault morphologies.

- This study focused on the high CO_2 area of the graben bounding fault encompassing the Brae fields (South, Central) and 'Trees' block fields. The more southerly T-block fields (see Figure 2.6) also exhibit similar high CO_2 volumes (15 – 20 mol %; Gambardo & Donagemma, 2003) which are presumed to have entered the fields up the graben margin. Investigation of potential fault hosted fracture cements in this region would enable a comparative study (petrography, stable isotopes, and fluid inclusions) with sections of the fault zone examined in this study, allowing the applicability of the proposed CO_2 flux up the graben margin to be assessed.

References

ABIYE, T. A. & HAILE, T. (2008) Geophysical exploration of the Boku geothermal area, Central Ethiopian Rift. *Geothermics*, **37**, 586 – 596.

ALLEN, D. E., STRAZISAR, B. R., SOONG, Y. & HEDGES, S. W. (2005) Modelling carbon dioxide sequestration in saline aquifers: significance of elevated pressures and salinities. *Fuel Processing Technology*, **86**, 1569 – 1580.

ANDERSON, S. & NEWELL, R. (2004) Prospects for Carbon Capture and Storage Technologies. *Annu. Rev. Environ. Resour*. **29**, 109 – 142.

ANDREWS-SPEED, C. P., OXBURGH, E. R. & COOPER, B. A. (1984) Temperatures and depth-dependent heat flow in western North Sea. *AAPG Bulletin*, **68**, 1764 – 1781.

BACHU, S. (2000) Sequestration of CO_2 in geological media: criteria and approach for site selection in response to climate change. *Energy Conversion & Management*. **41**, 953 – 970.

BACHU, S. (2003) Screening and ranking of sedimentary basins for sequestration of CO_2 in geological media in response to climate change. *Environmental Geology*. **44**, 277 – 289.

BADLEY, M. E., PRICE, J. D., RAMBECH DAHL, C. & AGDESTEIN, T. (1988) The structural evolution of the northern Viking Graben and its bearing upon extensional modes of basin formation. *Journal of the Geological Society of London*, **145**, 455 – 472.

BAINES, S. J. & WORDEN, R. H. (2004) The long-term fate of CO_2 in the subsurface: natural analogues for CO_2 storage. *In*: BAINES, S. J. & WORDEN, R. H. (eds.) *Geological Storage of Carbon Dioxide*. Geological Society, London, Special Publications. **233**, 59 – 86**.**

BAINES, S., BURLEY, S. D. & GIZE, A. (1991) Sulphide mineralisation and hydrocarbon migration in North Sea oilfields. *In:* PAGEL, M. & LEROY, J. (eds.) *Proceedings of the 25th Anniversary Mineral Deposita Meeting on Source, Transport, and Deposition of Metals, Nancy, 1991*, Balkema, Rotterdam, 87 – 91.

BALLETINE, C. J., O'NIONS, R. K. & COLEMAN, M. L. (1996) A Magnus opus: helium, neon and argon isotopes in a North Sea oilfield. *Geochim. Cosmochim. Acta*. **60**, 831 – 849.

BANKS, D. A., BOYCE, A. J. & SAMSON, I. M. (2002) Constraints on the origins of fluids forming Irish Zn-Pb-Ba deposits. Evidence from the composition of fluid inclusions. *Economic Geology*, **97**, 471 – 480.

BARCLAY, S. A. & WORDEN, R. H. (2000) Geochemical modelling of diagenetic reactions in a sub-arkosic sandstone. *Clay Minerals*. **35**, 57 – 67.

BAUMANN, A. & HOFMANN, R (1988) Strontium isotope systematics of hydrothermal vein minerals in deposits of West Germany. *Geologische Rundschau*, **77**, **3**, 747 – 762.

BECKER, J. A., BICKLE, M. J., GALY, A. & HOLLAND, T. J. B. (2008) *Himalayan metamorphic CO2 fluxes: Quantitative constraints from hydrothermal springs.* Earth and Planetary Science Letters, **265**, 616 – 629.

BERGFELD, D., GOFF, F. & JANIK, C. J. (2001) Carbon isotope systematics and CO_2 sources in The Geysers – Clear Lake region, northern California, USA. *Geothermics*, **30**, 303 – 331.

BJØRLYKKE, K. & GRAN, K. (1994) Salinity variations in North Sea formation waters: implications for large-scale fluid movements. *Marine and Petroleum Geology*. **11**, 1, 5 – 9.

BJØRLYKKE, K. (1989) Formation of secondary porosity: how important is it? *In:* MCDONALD D. A. & SURDHAM R.C. (eds.) *Clastic diagenesis*. AAPG Memoirs, **37**, 227 – 286.

BLANCHET, A., PAGEL, M., WALGENWITZ, F. & LOPEZ, A. (2003) Microspectoflourimetric and microthermometric evidence for variability in hydrocarbon fluid inclusions in quartz overgrowths: implications for inclusion trapping in the Alwyn North field, North Sea. *Organic Geochemistry*, **34**, 1477 – 1490.

BLUNT, M., FAYERS, F. J. & ORR, F. M. (1993) Carbon dioxide in enhanced oil recovery. *Energy Conversion & Management*. **34**, 1197 - 1204.

BODNAR, R. J. (1983) A method of calculating fluid inclusion volumes based on vapour bubble diameters and PVTX properties of inclusion fluids. *Economic Geology*, **78**, 535 – 542.

BODNAR, R. J. (1992) The system H_2O – NaCl (abs.).*PACROFI IV: Pan-American Conference on research on fluid inclusions, Lake Arrowhead, California, 21 – 25 May, 1992*.

BODNAR, R. J., BINNS, P. R. & HALL, D. L. (1989) Synthetic fluid inclusions – VI. Quantitative evaluation of the decrepitation behaviour of fluid inclusions in quartz at one atmosphere confining pressure. *Journal of Metamorphic Geology*, **7**, 229 – 242.

BOLES, J. R. & GRIVETTI, M. (2000) Calcite cementation along the Refugio/Carneros fault, Coastal California: a link between deformation, fluid movement and fluid-rock interaction at a basin margin. *Journal of Geochemical Exploration*, **69-70**, 313 – 316.

BOTTINGA, Y. (1968). Calculation of Fractionation Factors for Carbon and Oxygen Isotopic Exchange in the System Calcite–Carbon Dioxide–Water. *Journal of Physical Chemistry*, **72**, **5**, 800 – 808.

BOWERS, T. S. (1991) The deposition of gold and other metals: Pressure-induced immiscibility and associated stable isotope signatures. *Geochim. Cosmochim. Acta*, **55**, 2417 – 2434.

BROWN, A. A. (1999) Distinguishing mantle CO_2 from decarbonation CO_2 in High CO_2 gases. *AAPG Hedberg Research Conference: Natural Gas Formation and Occurrence, June 6-10, 1999, Durango Colarado*, Abstract.

BRYANT, E. (1997) Climate process and change. *Cambridge University Press*, pp. 225.

BUHRIG, G. C. (1989) Geopressured Jurassic reservoirs in the Viking Graben: modelling and geological significance. *Marine and Petroleum Geology*, **6**, 31 – 48.

BURKE, W. H., DENSION, R. E., HETHERINGTON, E. A., KOEPNICK, R. B., NELSON, H. F. & OTTO, J. B. (1982) Variation of sweater $^{87}Sr/^{86}Sr$ throughout the Phanerozoic time. *Geology*, **10**, 516 – 519.

BURLEY, S. D. (1993) Models of burial diagenesis for deep exploration plays in Jurassic fault traps of the Central and Northern North Sea. *In:* PARKER, J. R. (ed.) *Petroleum Geology of Northwest Europe: Proceedings of the 4th Conference*, Geological Society, London, 1353 – 1375.

BURLEY, S. D., MULLIS, J. & MATTER, A. (1989) Timing diagenesis in the Tartan reservoir (UK North Sea): constraints from combined cathodoluminescence microscopy and fluid inclusion studies. *Marine and Petroleum Geology*, **6**, 98 – 120.

CAINE, J. S., EVANS, J. P. & FORSTER, C. P. (1996) Fault zone architecture and permeability structure. *Geology*, **24**, 1125 – 1128.

CALDEIRA, K. & RAU, G. H. (2000) Accelerating carbonate dissolution to sequester carbon dioxide in the ocean: Geochemical implications. *Geophysical Research Letters*. **27**, 225 – 228.

CAPPA, F. & RUTQVIST, J. (2011) Modeling of couple deformation and permeability evolution during fault reactivation induced by deep underground injection of CO_2. *International Journal of Greenhouse Gas Control*. **5**, **2**, 336 – 346.

CARSTENS, H. & FINSTAD, K. G. (1981) Geothermal Gradients of the Northern North Sea Basin, 59-62°N. *IN:* ILLING, L .V & HOBSON, G. D. (eds.) *Petroleum Geology of the Continental Shelf of North-West Europe*, Institute of Petroleum Geology, London, 152 – 161.

CATHLES, L. M. & SMITH, J. E. (1983) Thermal constraints on the formation of Mississippi Valley-type lead-zinc deposits and their implications for episodic basin watering and deposit genesis. *Economic Geology*, **78**, 983 – 1002.

CAYLEY, G. T. (1987) Hydrocarbon migration in the central North Sea. *In:* BROOKS, J. & GLENNIE, K. W. (eds.) *Petroleum geology of northwest Europe, London*. Graham & Trotman, 549 – 555.

CHACKO, T. & DEINES, P. (2008) Theoretical calculation of oxygen isotope fractionation factors in carbonate systems. *Geochim. Cosmochim. Acta*, **72**, 3642 – 3660.

CHACKO, T., MAYEDA, T. K., CLAYTON, R. N. & GOLDSMITH, J. R. (1991) Oxygen and carbon isotope fractionations between CO_2 and calcite. *Geochim. Cosmochim. Acta*, **55**, 2867 – 2882.

CHERRY, S. T. J. (1993) The interaction of structure and sedimentary process controlling deposition of the Upper Jurassic Brae Formation Conglomerate, Block 16/7, North Sea. *In:* PARKER, J. R. (ed.) *Petroleum Geology of Northwest Europe: Proceedings of the 4th Conference*. The Geological Society of London, 387 – 400.

CLARK, J. A., STEWART, S. A. & CARTWRIGHT, J. A. (1998) Evolution of the NW margin of the North Permian Basin, UK North Sea. *Journal of the Geological Society, London*, **155**, 663 – 676.

CLAUSER, C. & VILLINGER, H. (1990) Analysis of conductive and convective heat transfer in a sedimentary basin, demonstrated for the Rheingraben. *Geophys. J. Int.*, **100**, 393 – 414.

CLAYTON, J. L., SPENCER, C. W., KONCZ, I. & SZALAY, A. (1990) Origin and migration of hydrocarbon gases and carbon dioxide, Békés Basin, southeastern Hungary. *Organic Geochemistry*, **15**, **3**, 233 – 247.

CLAYTON, R. N., FRIEDMAN, I., GRAF, D. L., MAYEDA, T. K., MEENTS, W. F. & SCHIMP, N. F. (1966) The origin of saline formation waters: 1. Isotopic composition. *Journal of Geophysical Research*, **71**, 3869 – 3882.

CLENNELL, M. B. (1997) Tortuosity: a guide through the maze. *In:* LOVELL, M. A. & HARVEY, P. K. (eds.) Developments in Petrophysics. *Geol. Soc. London. Spec. Publ.*, **122**, 299 – 344.

COCKINGS, J. H., GIFFORD KESSLER II, L., MAZZA, T. A. & RILEY, L. A. (1992) Bathonian to mid-Oxfordian sequence stratigraphy of the South Viking Graben, North Sea. *In:* HARDMAN, R. F. P. (ed.) *Exploration Britain: Insights for the Next Decade*, Spec. Publ. Geol. Soc. London, **67**, 65 – 105.

COLLINS, P. L. F. (1979) Gas Hydrates in CO_2-Bearing Fluid Inclusions and the Use of Freezing Data for Estimation of Salinity. *Economic Geology*, **74**, 1435 – 1444.

CORNFORD, C., (1998) Source rocks and hydrocarbons of the North Sea. *In:* GLENNIE, K.W. (ed.) *Petroleum geology of the North Sea: basic concepts and recent advances (4th edition)* Blackwell, 376 – 462.

CRAW, D., MORRISON, A. D. & WALCOTT, C. R. (1992) Fluid inclusion evidence for widespread shallow hydrothermal activity in South Victoria Land, Antarctica. *New Zealand Journal of Geology and Geophysics*, **35**, **1**, 21 – 28.

CURTIS, C. D. (1978) Possible links between sandstone diagenesis and depth related geochemical reactions occurring in enclosing mudstones. *Journal of Geological Society, London*, **135**, 107 – 117.

DAVIES, R. J., O'DONNELL, D., BENTHAM, P. N., GIBSON, J. P. C., CURRY, M. R., DUNAY, R. E. & MAYNARD, J. R. (1999) The origin and genesis of major Jurassic unconformities with the triple junction area of the North Sea, UK, *Petroleum Geology Conference series*, **5**, 117 – 131.

DEINES, P., LANGMUIR, D. & HARMON, R. S. (1974) Stable isotope ratios and the existence of a gas phase in the evolution of carbonate ground waters. *Geochim. Cosmochim. Acta*, **38**, 1147 – 1164.

DONATO, J. A. & TULLY, M. C. (1982) A proposed granite batholith along the western flank of the North Sea Viking Graben. *Geophysical Journal of the Royal Astronomical Society*, **69**, 187 – 195.

DUAN, Z. & SUN, R. (2003) An improved model calculating CO_2 solubility in pure water and aqueous NaCl solutions from 273 to 533 K and 0 to 2000 bar. *Chemical Geology*, **193**, 257 – 271.

EGEBERG, P .K. & AAGAARD, P. (1989) Origin and evolution of formation waters from oil fields on the Norwegian shelf. *Applied Geochemistry*, **4**, 131 – 142.

EICHHUBL, P. & BOLES, J. R. (2000) Rates of fluid flow in fault systems – evidence for episodic rapid fluid flow in the Miocene Monterey Formation, coastal California. *American Journal of Science*, **300**, 571 – 600.

EICHHUBL, P., DAVATZES, N. C. & BECKER, S. P. (2009) Structural and diagenetic Control of fluid migration and cementation along the Moab Fault, Utah. *AAPG Bulletin*, **93**, 653 – 681.

ENICK, P. M. & KLARA, S. M. (1990) CO_2 solubility in water and brine under reservoir conditions. *Chemical Engineering Communications*, **90**, 23 – 33.

EVANS, J. P., FORSTER, C. B., GODDARD, J. V. (1997) Permeability of fault-related rocks, and implications for hydraulic structure of fault zones. *Journal of Structural Geology*, **19**, 1393 – 1404.

EVANS, T. R. & COLEMAN, N. C. (1974) North Sea Geothermal Gradients. *Nature*, **247**, 28 – 30.

EVANS, T. R. (1977) Thermal properties of North Sea rocks. *Log Analyst*, **18**, **2**, 3 – 12.

FÆRSETH, R. B. (1996) Interaction of Permo-Triassic and Jurassic extensional fault-block during the development of the northern North Sea. *Journal of the Geological Society, London*, **153**, 931 – 944.

FAGERLAND, N. (1983) Tectonic Analysis of a Viking Graben Border Fault. *AAPG Bulletin*, **67, 11**, 2125 – 2136.

FAIRLEY, J. P. & HINDS, J. J. (2004a) Rapid transport pathways for geothermal fluids in an active Great Basin fault zone. *Geology*, **32**, 825 – 828.

FAIRLEY, J. P. & HINDS, J. J. (2004b) Field observation of fluid circulation patterns in a normal fault system, *Geophys. Res. Lett*., **31**, L19502, doi:10.1029/2004GL020812.

FARMER, R. E. (1965) Genesis of Subsurface Carbon Dioxide. *In:* YOUNG, A. & GALLEY, J. E. (eds.) *Fluids in Subsurface Environments*. AAPG Memoir, **4**, 378 – 385.

FAURE, G. (1986) *Principles of Isotope Geology (2nd Edition).* John Wiley & Sons, New York, pp. 183 – 199.

FINNIE, A. B. (2001) A case study of high pressure brine flows within the Zechstein Supergroup of the Southern North Sea. *SPE/IADC Drilling Conference, 27th February – 1st March 2001, Amsterdam, Netherlands*, pp 8.

FISCHER, M., BOTZ, R.VG, SCHMIDT, M., ROCKENBAUCH, K., GARBE-SCHÖNBERG, D., GLODNY, J., GERLING, P. & LITTKE, R. (2006) Origins of CO_2 in Permian carbonate reservoir rocks (Zechstein, Ca2) of the NW-German Basin (Lower Saxony). *Chemical Geology*, **227**, 184 – 213.

FISHER, M. J. & MUDGE, D. C. (1998) Triassic. In: GLENNIE, K. W. (ed.) *Petroleum geology of the North Sea: basic concepts and recent advances (4th edition)* Blackwell, 245–293.

FLETCHER, K. J. (2003a) The South Brae Field, Blocks 16/07a, 16/07b, UK North Sea. *In*: GLUYAS, J. G. & HICHENS, H. M. (eds.) 2003. *United Kingdom Oil and Gas Fields, Commemorative Millennium Volume.* Geological Society, London, Memoir, **20**, 211 – 221.

FLETCHER, K. J. (2003b) The Central Brae Field, Blocks 16/07a, 16/07b, UK North Sea. *In*: GLUYAS, J. G. & HICHENS, H. M. (eds.) 2003. *United Kingdom Oil and Gas Fields, Commemorative Millennium Volume.* Geological Society, London, Memoir, **20**, 183 – 190.

FOLK, R. L. & LAND, L. S. (1975) Mg/Ca ratios and salinity: two controls over crystallization of dolomite. *AAPG Bulletin*, **59**, **1**, 60 – 68.

FRANTZ, J. D., POPP, R. K. & HOERING, T. C. (1992) The compositional limits of fluid immiscibility in the system H_2O-NaCl-CO_2 as determined with the use of synthetic fluid inclusions in conjunction with mass spectrometry. *Chemical Geology*, **98**, 237 – 255.

FRIEDMAN, I. & O'NEIL, J. R. (1977) Compilation of Stable Isotope Fractionation Factors of Geochemical Interest. *In:* M. FLEISCHER (ed.) *Data of geochemistry (6th Edition)*. USGS Prof. Paper, 440 – KK. p. 12.

GALE, J. (2004) Why do we need to consider geological storage of CO_2? *In*: BAINES, S. J. & WORDEN, R. H. (eds.) *Geological Storage of Carbon Dioxide*. Geological Society, London, Special Publications. **233**, 7 – 15**.**

GAMBARO, M. & DONAGEMMA, V. (2003) The T-Block Fields, Block 16/17, UK North Sea. *In*: GLUYAS, J. G. & HITCHENS, H. M. (eds.) *United Kingdom Oil and Gas Fields, Commemorative Millennium Volume*, Geological Society Memoir, **20**, 369 – 382.

GARLAND, C. R. (1993) Miller Field: reservoir Stratigraphy and its impact on development. *In:* PARKER, J. R. (ed.), *Petroleum Geology of Northwest Europe: Proceedings of the 4th Conference*. The Geological Society, London, 401 – 414.

GARVEN, G. & RAFFENSPERGER, J. P. (1997) Hydrogeology and geochemistry of ore genesis in sedimentary basins. *In:* BARNES, H. L. (ed.) *Geochemistry of Hydrothermal Ore Deposits .3rd edition,* John Wiley & Sons, New York, 125 – 189.

GAUS, I., MOHAMED, A. & CZERNICHOWSKI-LAURIOL, I. (2005) Reactive transport modelling of the impact of CO2 injection on the clayey cap rock at Sleipner (North Sea). *Chemical Geology*. **217**, 319 – 337.

GAWTHORPE, R. L. & HURST, J. M. (1993) Transfer zones in extensional basins: their structural style and influence on drainage development and stratigraphy. *Journal of the Geological Society of London*, **150**, 1137 – 1152

GIRARD, J-P., MUNZ, I. A., JOHANSEN, H., LACHARPAGNE, J-C. & SOMMER, F. (2002) Diagenesis of the Hild Brent sandstones, northern North Sea: isotopic evidence for the prevailing influence of deep basinal water. *Journal of Sedimentary Research*, **72, 6**, 746 – 759.

GLASSMAN, J. R (1992) The fate of feldspar in the Brent Group reservoirs, North Sea: a regional synthesis of diagenesis in shallow, intermediate, and deep burial environments. *In:* MORTON A. C., HASZELDINE, R. S., GILES, M. R., & BROWN, S. (eds.) *Geology of the Brent Group*. Geological Society of London, Special Publication, **61**, 401 – 419.

GLEESON, S. A. & TURNER, W. A. (2006) Fluid inclusion constraints on the origin of the brines responsible for Pb-Zn mineralisation at Pine Point and coarse non-saddle dolomite formation in the southern Northwest Territories. *Geofluids*, **7**, **1**, 51 – 68.

GLENNIE, K. W. (1990) Outline of North Sea History & Structural Framework. *In*: GLENNIE, K. W. (ed.) *Introduction to the Petroleum Geology of the North Sea,* Blackwell Scientific Publications, 34 – 77.

GOLDSTEIN, R. H. & REYNOLDS, T. J. (1994) Systematics of fluid inclusions in diagenetic minerals. *Society of Economic Paleontologists and Mineralogists Short Course*, **31**, pp. 199.

GOLDSTEIN, R. H. (1986) Re-equilibration of fluid inclusions in low temperature calcium-carbonate cement. *Geology*, **14**, 792 – 795.

GOLDSTEIN, R. H. (2001) Fluid inclusions in sedimentary and diagenetic systems. *Lithos*, **55**, 159 – 193.

GREENWOOD, P. J. , SHAW, H. F. & FALLICK, A. E. (1994) Petrographic and isotopic evidence for diagenetic processes in middle Jurassic sandstones and mudrocks from the Brae area, North Sea. *Clay Minerals.* **29**, 637 – 650.

GREGG, J. M. (2004) Basin fluid flow, base-metal sulphide mineralization and the development of dolomite petroleum reservoirs. *In:* BRAITHWAITE, C. J. R., RIZZI, G. & DARKE, G. (eds.) *The Geometry and Petrogenesis of Dolomite Hydrocarbon Reservoirs.* Geological Society, London, Special Publications, **235**, 157 – 175.

HAAS, J. L. (1978) An empirical equation with the tables of smoothed solubilities of methane in water and aqueous sodium chloride solutions up to 25 weight percent, 360°C, and 138 MPa. *U.S.G.S. Open-File Report*, **78-1004**.

HAMILTON, P. J., FALLICK, A. E., MACINTYRE, R. M. & ELLIOT, S. (1987) Isotopic tracing of the provenance and diagenesis of Lower Brent Group sands, North Sea. *In:* BROOKS, J. & GLENNIE, K. (eds.) *Petroleum Geology of North West Europe*. London, Graham & Trotman, 939 – 949.

HANOR, J. S. (1980) Dissolved methane in sedimentary brines: potential effect on the PVT properties of fluid inclusions. *Economic Geology*, **75**, 603 – 609.

HANOR, J. S. (1994) Origin of saline fluids in sedimentary basins. *In:* PARNELL, J. (ed.) *Geofluids; origin, migration, and evolution of fluids in sedimentary basins*. Geological Society, London, Special Publications, **78**, 151 – 174.

HANOR, J. S. 2000. Barite-celestine geochemistry and environments of formation. *In:* ALPERS, C., JAMBOR, J. & NORSTROM, K. (eds.). *Sulfate minerals*. Reviews in Mineralogy and Geochemistry. **40**, 193 – 275.

HARDY, J. A. & HART, R. G. (1994) The South Brae Field. *In:* WARREN, E. A. & SMALLEY, P. C. (eds.) North Sea Formation Waters Atlas. *Geological Society London, Memoir* **15**, 65.

HARDY, J. A., BARTHORPE, R. T., PLUMMER, M. A. & RHUDY, J. S. 1994. Scale Control in the South Brae Field. *SPE Production & Facilities*. 127 – 131.

HARMS, J. C., TACKENBERG, P., PICKLES, E. & POLLOCK, R. E. (1981) The Brae Oilfield area. *In:* ILLING, L .V & HOBSON, G. D. (eds.) *Petroleum Geology of the Continental Shelf of North-West Europe*, Institute of Petroleum Geology, London, 352 – 357.

HARRIS, J. P. & FOWLER, R. M. (1987) Enhanced prospectivity of the Mid-Late Jurassic sediments of the South Viking Graben, northern North Sea. *In:* BROOKS, J. & GLENNIE, K. W. (eds.) *Petroleum Geology of North West Europe*, Graham & Trotman, 879 – 898.

HASZELDINE, R. S. (2009) Carbon Capture and Storage: How green can black be? *Science*, **325**, 1647 – 1652.

HASZELDINE, R. S., BRINT, J. F., FALLICK, A. E., HAMILTON, P. J. & BROWN S. (1992) Open and restricted hydrologies in Brent Group diagenesis: North Sea. *In:* MORTON A. C., HASZELDINE, R. S., GILES, M. R., & BROWN, S. (eds.) *Geology of the Brent Group*. Geological Society of London, Special Publication, **61**, 401 – 419.

HASZELDINE, R. S., QUINN, O., ENGLAND, G., WILKINSON, M. SHIPTON, Z. K., EVANS, J. P., HEATH, J., CROSSLEY, L., BALLENTINE, C. J. & GRAHAM, C. M. (2005) Natural geochemical analogues for carbon dioxide storage in deep geological porous reservoirs, a United Kingdom perspective. *Oil and Gas Technology – Review*. IFP **60**, **1**, 33 – 49.

HEDENQUIST, J. W. & HENLEY, R. W. (1985) The importance of CO_2 on freezing point measurements of fluid inclusions; evidence from active geothermal systems and implications for epithermal ore deposition. *Economic Geology*, **80**, 1379 – 1406.

HENDERSON, G. M., MARTEL, D. J., O'NIONS, R. K. & SHACKLETON, N. J. (1994) Evolution of seawater $^{87}Sr/^{86}Sr$ over the last 400 ka: the absence of glacial/interglacial cycles. *Earth and Planetary Science Letters*, **128**, **3-4**, 643 – 651.

HEPPLE, R. P. & BENSON, S. M. (2005) Geologic storage of carbon dioxide as a climate change mitigation strategy: performance requirements and the implications of surface seepage. *Environmental Geology*. **47**, 576 – 585.

HILGERS, C., KOEHN, D., BONS, P. D. & URAI, J. L. (2001) Development of crystal morphology during unitaxial growth in a progressively widening vein: II. Numerical simulations of the evolution of antiaxial fibrous veins. *Journal of Structural Geology*, **23**, 873 – 885.

HILL, C. A. (1995) H_2S-related porosity and sulphuric acid oil-field karst. *In:* BUDD, D. A., SALLER, A. H. & HARRIS, P. M. (eds.) *Unconformities and porosity in carbonate strata*. AAPG Memoir, 63, 301 – 306.

HODGSON, N. A., FARNSWORTH, J. & FRASER, A. J. (1992) Salt-related tectonics, sedimentation and hydrocarbon plays in the Central Graben, North Sea, UKCS. *In:* HARDMAN, R. F. P. (ed.) *Exploration Britain: Insights for the Next Decade*, Spec. Publ. Geol. Soc. London, **67**, 31 – 63.

HOLLAND, H. D. & MALININ, S. D. (1979) The solubility and occurrence of non-ore minerals. *In:* BARNES, H. L. (ed.) *Geochemistry of Hydrothermal Ore Deposits (2nd Edition)*, Wiley & Sons, 461 – 508.

HOLLOWAY, S. (1997) Safety of the underground disposal of carbon dioxide. *Energy Conversion & Management*. **38** suppl. 241 – 245.

HOLLOWAY, S., REAY, D. M., DONATO, J. A. & BEDDOE-STEPHENS, B. (1991) Distribution of granite and possible Devonian sediments in part of the East Shetland Platform. *Journal of Geological Society, London*, **148**, 635 – 638.

HOLM, G. M. (1998) Distribution and origin of overpressure in the Central Graben of the North Sea. *In:* LAW, B. E., ULMISEK, G. F. & SLAVIN, V. I. (eds.) *Abnormal pressures in hydrocarbon environments*. AAPG Memoir, **70**, 123 – 144.

HOOK, J., ABHVANI, A, GLUYAS, J. G. & LAWLOR, M. (2003) The Birch Field, Block 16/12a, UK North Sea. *In*: GLUYAS, J. G. & HICHENS, H. M. (eds.) 2003. *United Kingdom Oil and Gas Fields, Commemorative Millennium Volume.* Geological Society, London, Memoir, **20**, 161 – 181.

HOOKER, P. J. O'NIONS, R. K. & OXBURGH, E. R. (1985) Helium isotopes in North Sea gas fields and the Rhine rift. *Nature*. **318**, 273 – 275.

HORITA, J. (2008) The dolomite problem: Oxygen isotope fractionation to elevated temperatures. Goldschmidt Conference Abstracts, A391.

HORITA, J., COLE, D. R. & WESOLOWSKI, D. J. (1995) The activity-composition relationship of oxygen and hydrogen isotopes in aqueous salt solutions, III, Vapour-liquid water equilibration of NaCl solutions to 350°C. *Geochim. Cosmochim. Acta*, **59**, 1139 – 1151.

HOSPERS, J. & EDIRIWEERA, K. K. (1991) Depth and configuration of the crystalline basement in the Viking Graben Area, northern North Sea. *Journal of the Geological Society*, **148**, 261 – 265.

HUTCHEON, I. & ABERCROMBIE, H. (1990) Carbon dioxide in clastic rocks and silicate hydrolysis. *Geology*. **18**, 541 – 544

IRWIN, H. (1980) Early diagenetic carbonate precipitation and pore fluid migration in the Kimmeridge Clay of Dorset, England. *Sedimentology*, 27, 5, 577 – 591.

IRWIN, H., CURTIS, C. D. & COLEMAN, M. L. (1977) Isotopic evidence for source of diagenetic carbonates formed during burial of organic rich sediments. *Nature.* **269**, 209 – 213.

ISAKSEN, G. H., PATIENCE, R., VAN GRAAS, G. & JENSSEN, A. I. (2002) Hydrocarbon system analysis in a rift basin with mixed marine and nonmarine source rocks: The South Viking Graben, North Sea. *AAPG Bulletin*. **84, 4**, 557 – 591.

JACKSON, C. A-L. & LARSEN, E. (2008) Temporal constraints on basin inversion provided by 3D seismic and well data: a case study from the South Viking Graben, offshore Norway. *Basin Research*, **20**, 397 – 417.

JACKSON, C. A-L. & LARSEN, E. (2009) Temporal and spatial development of a gravity-driven normal fault array: Middle-Upper Jurassic, South Viking Graben, northern North Sea. *Journal of Structural Geology*, **31**, 388 – 402.

JAMES, A. T. (1990) Correlation of Reservoired Gases Using the Carbon Isotopic Compositions of Wet Gas Components. *AAPG Bulletin*. **74**, 1442 – 1458.

JANSSEN, C., ROMER, R. L.., PLESSEN, B., NAUMANN, R., HOFFMANN-ROTHE, A. & MATAR, A. (2007) Contrasting fluid regimes along the Dead Sea Transform. *Geofluids*, 7, 3, 275 – 291.

JENDEN, P. D., DRAZAN, D. J. & KAPLAN, I. R. (1993) Mixing of thermogenic natural gases in Northern Appalachian Basin. *AAPG Bulletin*. **77**, 980 – 998.

JOHNSON, J. W., OELKERS, E. H. & HELGESON, H. C. (1992) SUPCRT92: a software package for calculating the standard molal thermodynamic properties of minerals, gases, aqueous species, and reactions from 1 to 5000 bar and 0 to 1000°C. *Computer Geoscience*, **18**, 899 – 947.

JOWETT, E C., CATHLES, L. M. & DAVIS, B. W. (1993) Predicting depths of gypsum dehydration in evaporitic sedimentary basins. *AAPG Bulletin*, **77**, **3**, 402 – 413.

JUSTWAN, H., DAHL, B. & ISAKSEN, G. H. (2006) Geochemical characterization and genetic origin of oils and condensates in the South Viking Graben, Norway. *Marine and Petroleum Geology*. **23**, 213 – 239.

KASZUBA, J. P., JANECKY, D. R. & SNOW, M. G.(2005) Experimental evaluation of mixed fluid reactions between supercritical carbon dioxide and NaCl brine: Relevance to the integrity of a geologic carbon repository. *Chemical Geology*. **217**, 277 – 293.

KLUSMAN, R. W. (2003) Evaluation of leakage potential from a carbon dioxide EOR/sequestration project. *Energy Conversion and Management*. **44**, 1921 – 1940.

KNAUSS, K. G., JOHNSON, J. W. & STEEFEL, C. I. (2005) Evaluation of the impact of CO_2, co-contaminant gas, aqueous fluid and reservoir rock interactions on the geologic sequestration of CO_2. *Chemical Geology*. **217**, 339 – 350.

KNAUTH, L. P. & BEEUNAS, M. A. (1986) Isotope geochemistry of fluid inclusions in Permian halite with implications for the isotopic history of ocean water and the origin of saline of formation waters. *Geochim. Cosmochim. Acta*, **50**, 419 – 433.

KOPF, A., BEHRMANN, J. H., DEYHLE, A., ROLLER, S. & ERLENKEUSER, H. (2003) Isotopic evidence (B, C, O) of deep fluid processes in fault rocks from the active Woodlark Basin detachment zone. *Earth and Planetary Science Letters*, **208**, 51 – 68.

KORTE, C., JASPER, T., KOZUR, H. W. & VEIZER, J. (2006) $^{87}Sr/^{86}Sr$ record of Permian seawater. *Palaeogeography, Palaeoclimatology, Palaeoecology*, **240**, 89 – 107.

KREBS, W. & MACQUEEN, R. (1984) Sequence of diagenetic and mineralisation events: Pine Point lead-zinc property, NWT, Canada. *Bull. Can. Petrol. Geol*., **32**, 434 – 464.

LAMPE, C. & PERSON, M. (2000) Episodic hydrothermal fluid flow in the Upper Rhinegraben (Germany). *Journal of Geochemical Exploration*, **69 – 70**, 37 – 40.

LARTER S. R., APLIN A. C., BJOROY M., CARPENTIER B., CHEN M., CURTIS C., ENGLAND W. A., ESPITALIE J., FLEET A. J., GOODWIN N. S., HALL P.B., HUC A. Y., HUGHES C., JACKSON D. E., JENSEN H. K. B., LAFARGUE E., MACAULAY G., MACLEOD G., OXTOBY N. H., PETCH G. S., PRIMMER T., SMALLEY C. P. & TRABELSI K. (1995) THERMIE Reservoir Geochemistry Project: Miller Field Demonstration. *CEC THERMIE Reservoir Geochemistry Project*, pp. 44.

LE GUERN, L., SHANKLIN, E. & TEBOR, S. (1992) Witness accounts of the catastrophic event of August 1986 at Lake Nyos (Cameroon). *Journal of Volcanology and Geothermal Research*. **51**, **1-2**, 171 – 184.

LEACH, D. L., PLUMLEE, G. S., LANDIS, G. P., ROWAN, E. L. & VIETS, J. G. (1991) Origin of late dolomite cement by CO_2-saturated deep basin brines: Evidence from the Ozark region, central United States. *Geology*, **19**, 348 – 351.

LEE, M. R., MARTIN, R. W., TRAGER-COWAN, C. & EDWARDS, P. R. (2005) Imaging of cathodoluminescence zoning in calcite by scanning electron microscopy and hyperspectral mapping. *Journal of Sedimentary Research*, **75**, 313 – 322.

LU, J. (2008) CO_2 interaction with aquifer and seal on geological timescales: the Miller oilfield. Ph.D thesis, The University of Edinburgh, pp. 194.

LU, J., WILKINSON, M., HASZELDINE, R. S. & FALLICK, A. E. (2009) Long-term performance of a mudrock seal in natural CO_2 storage. *Geology*, **37**, **1**, 35 – 38.

MACAULAY, C. I., BOYCE, A. J., FALLICK, A. E. & HASZELDINE, R. S. (1997) Quartz veins record vertical flow at graben edge: Fulmar Oil Field, Central North Sea. *AAPG Bull*., **81, 12**, 2024 – 2035.

MACAULAY, C. I., FALLICK, A. E., MCLAUGHLIN, O. M., HASZELDINE, R. S. & PEARSON, M. J. (1998) The significance of $\delta^{13}C$ of carbonate cements in reservoir sandstones: a regional perspective from the Jurassic of the northern North Sea. *In:* MORAD, S. (ed.) *Carbonate Cementation of Sandstones*. Spec. Publ., Int. Assoc. Sedimentol., **26**, 395 – 408.

MACHEL, H. G. (1987) Saddle *dolomite* as a by-product of chemical compaction and thermochemical sulphate reduction. *Geology*. **15**, 936 – 940.

MACHEL, H. G., KROUSE, H. R. & SASSEN, R. (1995) Products and distinguishing criteria of bacterial and thermochemical sulphate reduction. *Applied Geochemistry*, **10**, **4**, 373 – 389.

MACKENZIE, A. S., PRICE, I., LEYTHAEUSER, D., MÜLLER, P., RADKE, M. & SCHAEFER, R. G. (1987) The expulsion of petroleum from Kimmeridge clay source-rocks in the area of the Brae Oilfield, UK continental shelf. *In:* BROOKS, J. & GLENNIE, K. (eds.) *Petroleum Geology of North West Europe*. London, Graham & Trotman, 865 – 877.

MAGARA, *K. (*1976) Water expulsion from clastic sediments during compaction - directions and volume. *AAPG Bulletin*, **60**, 543 – 553.

MALONE, M. J., BAKER, P. A. & BURNS, S. J. (1996) Hydrothermal dolomitization and recrystallization of dolomite breccias from the Miocene Monterey Formation, Tepusquet area, California. *Journal of Sedimentary Research*, **66**, **5**, 976 – 990.

MARCHAND, A. M. E. (2001) Diagenesis and porosity preservation in deepwater oilfield sandstones. Ph.D thesis, The University of Edinburgh, pp. 231.

MARCHAND, A. M. E., HASZELDINE, R. S., SMALLEY, P. C., MACAULAY, C. I. & FALLICK, A. E. (2001) Evidence for reduced quartz cementation rates in oil-field sandstones. *Geology*, **29**, 915 – 918.

MARCHAND, A.M.E., HASZELDINE, R.S., MACAULAY, C.I., SWENNEN, R. & FALLICK, A.E. (2000) Quartz cementation inhibited by crestal oil charge: Miller deepwater sandstone, UK North Sea. *Clay Minerals*, **35**, 123 – 137.

MARCHAND, A. M. E., MACAULAY, C. I., HASZELDINE, R. S. & FALLICK, A. E. (2002) Pore water evolution in oilfield sandstones: constraints from oxygen isotope microanalyses of quartz cement. *Chemical Geology*, **191**, 285 – 304.

MARSHALL, J. D. (1988) Cathodoluminescence of geological materials. Unwin Hyman. pp. 146.

MATTER, J. M., TAKAHASHI, T. & GOLDBERG, D. (2007) Experimental evaluation of in situ CO_2-water-rock reactions during CO_2 injection in basaltic rocks: implications for geological CO_2 sequestration. *Geochemistry, Geophysics, Geosystems*. **8, 2**, pp.19.

MATTHEWS, A. & KATZ, A. (1977) Oxygen isotope fractionation during the dolomitization of calcium carbonate. *Geochim. Cosmochim. Acta*. **44**, 1431 – 1438.

MAY, F. (2005) Alteration of wall rocks by CO_2-rich water ascending in fault zones: natural analogues for reactions induced by CO_2 migrating along faults in siliciclastic reservoir and cap rocks. *Oil and Gas Science and Technology*, **60, 1**, 19 – 32.

MCLAUGHLIN, Ó. M. (1994) Brae diagenesis and poroperm. Internal report: Marathon Oil U.K. Ltd. & Partners. p. 18.

MCLAUGHLIN, Ó. M., HASZELDINE, R. S., FALLICK, A. E. & ROGERS, G. (1994) The case of the missing clay, aluminium loss and secondary porosity, south Brae oilfield, North Sea. *Clay Minerals*. **29**, 651 – 663.

MCNEIL, B., SHAW, H. F. & RANKIN, A. H. (1995) Diagenesis of the Rotliegend Sandstones in the V-Fields, southern North Sea: a fluid inclusion study. *In:* CUBITT, J. M. & ENGLAND, W. A. (eds.) *The Geochemistry of Reservoirs*, Geol. Soc., London, Spec. Publ., **86**, 125 – 139.

MCNEIL, B., SHAW, H. F. & RANKIN, A. H. (1998) The timing of cementation in the Rotliegend sandstones of the Southern North Sea: a petrological and fluid inclusion study of cements. *Journal of Petroleum Geology*. **21**, **3**, 311 – 328.

MCNUTT, R. H., FRAPE, S. K. & DOLLAR, P. (1987). Strontium, oxygen and hydrogen isotopic composition of brines, Michigan and Appalachian basins, Ontario and Michigan. *Applied Geochemistry*, **2**, 495 – 505.

MEARNS, E. W. & MCBRIDE, J. B. (1999) Hydrocarbon filling history and reservoir continuity of oil fields evaluated using $^{87}Sr/^{86}Sr$ isotope variations in formation waters, with examples form the North Sea. *Petroleum Geoscience*, **5**, 17 – 27.

METZ, B., DAVIDSON, O., DE CONINCK, H. LOOS, M. & MEYER, L. (eds.) (2005) *Carbon Dioxide Capture and Storage*. IPCC Special Report. pp. 62

MONTANEZ, I. P. & READ, J. F. (1992) Fluid-rock interaction history during stabilization of early dolomites, Upper Knox Group (lower Ordovician) U.S. Appalachians. *Journal of Sedimentary Petrology*, **62**, 753 – 778.

MOORE, J., ADAMS, M., ALLIS, R., LUTZ, S. & RAUZI, S. (2005) Mineralogical and geochemical consequences of the long-term presence of CO_2 in natural reservoirs: An example from the Springerville-St. Johns Field, Arizona, and New Mexico, U.S.A. *Chemical Geology*. **217**, 365 – 385.

MORGAN, R. K. & CUTTS, P. L. (1993) Low-angle faulting in the Triassic of the South Viking Graben: implications for future correlations. *In:* PARKER, J. R. (ed.) *Petroleum Geology of Northwest Europe: Proceedings of the 4th Conference*. The Geological Society of London, 569 – 579.

MUDFORD, B. S., GRADSTEIN, F. M., KATSUBE, T. J. & BEST, M. E. (1991) Modelling 1D compaction-driven flow in sedimentary basins: a comparison of the Scotian Shelf, North Sea and Gulf Coast. *In:* ENGLAND, W. A. & FLEET, A. J. (eds.) *Petroleum Migration*. Geological Society, London, Special Publications, **59**, 65 – 85.

NOLLET, S., HILGERS, C. & URAI, J. (2005) Sealing of fluid pathways in overpressure cells: a case study from the Buntsandstein in the Lower Saxony Basin (NW Germany). *International Journal of Earth Sciences*, **94**, 1039 – 1055.

O'HARA, K. D. (1995) The effects of rupture and diffusion on the salinity of fault-related fluid inclusions. *Journal of Structural Geology*, **17**, 257 – 264.

OAKMAN, C. D. & PARTINGTON, M. A. (1998) Cretaceous. *In:* GLENNIE, K.W. (ed.) *Petroleum geology of the North Sea: basic concepts and recent advances (4th edition)* Blackwell, 294 – 349.

OHMOTO, H & GOLDHABER, M. B. (1997) Isotopes of Sulfur and Carbon. *In:* BARNES, H. L. (ed.) *Geochemistry of Hydrothermal Ore Deposits (3rd Edition)*, Wiley & Sons, 517 – 611.

OHMOTO, H. & RYE, R. O. (1979) Isotopes of Sulfur and Carbon. *In:* BARNES, H. L. (ed.) *Geochemistry of Hydrothermal Ore Deposits (2nd Edition)*, Wiley & Sons, 509 – 567.

OHMOTO, H. (1972) Systematics of Sulfur and Carbon Isotopes in Hydrothermal Ore Deposits. *Economic Geology*, **67, 5**, 551 – 578.

OLDENBURG, C. M. & UNGER, A. J. A. (2003) On Leakage and Seepage from Geologic Carbon Sequestration Sites: Unsaturated Zone Attenuation. *Vadose Zone Journal*. **2**, 287 – 296.

OSBORNE, M. & HASZELDINE, R. S. (1993) Evidence for resetting of fluid inclusion temperatures from quartz cements in oilfields. *Marine and Petroleum Geology*, **10**, 271 – 278.

OSBORNE, M. & HASZELDINE, R. S. (1995) Reply to a discussion of 'Evidence for resetting of fluid inclusion temperatures from quartz cements in oilfields' by Osborne and Haszeldine (1993). *Marine and Petroleum Geology*, **12**, **5**, 561 – 565.

OSBORNE, M. J. & SWARBRICK, R. E. (1997) Mechanisms for generating overpressure in sedimentary basins: a re-evaluation. *AAPG Bulletin*, **81**, **6**, 1023 – 1041.

OSBOURNE, C. G., RAVENSCROFT, P. D. & MCCRACKEN, I. R. (1994) Predicted water chemistry trends in North Sea formation brines. *Marine and Petroleum Geology*, **11**, 20 – 23.

OXBURGH, E. R., O'NIONS, R. K. & HILL, R. I. (1986) Helium isotopes in sedimentary basins. *Nature*. **324**, 632 – 635.

OXTOBY, N. H. (1994) The Gyda Field. *In:* WARREN, E. A. & SMALLEY, P. C. (eds.) North Sea Formation Waters Atlas. *Geological Society London, Memoir* **15**, p. 40.

PARKHURST, D. L. & APPELO, C. A. J. (1999) User's guide to PHREEQC (version 2) – A computer program for speciation, batch-reaction, one-dimensional transport, and inverse geochemical calcuations. *U.S.G.S. Water-Resources Investigations Report* 99-4259, pp. 312.

PARRY, W. T. (1998) Fault-fluid compositions from fluid-inclusion observations and solubilities of fracture-sealing minerals. *Tectonophysics*, **290**, 1 – 26.

PEARCE, J., CAERNICHOWSKI-LAURIOL, I., LOMBARDI, S., BRUNE, S., NADOR, A., BAKER, J., PAUWELS, H., HATZIYANNIS, G., BEAUBIEN, S. & FABER, E. (2004) A review of natural CO_2 accumulations in Europe as analogues for geological sequestration. *In*: BAINES, S. J. & WORDEN, R. H. (eds.) *Geological Storage of Carbon Dioxide*. Geological Society, London, Special Publications. **233**, 29 – 41**.**

PHILLIPS, W. J. (1972) Hydraulic fracturing and mineralisation. *Journal of Geological Society, London*, **128**, 337 – 359.

PICKERING, K. T. (1984) The Upper Jurassic 'Boulder Beds' and related deposits: a fault-controlled submarine slope, NE Scotland. *Journal of the Geological Society, London*. **141**, 357 – 374.

PRIBNOW, D. & SCHELLSCHMIDT, R. (2000) Thermal Tracking of Upper Crustal Fluid Flow in the Rhine Graben. *Geophysical Research Letters*, **27**, **13**, 1957 – 1960.

RADKE, B. M. & MATHIS, R. L. (1980) On the formation and occurrence of saddle dolomite. *Journal of Sedimentary Petrology*, **50**, **4**, 1149 – 1168.

RAISTRICK, M., HUTCHEON, I., SHEVALIER, M., NIGHTINGALE, M., JOHNSON, G., TAYLOR, S., MAYER, B., DUROCHER, K., PERKINS, E., & GUNTER, B. (2009) Carbon dioxide-water-silicate mineral reactions enhance CO_2 storage; evidence from produced fluid measurements and geochemical modelling at the IEA Weyburn-Midale Project. *Energy Procedia*, **1**, **1**, 3149 – 3155.

RAYLEIGH, L. (1902) On the distillation of binary mixtures. *Phil. Mag. Sci*. **6**, **4**, 521 – 537.

REITSEMA, R. H. (1983) Geochemistry of North and South Brae Areas, North Sea. *Geological Society, London, Special Publications*. **12**, 203 – 212.

ROBERTS, M. J. (1991) The South Brae Field, Block 16/7a, UK North Sea. *In:* ABBOTTS, I. L. (ed.), *United Kingdom Oil and Gas Fields, 25 Years Commemorative Volume*, Geological Society Memoir, **14**, 55 – 62.

ROBINSON, A., GRANT, S. & OXTOBY, N. (1992) Evidence against natural deformation of fluid inclusions in diagenetic quartz. *Marine and Petroleum Geology*, **9**, 568 – 572.

ROEDDER, E. (1984) Fluid Inclusions. *Mineralogical Society of America Reviews in Mineralogy*, **12**, pp. 644.

ROOKSBY, S. K. (1991) The Miller Field, Blocks 16/7b, 16/8b, UK North Sea. *In:* ABBOTTS, I. L. (ed.), *United Kingdom Oil and Gas Fields, 25 Years Commemorative Volume*, Geological Society Memoir, **14**, 159 – 164.

RYBACH, L. (2007) The geothermal conditions in the Rhine Graben – a summary. *Bull. Angew. Geol*., **12, 1**, 29 – 32.

SACCHI, E., DEMATTEIS, A. & ROSETTI, P. (2003) Past and present circulation of CO_2-bearing fluids in the crystalline Gran Paradiso Massif (Orco Valley, north-western Italian Alps): tectonic and geochemical constraints. *Applied Geochemistry*, **19**, 395 – 412.

SADADA, M. (1985) CO_2-bearing fluid inclusions from geothermal fields. *Transactions of the Geothermal Resources Council*, **9**, 351 – 356.

SAMSON, I., ANDERSON, A. & MARSHALL, D. (eds.) (2003) Fluid Inclusions: Analysis and Interpretation. *Mineralogical Association of Canada Short Course Series*, **32**, pp. 374.

SCHIERMEIER, Q. (2006) Putting the carbon back: the hundred billion tonne challenge. *Nature*. **442**, 620 – 623.

SCHROEDER, F. W. & SYLTA, O. (1993) Modelling the hydrocarbon system of the North Viking Graben: a case study. *In:* DORÉ, A. G., AUGUSTON, J. H., HERMANRUD, C., STEWART, D. J. & SYLTA, O. (eds.) *Basin Modelling: Advances and Applications.* NPF Special Publications, Elsevier, Amsterdam, 469 – 484.

SCOTCHMAN, I. C. (1993) Diagenetic pore fluid evolution in the Kimmeridge Clay Formation: from concretions to sandstone cements. *In:* MANNING, D. A. C., HALL, P. L. & HUGHES, C. R. (eds.). *Geochemistry of Clay-Pore Fluid Interactions*. The Mineralogical Society Series **4**, 128 – 159.

SCOTCHMAN, I. C., CARR, A. D. & ASTIN, T. R. (2000) Porefluid evolution in the Kimmeridge Clay Formation of the UK Outer Moray Firth. *Journal of Geochemical Exploration*, **69-70**, 53 – 57.

SCOTCHMAN, I. C., CARR, A. D., ASTIN, T. R. & KELLY, J. (2002) Pore fluid evolution in the Kimmeridge Clay Formation of the UK Outer Moray Firth: implications for sandstone diagenesis. *Marine and Petroleum Geology*, **19**, 247 – 273.

SEARL, A. (1989) Saddle dolomite: a new view of its nature and origin. *Mineralogical Magazine*, **53**, 547 – 555.

SEGNIT, E. R., HOLLAND, H. D. & BISCARDI, C. J. (1962) The solubility of calcite in aqueous solutions. 1. The solubility of calcite in water between 75-degrees and 200-degrees at CO_2 pressures up to 60-atm. *Geochimica et Cosmochimica Acta*, **26**, 1301 – 1331.

SHAW, H. F. & PRIMMER, T. J. (1991) Diagenesis of mudrocks from the Kimmeridge Clay Formation of the Brae Area, UK North Sea. *Marine and Petroleum Geology*. **8**, 270 – 277.

SHEPHERD, T. J., RANKIN, A. H. & ALDERTON, D. H. M. (1985) A practical guide to fluid inclusion studies. *Blackie & Son Ltd.*, pp. 239.

SHEPPARD, S. M. & SCHWARZ, H. P. (1970) Fractionation of carbon and oxygen isotopes and magnesium between coexisting metamorphic calcite and dolomite. *Contributions to Mineralogy and Petrology*, **26**, 161 – 198.

SHEPPARD, S. M. F. (1986) Characterisation and isotopic variations in natural waters. *In:* VALLEY, J. W., TAYLOR, H. P. & O'NEIL, J. R. (eds.) *Stable isotopes in high temperature geological processes*. Mineralogical Society of America, Reviews in Mineralogy, **16**, 165 – 183.

SHIPTON, Z. K., EVANS, J. P., KIRCHNER, D., KOLESAR, P. T., WILLIAMS, A. P. & HEATH, J. (2004) Analysis of CO_2 leakage through low-permeability faults from natural reservoirs in the Colorado Plateau, southern Utah. *In*: BAINES, S. J. & WORDEN, R. H. (eds.) *Geological Storage of Carbon Dioxide*. Geological Society, London, Special Publications. **233**, 43 – 58**.**

SIBSON, R. H. (1981) Fluid flow accompanying faulting: field evidence and models. *In:* SIMPSON, D. W. & RICHARDS, P. G. (eds.) *Earthquake prediction: an International Review*. American Geophysical Union, Maurice Ewing Series, **4**, 593 – 603.

SIBSON, R. H. (1986) Brecciation processes in Fault Zones: Inferences from Earthquake Rupturing. *Pure and Applied Geophysics*, **124**, 159 – 175.

SIBSON, R. H. (1987) Earthquake rupturing as a mineralizing agent in hydrothermal systems. *Geology*, **15**, **8**, 701 – 704.

SIBSON, R. H. (1992) Implications of fault-valve behaviour for rupture, nucleation and recurrence. *Tectonophysics*, **21**, **1**, 283 – 293.

SIBSON, R. H. (1994) Crustal stress, faulting, and fluid flow. *In:* PARNELL, J. (ed.) *Geofluids; origin, migration, and evolution of fluids in sedimentary basins*. Geological Society, London, Special Publications, **78**, 69 – 84.

SIBSON, R. H. (2000) Fluid movement in normal faulting. *Journal of Geodynamics*, **49**, 469 – 499.

SIBSON, R. H., ROBERT, F. & POULSEN, K. H. (1988) High angle reverse faults, fluid pressure cycling, and mesothermal gold-quartz deposits. *Geology*, **16**, 551 – 555.

SIEGEL, D. I, LESNIAK, K. A., STUTE, M. & FRAPE, S. (2004) Isotopic geochemistry of the Saratoga springs: Implications for the origin of solutes and source of carbon dioxide. *Geology*, **32**, **3**, 257 – 260.

SMALLEY, P. C. & WARREN, E. A. (1994) The Miller Field. *In:* WARREN, E. A. & SMALLEY, P. C. (eds.) North Sea Formation Waters Atlas. *Geological Society London, Memoir* **15**, 52.

SMALLEY, P. C., LØNØY, A. & RÅHEIM, A. (1992) Spatial $^{87}Sr/^{86}Sr$ variations in formation water and calcite from the Ekofisk chalk oil field: implications for reservoir connectivity and fluid composition. *Applied Geochemistry*, **7**, 341 – 350.

SMITH, M. P., SAVARY, V., YARDLEY, B. W. D., VALLEY, J. W., ROYER, J. J. & DUBOIS, M. (1998). The evolution of the deep flow regime at Soultz-sous-Forêts, Rhine Graben, eastern France: Evidence from a composite quartz vein. *Journal of Geophysical Research*, **103, B11**, 27, 223 – 237.

SMITH, R. I., HODGSON, N. & FULTON, M. (1993) Salt control on Triassic reservoir distribution, UKCS Central North Sea. *In:* PARKER, J. R. (ed.) *Petroleum Geology of Northwest Europe: Proceedings of the 4th Conference*. The Geological Society of London, 547 – 557.

SOONG, Y., GOODMAN, A. L., MCCARTHY-JONES, J. R. & BALTRUS, J. P. (2004) Experimental and simulation studies on mineral trapping of CO_2 with brine. *Energy Conversion and Management*, 45**, 11-12**, 1845 – 1859.

SPANGENBERG, J., FONTBOTÉ, L, SHARP, Z. D. & HUNZIKER, J. (1996) Carbon and oxygen isotope study of hydrothermal carbonates in the zinc-lead deposits of the San Vicente district, central Peru: a quantitative modelling on mixing processes and CO_2 degassing. *Chem. Geol*., **133**, 289 – 315.

SPÖTL, C. & PITMAN, J. K. (1998) Saddle (baroque) dolomite in carbonates and sandstones: a reappraisal of a burial-diagentic concept. *In:* MORAD, S. (ed.) *Carbonate Cementation of Sandstones*. Spec. Publ., Int. Assoc. Sedimentol., **26**, 437 – 460.

STOW, D. A. V. & ATKIN, B. P. (1987) Sediment facies and geochemistry of Upper Jurassic mudrocks in the central North Sea area. *In:* BROOKS, J. & GLENNIE, K. (eds.) *Petroleum Geology of North West Europe*. London, Graham & Trotman. 797 – 808.

STOW, D. A. V., BISHOP, C. D. & MILLS, S. J. (1982) Sedimentology of the Brae oilfield, North Sea – fan models and controls. *Journal of Petroleum Geology*. **5, 2**, 129 – 148.

SULLIVAN, M. D., HASZELDINE, R. S. & FALLICK, A. E. (1990) Linear coupling of carbon and strontium isotopes in Rotliegend Sandstone, North Sea: Evidence for cross-formational flow. *Geology*, **18**, 1215 – 1218.

SURDAM, R. C., BOESE, S. W. & CROSSEY, L. J. (1984) The chemistry of secondary porosity. In: MCDONALD, D. A. & SURDAM, R. C. (eds.) *Clastic diagenesis*. AAPG Memoir, **37**, 127 – 151.

SURDAM, R. C., CROSSLEY, L. J., HAGEN, E. S. & HEASLER, H. P. (1989) Organic-inorganic interactions and sandstone diagenesis. *AAPG Bulletin*. **73**, 1 – 23.

SZARAN, J. (1998) Carbon isotope fractionation between dissolved and gaseous carbon dioxide. *Chemical Geology*, **150**, 331 – 337.

TANS, P. (2011) Weekly mean CO_2 and historical comparisons, *NOAA/ESRL* (www.esrl.noaa.gov/gmd/ccgg/trends).

TAYLOR, H. P. (1977) Water/rock interactions and the origin of H_2O in granitic batholiths. *J. Geol. Soc. London*, **133**, 509 – 558.

TAYLOR, J. C. (1981) Zechstein facies and petroleum prospects in the Central and Northern North Sea. *In:* ILLING, L .V & HOBSON, G. D. (eds.) *Petroleum Geology of the Continental Shelf of North-West Europe*, Institute of Petroleum Geology, London, 176 – 185.

THOMAS, D. W. & COWARD, M. P. (1996) Mesozoic regional tectonics and South Viking Graben formation: evidence for localized thin-skinned detachments during rift development and inversion. *Marine and Petroleum Geology*, **13, 2**, 149 – 177.

THRASHER, J. & FLEET, A. J. (1995) Predicting the risk of carbon dioxide `pollution' in petroleum reservoirs. *In*: GRIMALT, J. O. & DORRONSORO, C. (eds.) *Organic Geochemistry: Developments and Applications to Energy, Climate, Environment and Human History*, Proceedings 17th International Meeting on Organic Geochemistry, San Sebastian, Spain,1086 – 1088.

TURNER, C. C. & ALLEN, P. J. (1991) The Central Brae Field, Block 16/7a, UK North Sea. *In:* ABBOTTS, I. L. (ed.), *United Kingdom Oil and Gas Fields, 25 Years Commemorative Volume*, Geological Society Memoir, **14**, 49 – 54.

TURNER, C. C., COHEN, J. M., CONNELL, E. R. & COOPER, D. M. (1987) A depositional model for the South Brae oilfield. *In:* BROOKS, J. & GLENNIE, K. (eds.) *Petroleum Geology of North West Europe*. London, Graham & Trotman, 853 – 864.

UNDERHILL, J. R. & PARTINGTON, M. A. (1993) Jurassic thermal doming and deflation in the North Sea: implication of the sequence stratigraphic evidence. *In:* PARKER, J. R. (ed.) *Petroleum Geology of Northwest Europe: Proceedings of the 4th Conference*, Geological Society, London, 337 – 345.

UNDERHILL, J. R. (1998) Jurassic. *In:* GLENNIE, K.W. (ed.) *Petroleum geology of the North Sea: basic concepts and recent advances (4th edition)* Blackwell, 245 – 293.

UNDERHILL, J. R. (2003) The tectonic and stratigraphic framework of the United Kingdom's oil and gas fields. *In*: GLUYAS, J. G. & HITCHENS, H. M. (eds.) *United Kingdom Oil and Gas Fields, Commemorative Millennium Volume*, Geological Society Memoir, **20**, 17 – 59.

VAN RUTH, P. J., NELSON, E. J. & HILLIS, R. R. (2006) Fault reactivation potential during CO_2 injection in the Gippsland Basin, Australia. *Exploration Geophysics* **37**, 50 – 59.

VASCONCELOS, C., MCKENZIE, J. A., WARTHMAN, R. & BERNASCONI, S. M. (2005) Calibration of the $\delta^{18}O$ paleothermometer for dolomite precipitated in microbial cultures and natural environments. *Geology*, **33**, **4**, 317 – 320.

VEIZER, J. (1983) Trace elements and isotopes in sedimentary carbonates. *In:* REEDER, R. J. (ed.) *Carbonates: mineralogy and chemistry*. Mineralogical Society of America Reviews in Mineralogy and Geochemistry, **11**, 265 – 299.

VEIZER, J., et al. (1999) $^{87}Sr/^{86}Sr$, $\delta^{13}C$ and $\delta^{18}O$ evolution of Phanerozoic seawater. *Chemical Geology*, **161**, 59 – 88.

VOGEL, J. C., GROOTES, P. M. & MOOK, W. G. (1970) Isotopic fractionation between gaseous and dissolved carbon dioxide. *Z. Physik*, **230**, 225 – 238.

WARREN, E. A., & SMALLEY, P. C. (eds.) (1994) *North Sea Formation Waters Atlas*. Geological Society (London) Memoir **15**, pp. 208.

WARREN, E. A., & SMALLEY, P. C. (eds.) (1994) The chemical composition of North Sea formation waters: a review of their heterogeneity and potential applications. *In:* PARKER, J. R. (ed.) *Petroleum Geology of Northwest Europe: Proceedings of the 4th Conference*. The Geological Society of London, 1347 – 1352.

WARREN, J. (2000a) Dolomite: occurrence, evolution and economically important associations. *Earth Science Reviews*, **52**, 1 – 81.

WARREN, J. K. (2000b) Burial hydrology and chemistry. *In:* WARREN, J. K. (ed.) *Evaporites: sediments, resources, and hydrocarbons*. Springer, New York, 567 – 615.

WILKINSON, J. J. (2001) Fluid inclusions in hydrothermal ore deposits. *Lithos*, **55**, 229 – 272.

WILKINSON, J. J., BOYCE, A. J., EARLS, G. & FALLICK, A. E. (1999) Gold remobilization by low temperature brines: evidence from the Curraghinalt gold deposit, Northern Ireland. *Economic Geology*, **94**, 289 – 296.

WILKINSON, M., DARBY, D., HASZELDINE, R. S. & COUPLES, G. D. (1997) Secondary porosity generation during deep burial associated with overpressure leak-off: Fulmar Formation UKCS. *AAPG Bulletin*. **81**, 803 – 813.

WILKINSON, M., HASZELDINE, R. S., FALLICK, A. E., ODLING, N., STOKER, S. J. & GATLIFF, R. W. (2009) CO_2–Mineral Reaction in a Natural Analogue for CO_2 Storage – Implications for Modelling. *Journal of Sedimentary Research*, **79**, **7**, 486 – 494.

WINTER, B. L. & KNAUTH, L. P. (1992) Stable isotope geochemistry of carbonate fracture fills in the Monterey Formation, California. *Journal of Sedimentary Petrology*. **62**, **2**, 208 – 219.

WINTER, B. L., JOHNSON, C. M. SIMO, J. A. & VALLEY, J. W. (1995) Paleozoic fluid history of the Michigan Basin: evidence from dolomite geochemistry in the Middle Ordovician St. Peter Sandstone. *Journal of Sedimentary Research*, **A65**, **2**, 306 – 320.

WINTER, B. L., JOHNSON, C. M., SIMO, J. A. & VALLEY, J. W. (1995) Paleozoic fluid history of the Michigan Basin: evidence from dolomite geochemistry in the Middle Ordovician St. Peter Sandstone. *Journal of Sedimentary Research*, **A65**, **2**, 306 – 320.

WORDEN, R. H. (2006) Dawsonite cement in the Triassic Lam Formation, Shabwa Basin, Yemen: a natural analogue for a potential mineral product of subsurface CO_2 storage for greenhouse gas reduction.. *Marine and Petroleum Geology*, **23**, 61 – 67.

WORDEN, R. H., WARREN, E. A., SMALLEY, P. C., PRIMMER, T. J. & OXTOBY, N. H. (1995) Discussion of 'Evidence for resetting of fluid inclusion temperatures from quartz cements in oilfields' by Osborne and Haszeldine (1993). *Marine and Petroleum Geology*, **12**, **5**, 566 – 570.

WORDEN. R. H. & BARCLAY, S. A. (2000) Internally-sourced quartz cement due to externally-derived CO_2 in sub-arkosic sandstones, North Sea. *Journal of Geochemical Exploration*. **69-70**, 645 – 649.

WYCHERLEY, H., FLEET, A. & SHAW, H. (1999) Some observations on the origins of large volumes of carbon dioxide accumulations in sedimentary basins. *Marine and Petroleum Geology*. **16**, 489 – 494.

XU, T., APPS, J. A. & PRUSS, K. (2005) Mineral sequestration of carbon dioxide in a sandstone-shale system. *Chemical Geology.* **217**, 295 - 318.

YUI, T. F. & GONG, S. Y. (2003) Stoichiometry effect on stable isotope analysis of dolomite. *Chem. Geol*., **201**, 359 – 368.

ZERAI, B., SAYLOR, B. Z., MATISOFF, G. (2006) Computer simulation of CO_2 trapped through mineral precipitation in the Rose Run Sandstone, Ohio. *Applied Geochemistry*. **22**, **2**, 223 – 240.

ZHANG, J., QUAY, P. D. & WILBUR, D. O. (1995) Carbon isotope fractionation during gas-water exchange and dissolution of CO_2. *Geochimica et Cosmochimica Acta*, **59, 1**, 107 – 114.

ZHENG, Y.-F. & HOEFS, J. (1993) Carbon and oxygen isotopic covariations in hydrothermal calcites: theoretical modelling on mixing processes and application to Pb-Zn deposits in the Harz Mountains, Germany. *Mineral. Deposita*, **28**, 79 – 89.

ZHENG, Y.-F. (1990) Carbon-oxygen isotopic covariation in hydrothermal calcite during degassing of CO_2: a quantitative evaluation and application to the Kushikino gold mining area in Japan. *Mineral. Deposita*, **25**, 246 – 250.

ZIEGLER, P. A. (1981) Evolution of sedimentary basins in north-west Europe. *In:* ILLING, L .V & HOBSON, G. D. (eds.) *Petroleum Geology of the Continental Shelf of North-West Europe*, Institute of Petroleum Geology, London, 3 – 39.

ZIEGLER, P. A. (1982) Faulting and graben formation in western and central Europe. *Phil. Trans. R. Soc. London*. A **305**, 113 – 143.

ZIEGLER, P. A. (1990) Tectonic and palaeogeographic development of the North Sea rift system. *In:* BLUNDELL, D. J. & GIBBS, A. D. (eds.) *Tectonic Evolution of the North Sea Rifts*. Oxford Science Publications, 1 – 36.

Appendix I

Appendix I.a. Annotated seismic lines from the T-Block fields highlighting the contrasting morphology of the graben bounding fault (GBF) along the basin margin. Modified from Cherry (1993).

i) steep planar boundary fault geometry

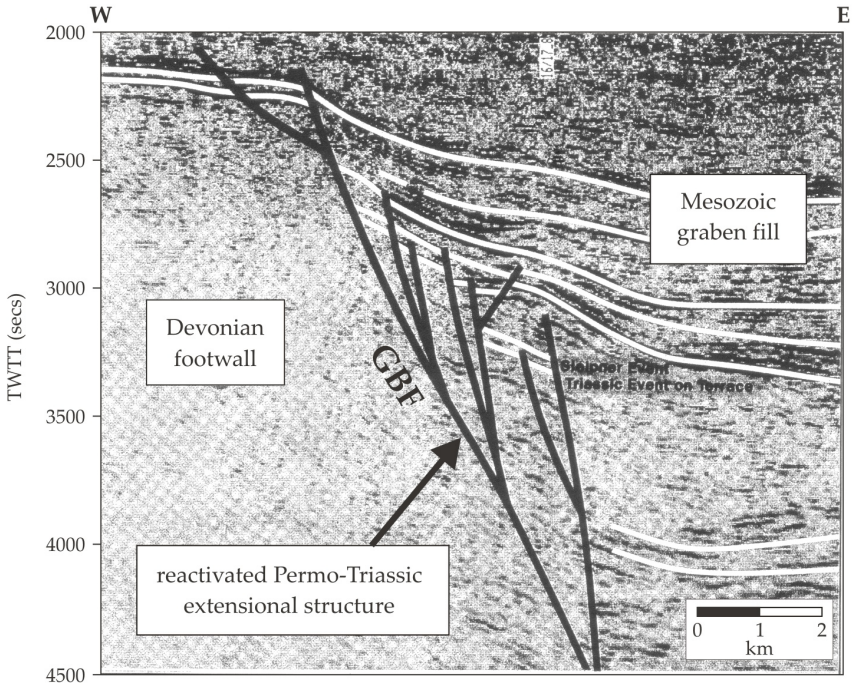

ii) ramp-flat listric boundary fault geometry

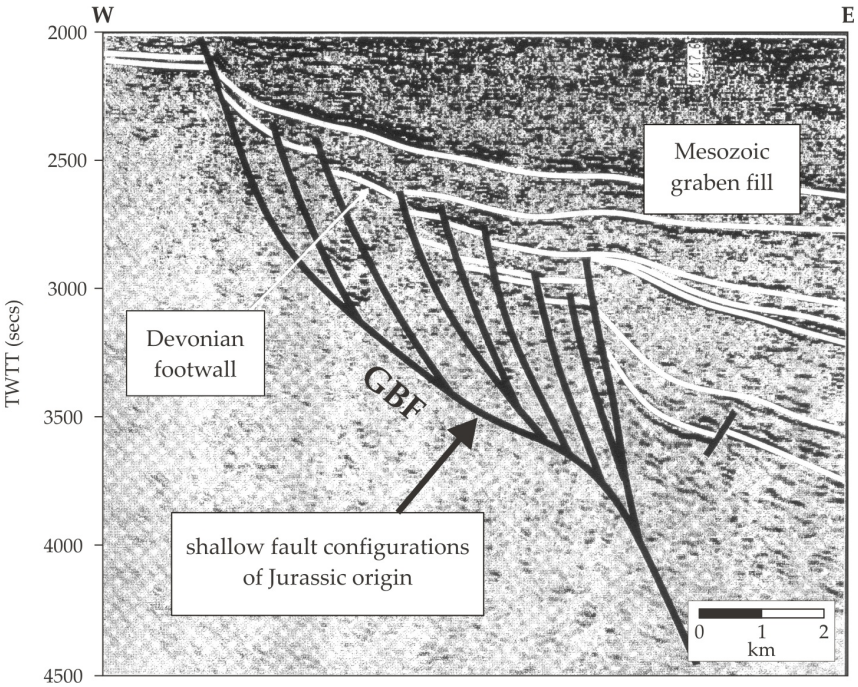

Appendix I.b. Electron microprobe data showing elemental weight percent (wt.%) of dominant (Ca, Mg, Fe, & Mn) and trace (Na, Sr, K, Ba, & S) elements from carbonate cement generations A to E. (* denotes replacement dolomite in cement A).

Zone A

					wt. %				
Data point	**Mg**	**Ca**	**Na**	**S**	**K**	**Mn**	**Fe**	**Sr**	**Ba**
A14 / 1 . 01	0.081	38.247	0.000	0.014	0.008	0.163	0.785	0.047	0.005
A14 / 2 . 02	0.086	38.129	0.003	0.012	0.004	0.171	0.779	0.046	-0.001
A14 / 3 . 03	0.078	38.752	0.001	0.006	0.007	0.179	0.811	0.044	-0.002
A14 / 4 . 04	0.086	37.839	0.002	0.004	0.002	0.164	0.766	0.058	0.008
A14 / 5 . 05	0.078	38.137	0.000	0.003	0.015	0.163	0.706	0.042	-0.008
A14 / 6 . 06	0.080	37.910	0.001	0.012	0.001	0.186	0.776	0.052	0.004
A14 / 7 . 07	0.075	37.823	0.004	0.013	0.016	0.168	0.759	0.041	-0.009
A14 / 8 . 08	0.056	38.427	0.002	0.008	0.012	0.192	0.682	0.029	-0.013
A13 / 1 . 09*	9.690	20.568	0.006	0.000	-0.003	0.701	4.692	0.010	-0.004
A13 / 2 . 10*	9.957	20.839	0.008	0.005	0.001	0.675	4.142	-0.012	0.008
A13 / 3 . 11*	9.819	20.628	0.010	0.007	0.000	0.688	4.431	0.005	-0.007
A13 / 4 . 12*	9.345	20.457	0.007	0.013	-0.004	0.732	5.285	0.021	-0.007
A13 / 5 . 13*	8.790	20.678	-0.001	0.006	-0.004	0.738	5.985	0.007	-0.026
A13 / 6 . 14*	9.284	20.893	0.004	0.012	-0.001	0.656	5.076	0.009	0.012
A13 / 7 . 15*	9.503	20.526	0.000	0.046	-0.004	0.665	4.904	0.011	-0.017
A15 / 1 . 16*	9.999	20.729	0.003	0.006	-0.006	0.691	3.962	-0.001	-0.016
A15 / 2 . 17*	9.871	20.793	0.002	0.002	0.004	0.668	4.284	0.008	-0.010
A15 / 3 . 18*	9.829	20.738	0.010	0.010	0.002	0.690	4.242	0.006	-0.011
A15 / 4 . 19*	9.968	20.935	0.005	0.007	0.003	0.648	4.101	0.004	-0.018
A15 / 5 . 20*	9.960	20.683	0.008	0.002	0.008	0.707	4.359	-0.009	-0.004

Zone B

					wt. %				
Data point	**Mg**	**Ca**	**Na**	**S**	**K**	**Mn**	**Fe**	**Sr**	**Ba**
B8 / 1 . 01	10.404	21.882	0.004	0.003	0.006	0.297	0.011	0.014	-0.008
B8 / 1 . 02	11.980	21.758	0.004	0.006	-0.002	0.305	0.028	0.007	-0.013
B4 / 1 . 03	11.946	21.673	0.001	0.002	-0.006	0.279	0.057	0.008	-0.012
B8 / 1 . 04	10.605	21.494	0.008	0.007	0.005	0.319	0.002	0.008	-0.014
B1 / 1 . 05	11.123	22.018	0.010	0.003	0.002	0.332	0.002	0.005	-0.018
B5 / 1 . 06	11.256	21.621	0.007	0.005	0.005	0.321	0.016	-0.008	-0.004
B6 / 1 . 07	11.158	21.752	-0.001	0.002	0.002	0.320	0.017	0.006	-0.012
B4 / 6 . 08	10.966	21.862	0.000	0.000	0.005	0.350	0.022	0.000	-0.009
B8 / 1 . 09	10.655	21.953	-0.001	-0.002	0.001	0.336	0.041	-0.005	-0.008
B2 / 1 . 10	12.067	21.061	0.006	-0.002	0.005	0.883	0.063	0.005	-0.022
B3 / 1 . 11	10.754	21.524	-0.003	0.007	-0.001	0.323	0.052	0.003	0.004
B4 / 7 . 12	12.337	21.860	0.005	-0.001	-0.002	0.330	0.031	-0.002	-0.016
B6 / 1 . 13	10.191	21.676	0.006	0.009	-0.001	0.340	-0.003	-0.006	-0.017
B5 / 1 . 14	10.040	21.897	0.004	0.002	0.006	0.326	0.014	-0.004	-0.006
B7 / 1 . 15	12.032	21.785	0.002	0.010	0.001	0.309	0.065	0.006	-0.017
B13 / 1 . 16	10.366	21.500	-0.001	-0.001	-0.003	0.325	0.029	-0.004	-0.015
B9 / 1 . 17	10.505	21.737	0.004	0.005	0.003	0.318	0.042	-0.004	0.000
B7 / 1 . 18	10.699	21.673	0.002	0.003	0.002	0.312	0.049	0.005	-0.013
B9 / 1 . 19	12.077	21.675	0.002	0.006	0.009	0.310	0.041	-0.002	-0.010
B11 / 1 . 20	11.097	21.855	0.007	0.001	0.008	0.332	0.012	-0.005	-0.003
B1 / 3 . 21	11.048	21.632	0.003	0.006	-0.001	0.326	0.016	0.007	-0.010

B5 / 1 . 22	11.151	21.794	0.012	0.006	0.004	0.335	0.012	-0.001	-0.005
B4 / 3 . 23	11.966	21.718	0.009	0.004	0.003	0.299	0.094	0.016	-0.013
B4 / 1 . 24	11.057	21.563	0.004	0.006	0.006	0.362	0.023	-0.012	-0.022
B10 / 1 . 25	10.950	21.581	0.000	0.009	0.004	0.352	0.035	0.002	-0.008
B4 / 5 . 26	12.002	22.120	0.007	0.003	-0.008	0.314	0.094	-0.007	-0.006
B3 / 1 . 27	10.793	21.710	0.004	0.000	0.003	0.318	0.073	0.002	0.005
B12 / 1 . 28	10.758	21.655	0.008	0.005	0.001	0.334	0.058	0.003	-0.009
B4 / 4 . 29	11.942	21.882	0.001	0.002	0.005	0.324	0.086	0.003	-0.011
B1 / 1 . 30	11.750	21.822	0.000	0.006	0.003	0.294	0.113	0.002	-0.007
B10 / 1 . 31	10.417	21.663	0.007	0.007	0.000	0.318	0.081	0.000	-0.010
B17 / 1 . 32	11.752	21.474	0.000	0.004	0.000	0.411	0.005	0.013	-0.018
B14 / 1 . 33	10.434	22.178	0.007	0.008	0.002	0.329	0.080	-0.003	-0.010
B4 / 1 . 34	10.651	21.765	0.006	0.009	-0.004	0.319	0.097	-0.001	-0.016
B1 / 2 . 35	12.362	21.594	0.004	0.004	0.013	0.409	0.042	0.008	-0.002
B9 / 1 . 36	10.806	21.828	0.004	0.008	0.004	0.380	0.057	-0.009	-0.015
B7 / 1 . 37	10.237	21.815	0.003	0.018	0.009	0.334	0.100	0.018	-0.021
B10 / 1 . 38	10.087	21.800	0.003	0.010	-0.001	0.350	0.084	-0.001	-0.008
B4 / 2 . 39	11.985	21.847	0.003	0.006	0.003	0.323	0.153	-0.007	-0.018
B7 / 1 . 40	11.484	21.141	0.002	0.002	-0.001	1.060	0.064	0.001	-0.004
B6 / 1 . 41	9.736	21.045	-0.002	0.008	-0.002	1.012	0.080	0.002	-0.013
B2 / 1 . 42	11.681	21.023	0.003	-0.003	0.002	1.119	0.072	-0.004	-0.009
B12 / 1 . 43	11.719	21.404	-0.001	0.004	-0.005	1.163	0.087	0.009	-0.009
B9 / 1 . 44	10.253	22.108	0.005	0.004	0.005	0.438	0.222	-0.006	-0.017
B11 / 1 . 45	10.222	21.766	0.008	0.010	-0.004	0.359	0.299	0.002	-0.013
B2 / 1 . 46	10.671	21.286	0.005	0.004	0.003	0.597	0.095	0.004	-0.016
B4 / 1 . 47	10.074	22.079	0.002	0.002	0.004	0.486	0.220	0.001	-0.019
B10 / 1 . 48	10.202	21.562	0.001	0.004	0.002	0.386	0.491	0.005	-0.019
B4 / 9 . 49	11.984	21.301	0.005	0.004	0.000	0.704	0.034	-0.004	-0.012
B18 / 1 . 50	11.746	21.296	-0.002	-0.001	-0.002	0.747	0.044	0.017	-0.003
B4 / 8 . 51	11.977	21.356	-0.001	0.006	-0.005	0.810	0.088	0.006	-0.015
B3 / 1 . 52	9.834	21.367	-0.001	-0.002	0.000	0.902	0.081	0.006	0.008
B1 / 4 . 53	11.626	20.947	0.009	0.001	-0.009	0.965	0.095	0.006	-0.017
B20 / 1 . 54	11.439	21.207	0.002	0.002	0.006	1.084	0.024	0.006	-0.006
B19 / 1 . 55	11.107	21.629	0.003	0.001	-0.004	0.474	0.018	-0.009	-0.008
B1 / 1 . 56	10.732	21.989	0.005	0.002	0.006	0.349	0.181	0.009	-0.004
B1 / 7 . 57	10.171	21.694	0.001	0.009	0.001	0.521	0.057	-0.005	-0.004
B1 / 6 . 58	10.242	21.777	0.003	0.008	-0.001	0.362	0.275	0.006	0.000
B1 / 5 . 59	11.645	21.243	0.004	0.003	-0.004	1.172	0.109	0.009	0.011

Zone C

wt. %

Data point	Mg	Ca	Na	S	K	Mn	Fe	Sr	Ba
C9 / 1 . 01	8.543	20.515	-0.003	-0.001	-0.001	0.870	6.979	0.006	-0.006
C10 / 1 . 02	8.254	20.619	0.002	0.003	0.001	0.970	7.259	0.012	-0.007
C11 / 1 . 03	9.953	21.287	-0.001	0.002	0.007	0.982	0.096	0.006	-0.003
C12 / 1 . 04	9.275	20.926	0.006	-0.001	0.002	1.626	0.340	0.007	-0.009
C13 / 1 . 05	8.596	21.248	0.003	0.006	0.002	0.724	3.794	0.011	-0.017
C14 / 1 . 06	9.100	20.924	0.001	0.005	-0.006	1.973	0.301	-0.016	-0.001
C15 / 1 . 07	9.753	21.012	0.000	0.007	0.000	1.184	0.076	-0.002	-0.023
C16 / 1 . 08	9.426	21.338	0.002	0.000	0.000	1.748	0.228	-0.003	-0.027
C17 / 1 . 09	9.277	20.916	0.002	0.003	0.001	1.997	0.496	0.001	-0.010
C18 / 1 . 10	9.915	21.271	0.005	0.001	0.005	1.034	0.101	0.000	-0.018
C19 / 1 . 11	9.659	21.002	-0.004	0.006	0.001	1.210	0.083	0.001	-0.004

C20 / 1 . 12	9.818	21.282	0.006	0.000	-0.009	0.848	0.134	0.000	-0.021
C2 / 1 . 13	9.678	20.823	0.003	0.002	-0.001	0.864	4.699	0.003	-0.016
C2 / 2 . 14	9.497	20.832	0.002	0.009	-0.006	0.904	5.184	-0.002	-0.008
C2 / 3 . 15	9.556	20.945	0.008	0.004	0.001	0.912	5.369	0.000	-0.014
C2 / 4 . 16	9.283	20.743	0.006	0.004	0.005	0.969	5.489	0.003	0.012
C3 / 1 . 17	8.945	20.961	-0.001	0.009	0.000	0.961	5.586	0.015	-0.016
C3 / 2 . 18	9.138	20.610	-0.001	-0.001	0.005	0.972	5.604	0.001	-0.022
C3 / 3 . 19	9.628	20.616	0.003	0.004	0.001	0.901	5.192	-0.013	-0.006
C3 / 4 . 20	9.520	20.649	-0.005	0.005	-0.002	0.885	5.234	0.009	-0.010
C3 / 5 . 21	9.169	20.624	0.002	0.003	0.003	0.901	5.722	0.009	0.006
C5 / 1 . 22	9.154	20.772	0.005	0.005	-0.003	0.823	5.256	0.002	-0.006
C5 / 2 . 23	9.022	20.609	0.001	0.001	-0.003	0.957	5.592	0.001	-0.007
C5 / 3 . 24	8.989	20.608	0.005	0.005	-0.006	0.981	5.613	-0.009	-0.008
C5 / 4 . 25	8.921	20.632	-0.003	-0.002	0.002	0.996	5.720	0.003	-0.012
C5 / 5 . 26	9.115	20.608	0.006	0.008	0.001	1.008	5.464	0.007	-0.013
C5 / 6 . 27	9.039	20.537	0.003	0.008	0.006	0.899	5.889	0.009	-0.006
C5 / 7 . 28	9.119	20.877	0.007	0.000	0.003	0.974	5.419	-0.009	-0.010
C6 / 1 . 29	9.338	20.994	0.001	0.002	0.000	0.826	5.399	-0.007	-0.006
C6 / 2 . 30	8.992	20.635	0.002	0.002	0.003	0.909	5.843	-0.006	-0.011
C6 / 3 . 31	9.061	20.657	0.003	-0.001	-0.003	0.864	5.956	0.012	-0.006
C6 / 4 . 32	8.923	20.742	0.007	0.004	0.014	0.813	5.899	0.023	-0.002
C6 / 5 . 33	8.640	20.666	0.008	0.003	0.005	0.961	6.270	0.006	-0.012
C6 / 6 . 34	8.417	20.583	0.000	0.003	0.002	1.024	6.843	0.002	-0.011
C6 / 7 . 35	8.445	20.679	0.001	0.004	0.003	1.003	6.573	0.007	-0.011

Zone D

wt. %

Data point	Mg	Ca	Na	S	K	Mn	Fe	Sr	Ba
D11 / 1 . 01	9.344	20.747	0.006	0.010	0.003	0.740	5.389	0.005	-0.016
D12 / 1 . 02	9.649	20.699	0.005	0.003	0.004	0.738	4.728	0.015	-0.009
D1 / 1 . 03	8.537	20.486	-0.003	-0.001	0.010	0.845	6.739	-0.002	-0.026
D2 / 1 . 04	8.116	20.631	0.000	0.000	-0.002	0.955	7.088	-0.004	-0.024
D3 / 1 . 05	7.934	20.618	0.004	0.002	0.004	0.952	7.317	0.002	-0.008
D4 / 1 . 06	7.952	20.523	-0.004	-0.001	-0.001	1.013	7.269	0.005	-0.021
D5 / 1 . 07	7.393	20.315	-0.001	0.005	-0.003	1.130	8.101	0.003	-0.006
D6 / 1 . 08	8.074	20.556	0.003	0.003	0.001	0.904	7.177	-0.002	-0.015
D7 / 1 . 09	9.450	20.571	0.003	0.011	0.000	0.693	4.577	-0.009	-0.018
D8 / 1 . 10	8.457	20.688	0.005	0.001	0.007	0.748	6.563	0.002	-0.019
D9 / 1 . 11	9.925	20.919	0.008	0.005	0.001	0.656	3.268	-0.001	-0.006
D10 / 1 . 12	9.842	20.743	0.007	0.013	0.006	0.790	3.960	0.007	-0.009
D21 / 1 . 13	7.984	20.523	0.006	0.004	0.002	0.740	4.882	0.003	0.000
D22 / 1 . 14	7.900	20.687	0.005	0.001	0.008	0.790	4.712	0.001	-0.011
D23 / 1 . 15	8.482	20.595	0.006	0.004	0.003	0.710	3.728	0.004	-0.009
D24 / 1 . 16	8.413	20.827	0.001	0.005	-0.001	0.678	3.563	0.006	0.001
D25 / 1 . 17	8.044	20.613	0.003	0.001	-0.002	0.754	4.600	-0.005	-0.010
D26 / 1 . 18	8.480	20.605	0.007	0.006	0.006	0.675	3.843	-0.003	-0.018
D27 / 1 . 19	7.936	20.701	0.003	0.010	0.010	0.728	4.531	-0.008	-0.013
D28 / 1 . 20	7.726	20.674	0.003	0.003	-0.001	0.809	5.329	0.004	-0.015
D29 / 1 . 21	6.987	20.841	0.000	0.013	-0.003	0.794	5.817	0.003	-0.012
D7 / 1 . 22	10.183	20.630	0.010	0.001	0.002	0.702	3.752	-0.006	0.006
D7 / 2 . 23	10.391	20.611	0.007	0.007	0.000	0.700	3.553	0.001	0.005
D7 / 3 . 24	10.215	20.511	0.010	0.008	0.006	0.759	3.966	0.006	-0.011
D7 / 4 . 25	10.506	20.706	0.005	0.008	0.003	0.706	3.800	0.016	0.008

D7 / 5 . 26	10.391	21.045	0.005	0.007	0.006	0.674	3.698	0.003	-0.026
D7 / 6 . 27	9.806	21.266	0.002	0.003	-0.001	0.687	4.816	-0.012	-0.017
D8 / 1 . 28	10.331	20.858	0.008	0.007	-0.001	0.713	3.715	-0.006	-0.009
D8 / 2 . 29	10.064	20.764	0.007	0.003	0.009	0.725	4.121	0.010	-0.024
D8 / 3 . 30	10.069	20.525	0.005	0.001	-0.004	0.720	4.238	-0.002	-0.002
D8 / 4 . 31	10.344	20.958	0.001	0.003	0.001	0.703	3.840	-0.002	-0.023
D8 / 5 . 32	10.333	20.426	0.009	0.010	0.002	0.748	3.548	0.000	-0.015
D8 / 6 . 33	10.606	21.016	0.007	0.006	-0.001	0.688	3.244	-0.002	-0.022
D11 / 1 . 34	10.304	20.807	0.003	0.002	-0.002	0.687	3.637	0.002	-0.008
D11 / 2 . 35	10.274	20.666	0.017	0.001	-0.005	0.774	3.936	0.001	0.008
D11 / 3 . 36	10.270	20.915	0.005	0.002	-0.003	0.720	3.956	0.003	0.006
D11 / 4 . 37	7.911	20.151	0.005	0.002	0.003	1.014	7.638	0.013	-0.012
D11 / 5 . 38	7.664	20.751	-0.001	0.011	0.006	1.158	7.973	-0.002	-0.021
D11 / 6 . 39	7.914	20.259	0.011	0.007	0.000	0.899	8.095	-0.001	-0.007
D11 / 7 . 40	8.128	20.392	0.001	0.002	-0.001	0.970	7.347	0.009	0.002
D21 / 1 . 41	10.152	20.844	0.008	0.005	-0.004	0.706	3.615	-0.014	-0.002
D22 / 1 . 42	9.859	21.082	0.009	-0.002	0.001	0.718	3.719	-0.012	-0.014
D23 / 1 . 43	10.099	20.850	0.007	0.004	-0.001	0.717	3.478	-0.006	-0.002
D24 / 1 . 44	10.006	20.750	0.012	0.009	-0.001	0.719	3.772	0.006	-0.015
D25 / 1 . 45	9.678	20.786	-0.001	0.002	-0.007	0.690	4.158	0.001	-0.008

Zone E

wt. %

Data point	Mg	Ca	Na	S	K	Mn	Fe	Sr	Ba
E1 / 1 . 01	6.377	20.879	0.007	0.006	0.001	0.913	7.362	0.002	-0.009
E2 / 1 . 02	6.956	20.598	0.000	0.006	0.000	0.985	7.195	0.004	-0.017
E3 / 1 . 03	7.111	20.965	0.006	0.004	0.014	0.816	6.661	0.002	-0.028
E5 / 1 . 04	6.322	21.537	0.017	0.011	0.000	0.961	6.972	-0.002	-0.014
E6 / 1 . 05	4.344	21.610	0.004	0.002	0.001	0.762	10.403	0.002	-0.011
E7 / 1 . 06	4.778	21.843	0.011	0.007	0.009	0.565	9.184	0.012	0.010
E16 / 1 . 07	5.123	23.261	0.005	0.015	0.005	0.941	7.651	0.009	0.001
E9 / 1 . 08	5.085	20.970	0.002	0.003	0.003	0.934	11.587	0.004	-0.005
E9 / 2 . 09	5.017	21.416	0.002	-0.004	0.004	0.620	11.570	-0.005	-0.003
E9 / 3 . 10	5.100	21.880	0.008	0.005	-0.001	0.457	11.293	0.005	-0.008
E9 / 4 . 11	5.030	21.939	0.003	0.005	0.006	0.308	11.283	0.018	-0.001
E9 / 5 . 12	5.017	22.499	0.009	0.007	0.001	0.401	10.745	0.021	-0.013
E10 / 1 . 13	6.569	23.091	0.011	0.011	0.002	0.559	7.350	0.006	0.001
E10 / 2 . 14	6.451	22.358	0.003	0.013	-0.001	0.414	8.279	0.018	-0.005
E10 / 3 . 15	6.034	22.187	0.000	0.005	-0.005	0.731	9.042	-0.010	-0.018
E10 / 4 . 16	5.634	22.173	0.009	0.000	0.007	0.629	9.946	0.011	-0.005
E10 / 5 . 17	5.443	22.071	0.006	0.004	0.009	0.456	10.448	0.013	0.005
E12 / 1 . 18	6.654	22.648	0.011	0.014	0.000	0.533	7.507	0.025	-0.022
E12 / 2 . 19	6.948	22.918	0.012	0.011	0.000	0.242	7.054	0.026	-0.019
E12 / 3 . 20	7.066	22.793	0.006	0.012	-0.004	0.353	7.073	0.013	-0.003
E12 / 4 . 21	6.714	22.174	0.009	0.009	-0.002	0.305	8.390	0.009	-0.008
E12 / 5 . 22	6.008	22.429	0.000	0.004	0.000	0.344	9.726	-0.004	-0.005
E12 / 6 . 23	5.703	22.548	-0.004	0.003	-0.003	0.584	9.181	0.001	-0.010
E16 / 1 . 24	5.217	21.562	0.005	0.001	-0.002	0.831	10.984	-0.005	-0.007
E16 / 2 . 25	4.833	21.305	0.000	0.005	0.002	0.621	11.857	0.000	-0.030
E16 / 3 . 26	5.230	21.623	0.009	0.006	0.004	0.627	11.354	0.007	-0.028
E16 / 4 . 27	4.932	22.237	0.006	0.005	0.000	0.250	11.245	0.013	-0.019
E16 / 5 . 28	4.740	22.537	0.009	0.007	0.000	0.359	11.015	0.005	-0.012
E16 / 6 . 29	4.999	22.410	0.012	0.006	0.003	0.511	10.313	0.013	-0.024

Appendix I.c. Normalised calcium, magnesium, iron, and manganese percentages in cement generations A to E highlighting the degree of stoichiometry in the dolomite system: $Ca_x Mg_x Fe_x Mn_x (CO_3)_2$. In this study Fe and Mn are grouped together.

Zone A

	$x\ (CO_3)_2$		
Data point	**Ca**	**Mg**	**Fe+Mn**
A14 / 1 . 01	0.974	0.002	0.024
A14 / 2 . 02	0.974	0.002	0.024
A14 / 3 . 03	0.973	0.002	0.025
A14 / 4 . 04	0.974	0.002	0.024
A14 / 5 . 05	0.976	0.002	0.022
A14 / 6 . 06	0.973	0.002	0.025
A14 / 7 . 07	0.974	0.002	0.024
A14 / 8 . 08	0.976	0.001	0.022
A13 / 1 . 09*	0.577	0.272	0.151
A13 / 2 . 10*	0.585	0.280	0.135
A13 / 3 . 11*	0.580	0.276	0.144
A13 / 4 . 12*	0.571	0.261	0.168
A13 / 5 . 13*	0.571	0.243	0.186
A13 / 6 . 14*	0.582	0.259	0.160
A13 / 7 . 15*	0.577	0.267	0.156
A15 / 1 . 16*	0.586	0.283	0.132
A15 / 2 . 17*	0.584	0.277	0.139
A15 / 3 . 18*	0.584	0.277	0.139
A15 / 4 . 19*	0.587	0.280	0.133
A15 / 5 . 20*	0.579	0.279	0.142

Zone B

	$x\ (CO_3)_2$		
Data point	**Ca**	**Mg**	**Fe+Mn**
B8 / 1 . 01	0.671	0.319	0.009
B8 / 1 . 02	0.639	0.352	0.010
B4 / 1 . 03	0.638	0.352	0.010
B8 / 1 . 04	0.663	0.327	0.010
B1 / 1 . 05	0.658	0.332	0.010
B5 / 1 . 06	0.651	0.339	0.010
B6 / 1 . 07	0.654	0.336	0.010
B4 / 6 . 08	0.658	0.330	0.011
B8 / 1 . 09	0.666	0.323	0.011
B2 / 1 . 10	0.618	0.354	0.028
B3 / 1 . 11	0.659	0.329	0.011
B4 / 7 . 12	0.633	0.357	0.010
B6 / 1 . 13	0.673	0.316	0.010
B5 / 1 . 14	0.678	0.311	0.011
B7 / 1 . 15	0.637	0.352	0.011
B13 / 1 . 16	0.667	0.322	0.011
B9 / 1 . 17	0.667	0.322	0.011
B7 / 1 . 18	0.662	0.327	0.011
B9 / 1 . 19	0.636	0.354	0.010
B11 / 1 . 20	0.656	0.333	0.010
B1 / 3 . 21	0.655	0.335	0.010

B5 / 1 . 22	0.655	0.335	0.010
B4 / 3 . 23	0.637	0.351	0.012
B4 / 1 . 24	0.653	0.335	0.012
B10 / 1 . 25	0.656	0.333	0.012
B4 / 5 . 26	0.641	0.348	0.012
B3 / 1 . 27	0.660	0.328	0.012
B12 / 1 . 28	0.660	0.328	0.012
B4 / 4 . 29	0.639	0.349	0.012
B1 / 1 . 30	0.642	0.346	0.012
B10 / 1 . 31	0.667	0.321	0.012
B17 / 1 . 32	0.638	0.349	0.012
B14 / 1 . 33	0.672	0.316	0.012
B4 / 1 . 34	0.663	0.324	0.013
B1 / 2 . 35	0.628	0.359	0.013
B9 / 1 . 36	0.660	0.327	0.013
B7 / 1 . 37	0.672	0.315	0.013
B10 / 1 . 38	0.674	0.312	0.013
B4 / 2 . 39	0.637	0.349	0.014
B7 / 1 . 40	0.626	0.340	0.033
B6 / 1 . 41	0.660	0.305	0.034
B2 / 1 . 42	0.620	0.345	0.035
B12 / 1 . 43	0.623	0.341	0.036
B9 / 1 . 44	0.669	0.311	0.020
B11 / 1 . 45	0.667	0.313	0.020
B2 / 1 . 46	0.652	0.327	0.021
B4 / 1 . 47	0.672	0.307	0.021
B10 / 1 . 48	0.661	0.313	0.027
B4 / 9 . 49	0.626	0.352	0.022
B18 / 1 . 50	0.629	0.347	0.023
B4 / 8 . 51	0.624	0.350	0.026
B3 / 1 . 52	0.664	0.306	0.031
B1 / 4 . 53	0.623	0.346	0.032
B20 / 1 . 54	0.628	0.339	0.033
B19 / 1 . 55	0.651	0.334	0.015
B1 / 1 . 56	0.661	0.323	0.016
B1 / 7 . 57	0.669	0.313	0.018
B1 / 6 . 58	0.667	0.314	0.020
B1 / 5 . 59	0.622	0.341	0.037

Zone C

	$x\ (CO_3)_2$		
Data point	**Ca**	**Mg**	**Fe+Mn**
C9 / 1 . 01	0.556	0.231	0.213
C10 / 1 . 02	0.556	0.222	0.222
C11 / 1 . 03	0.659	0.308	0.033
C12 / 1 . 04	0.651	0.288	0.061
C13 / 1 . 05	0.618	0.250	0.131
C14 / 1 . 06	0.648	0.282	0.070
C15 / 1 . 07	0.656	0.305	0.039
C16 / 1 . 08	0.652	0.288	0.060
C17 / 1 . 09	0.640	0.284	0.076
C18 / 1 . 10	0.658	0.307	0.035
C19 / 1 . 11	0.657	0.302	0.040
C20 / 1 . 12	0.663	0.306	0.031

C2 / 1 . 13	0.577	0.268	0.154
C2 / 2 . 14	0.572	0.261	0.167
C2 / 3 . 15	0.569	0.260	0.171
C2 / 4 . 16	0.569	0.254	0.177
C3 / 1 . 17	0.575	0.245	0.180
C3 / 2 . 18	0.567	0.252	0.181
C3 / 3 . 19	0.567	0.265	0.168
C3 / 4 . 20	0.569	0.262	0.169
C3 / 5 . 21	0.566	0.252	0.182
C5 / 1 . 22	0.577	0.254	0.169
C5 / 2 . 23	0.570	0.249	0.181
C5 / 3 . 24	0.569	0.248	0.182
C5 / 4 . 25	0.569	0.246	0.185
C5 / 5 . 26	0.569	0.252	0.179
C5 / 6 . 27	0.565	0.249	0.187
C5 / 7 . 28	0.574	0.251	0.176
C6 / 1 . 29	0.574	0.255	0.170
C6 / 2 . 30	0.567	0.247	0.186
C6 / 3 . 31	0.565	0.248	0.187
C6 / 4 . 32	0.570	0.245	0.185
C6 / 5 . 33	0.566	0.236	0.198
C6 / 6 . 34	0.558	0.228	0.213
C6 / 7 . 35	0.563	0.230	0.206

Zone D

	$x\ (CO_3)_2$		
Data point	**Ca**	**Mg**	**Fe+Mn**
D11 / 1 . 01	0.573	0.258	0.169
D12 / 1 . 02	0.578	0.269	0.153
D1 / 1 . 03	0.560	0.233	0.207
D2 / 1 . 04	0.561	0.221	0.219
D3 / 1 . 05	0.560	0.215	0.225
D4 / 1 . 06	0.558	0.216	0.225
D5 / 1 . 07	0.550	0.200	0.250
D6 / 1 . 08	0.560	0.220	0.220
D7 / 1 . 09	0.583	0.268	0.149
D8 / 1 . 10	0.567	0.232	0.201
D9 / 1 . 11	0.602	0.285	0.113
D10 / 1 . 12	0.587	0.279	0.134
D21 / 1 . 13	0.601	0.234	0.165
D22 / 1 . 14	0.607	0.232	0.161
D23 / 1 . 15	0.615	0.253	0.132
D24 / 1 . 16	0.622	0.251	0.127
D25 / 1 . 17	0.606	0.237	0.157
D26 / 1 . 18	0.613	0.252	0.134
D27 / 1 . 19	0.611	0.234	0.155
D28 / 1 . 20	0.599	0.224	0.178
D29 / 1 . 21	0.605	0.203	0.192
D7 / 1 . 22	0.585	0.289	0.126
D7 / 2 . 23	0.585	0.295	0.121
D7 / 3 . 24	0.579	0.288	0.133
D7 / 4 . 25	0.580	0.294	0.126
D7 / 5 . 26	0.588	0.290	0.122

D7 / 6 . 27	0.581	0.268	0.150
D8 / 1 . 28	0.586	0.290	0.124
D8 / 2 . 29	0.582	0.282	0.136
D8 / 3 . 30	0.577	0.283	0.139
D8 / 4 . 31	0.585	0.289	0.127
D8 / 5 . 32	0.583	0.295	0.123
D8 / 6 . 33	0.591	0.298	0.111
D11 / 1 . 34	0.587	0.291	0.122
D11 / 2 . 35	0.580	0.288	0.132
D11 / 3 . 36	0.583	0.286	0.130
D11 / 4 . 37	0.549	0.215	0.236
D11 / 5 . 38	0.553	0.204	0.243
D11 / 6 . 39	0.545	0.213	0.242
D11 / 7 . 40	0.554	0.221	0.226
D21 / 1 . 41	0.590	0.287	0.122
D22 / 1 . 42	0.596	0.279	0.125
D23 / 1 . 43	0.593	0.287	0.119
D24 / 1 . 44	0.589	0.284	0.127
D25 / 1 . 45	0.589	0.274	0.137

Zone E

	$x\ (CO_3)_2$		
Data point	**Ca**	**Mg**	**Fe+Mn**
E1 / 1 . 01	0.588	0.179	0.233
E2 / 1 . 02	0.576	0.195	0.229
E3 / 1 . 03	0.590	0.200	0.210
E5 / 1 . 04	0.602	0.177	0.222
E6 / 1 . 05	0.582	0.117	0.301
E7 / 1 . 06	0.601	0.131	0.268
E16 / 1 . 07	0.629	0.139	0.232
E9 / 1 . 08	0.544	0.132	0.325
E9 / 2 . 09	0.554	0.130	0.316
E9 / 3 . 10	0.565	0.132	0.303
E9 / 4 . 11	0.569	0.130	0.301
E9 / 5 . 12	0.582	0.130	0.288
E10 / 1 . 13	0.615	0.175	0.211
E10 / 2 . 14	0.596	0.172	0.232
E10 / 3 . 15	0.584	0.159	0.257
E10 / 4 . 16	0.578	0.147	0.276
E10 / 5 . 17	0.574	0.142	0.284
E12 / 1 . 18	0.607	0.178	0.215
E12 / 2 . 19	0.617	0.187	0.196
E12 / 3 . 20	0.611	0.190	0.199
E12 / 4 . 21	0.590	0.179	0.231
E12 / 5 . 22	0.582	0.156	0.262
E12 / 6 . 23	0.593	0.150	0.257
E16 / 1 . 24	0.559	0.135	0.306
E16 / 2 . 25	0.552	0.125	0.323
E16 / 3 . 26	0.557	0.135	0.309
E16 / 4 . 27	0.575	0.128	0.297
E16 / 5 . 28	0.583	0.123	0.294
E16 / 6 . 29	0.586	0.131	0.283

Appendix II

Appendix II.a. Equation for calculating the density (g cm^{-3}) of fluids in vapour saturated H_2O-NaCl solutions (Bodnar, 1983):

$$
\begin{aligned}
= \quad & 0.9923 - 3.0512 \times 10^{-2}\ A^2 \\
& - 2.1977 \times 10^{-4}\ A^4 + 8.6241 \times 10^{-2}\ B \\
& - 4.1768 \times 10^{-2}\ AB + 1.4825 \times 10^{-2}\ A^2B \\
& + 1.4460 \times 10^{-3}\ A^3B - 3.0852 \times 10^{-9}\ A^8B \\
& + 1.3051 \times 10^{-2}\ AB^2 - 6.1402 \times 10^{-3}\ A^2B^2 \\
& - 1.2843 \times 10^{-3}\ AB^3 + 3.7604 \times 10^{-4}\ A^2B^3 \\
& - 9.99594 \times 10^{-9}\ A^2B^7
\end{aligned}
$$

Where A = temperature (0°C / 100), and B = salinity (wt.% NaCl / 10)

Appendix II.b. Plot illustrating the determined shape factor and measured T_h of the fluid inclusions analysed. Shape factor was determined using the qualitative estimations of Osborne & Haszeldine (1993) and Blanchet *et al*. (2003).

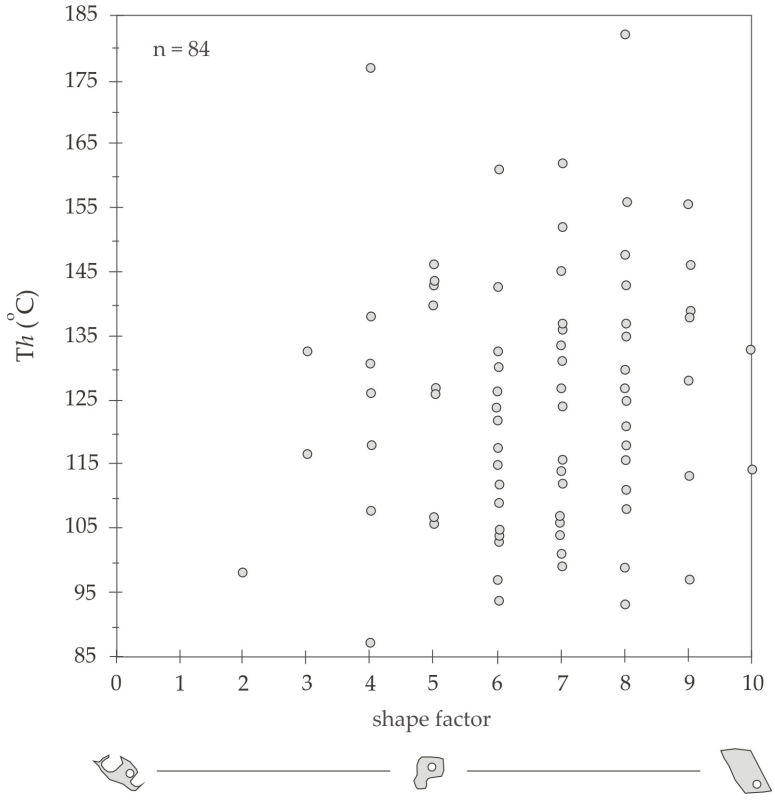

Appendix II.c. Inclusion volume vs. T_h plots for individual carbonate cement generations A to E. Lower T_h inclusions within each generation typically exhibit larger volumes compared to higher T_h inclusions, suggesting larger inclusions are less resistant to resetting compared to smaller inclusions(c.f. Bodnar *et al.,* 1989) .

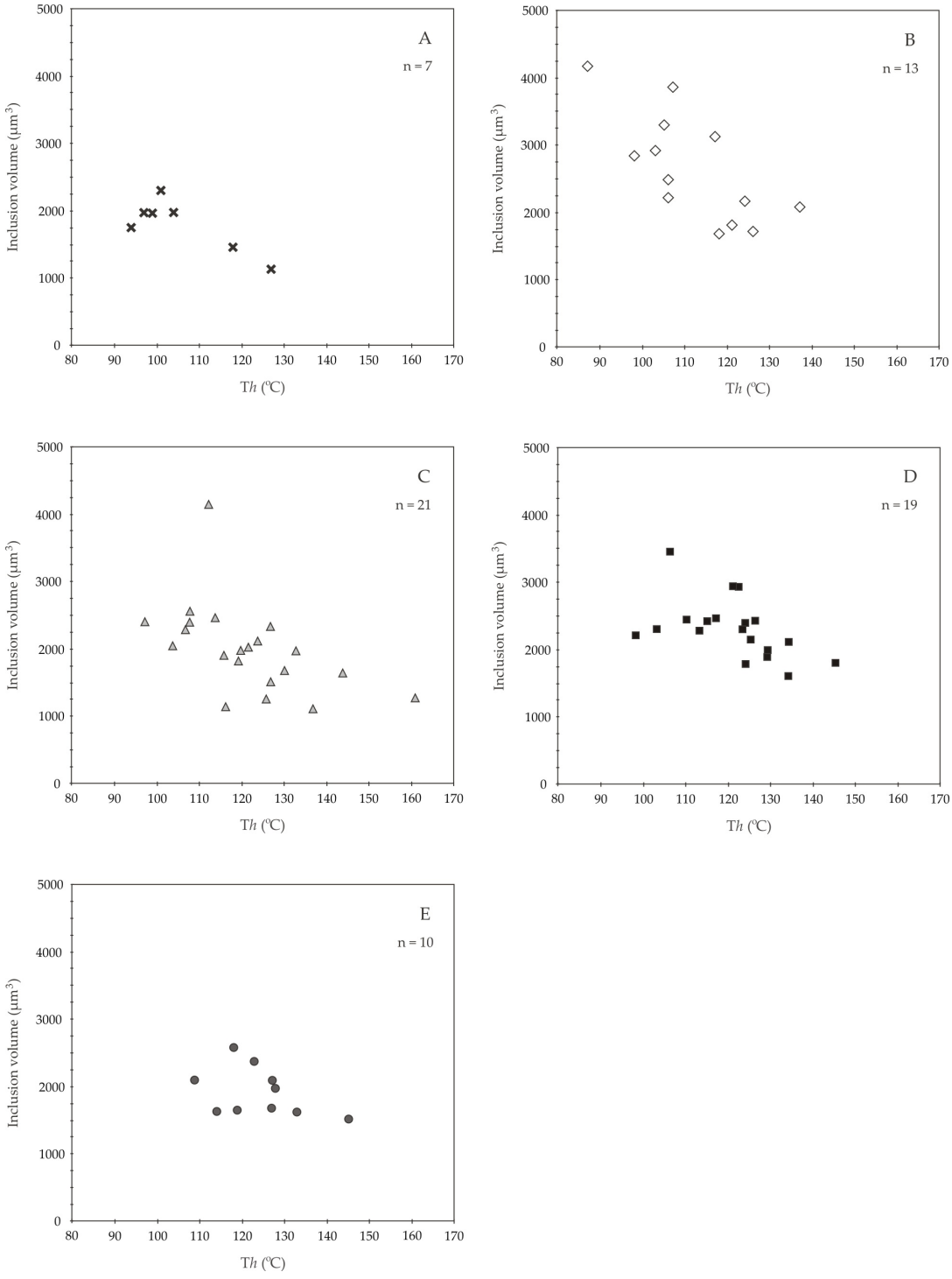

Appendix II.d. Plot of T_h vs. salinity for the fracture cement (A to E) showing fluid inclusions producing T_h values greater than present-day formation temperatures (>120°C), typically exhibiting salinities greater than present-day waters (~8 wt.% NaCl).

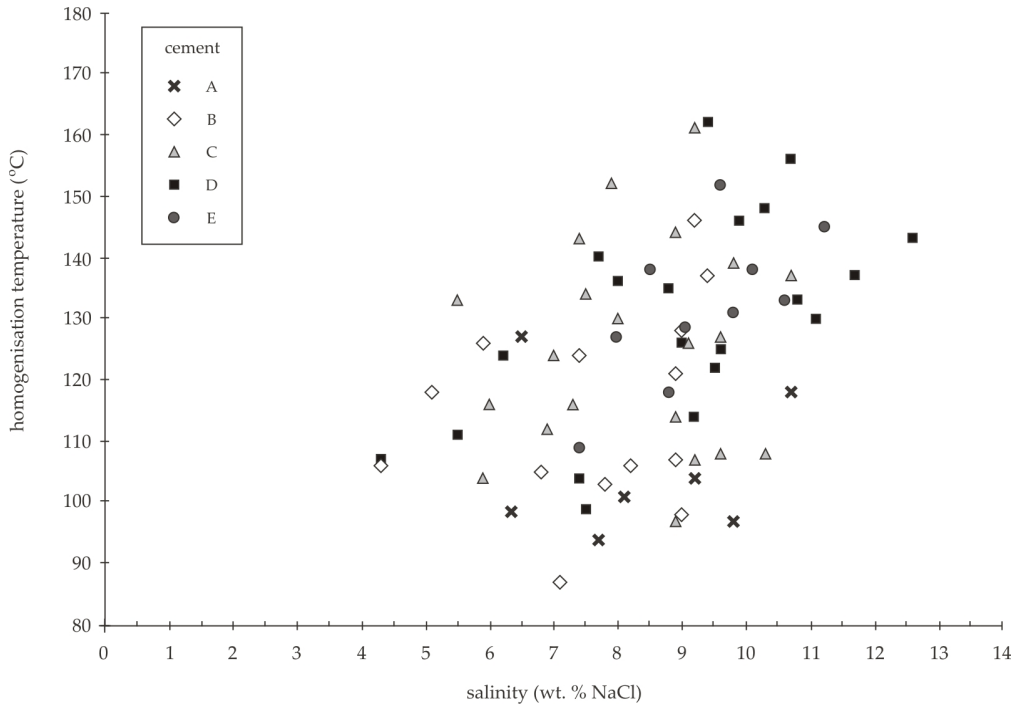

Appendix III

Appendix III.a. Parameters and results of PHREEQC simulations for differing wallrock scenarios assuming hydrostatic pressure and thermal equilibrium with the regional geothermal gradient (37°C/km).

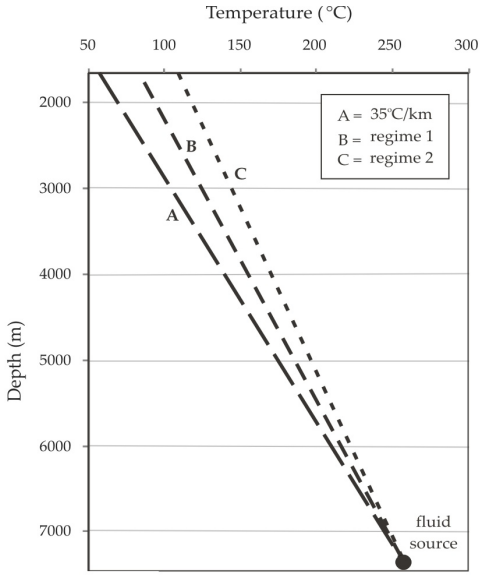

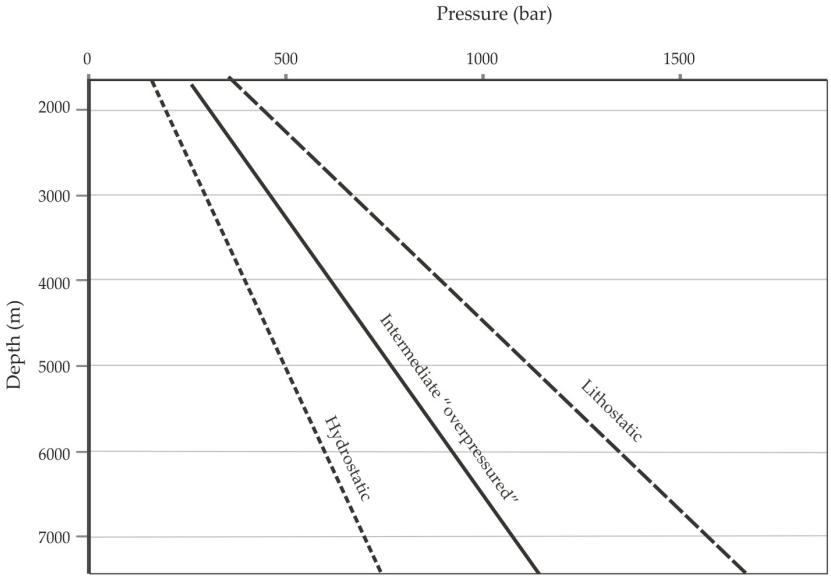

Appendix III.b. Parameters and results of PHREEQC simulations for ascent of fluids with varying salinities (0, 1, 2, and 5 wt.%) at intermediate pressure and rpaid fluid flow rate (temperature regime c). Results relate to those in Figure 7.3. See appendix IIIa for conditions.

5% Salinity

	mol					
salinity	Na	Cl	SO_4^{-2}	K	Mg	Ca
5%	0.67	0.78	4.03E-02	1.46E-02	7.54E-02	1.47E-02

						Saturation index		mol C			
Temp (°C)	Pressure (MPs)	pH	C	Ca	Mg	calcite	dolomite	calcite	dolomite	$CO_{2(g)}$	in solution
102	352	4.326	2.10	9.91E-03	7.14E-02	-1.06	0.18	0.00E+00	6.02E-04	0.103	2.097
120	440	4.328	2.20	1.05E-02	7.20E-02	-0.92	0.48	0.00E+00	6.17E-04	0.132	2.200
138	527	4.328	2.33	1.11E-02	7.26E-02	-0.80	0.72	0.00E+00	6.21E-04	0.162	2.332
155	615	4.328	2.49	1.18E-02	7.32E-02	-0.72	0.93	0.00E+00	6.10E-04	0.211	2.494
172	703	4.326	2.70	1.24E-02	7.38E-02	-0.65	1.05	0.00E+00	5.94E-04	0.265	2.705
190	791	4.325	2.97	1.30E-02	7.44E-02	-0.59	1.17	0.00E+00	5.63E-04	0.335	2.970
208	879	4.326	3.30	1.35E-02	7.50E-02	-0.55	1.27	1.43E-04	3.36E-04	0.386	3.305
225	967	4.329	3.69	1.40E-02	7.53E-02	-0.52	1.34	2.88E-04	1.38E-04	0.499	3.691
243	1055	4.336	4.19	1.44E-02	7.54E-02	-0.50	1.41	2.87E-04	0.00E+00	0.573	4.189
260	1143	4.351	4.76								

		% initial C				distribution (cumulative)		
Temp (°C)	Pressure (MPs)	in solution	exsolved (CO_2)	calcite	dolomite	$CO_{2(g)}$ (m^3) @ STP	calcite g/l	dolomite g/l
102	352	44.04	55.98	1.51E-02	1.71E-01	0.059	7.18E-02	7.52E-01
120	440	46.20	53.82	1.51E-02	1.46E-01	0.057	7.18E-02	6.41E-01
138	527	48.98	51.05	1.51E-02	1.20E-01	0.054	7.18E-02	5.28E-01
155	615	52.38	47.65	1.51E-02	9.41E-02	0.050	7.18E-02	4.13E-01
172	703	56.81	43.22	1.51E-02	6.85E-02	0.046	7.18E-02	3.01E-01
190	791	62.37	37.65	1.51E-02	4.35E-02	0.040	7.18E-02	1.91E-01
208	879	69.40	30.62	1.51E-02	1.99E-02	0.032	7.18E-02	8.73E-02
225	967	77.50	22.51	1.21E-02	5.78E-03	0.024	5.76E-02	2.54E-02
243	1055	87.97	12.03	6.02E-03	0.00E+00	0.013	2.87E-02	0.00E+00
260	1143							

2% Salinity

	mol					
salinity	Na	Cl	SO_4^{-2}	K	Mg	Ca
2%	0.268	0.312	1.61E-02	5.83E-03	3.02E-02	5.89E-03

Temp (°C)	Pressure (MPs)	pH	C	Ca	Mg	Saturation index calcite	Saturation index dolomite	mol C calcite	mol C dolomite	mol C $CO_{2(g)}$	mol C in solution
102	352	4.352	2.35	2.98E-03	2.75E-02	-1.47	-0.58	0.00E+00	3.61E-04	0.115	2.351
120	440	4.344	2.47	3.34E-03	2.78E-02	-1.31	-0.28	0.00E+00	4.34E-04	0.190	2.466
138	527	4.331	2.66	3.77E-03	2.83E-02	-1.19	-0.04	0.00E+00	3.52E-04	0.144	2.656
155	615	4.326	2.80	4.12E-03	2.86E-02	-1.09	0.17	0.00E+00	3.94E-04	0.235	2.800
172	703	4.316	3.03	4.52E-03	2.90E-02	-1.02	0.29	0.00E+00	3.85E-04	0.301	3.035
190	791	4.307	3.34	4.90E-03	2.94E-02	-0.95	0.41	0.00E+00	3.62E-04	0.380	3.336
208	879	4.301	3.72	5.27E-03	2.97E-02	-0.91	0.51	0.00E+00	2.64E-04	0.440	3.716
225	967	4.298	4.16	5.53E-03	3.00E-02	-0.88	0.58	0.00E+00	1.81E-04	0.569	4.155
243	1055	4.299	4.72	5.71E-03	3.02E-02	-0.86	0.64	1.77E-04	0.00E+00	0.654	4.724
260	1143	4.308	5.38								

Temp (°C)	Pressure (MPs)	% initial C in solution	% initial C exsolved (CO_2)	% initial C calcite	% initial C dolomite	distribution (cumulative) $CO_{2(g)}$ (m^3) @ STP	distribution (cumulative) calcite g/l	distribution (cumulative) dolomite g/l
102	352	43.71	56.30	3.28E-03	1.02E-01	0.067	1.77E-02	5.04E-01
120	440	45.85	54.17	3.28E-03	8.82E-02	0.065	1.77E-02	4.37E-01
138	527	49.38	50.63	3.28E-03	7.21E-02	0.061	1.77E-02	3.57E-01
155	615	52.06	47.95	3.28E-03	5.90E-02	0.057	1.77E-02	2.92E-01
172	703	56.43	43.58	3.28E-03	4.43E-02	0.052	1.77E-02	2.20E-01
190	791	62.03	37.99	3.28E-03	3.00E-02	0.045	1.77E-02	1.49E-01
208	879	69.09	30.92	3.28E-03	1.65E-02	0.037	1.77E-02	8.20E-02
225	967	77.27	22.74	3.28E-03	6.73E-03	0.027	1.77E-02	3.34E-02
243	1055	87.84	12.16	3.28E-03	0.00E+00	0.015	1.77E-02	0.00E+00
260	1143							

1% Salinity

salinity	mol Na	mol Cl	mol SO_4^{-2}	mol K	mol Mg	mol Ca
1%	0.134	0.156	8.06E-03	2.91E-03	1.51E-02	2.94E-03

Temp (°C)	Pressure (MPs)	pH	C	Ca	Mg	Saturation index calcite	Saturation index dolomite	mol C calcite	mol C dolomite	mol C $CO_{2(g)}$	mol C in solution
102	352	4.333	2.44	1.21E-03	1.35E-02	-1.81	-1.21	0.00E+00	1.98E-04	0.120	2.439
120	440	4.319	2.56	1.41E-03	1.37E-02	-1.65	-0.91	0.00E+00	2.20E-04	0.154	2.559
138	527	4.304	2.71	1.63E-03	1.39E-02	-1.52	-0.67	0.00E+00	2.30E-04	0.195	2.713
155	615	4.288	2.91	1.86E-03	1.41E-02	-1.42	-0.46	0.00E+00	2.44E-04	0.244	2.908
172	703	4.272	3.15	2.10E-03	1.44E-02	-1.34	-0.34	0.00E+00	2.35E-04	0.314	3.152
190	791	4.256	3.47	2.34E-03	1.46E-02	-1.27	-0.22	0.00E+00	2.24E-04	0.396	3.466
208	879	4.244	3.86	2.56E-03	1.48E-02	-1.22	-0.12	0.00E+00	1.60E-04	0.460	3.862
225	967	4.235	4.32	2.72E-03	1.50E-02	-1.19	-0.05	0.00E+00	1.10E-04	0.594	4.322
243	1055	4.230	4.92	2.83E-03	1.51E-02	-1.17	0.00	1.10E-04	4.03E-06	0.684	4.916
260	1143	4.232	5.60								

Temp (°C)	Pressure (MPs)	% initial C in solution	% initial C exsolved (CO_2)	% initial C calcite	% initial C dolomite	distribution (cumulative) $CO_{2(g)}$ (m^3) @ STP	distribution (cumulative) calcite g/l	distribution (cumulative) dolomite g/l
102	352	43.56	56.45	1.97E-03	5.80E-02	0.070	1.10E-02	3.00E-01
120	440	45.70	54.30	1.97E-03	5.10E-02	0.068	1.10E-02	2.63E-01
138	527	48.45	51.55	1.97E-03	4.31E-02	0.064	1.10E-02	2.23E-01
155	615	51.94	48.07	1.97E-03	3.49E-02	0.060	1.10E-02	1.80E-01
172	703	56.29	43.71	1.97E-03	2.62E-02	0.054	1.10E-02	1.35E-01
190	791	61.90	38.11	1.97E-03	1.78E-02	0.047	1.10E-02	9.18E-02
208	879	68.97	31.04	1.97E-03	9.77E-03	0.039	1.10E-02	5.04E-02
225	967	77.18	22.82	1.97E-03	4.06E-03	0.028	1.10E-02	2.10E-02
243	1055	87.79	12.21	1.97E-03	1.44E-04	0.015	1.10E-02	7.44E-04
260	1143							

0% Salinity

Temp (°C)	Pressure (MPs)	pH	C	Ca	Mg	Saturation index calcite	Saturation index dolomite	mol C calcite	mol C dolomite	mol C $CO_{2(g)}$	mol C in solution
102	352	3.708	2.52	-	-	-	-	-	-	0.127	2.517
120	440	3.687	2.64	-	-	-	-	-	-	0.163	2.644
138	527	3.663	2.81	-	-	-	-	-	-	0.206	2.807
155	615	3.635	3.01	-	-	-	-	-	-	0.256	3.013
172	703	3.604	3.27	-	-	-	-	-	-	0.329	3.269
190	791	3.569	3.60	-	-	-	-	-	-	0.415	3.598
208	879	3.532	4.01	-	-	-	-	-	-	0.480	4.013
225	967	3.497	4.49	-	-	-	-	-	-	0.620	4.493
243	1055	3.461	5.11	-	-	-	-	-	-	0.715	5.113
260	1143	3.430	5.83								

Temp (°C)	Pressure (MPs)	% initial C in solution	% initial C exsolved (CO_2)	% initial C calcite	% initial C dolomite	distribution (cumulative) $CO_{2(g)}$ (m^3) @ STP	distribution (cumulative) calcite g/l	distribution (cumulative) dolomite g/l
102	352	43.19	56.81	-	-	0.074	-	-
120	440	45.37	54.63	-	-	0.071	-	-
138	527	48.16	51.84	-	-	0.067	-	-
155	615	51.70	48.30	-	-	0.063	-	-
172	703	56.09	43.91	-	-	0.057	-	-
190	791	61.74	38.26	-	-	0.050	-	-
208	879	68.86	31.14	-	-	0.040	-	-
225	967	77.09	22.91	-	-	0.030	-	-
243	1055	87.73	12.27	-	-	0.016	-	-
260	1143							

Appendix III.c. Parameters and results of PHREEQC simulations for ascent of 1 wt%. salinity fluid at intermediate fluid pressures in a host of temperature regimes related to fluid flow rates. Results illustrated in Figure 7.4. See appendix IIIa for conditions.

Temperature regime 1

						Saturation index		mol C			
Temp (°C)	Pressure (MPs)	pH	C	Ca	Mg	calcite	dolomite	calcite	dolomite	$CO_{2(g)}$	in solution
80	352	4.304	2.79	1.14E-03	1.35E-02	-2.03	-1.65	0.00E+00	1.28E-04	0.000	2.790
100	440	4.305	2.79	1.27E-03	1.36E-02	-1.82	-1.16	0.00E+00	1.55E-04	0.009	2.790
120	527	4.306	2.80	1.42E-03	1.38E-02	-1.65	-0.90	0.00E+00	2.02E-04	0.095	2.799
140	615	4.298	2.89	1.63E-03	1.40E-02	-1.50	-0.64	0.00E+00	2.59E-04	0.181	2.895
160	703	4.285	3.08	1.88E-03	1.42E-02	-1.39	-0.43	0.00E+00	2.76E-04	0.271	3.076
180	791	4.270	3.35	2.16E-03	1.45E-02	-1.30	-0.27	0.00E+00	2.59E-04	0.372	3.347
200	879	4.254	3.72	2.42E-03	1.48E-02	-1.24	-0.15	0.00E+00	2.18E-04	0.482	3.718
220	967	4.242	4.20	2.64E-03	1.50E-02	-1.20	-0.06	8.27E-05	9.17E-05	0.620	4.200
240	1055	4.233	4.82	2.81E-03	1.51E-02	-1.17	0.00	1.32E-04	0.00E+00	0.780	4.820
260	1143	4.232	5.60	2.94E-03	1.51E-02			2.14E-04	1.59E-03		5.603

		% initial C				distribution (cumulative)		
Temp (°C)	Pressure (MPs)	in solution	exsolved (CO_2)	calcite	dolomite	$CO_{2(g)}$ (m^3) @ STP	calcite g/l	dolomite g/l
80	352	49.83	50.18	3.83E-03	5.67E-02	0.062	2.15E-02	2.93E-01
100	440	49.83	50.18	3.83E-03	5.22E-02	0.062	2.15E-02	2.69E-01
120	527	49.99	50.02	3.83E-03	4.66E-02	0.062	2.15E-02	2.41E-01
140	615	51.69	48.32	3.83E-03	3.94E-02	0.060	2.15E-02	2.04E-01
160	703	54.92	45.09	3.83E-03	3.02E-02	0.056	2.15E-02	1.56E-01
180	791	59.76	40.25	3.83E-03	2.03E-02	0.050	2.15E-02	1.05E-01
200	879	66.40	33.61	3.83E-03	1.11E-02	0.042	2.15E-02	5.71E-02
220	967	75.00	25.00	3.83E-03	3.27E-03	0.031	2.15E-02	1.69E-02
240	1055	86.07	13.93	2.35E-03	0.00E+00	0.017	1.32E-02	0.00E+00
260	1143							

Temperature regime 2

						Saturation index		mol C			
Temp (°C)	Pressure (MPs)	pH	C	Ca	Mg	calcite	dolomite	calcite	dolomite	$CO_{2(g)}$	in solution
102	352	4.333	2.44	1.21E-03	1.35E-02	-1.81	-1.21	0.00E+00	1.98E-04	0.120	2.439
120	440	4.319	2.56	1.41E-03	1.37E-02	-1.65	-0.91	0.00E+00	2.20E-04	0.154	2.559
138	527	4.304	2.71	1.63E-03	1.39E-02	-1.52	-0.67	0.00E+00	2.30E-04	0.195	2.713
155	615	4.288	2.91	1.86E-03	1.41E-02	-1.42	-0.46	0.00E+00	2.44E-04	0.244	2.908
172	703	4.272	3.15	2.10E-03	1.44E-02	-1.34	-0.34	0.00E+00	2.35E-04	0.314	3.152
190	791	4.256	3.47	2.34E-03	1.46E-02	-1.27	-0.22	0.00E+00	2.24E-04	0.396	3.466
208	879	4.244	3.86	2.56E-03	1.48E-02	-1.22	-0.12	0.00E+00	1.60E-04	0.460	3.862
225	967	4.235	4.32	2.72E-03	1.50E-02	-1.19	-0.05	0.00E+00	1.10E-04	0.594	4.322
243	1055	4.230	4.92	2.83E-03	1.51E-02	-1.17	0.00	1.10E-04	4.03E-06	0.684	4.916
260	1143	4.232	5.60	2.94E-03	1.51E-02					-5.600	5.600

Temp (°C)	Pressure (MPs)	% initial C in solution	% initial C exsolved (CO_2)	% initial C calcite	% initial C dolomite	distribution (cumulative) $CO_{2(g)}$ (m^3) @ STP	distribution (cumulative) calcite g/l	distribution (cumulative) dolomite g/l
102	352	43.56	56.45	1.97E-03	5.80E-02	0.070	1.10E-02	3.00E-01
120	440	45.70	54.30	1.97E-03	5.10E-02	0.068	1.10E-02	2.63E-01
138	527	48.45	51.55	1.97E-03	4.31E-02	0.064	1.10E-02	2.23E-01
155	615	51.94	48.07	1.97E-03	3.49E-02	0.060	1.10E-02	1.80E-01
172	703	56.29	43.71	1.97E-03	2.62E-02	0.054	1.10E-02	1.35E-01
190	791	61.90	38.11	1.97E-03	1.78E-02	0.047	1.10E-02	9.18E-02
208	879	68.97	31.04	1.97E-03	9.77E-03	0.039	1.10E-02	5.04E-02
225	967	77.18	22.82	1.97E-03	4.06E-03	0.028	1.10E-02	2.10E-02
243	1055	87.79	12.21	1.97E-03	1.44E-04	0.015	1.10E-02	7.44E-04
260	1143							

Temperature regime 3

Temp (°C)	Pressure (MPs)	pH	C	Ca	Mg	Saturation index calcite	Saturation index dolomite	mol C calcite	mol C dolomite	mol C $CO_{2(g)}$	mol C in solution
125	352	4.357	2.22	1.32E-03	1.37E-02	-1.62	-0.83	0.00E+00	2.48E-04	0.251	2.216
140	440	4.327	2.47	1.57E-03	1.39E-02	-1.51	-0.64	0.00E+00	2.39E-04	0.249	2.467
155	527	4.303	2.72	1.81E-03	1.42E-02	-1.42	-0.48	0.00E+00	2.23E-04	0.265	2.716
170	615	4.283	2.98	2.03E-03	1.44E-02	-1.34	-0.35	0.00E+00	2.16E-04	0.295	2.981
185	703	4.267	3.28	2.25E-03	1.46E-02	-1.28	-0.24	0.00E+00	1.97E-04	0.335	3.276
200	791	4.254	3.61	2.45E-03	1.48E-02	-1.24	-0.15	0.00E+00	1.64E-04	0.392	3.611
215	879	4.243	4.00	2.61E-03	1.50E-02	-1.20	-0.08	0.00E+00	1.30E-04	0.449	4.003
230	967	4.236	4.45	2.74E-03	1.51E-02	-1.18	-0.02	1.32E-04	0.00E+00	0.530	4.452
245	1055	4.231	4.98	2.87E-03	1.51E-02	-1.16	0.02	7.17E-05	0.00E+00	0.618	4.982
260	1143	4.232	5.60	2.94E-03	1.51E-02					-5.600	5.600

Temp (°C)	Pressure (MPs)	% initial C in solution	% initial C exsolved (CO_2)	% initial C calcite	% initial C dolomite	distribution (cumulative) $CO_{2(g)}$ (m^3) @ STP	distribution (cumulative) calcite g/l	distribution (cumulative) dolomite g/l
125	352	39.58	60.43	3.63E-03	5.06E-02	0.075	2.04E-02	2.61E-01
140	440	44.06	55.95	3.63E-03	4.18E-02	0.070	2.04E-02	2.16E-01
155	527	48.51	51.50	3.63E-03	3.32E-02	0.064	2.04E-02	1.72E-01
170	615	53.24	46.77	3.63E-03	2.53E-02	0.058	2.04E-02	1.30E-01
185	703	58.51	41.50	3.63E-03	1.75E-02	0.052	2.04E-02	9.05E-02
200	791	64.49	35.52	3.63E-03	1.05E-02	0.044	2.04E-02	5.42E-02
215	879	71.49	28.52	3.63E-03	4.64E-03	0.035	2.04E-02	2.40E-02
230	967	79.50	20.50	3.63E-03	0.00E+00	0.026	2.04E-02	0.00E+00
245	1055	88.97	11.04	1.28E-03	0.00E+00	0.014	7.17E-03	0.00E+00
260	1143							

Appendix III.d. Parameters and results of PHREEQC simulations for ascent of 1 wt%. salinity fluid in thermal equilibrium with geothermal gradient (37°C/km) at a range of pressures (hydrostatic, intermediate, and lithostatic). Results relate to those in Figure 7.5. See appendix IIIa for conditions.

Hydrostatic pressure – 37°C/km geothermal gradient

						Saturation index		mol C			
Temp (°C)	Pressure (MPs)	pH	C	Ca	Mg	calcite	dolomite	calcite	dolomite	$CO_{2(g)}$	in solution
80	229	4.488	2.16	9.81E-04	1.32E-02	-1.84	-1.22	0.00E+00	1.26E-04	0.000	2.164
100	284	4.488	2.16	1.11E-03	1.33E-02	-1.62	-0.80	0.00E+00	1.83E-04	0.056	2.164
120	343	4.480	2.22	1.29E-03	1.35E-02	-1.43	-0.46	0.00E+00	2.43E-04	0.123	2.220
140	400	4.465	2.34	1.53E-03	1.38E-02	-1.28	-0.19	0.00E+00	2.78E-04	0.195	2.344
160	457	4.444	2.54	1.81E-03	1.40E-02	-1.16	0.02	0.00E+00	3.12E-04	0.271	2.539
180	514	4.423	2.81	2.12E-03	1.43E-02	-1.06	0.19	0.00E+00	2.92E-04	0.364	2.810
200	571	4.402	3.17	2.42E-03	1.46E-02	-0.99	0.32	0.00E+00	2.40E-04	0.459	3.173
220	629	4.386	3.63	2.66E-03	1.49E-02	-0.94	0.42	0.00E+00	1.76E-04	0.592	3.632
240	686	4.376	4.22	2.83E-03	1.51E-02	-0.91	0.50	6.45E-05	4.77E-05	0.745	4.224
260	743	4.373	4.97	2.94E-03	1.51E-02			6.45E-05	1.90E-03		4.973

		% initial C				distribution (cumulative)		
Temp (°C)	Pressure (MPs)	in solution	exsolved (CO_2)	calcite	dolomite	$CO_{2(g)}$ (m^3) @ STP	calcite g/l	dolomite g/l
80	229	43.56	56.45	1.30E-03	7.64E-02	0.062	6.45E-03	3.50E-01
100	284	43.56	56.45	1.30E-03	7.13E-02	0.062	6.45E-03	3.27E-01
120	343	44.69	55.32	1.30E-03	6.39E-02	0.061	6.45E-03	2.93E-01
140	400	47.16	52.85	1.30E-03	5.42E-02	0.058	6.45E-03	2.48E-01
160	457	51.09	48.92	1.30E-03	4.30E-02	0.054	6.45E-03	1.97E-01
180	514	56.54	43.47	1.30E-03	3.04E-02	0.048	6.45E-03	1.39E-01
200	571	63.87	36.14	1.30E-03	1.87E-02	0.040	6.45E-03	8.55E-02
220	629	73.10	26.91	1.30E-03	9.00E-03	0.030	6.45E-03	4.12E-02
240	686	85.01	14.99	1.30E-03	1.92E-03	0.017	6.45E-03	8.79E-03
260	743							

Intermediate pressure – 37°C/km geothermal gradient

						Saturation index		mol C			
Temp (°C)	Pressure (MPs)	pH	C	Ca	Mg	calcite	dolomite	calcite	dolomite	$CO_{2(g)}$	in solution
80	352	4.304	2.79	1.14E-03	1.35E-02	-2.03	-1.65	0.00E+00	1.28E-04	0.000	2.790
100	440	4.305	2.79	1.27E-03	1.36E-02	-1.82	-1.16	0.00E+00	1.55E-04	0.009	2.790
120	527	4.306	2.80	1.42E-03	1.38E-02	-1.65	-0.90	0.00E+00	2.02E-04	0.095	2.799
140	615	4.298	2.89	1.63E-03	1.40E-02	-1.50	-0.64	0.00E+00	2.59E-04	0.181	2.895
160	703	4.285	3.08	1.88E-03	1.42E-02	-1.39	-0.43	0.00E+00	2.76E-04	0.271	3.076
180	791	4.270	3.35	2.16E-03	1.45E-02	-1.30	-0.27	0.00E+00	2.59E-04	0.372	3.347
200	879	4.254	3.72	2.42E-03	1.48E-02	-1.24	-0.15	0.00E+00	2.18E-04	0.482	3.718
220	967	4.242	4.20	2.64E-03	1.50E-02	-1.20	-0.06	8.27E-05	9.17E-05	0.620	4.200
240	1055	4.233	4.82	2.81E-03	1.51E-02	-1.17	0.00	1.32E-04	0.00E+00	0.780	4.820
260	1143	4.232	5.60	2.94E-03	1.51E-02			0.0	0.0		5.603

Temp (°C)	Pressure (MPs)	% initial C in solution	% initial C exsolved (CO_2)	% initial C calcite	% initial C dolomite	distribution (cumulative) $CO_{2(g)}$ (m^3) @ STP	distribution (cumulative) calcite g/l	distribution (cumulative) dolomite g/l
80	352	49.83	50.18	3.83E-03	5.67E-02	0.062	2.15E-02	2.93E-01
100	440	49.83	50.18	3.83E-03	5.22E-02	0.062	2.15E-02	2.69E-01
120	527	49.99	50.02	3.83E-03	4.66E-02	0.062	2.15E-02	2.41E-01
140	615	51.69	48.32	3.83E-03	3.94E-02	0.060	2.15E-02	2.04E-01
160	703	54.92	45.09	3.83E-03	3.02E-02	0.056	2.15E-02	1.56E-01
180	791	59.76	40.25	3.83E-03	2.03E-02	0.050	2.15E-02	1.05E-01
200	879	66.40	33.61	3.83E-03	1.11E-02	0.042	2.15E-02	5.71E-02
220	967	75.00	25.00	3.83E-03	3.27E-03	0.031	2.15E-02	1.69E-02
240	1055	86.07	13.93	2.35E-03	0.00E+00	0.017	1.32E-02	0.00E+00
260	1143							

Lithostatic pressure – 37°C/km geothermal gradient

Temp (°C)	Pressure (MPs)	pH	C	Ca	Mg	Saturation index calcite	Saturation index dolomite	mol C calcite	mol C dolomite	mol C $CO_{2(g)}$	mol C in solution
80	508	4.137	3.16	1.38E-03	1.37E-02	-2.23	-2.10	0.00E+00	1.48E-04	0.000	3.159
100	635	4.140	3.16	1.53E-03	1.38E-02	-2.02	-1.68	0.00E+00	1.53E-04	0.000	3.159
120	762	4.143	3.16	1.68E-03	1.40E-02	-1.85	-1.35	0.00E+00	1.73E-04	0.024	3.159
140	889	4.145	3.18	1.86E-03	1.42E-02	-1.72	-1.09	0.00E+00	2.15E-04	0.121	3.183
160	1016	4.140	3.30	2.07E-03	1.44E-02	-1.62	-0.89	0.00E+00	2.32E-04	0.217	3.304
180	1143	4.131	3.52	2.30E-03	1.46E-02	-1.54	-0.74	0.00E+00	2.18E-04	0.318	3.521
200	1270	4.121	3.84	2.52E-03	1.48E-02	-1.48	-0.63	0.00E+00	1.80E-04	0.422	3.839
220	1397	4.114	4.26	2.70E-03	1.50E-02	-1.45	-0.55	2.73E-05	9.80E-05	0.552	4.261
240	1524	4.110	4.81	2.83E-03	1.51E-02	-1.43	-0.50	1.17E-04	0.00E+00	0.698	4.813
260	1651	4.112	5.51	2.94E-03	1.51E-02			1.44E-04	1.42E-03		5.514

Temp (°C)	Pressure (MPs)	% initial C in solution	% initial C exsolved (CO_2)	% initial C calcite	% initial C dolomite	distribution (cumulative) $CO_{2(g)}$ (m^3) @ STP	distribution (cumulative) calcite g/l	distribution (cumulative) dolomite g/l
80	508	57.33	42.68	2.62E-03	5.14E-02	0.052	1.44E-02	2.61E-01
100	635	57.33	42.68	2.62E-03	4.60E-02	0.052	1.44E-02	2.34E-01
120	762	57.33	42.68	2.62E-03	4.05E-02	0.052	1.44E-02	2.06E-01
140	889	57.76	42.24	2.62E-03	3.42E-02	0.052	1.44E-02	1.74E-01
160	1016	59.96	40.05	2.62E-03	2.64E-02	0.049	1.44E-02	1.34E-01
180	1143	63.90	36.11	2.62E-03	1.80E-02	0.044	1.44E-02	9.14E-02
200	1270	69.67	30.34	2.62E-03	1.01E-02	0.037	1.44E-02	5.13E-02
220	1397	77.32	22.68	2.62E-03	3.56E-03	0.028	1.44E-02	1.81E-02
240	1524	87.34	12.67	2.12E-03	0.00E+00	0.016	1.17E-02	0.00E+00
260	1651							

Appendix III.e. Parameters and results of PHREEQC simulations for ascent of 1 wt.% salinity fluid interacting with differing wallrock scenarios assuming hydrostatic pressure and thermal equilibrium with the regional geothermal gradient (37°C/km). Results illustrated in Figure 7.6. See appendix IIIa for conditions.

	mol					
salinity	Na	Cl	SO_4^{-2}	K	Mg	Ca
1%	0.134	0.156	8.06E-03	2.91E-03	1.51E-02	2.94E-03

Walrock: sandstone #1 (quartz 0.5: K-feldspar 0.01 available to react at each increment)

						Saturation index		mol C			
Temp (°C)	Pressure (MPs)	pH	C	Ca	Mg	calcite	dolomite	calcite	dolomite	$CO_{2(g)}$	in solution
80	229	4.55	2.152	6.17E-04	1.28E-02	-1.89	-1.21	0.0	1.91E-04	0.000	2.152
100	284	4.53	2.152	8.08E-04	1.30E-02	-1.66	-0.79	0.0	1.97E-04	0.070	2.152
120	343	4.52	2.222	1.01E-03	1.32E-02	-1.47	-0.46	0.0	2.51E-04	0.122	2.223
140	400	4.49	2.344	1.26E-03	1.34E-02	-1.31	-0.19	0.0	2.98E-04	0.193	2.345
160	457	4.47	2.538	1.55E-03	1.37E-02	-1.18	0.02	0.0	3.39E-04	0.270	2.539
180	514	4.44	2.809	1.89E-03	1.41E-02	-1.08	0.19	0.0	3.35E-04	0.362	2.810
200	571	4.42	3.172	2.23E-03	1.44E-02	-1.00	0.32	0.0	2.92E-04	0.450	3.173
220	629	4.40	3.622	2.52E-03	1.47E-02	-0.95	0.42	0.0	2.31E-04	0.597	3.622
240	686	4.38	4.219	2.75E-03	1.49E-02	-0.91	0.50	0.0	1.91E-04	0.749	4.219
260	743	4.37	4.969	2.94E-03	1.51E-02			0.0	2.32E-03		4.974

		% initial C				distribution (cumulative)		
Temp (°C)	Pressure (MPs)	in solution	exsolved (CO_2)	calcite	dolomite	$CO_{2(g)}$ (m^3) @ STP	calcite g/l	dolomite g/l
80	229	43.32	56.69	0.0	7.69E-03	0.063	0.00E+00	4.29E-01
100	284	43.32	56.69	0.0	7.93E-03	0.063	0.00E+00	3.93E-01
120	343	44.73	55.28	0.0	1.01E-02	0.061	0.00E+00	3.57E-01
140	400	47.18	52.83	0.0	1.20E-02	0.058	0.00E+00	3.11E-01
160	457	51.09	48.92	0.0	1.37E-02	0.054	0.00E+00	2.56E-01
180	514	56.54	43.47	0.0	1.35E-02	0.048	0.00E+00	1.93E-01
200	571	63.85	36.16	0.0	1.17E-02	0.040	0.00E+00	1.32E-01
220	629	72.90	27.11	0.0	9.31E-03	0.030	0.00E+00	7.79E-02
240	686	84.91	15.09	0.0	7.69E-03	0.017	0.00E+00	3.52E-02
260	743						9.36E-02	

Wallrock: sandstone #2 (quartz 0.5: illite 0.01 mol available to react at each increment)

						Saturation index		mol C			
Temp (°C)	Pressure (MPs)	pH	C	Ca	Mg	calcite	dolomite	calcite	dolomite	$CO_{2(g)}$	in solution
80	229	4.49	2.149	9.76E-04	1.32E-02	-1.83	-1.21	0.0	1.28E-04	0.000	2.149
100	284	4.49	2.149	1.10E-03	1.33E-02	-1.62	-0.79	0.0	1.78E-04	0.071	2.149
120	343	4.48	2.220	1.28E-03	1.35E-02	-1.43	-0.46	0.0	2.41E-04	0.123	2.220
140	400	4.47	2.343	1.52E-03	1.37E-02	-1.28	-0.19	0.0	2.76E-04	0.194	2.344

160	457	4.45	2.538	1.80E-03	1.40E-02	-1.16	0.02	0.0	3.10E-04	0.271	2.539
180	514	4.42	2.809	2.11E-03	1.43E-02	-1.06	0.19	0.0	2.93E-04	0.363	2.810
200	571	4.40	3.173	2.40E-03	1.46E-02	-0.99	0.32	0.0	2.51E-04	0.467	3.174
220	629	4.39	3.640	2.65E-03	1.49E-02	-0.94	0.42	0.0	1.88E-04	0.583	3.640
240	686	4.38	4.224	2.84E-03	1.51E-02	-0.91	0.50	8.51E-05	1.70E-05	0.745	4.224
260	743	4.37	4.969	2.94E-03	1.51E-02			8.51E-05	1.88E-03		4.973

		% initial C				distribution (cumulative)		
Temp (°C)	Pressure (MPs)	in solution	exsolved (CO_2)	calcite	dolomite	$CO_{2(g)}$ (m^3) @ STP	calcite g/l	dolomite g/l
80	229	43.25	56.75	1.71E-03	7.57E-02	0.063	8.52E-03	3.47E-01
100	284	43.26	56.75	1.71E-03	7.05E-02	0.063	8.52E-03	3.23E-01
120	343	44.69	55.32	1.71E-03	6.34E-02	0.061	8.52E-03	2.90E-01
140	400	47.16	52.85	1.71E-03	5.37E-02	0.058	8.52E-03	2.46E-01
160	457	51.09	48.92	1.71E-03	4.26E-02	0.054	8.52E-03	1.95E-01
180	514	56.54	43.47	1.71E-03	3.01E-02	0.048	8.52E-03	1.38E-01
200	571	63.87	36.14	1.71E-03	1.83E-02	0.040	8.52E-03	8.40E-02
220	629	73.26	26.75	1.71E-03	8.24E-03	0.030	8.52E-03	3.77E-02
240	686	85.01	14.99	1.71E-03	6.86E-04	0.017	8.52E-03	3.14E-03
260	743							

Wallrock: carbonate (calcite 0.5: dolomite 0.05 mol available to react at each increment)

						Saturation index		mol C			
Temp (°C)	Pressure (MPs)e	pH	C	Ca	Mg	calcite	dolomite	calcite	dolomite	$CO_{2(g)}$	in solution
80	229	4.43	2.160	2.02E-03	1.05E-02	-1.66	-1.22	-5.69E-04	5.82E-04	0.000	2.161
100	284	4.44	2.161	2.03E-03	1.10E-02	-1.48	-0.80	-5.67E-04	6.42E-04	0.057	2.162
120	343	4.44	2.218	2.11E-03	1.17E-02	-1.33	-0.46	-5.94E-04	7.02E-04	0.123	2.219
140	400	4.43	2.342	2.21E-03	1.24E-02	-1.21	-0.19	-6.44E-04	7.40E-04	0.194	2.343
160	457	4.42	2.537	2.31E-03	1.31E-02	-1.12	0.02	-6.83E-04	7.70E-04	0.271	2.538
180	514	4.41	2.809	2.40E-03	1.39E-02	-1.05	0.19	-3.76E-04	5.32E-04	0.362	2.810
200	571	4.40	3.172	2.55E-03	1.44E-02	-0.99	0.32	-1.27E-04	3.17E-04	0.459	3.173
220	629	4.38	3.632	2.74E-03	1.47E-02	-0.94	0.42	-2.26E-04	3.11E-04	0.592	3.632
240	686	4.38	4.224	2.83E-03	1.51E-02	-0.91	0.50	6.90E-05	4.45E-05	0.744	4.224
260	743	4.37	4.969	2.94E-03	1.51E-02			-3.72E-03	4.64E-03		4.975

		% initial C				distribution (cumulative)		
Temp (°C)	Pressure (MPs)	in solution	exsolved (CO_2)	calcite	dolomite	$CO_{2(g)}$ (m^3) @ STP	calcite g/l	dolomite g/l
80	229	43.48	56.53	-1.14E-02	2.34E-02	0.062	-3.72E-01	8.56E-01
100	284	43.50	56.51	-1.14E-02	2.59E-02	0.062	-3.15E-01	7.48E-01
120	343	44.65	55.36	-1.20E-02	2.82E-02	0.061	-2.58E-01	6.30E-01
140	400	47.15	52.87	-1.30E-02	2.98E-02	0.058	-1.99E-01	5.01E-01
160	457	51.07	48.94	-1.37E-02	3.10E-02	0.054	-1.34E-01	3.64E-01
180	514	56.54	43.47	-7.56E-03	2.14E-02	0.048	-6.59E-02	2.22E-01
200	571	63.85	36.16	-2.55E-03	1.28E-02	0.040	-2.84E-02	1.24E-01
220	629	73.10	26.91	-4.55E-03	1.25E-02	0.030	-1.57E-02	6.55E-02
240	686	85.01	14.99	1.39E-03	1.79E-03	0.017	6.91E-03	8.21E-03
260	743				1.87E-01			

No wallrock

Temp (°C)	Pressure (MPs)	pH	C	Ca	Mg	Saturation index		mol C			
						calcite	dolomite	calcite	dolomite	$CO_{2(g)}$	in solution
80	229	4.49	2.164	9.81E-04	1.32E-02	-1.84	-1.22	0.0	1.26E-04	0.000	2.164
100	284	4.49	2.164	1.11E-03	1.33E-02	-1.62	-0.80	0.0	1.83E-04	0.071	2.164
120	343	4.48	2.220	1.29E-03	1.35E-02	-1.43	-0.46	0.0	2.43E-04	0.123	2.220
140	400	4.47	2.343	1.53E-03	1.38E-02	-1.28	-0.19	0.0	2.78E-04	0.194	2.344
160	457	4.44	2.538	1.81E-03	1.40E-02	-1.16	0.02	0.0	3.12E-04	0.271	2.539
180	514	4.42	2.809	2.12E-03	1.43E-02	-1.06	0.19	0.0	2.92E-04	0.363	2.810
200	571	4.40	3.173	2.42E-03	1.46E-02	-0.99	0.32	0.0	2.40E-04	0.467	3.173
220	629	4.39	3.632	2.66E-03	1.49E-02	-0.94	0.42	0.0	1.76E-04	0.583	3.632
240	686	4.38	4.224	2.83E-03	1.51E-02	-0.91	0.50	6.45E-05	4.77E-05	0.745	4.224
260	743	4.37	4.969	2.94E-03	1.51E-02			6.45E-05	1.90E-03		4.973

Temp (°C)	Pressure (MPs)	% initial C				distribution (cumulative)		
		in solution	exsolved (CO_2)	calcite	dolomite	$CO_{2(g)}$ (m^3) @ STP	calcite g/l	dolomite g/l
80	229	43.56	56.45	0.0	5.08E-03	0.062	6.45E-03	3.50E-01
100	284	43.56	56.45	0.0	7.35E-03	0.062	6.45E-03	3.27E-01
120	343	44.69	55.32	0.0	9.78E-03	0.061	6.45E-03	2.93E-01
140	400	47.16	52.85	0.0	1.12E-02	0.058	6.45E-03	2.48E-01
160	457	51.09	48.92	0.0	1.25E-02	0.054	6.45E-03	1.97E-01
180	514	56.54	43.47	0.0	1.17E-02	0.048	6.45E-03	1.39E-01
200	571	63.87	36.14	0.0	9.67E-03	0.040	6.45E-03	8.55E-02
220	629	73.10	26.91	0.0	7.08E-03	0.030	6.45E-03	4.12E-02
240	686	85.01	14.99	1.30E-03	1.92E-03	0.017	6.45E-03	8.79E-03
260	743				7.64E-02			